Of Triggers, Supersymmetry and Photons

Triggers for Dark Matter and a Search for Gauge-Mediated Supersymmetry Breaking with the ATLAS detector at the LHC



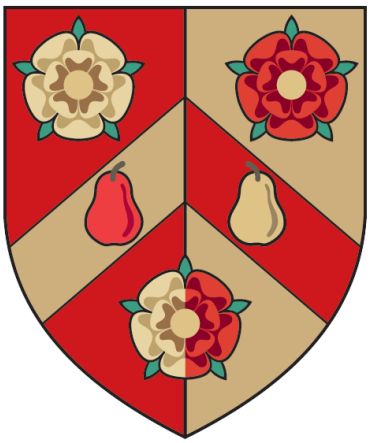

Jonas Würzinger

Wolfson College

University of Oxford

A thesis submitted for the degree of

Doctor of Philosophy

Trinity 2022

Abstract

This thesis summarises research using the ATLAS experiment to search for Dark Matter. A performance study of the ATLAS Run 2 $E_{\mathrm{T}}^{\mathrm{miss}}$ trigger is presented, introducing relevant performance metrics and the algorithms that have lead to the successful operation of the trigger during LHC Run 2. The `trktc` algorithm, a candidate algorithm for the Run 3 $E_{\mathrm{T}}^{\mathrm{miss}}$ trigger, and its performance are discussed in detail, motivating the combination of a tracking-based algorithm with a Run 2 algorithm in constructing the Run 3 primary trigger. A search for new physics in hh+invisible in $139\,\mathrm{fb}^{-1}$ of pp data collected at $\sqrt{s} = 13\,\mathrm{TeV}$ with the ATLAS experiment is presented. Searches are performed for events in which one Higgs boson decays to $\gamma\gamma$ and the other to $b\bar{b}$. The final state of $\gamma\gamma b\bar{b} + E_{\mathrm{T}}^{\mathrm{miss}}$ was previously unexplored by the ATLAS experiment. No evidence for physics beyond the Standard Model has been found. Results are interpreted in the context of Gauge-Mediated Supersymmetry Breaking models. Limits are presented assuming a pure Higgsino neutralino, which decays via $\tilde{\chi}_1^0 \to h\tilde{G}$ or $\tilde{\chi}_1^0 \to Z\tilde{G}$. Assuming $\mathrm{BF}(\tilde{\chi}_1^0 \to h\tilde{G}) = 100\,\%$, models with $m(\tilde{\chi}_1^0) \leq 300\,\mathrm{GeV}$ are excluded. For lower branching fractions of $\mathrm{BF}(\tilde{\chi}_1^0 \to h\tilde{G}) = 75\,\%$, models with neutralino masses of up to $\sim 250\,\mathrm{GeV}$ are excluded. Models with $m(\tilde{\chi}_1^0) = 130\,\mathrm{GeV}$ are excluded for branching fractions as low as $40\,\%$. The presented search almost completely closes a gap in the ATLAS experiment's sensitivity to Dark Matter models.

Acknowledgements

It is an incredible honour and privilege to fulfil my dream of being a part of particle physics research and the hunt for Dark Matter. Fulfilling this dream would not have been possible without the tireless support of many great people, especially during the last two years. I want to take this opportunity to express my sincerest gratitude to them.

First and foremost, I want to thank Yan-Ting Schnellbach for her support in my professional and personal life. You have changed my life in so many ways and have given me the courage to dream big and shoot my shots and for that I will be forever grateful to you. I want to say "danke vielmals" to my parents Claudia and Andreas Würzinger, my brothers Aaron and Niklas, Zoé and Thomas, and my dearest Oma and Opa for always believing in me and listening to me ramble about physics even though you often did not understand a word. I want to express my gratitude to Yan-Jie Schnellbach for always making time for my problems and giving the best advice.

Very special thanks I want to express to Camiel Pieterse, Patrick Willemsen, Niek Gerfen and Magnus Bark for making sure I do not forget the Dutch language. Somewhat ironically, staring at maps and planning imaginary conquests with you once a week has kept me sane throughout these years.

I am grateful to my supervisor Alan Barr for giving me this amazing opportunity of doing a DPhil and for giving me freedom, support and guidance in developing my own ideas about research. For your support during the more difficult parts of the last two years, I am especially grateful. I want to wholeheartedly thank Brian Petersen for teaching me the basics about particle physics as a CERN Summer Student and for supporting me before and during my DPhil. Additionally, I want to thank Alan, Brian and Rosa Simoniello for making the next step in my career possible. I am excited to be given the opportunity to continue my journey through particle physics research.

I want to express my sincerest gratitude to Claudia Merlassino for her patience and trust in me. Almost all I know now about analysis work and ATLAS I have learnt either directly from you or from your support in exploring it myself. My sincerest

thanks go to the other current and former members of the Oxford Standard Model and Beyond ATLAS group Claire Gwenlan, Koichi Nagai, Eimear Conroy, Ynyr Harris, Alessandro Ruggiero, Olivier Salin, Param Luhadiya, Andrei Cristea, Baris Tuncay, Agi Wierzchucka, Clelia Altomonte, Jesse Liu, Mike Nelson, Gabriel Gallardo and Aaron O'Neill for many interesting discussions and for giving me something to look forward to on quarantine Mondays.

I want to thank the members of the ATLAS pMSSM groups for the interesting discussions about Supersymmetric phenomenology and sampling methods in high-dimensional parameter spaces. Very special thanks to Antonia Strubig, Yosse Andrean and Frederik Rühr for pushing the third generation scan ahead with me. The ATLAS $E_{\mathrm{T}}^{\mathrm{miss}}$ trigger group and especially Jon Burr have my gratitude for taking me under their wings during my qualification task and teaching me many fascinating details about triggers.

My sincere gratitude goes to Simon Harrison for his support through the Wolfson Harrison UK Research Council Physics Scholarship. I want to thank Alan Barr, Jon Burr and Yan-Jie Schnellbach for providing feedback on this thesis.

Even if my time in Oxford was relatively short for reasons not of my own choosing, I have had the opportunity to meet many people who have certainly left a mark. I am lucky to have spent time with Federico Celli, Daniel Barrow, Denis Hartmann, Kamil Fischer and Philipp Windischhofer and I will forever treasure your friendship.

There are many names of amazing people which I have not mentioned here. If you are reading this and your name was not yet mentioned, know that I am lucky for being given the opportunity to have met you. Let it be said that I am forever grateful to all of you for supporting me through this journey and letting me take part in yours.

Preface

The main chapters 4 and 5 of this thesis are comprised of work which I have done for the ATLAS collaboration. As this collaboration has more than 3000 active members, results are typically produced in collaboration with others. Below, I will provide a list of my own contributions to the ATLAS experiment.

Any figure or table shown in this thesis was produced by me, unless otherwise specified in the caption. Plots accepted for publication have been marked with '**ATLAS**'.

Run 2 $E_{\mathrm{T}}^{\mathrm{miss}}$ Trigger performance review - I have contributed to the Run 2 performance review of the software-based High Level $E_{\mathrm{T}}^{\mathrm{miss}}$ trigger in ATLAS, studying the performance of different algorithms determining the Missing Transverse Momentum on a trigger level and the impact of their combination, which had lead to the success of the $E_{\mathrm{T}}^{\mathrm{miss}}$ trigger in LHC Run 2. The results of my performance study were collected in an internal note [1] and published in Ref. [2]. A selection of the published results will be shown later in the first half of chapter 4. I was also involved in algorithm combination studies for the Run 3 hardware-based Level-1 $E_{\mathrm{T}}^{\mathrm{miss}}$ trigger, the results of which are not covered in this thesis.

Run 3 $E_{\mathrm{T}}^{\mathrm{miss}}$ Trigger algorithm development - To capitalise on the ability of performing tracking-based algorithms on a trigger level in ATLAS during LHC Run 3, I contributed to the development and evaluation of the `trktc` algorithm for the High Level $E_{\mathrm{T}}^{\mathrm{miss}}$ trigger. The algorithm had previously been developed by collaborators and I separated it into its constituents and studied their performance. This study is presented in detail in the second half of chapter 4.

$\gamma\gamma$bb analysis - This search for new physics considers the previously unexplored final state of $\gamma\gamma$bb+$E_{\mathrm{T}}^{\mathrm{miss}}$. Results are interpreted in terms of a Gauge-Mediated Supersymmetry Breaking model involving decays of the lightest neutralino $\tilde{\chi}_1^0$ to a near-massless gravitino $\tilde{G}$ and either a Standard Model Higgs or a Z-boson. As analysis contact and main analyser, I have contributed to the design and execution of all aspects of the analysis. This includes the development and maintenance of the analysis software framework, including the implementation of the fully data-driven estimation of the non-resonant di-photon and fake-photon backgrounds as

well as the formulation and implementation of a modified ABCD method. Both of these background estimation techniques are vital in achieving sensitivity with this analysis. Additionally, I have defined the signal, control and validation regions of the analysis and implemented the statistical interpretation of the analysis. One of my responsibilities also was the production and validation of signal samples with `MadGraph` and `Pythia 8`. I am also the main author of the analysis internal note [3]. My contributions to the analysis are covered in detail in chapter 5. I have also implemented the statistical interpretation of the analysis based on the shape of the invariant di-photon mass $m_{\gamma\gamma}$, which required the implementation of a spurious signal fit. The shape fit-based statistical interpretation did not offer any significant improvement to the sensitivity reach of the analysis. The results of this study are summarised elsewhere in the analysis internal note and are not included in this thesis.

Physics and trigger validation - I have contributed to the validation of a new ATLAS software release for Run 3, for which I have periodically validated reprocessed data samples produced by collaborators and presented the results within the collaboration.

ATLAS pMSSM studies - The ATLAS pMSSM efforts aim to re-interpret results of existing searches for Supersymmetry in the more general theoretical framework of the phenomenological MSSM (pMSSM). I was analysis contact for the third-generation pMSSM effort, which focuses on top and bottom squarks, and an analysis team member of the general pMSSM effort, which aims to provide an overview of the full 19-dimensional pMSSM. One of my main responsibilities was the development and maintenance of a framework used for sampling the 19-dimensional pMSSM, generating corresponding models and calculating observables such as the predicted Dark Matter relic density Ωh^2 or the anomalous magnetic moment of the muon $(g-2)_\mu/2$. I have performed studies on correlations of these and other observables and their consequences for the model generation and investigated a Markov chain Monte Carlo-based sampling technique and implemented it in the framework. These results are not included in this thesis.

Muon $(g-2)_\mu/2$ and ATLAS - I have used the framework which I developed for sampling the pMSSM to generate Supersymmetric models which are compatible with the recent muon $g-2$ measurement performed at Brookhaven [4]. A plot summarising my results was produced by another member of the ATLAS collaboration and published in Ref. [5]. The results of this study are not included in this thesis.

Contents

1 Introduction **1**

2 The Theory of Particle Physics **5**

2.1 The Standard Model of Particle Physics 6

2.1.1 Fields and the Lagrange Formalism 8

2.1.2 Shortcomings of the Standard Model 13

2.2 Supersymmetry 18

2.2.1 The Minimal Supersymmetric Standard Model 19

2.2.2 Gauge-Mediated Supersymmetry Breaking 23

2.2.3 Current Experimental Limits 24

3 The LHC and ATLAS **27**

3.1 Exploring the Microscopic World 28

3.2 Large Hadron Collider 31

3.3 ATLAS detector 35

3.3.1 Inner Detector 39

3.3.2 Calorimeter 42

3.3.3 Muon Spectrometer 44

3.3.4 Trigger and data acquisition 46

4 The $E_{\mathrm{T}}^{\mathrm{miss}}$ trigger **49**

4.1 Introduction 50

4.2 Run 2 performance 53

4.2.1 $E_{\mathrm{T}}^{\mathrm{miss}}$ trigger algorithms 53

4.2.2 Trigger performance metrics 59

4.3 Run 3 tracking ideas 71

4.3.1 The `trktc` algorithm 71

4.3.2 Performance of the `trktc` constituents 76

5 The $\gamma\gamma$bb analysis **81**

5.1 Gauge-Mediated Supersymmetry breaking at the LHC 82

5.2 Data and Simulation Samples 86

5.2.1 Background Samples 86

5.2.2 Signal Samples 88

5.3 Event Reconstruction, Selection & Categorisation 91

5.3.1 Event Reconstruction 91

5.3.2 Event Selection 93

5.3.3 Signal Region Optimisation 95

5.3.4 Event Categorisation 101

5.4 Background Estimation Techniques 103

5.4.1 2x2D Sideband Method 104

5.4.2 Modified ABCD Method - used for SR2 only 114

5.4.3 Validation of Background Modelling 119

5.5 Signal Region Sensitivity 125

5.6 Systematic Uncertainties 128

5.7 Results 131

5.8 Conclusions 137

6 In Summary **139**

References **143**

Appendices

A Appendix: The $\gamma\gamma$bb analysis **165**

A.1 Signal sample re-weighting factor 165

A.1.1 $hh \to \gamma\gamma b\bar{b}$ signal samples 165

A.1.2 $Zh \to \gamma\gamma b\bar{b}$ signal samples 167

A.2 Asymmetric m_{bb} Selection 169

A.3 2x2D expressions 172

A.4 Region Yields 177

List of Abbreviations **179**

List of Figures **183**

List of Tables **187**

1

Introduction

The Standard Model (SM) of Particle Physics describes all currently known matter and forces excellently but cannot provide a Dark Matter (DM) candidate. However, DM is estimated to constitute about 85% of the total matter content of our universe [6], implying that the origin of a large fraction of the universe's matter content is unknown. As physicists strive towards the goal of a 'theory of everything', this thought can sometimes feel a bit unnerving, making the question of the nature and origin of DM especially intriguing. The hunt for DM can therefore be seen as one of the biggest challenges in the history of physics. While many theories can account for DM, the searches presented in this thesis are motivated by the theory of Supersymmetry, which remains one of the best motivated candidates for physics Beyond the Standard Model (BSM) due to its theoretical motivations and its ability to address a wide range of experimental shortcomings of the SM. This thesis contributes to the search for DM using the ATLAS experiment at the LHC through studies on the performance of the ATLAS missing transverse momentum trigger in LHC Run 2, the development of new trigger algorithms for Run 3, as well as a search for Supersymmetric DM.

In the search for new physics, a detailed understanding of theoretical predictions is essential. This is true for the SM as well as for theories of new physics, such as Supersymmetry. The main concepts of the SM, DM as well as Supersymmetry and its motivations are introduced in chapter 2.

The LHC as well as the ATLAS detector and all its subsystems are discussed in chapter 3. One of these subsystems, the trigger, is explored further in chapter 4. A trigger for invisible (potentially DM) particles, the $E_{\mathrm{T}}^{\mathrm{miss}}$ trigger, is introduced. This chapter covers the trigger's performance during LHC Run 2 (2015 - 2018) by introducing the most important trigger performance metrics and explaining the details of the different algorithms employed by the Run 2 $E_{\mathrm{T}}^{\mathrm{miss}}$ trigger which have led to its successful operation. Additionally, the chapter also includes a detailed study of a Run 3 candidate algorithm as well as its prospective performance, which drove the choice of the ATLAS primary $E_{\mathrm{T}}^{\mathrm{miss}}$ trigger for LHC Run 3.

A search for new physics in final states of $\gamma\gamma b\bar{b} + E_{\mathrm{T}}^{\mathrm{miss}}$ is presented in chapter 5. The search is performed in $139\,\mathrm{fb}^{-1}$ of data at $\sqrt{s} = 13\,\mathrm{TeV}$ collected by the ATLAS experiment. Results are interpreted in the context of Gauge-Mediated Supersymmetry Breaking (GMSB) models. Such models can provide viable DM candidates while providing an explicit breaking mechanism to Supersymmetry, making them especially interesting models to explore. As there are many possible sources of photon mismeasurement in ATLAS, dedicated background estimation methods developed for this analysis are presented. These methods are validated in detail and shown to successfully estimate the non-resonant di-photon and fake-photon backgrounds. The search contributes to closing the gap in the ATLAS experiment's sensitivity to GMSB models for low Higgsino masses.

The findings presented in this thesis are summarised in chapter 6.

2

The Theory of Particle Physics

Contents

2.1 The Standard Model of Particle Physics 6
2.1.1 Fields and the Lagrange Formalism 8
2.1.2 Shortcomings of the Standard Model 13
2.2 Supersymmetry 18
2.2.1 The Minimal Supersymmetric Standard Model 19
2.2.2 Gauge-Mediated Supersymmetry Breaking 23
2.2.3 Current Experimental Limits 24

The field of particle physics is governed by the scientific method. Hypotheses are formed using theoretical predictions which are then tested in experiments. While this is true for any area of science, particle physics experiments have reached unprecedented scale and precision. This thesis focuses on the experimental capabilities in the search for new physics with the ATLAS detector, which will be introduced in chapter 3. With the increasing experimental precision, there is a rising demand on the precision of theoretical predictions of quantum mechanical observables. The remainder of this chapter will focus on how theoretical predictions are made in particle physics. This chapter will introduce the Standard Model (SM) of particle physics as well as the main motivations for Physics Beyond the Standard Model (BSM) and the main concepts behind Supersymmetry (SUSY), one of the leading candidates for BSM physics.

This chapter is structured as follows: The Standard Model of particle physics, its particle content, Lagrangian, as well as shortcomings will be introduced in section 2.1. Supersymmetry, one of the prime candidates for BSM physics and the basis of this thesis will be introduced in section 2.2. This chapter draws inspiration from the treatment in Refs. [7–10].

2.1 The Standard Model of Particle Physics

The Standard Model (SM) of particle physics collects all known particles and quantised fields in one theory. It contains the strong nuclear force, the weak nuclear force and the electromagnetic force, which are all known forces with the exception of gravity. A schematic overview of the SM can be seen in figure 2.1.

The particles in the Standard Model are separated by spin, where the matter particles have spin-$\frac{1}{2}$ (fermions) and the force carriers have spin-1 (bosons). The Higgs boson is the only scalar particle in the SM with 0 spin. Quarks are separated by their charge into up-type with $2/3$ charge and down-type with $-1/3$ charge, where all charges are given in units of the electron charge e. There are three generations of

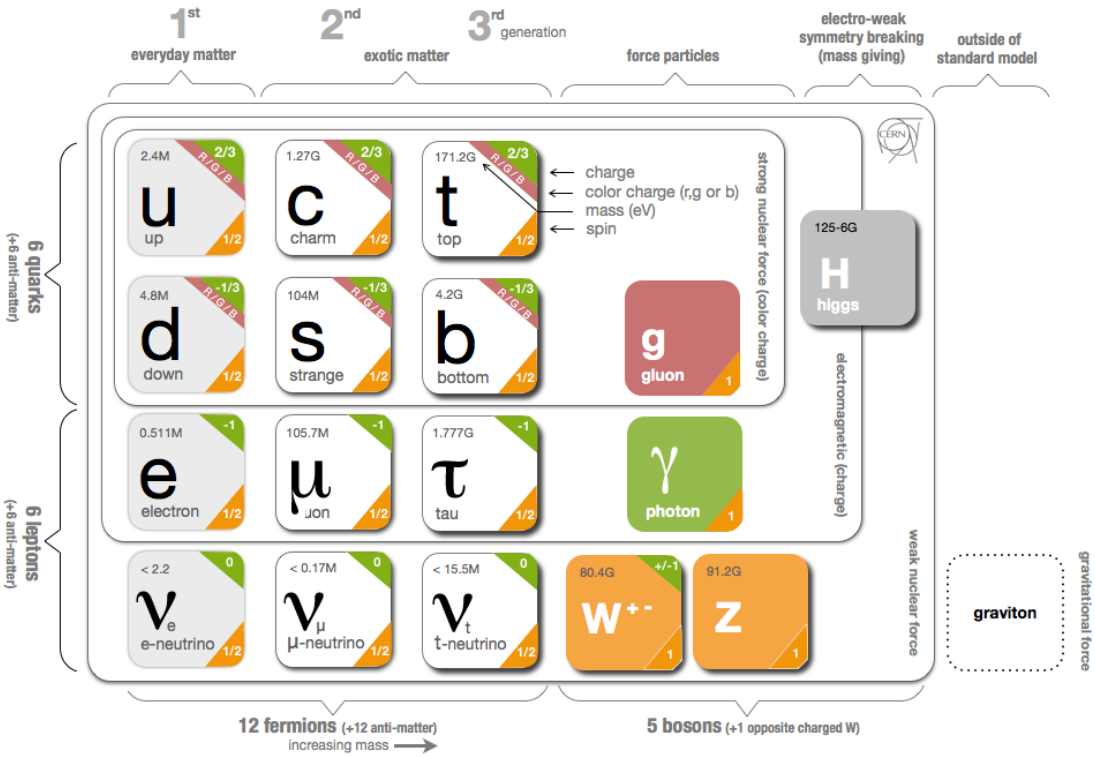

Figure 2.1: Schematic overview of the particle content of the Standard Model. Particles are separated into fermions (left) and bosons (right), with the fermions grouped by generations of increasing mass. Rectangles are included to indicate interactions between the gauge bosons and fermions. The charge, colour charge, mass (in eV) and spin are included. A graviton is not included in the Standard Model. Figure and caption adapted from Ref. [11].

both quarks and leptons, which are ordered by increasing mass. The up- and down-quarks u and d bind together to form protons and neutrons, which in turn form nucei. The nuclei then form bound states with electrons, creating the atoms and molecules which surround us. The fermions of the first generation are therefore referred to as "everyday matter" particles.

The gluon g couples to the quarks via the strong nuclear force, the photon γ couples to the quarks and charged leptons via the electromagnetic force and the $W^{\pm}$- and Z-bosons couple to both quarks and leptons via the weak nuclear force. The Higgs boson plays a vital role in obtaining mass terms for other particles and couples to all particles with a mass. The graviton G, a hypothetical particle mediating gravity, is

not included in the Standard Model. There are theories which include gravity, such as Gauge-Mediated Supersymmetry Breaking, which will be discussed in section 2.2.2.

Theoretical predictions for the behaviour of particles are made using Quantum Field Theory [12], which links each physical particle described above to a quantum field. The next section briefly summarises the theoretical formalism behind the fields contained in the Standard Model.

2.1.1 Fields and the Lagrange Formalism

The structure of the SM is governed by the $\mathrm{SU}(3)_C \times \mathrm{SU}(2)_L \times \mathrm{U}(1)_Y$ gauge group, where C, L and Y indicate colour charge, chirality and hypercharge, respectively. The theory of the SM makes use of fields to represent each particle. Different fields are used for particles with spin 0, $1/2$ and 1. The Higgs boson is associated to a complex scalar field ϕ with 0 spin, Weyl spinors ψ are used to describe the fermion fields with $s = 1/2$, while vector fields A are used for $s = 1$. The vector fields consist of eight fields g for the gluons associated to $\mathrm{SU}(3)_C$, two charged fields $W^{1,2}$ and one neutral field W^3 for the bosons associated to $\mathrm{SU}(2)_L$ and a hypercharge boson field B associated to $\mathrm{U}(1)_Y$. The $W^a = (W^1, W^2, W^3)$ and B bosons mix during electroweak symmetry breaking [13–16] to form the charged $W^{\pm}$-bosons and the neutral Z-boson and photon γ, as will be explored later in this section.

The field content of the SM is collected in the Lagrangian $\mathcal{L}$, given by [17]

$$\mathcal{L} = -\frac{1}{4}F^2 + i\bar{\psi}\not{D}\psi + \bar{\psi}\boldsymbol{y}\psi\phi + |\mathrm{D}\phi|^2 - V(\phi) + \mathrm{h.c.}, \tag{2.1}$$

where all sums over indices have been suppressed to improve readability, following the method developed in Ref. [10]. All terms are required to be invariant under the Standard Model gauge group, invariant under Lorentz transformations and translations, renormalisable and satisfy energetic stability (there should be a vacuum state with lowest possible energy) [18]. The six terms of equation 2.1 are the only possible combinations of SM fields which satisfy these requirements, with one

exception. An additional term of $\theta\epsilon_{\mu\nu\rho\sigma}F_{\mu\nu}F^{\rho\sigma}$, with $\epsilon_{\mu\nu\rho\sigma}$ the Levi-Civita tensor, is also possible. This term, however, has no consequences in perturbative theories and, if present, manifests itself in the Electric Dipole Moment (EDM) of the neutron, which has not been observed yet, implying that θ be very close to 0 [16]. A non-zero neutron EDM would be an important source of matter-antimatter asymmetry (CP violation), which the SM cannot provide enough of (see section 2.1.2). Nevertheless, as no neutron EDM has been observed yet, this 'topological' term is not relevant for the physics discussed in this thesis and will not be considered further. This absence of any evidence for CP violation in the strong sector is referred to as the strong CP problem [19–21] and will be explored more in section 2.1.2.

The first of the six terms of equation 2.1, the Yang-Mills term $-\frac{1}{4}F^2$, serves as a kinetic term and a term describing the self-interactions of the gauge fields [22]. Here, F is known as the field strength tensor given by $-igF = [\mathrm{D}, \mathrm{D}]$, where $\mathrm{D} = \partial - igA$ the covariant derivative [16]. Each of the three gauge groups is assigned a unique set of a coupling g and gauge fields A. Here, the couplings g can be matrices.

The Dirac term $i\bar{\psi}\not{\mathrm{D}}\psi$ describes the interaction of the Weyl spinors ψ with the gauge fields, which enter this term through the covariant derivative. As all gauge fields enter this term, it describes the interactions of the electromagnetic, weak and strong force carriers with the fermionic matter particles [17]. Here we are using the Feynman slash notation $\not{\mathrm{D}} = \gamma\mathrm{D}$ to indicate Lorentz contraction between the gamma matrices and the covariant derivative. The gamma matrices γ are defined by their anticommutator $\{\gamma, \gamma\} = 2\eta$, with $\eta = \mathrm{diag}(1, -1, -1, -1)$ the Minkowski spacetime metric tensor. The gamma matrices are required to ensure that this term obeys Lorentz symmetry.

The Yukawa terms $\bar{\psi}\boldsymbol{y}\psi\phi + \mathrm{h.c.}$ describe the coupling of the Weyl spinor fields ψ to the Higgs field ϕ [16]. After electroweak symmetry breaking, it describes the coupling of quarks and leptons to the Higgs boson as well as the mass terms for the quarks and leptons. Here, $\boldsymbol{y}$ is a 3×3 matrix in family space, which quantifies the masses of quarks and charged leptons as well as the flavour mixing terms and $\mathrm{h.c.}$ indicates the

hermitian conjugate. The mixing occurs through the Cabbibo-Kobayashi-Maskawa (CKM) matrix in the case of the quarks, which gives rise to flavour oscillations through the mixing of neutral mesons [23] or the Pontecorvo-Maki-Nakagawa-Sakawa (PMNS) matrix in the case of neutrinos, which gives rise to neutrino oscillations [24].[1]

The Higgs sector is described by the kinetic term $|\mathrm{D}\phi|^2$ and the Higgs potential $V(\phi)$, where the Higgs potential is given by $V(\phi) = \mu^2\phi^2 + \frac{1}{4}\lambda\phi^4$ [16] and describes the Higgs field self-interaction $\mu^2\phi^2$ and the quadratic self-interaction $\frac{1}{4}\lambda\phi^4$ quantified by the dimensionless coupling $\lambda > 0$.

The Higgs sector changes during electroweak symmetry breaking [13–16]. Assuming that the self-coupling parameter $\mu^2 < 0$, the complex scalar ϕ is expanded around the minimum of the potential by

$$\phi = \frac{1}{\sqrt{2}} \begin{pmatrix} 0 \\ v + h \end{pmatrix}, \tag{2.2}$$

where v is the vacuum expectation value given by $v = 2\sqrt{-\mu^2/\lambda}$ and h the field associated to the Higgs boson. We can write the covariant derivative explicitly as $\mathrm{D} = \partial - i\frac{1}{2}g_1 B - i\frac{1}{2}g_2 \sum_{a=1}^{3} \boldsymbol{\sigma}^a W^a$, with $\boldsymbol{\sigma}^a$ the Pauli matrices [16]. Using this explicit form during the expansion of ϕ, the kinetic term becomes:

$$\begin{aligned} |\mathrm{D}\phi|^2 =& (\mathrm{D}\phi)^\dagger (\mathrm{D}\phi) \\ =& \frac{v^2}{8}\Big[g_2^2(W^1 - iW^2)(W^1 + iW^2) \\ &+ g_1^2 BB + g_2^2 W^3 W^3 - g_1 g_2 (BW^3 + W^3 B)\Big] + F(\partial\phi, \phi), \end{aligned} \tag{2.3}$$

where $F(\partial\phi, \phi)$ contains all terms containing partial derivatives $\partial\phi$. Recognising that mass terms in the Lagrangian take the form of $\frac{1}{2}m^2 VV$ for neutral real vector fields V and $m^2 V^+ V^-$ for a conjugate pair of complex vectors $V^\pm$ [16], it becomes evident that the expansion of the ϕ field has generated masses of the B and W^a

[1] To make neutrino oscillations possible, neutrinos have to be massive, meaning that the addition of a neutrino mass term to the Lagrangian is necessary. As it is not clear yet, what shape such a mass term would take, neutrino masses and the PMNS matrix are considered as BSM physics for the scope of this thesis.

bosons, where there are some mixed mass terms containing B and W^3. The $W^\pm$ bosons and their masses are therefore given by [16]

$$W^\pm = \frac{1}{\sqrt{2}}(W^1 \mp iW^2) \qquad \text{with mass } m = \frac{1}{2}vg_2. \tag{2.4}$$

The off-diagonal terms in the mass matrix can be eliminated by diagonalising the mass matrix, resulting in one massive and one massless neutral boson [16]

$$\begin{aligned} Z &= \frac{1}{\sqrt{g_1^2 + g_2^2}}(g_2W^3 - g_1B) \qquad && \text{with mass } m = \frac{1}{2}v\sqrt{g_1^2 + g_2^2}, \\ A &= \frac{1}{\sqrt{g_1^2 + g_2^2}}(g_2W^3 + g_1B) && \text{with mass } m = 0, \end{aligned} \tag{2.5}$$

where Z and A are the fields associated to the Z-boson and the photon. This process is referred to as electroweak symmetry breaking as only one of the two gauge bosons obtains a mass.

To summarise, the four electroweak bosons W^a and B undergo mixing to form mass eigenstates during electroweak symmetry breaking. The charged W^1 and W^2 mix to form the two charged $W^\pm$-bosons, while the neutral W^3 and B mix to form form the neutral Z-boson and photon γ. The Higgs field ϕ retains one degree of freedom in the form of the neutral scalar Higgs boson h. The $W^\pm$- and Z-bosons obtain their masses during this process, while the photon remains massless. The Higgs boson also obtains its mass during electroweak symmetry breaking, but its mass terms arise from the $\mu^2\phi^2 + \frac{1}{4}\lambda\phi^4$ terms. The mass of the Higgs boson comes out to be $m_h = \sqrt{-2\mu^2}$ [16].

As the Lagrangian itself is not an observable and therefore cannot be measured by experiments, predictions are made for event rates and cross sections σ, which are measures for the probability of a particular process [23]. Both are calculated using the action S, given by the integral over the Lagrangian $S = \int \mathcal{L}\mathrm{d}^4x$. From the action, the scattering amplitude $|\mathcal{M}|$ can be calculated via a path integral [23]

$$|\mathcal{M}| \sim \int \mathcal{D}\mathrm{e}^{iS}. \tag{2.6}$$

Assuming $2 \to n$ scattering, the cross section can finally be obtained by [23]

$$\sigma = \frac{1}{4E_1E_2|\vec{v}_1 - \vec{v}_2|} \int |\mathcal{M}|^2 \mathrm{d}\Pi_{\mathrm{LIPS}}, \tag{2.7}$$

where E_i and $\vec{v}_i$ are the energies and velocities of the two incoming particles and Π_{LIPS} is the Lorentz-invariant phase space accessible in the final state.

The Standard Model can provide precise predictions of cross sections for various processes. A summary of several SM cross section measurements with the ATLAS experiment is shown in figure 2.2. As the vast majority of measurements agree with the SM prediction, the Standard Model can be seen as the most successful theory to date. Nevertheless, the theory has several substantial shortcomings, which will be explored in the next section.

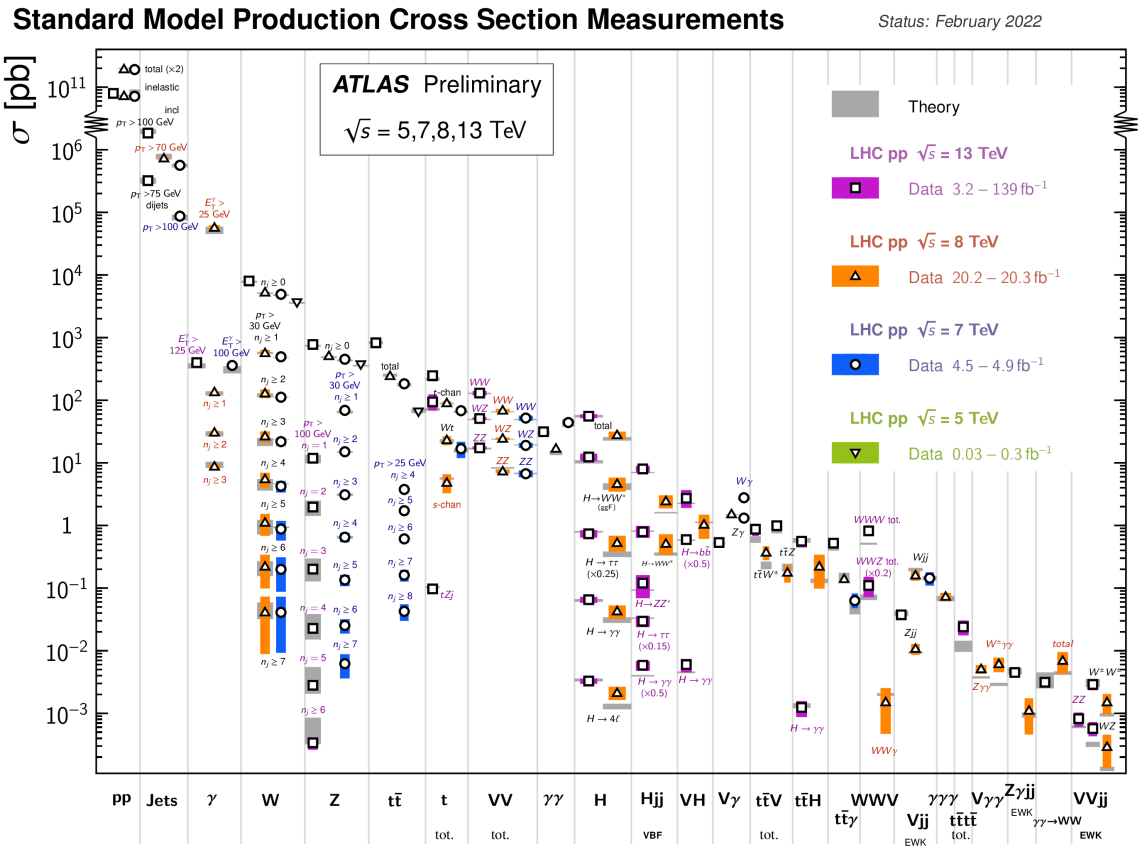

Figure 2.2: Summary of several Standard Model total and fiducial cross section measurements by the ATLAS experiment, where fiducial means within the acceptance of the detector. The measurements are corrected for branching fractions, compared to the corresponding theoretical expectations. In some cases, the fiducial selection is different between measurements in the same final state for different centre-of-mass energies $\sqrt{s}$, resulting in lower cross section values at higher $\sqrt{s}$. Figure and caption adapted from Ref. [25].

2.1.2 Shortcomings of the Standard Model

The shortcomings of the Standard Model are of both theoretical and experimental nature. The theoretical shortcomings are features of the theory which do not align with expectations for a complete theory. The experimental shortcomings are a collection of measurements which show a disagreement with the SM expectation that can be solved by introducing new fields and thus new particles.

Theoretical Shortcomings

Grand unification. The Standard Model offers no explanation for its gauge group structure or representations. There is no deeper reason for the number of free parameters in the SM and consequentially for the number of generations of fermions. It is unclear why the fermions follow a chiral structure and there is no explanation for the hierarchy of gauge and Yukawa couplings and consequentially the fermion mass hierarchy. These issues can be addressed by a unification of the strong and electroweak forces in a Grand Unified Theory (GUT). This unification is achieved easily in Supersymmetric theories, as the evolution of the gauge couplings is changed by the addition of Supersymmetric particles such that there is approximate unification at a unification scale $M_U \sim 1.5 \times 10^{16}\,\text{GeV}$ in the Minimal Supersymmetric Standard Model (MSSM) [7, 26–29]. Supersymmetry does not achieve unification with gravity.

Hierarchy problem. The value of the Higgs boson mass m_h receives loop corrections from other particles in the theory. Assuming the existence of a fundamental length scale κ^{-1}, corresponding to the Planck scale $\kappa = \mathcal{O}(10^{19}\,\text{GeV})$, the Higgs boson mass receives a correction from the ultraviolet cutoff of $\sim \kappa^2$, i.e. a correction of the order of $10^{38}\,\text{GeV}$ [30–34]. Hence, for the Higgs boson mass to take the observed value of $m_h = 125\,\text{GeV}$ [35], it has to be fine-tuned over more than 30 orders of magnitude. While this is not impossible, theorists have argued such a mechanism to be unnatural [33, 34]. Supersymmetry solves the hierarchy problem by introducing new particles, which correspond to loop contributions with equal size but opposite sign, effectively cancelling the dependence on κ^2.

Experimental Shortcomings

Neutrino sector. The observation of neutrino oscillations [36, 37] implies the existence of a mass difference between the different flavours of neutrinos, thus implying that neutrinos have mass. As mentioned in footnote 1 in the previous section, a mass term for the neutrinos is not included in the SM Lagrangian as it is not clear which

shape the mass term should take [38]. Additionally, anomalies have been found in neutrino oscillations in short baseline and reactor neutrino experiments [39–42]. These anomalies can be explained by requiring the existence of a fourth neutrino type.

Lack of CP violation. The combination of charge and parity symmetries, also known as CP-symmetry, is only minimally violated in the SM, implying that similar numbers of particles and anti-particles are expected in the Standard Model. However, as antiparticles are quite rare in our universe, there is a matter-antimatter asymmetry of about 6×10^{-10}, while the Standard Model can only account for an asymmetry of $\sim 10^{-20}$ [43, 44]. Furthermore, there is no observed CP violation in the strong sector, which the Standard Model can not offer an explanation for. This is known as the strong CP problem [19–21]. A popular solution to the strong CP problem is to introduce a chiral symmetry (Peccei-Quinn symmetry) to the SM, the breaking of which leads to a light pseudoscalar particle, the axion [45].

Lepton flavour universality. In the Standard Model, the different flavours of leptons are universal. However, many recent measurements suggest different behaviours in decay rates to the different lepton flavours, thus breaking lepton flavour universality [46–51]. A common solution to the breaking of lepton flavour universality is the addition of leptoquarks, hypothetical particles which couple to both quarks and leptons and thus would allow transitions from quarks to leptons (and vice-versa) [52].

Anomalous magnetic moment of the muon. In 2021, the Fermilab National Accelerator Laboratory Muon $g-2$ experiment [53] confirmed the measurement of the magnetic moment of the muon previously made at Brookhaven National Laboratory [4] in 2006. The two results are compatible and in significant tension with the Standard Model. Here, new physics such as Supersymmetry can again enter in the calculation through loop contributions, thereby significantly impacting the theoretical prediction.[2]

[2]It should be noted that the measured result is compatible with the SM prediction when using a Hadronic Vacuum Polarisation as calculated in lattice QCD by the BMW collaboration [54, 55].

W-boson mass. A recent measurement of the W-boson mass is in significant tension with the Standard Model [56]. Just like the Higgs boson, the W-boson receives loop contributions from other particles of the theory. The introduction of new physics can therefore relieve this tension.

Inflation. Cosmological inflation [57–59], a phase of exponential expansion in the early universe, requires the existence of a scalar field which drives the expansion. While one of the candidates for this field is the Higgs field, many models consider fields not included in the SM [60]. As new scalars naturally arise in Supersymmetry, the theory can provide many models for inflation [61].

Dark matter. There are a number of astrophysical observations which indicate that the amount of visible matter in the universe is not sufficient, indicating the existence of 'invisible matter' which is at most only very weakly coupled to the particles of the Standard Model. This form of matter is known as Dark Matter (DM). Historically, the first evidence for DM came from the measurement of galactic rotation velocity distributions first in the Milky Way [62] and then later in other galaxies [63, 64]. The DM hypothesis was further strengthened by results from weak and strong gravitational lensing [65, 66]. While the behaviour of galactic rotation curves and gravitational lensing can also be explained by modifications of gravitational interactions, such as Modified Newtonian Dynamics (MOND) [67], there are a number of observations compatible with the existence of DM which such modifications of gravity can not explain. Firstly, there are fluctuations in the Cosmic Microwave Background (CMB) which can be explained by particle Dark Matter abundances compatible with results from galactic rotation curves and gravitational lensing [6, 68]. Secondly, DM also provides a solution to the problem of structure formation, where additional gravitational attraction is needed in the early universe dominated by radiation, such that galaxies can form [69, 70]. Lastly, modified gravity theories are incompatible with observations related to the Bullet Cluster, a galaxy cluster resulting from the recent collision of two galaxies [71] and with the existence of galaxies without any DM-like signatures, which have recently been found [72].

Dark energy. The observed accelerated expansion of the universe driven by the cosmological constant can not be explained by the Standard Model [68, 73–76]. Additionally, measurements of the CMB indicate that the universe is largely flat, indicating that a large fraction of the universe's energy density is missing to reach the critical density needed in a flat universe [6, 70].

2.2 Supersymmetry

As mentioned in the previous section, Supersymmetry (SUSY) provides a solution to the hierarchy problem. This is done by imposing a overarching symmetry linking bosonic fields to fermionic fields. As fermionic loop contributions to the Higgs mass receive a relative minus sign to bosonic contributions, the two cancel exactly, if a new boson with the same quantum numbers (with the exception of spin) is assigned to every fermion and vice-versa. The exact cancellation occurs only for an unbroken Supersymmetry.

In its minimal form, the Minimal Supersymmetric Standard Model (MSSM), Supersymmetry therefore introduces a 'superpartner' (also: 'sparticle') for every particle in the Standard Model, as well as two Higgs doublets containing the SM Higgs. It not only addresses the hierarchy problem, but also improves grand unification and can provide a DM candidate which depends on the considered model [7], while being able to explain the deviation in the W-boson mass [56], the anomalous magnetic moment of the muon [5, 77] and providing candidates for inflationary models [61]. Chapter 2.2.1 covers the particle and field content of the MSSM in more detail.

As no sparticles have been observed by experiments yet, the sparticle masses have to be different from the masses of the corresponding SM partners. Supersymmetry, if realised in nature, therefore has to be a broken symmetry. Different candidates for SUSY breaking mechanisms are discussed in section 2.2.2. In particular, Gauge-Mediated Supersymmetry Breaking (GMSB) is discussed. This mechanism leads to the introduction of a new sparticle[3], which can be searched for in collider experiments. A search for GMSB models is presented in chapter 5.

[3] In addition to the sparticles introduced by the MSSM.

2.2.1 The Minimal Supersymmetric Standard Model

The Minimal Supersymmetric Standard Model (MSSM) extends the Standard Model by collecting the SM fields and their corresponding superpartners in a supermultiplet, as shown in table 2.1.

Chiral supermultiplets			
Names	spin-0	spin-1/2	$(SU(3)_C, SU(2)_L, U(1)_Y)$
Higgs, higgsinos	$(H_u^+ \; H_u^0)$ $\left(H_d^0 \; H_d^-\right)$	$\left(\tilde{H}_u^+ \; \tilde{H}_u^0\right)$ $\left(\tilde{H}_d^0 \; \tilde{H}_d^-\right)$	**(1, 2,** 1**)** **(1, 2,** -1**)**
squarks, quarks (× 3 generations)	$(\tilde{u} \; \tilde{d})_L$ $\tilde{u}_R^*$ $\tilde{d}_R^*$	$(u_L \; d_L)$ $u_R^\dagger$ $d_R^\dagger$	**(3, 2,** $\frac{1}{3}$**)** **(**$\bar{\mathbf{3}}$**, 1,** $-\frac{4}{3}$**)** **(**$\bar{\mathbf{3}}$**, 1,** $\frac{2}{3}$**)**
sleptons, leptons (× 3 generations)	$(\tilde{\nu}_e \; \tilde{e})_L$ $\tilde{e}_R^*$	$(\nu_e \; e)_L$ $e_R^\dagger$	**(1, 2,** -1**)** **(1, 1,** 2**)**
Gauge supermultiplets			
Names	spin-1/2	spin-1	$(SU(3)_C, SU(2)_L, U(1)_Y)$
gluino, gluon winos, W^a bosons bino, B boson	$\tilde{g}$ $\tilde{W}^a$ $\tilde{B}$	g W^a B	**(8, 1,** 0**)** **(1, 3,** 0**)** **(1, 1,** 0**)**

Table 2.1: Supermultiplets in the MSSM and the corresponding representations under $(SU(3)_C, SU(2)_L, U(1)_Y)$. The electric charge is given by $Q = I_3 + \frac{1}{2}Y$, where I_3 is the $SU(2)_L$ eigenvalue and the hypercharge Y the $U(1)_Y$ eigenvalue. The subscripts L and R indicate left and right chirality. The spin-0 fields are scalars, while the spin-1/2 fields are two-component Weyl fermions, causing a difference in conjugation. Table adapted from Ref. [7].

In the spin-0 sector, the MSSM introduces two neutral Higgs fields, H_u^0 and H_d^0, which give masses to the up- and down-type quarks respectively through their Yukawa interactions, as well as two corresponding charged Higgs fields H_u^+ and H_d^-, thereby extending the spin-0 Higgs sector to two Higgs doublets from only one in the SM. In the spin-$\frac{1}{2}$ Higgs sector, there are two doublets containing charged and neutral superpartners of the Higgs fields, the Higgsino fields $\tilde{H}$. The SM Higgs boson field h is a linear combination of the two neutral fields H_u^0 and H_d^0. It should be noted that, while the Higgs boson is the only scalar particle in the Standard Model, it is integrated into the overall structure of Supersymmetric theories. The quarks q are

assigned scalar (spin-0) superpartners, the squarks $\tilde{q}$, while the leptons are assigned scalar superpartners called sleptons $\tilde{l}$. The Higgs and Higgsino fields as well as the SM fermions f and their superpartners, referred to as sfermions $\tilde{f}$ in the following, are collected in chiral supermultiplets. A similar strategy is employed for the SM gauge boson fields, which are collected with their gaugino superpartners in gauge supermultiplets. To serve as an extension of the Standard Model, the supermultiplet's representations under $\mathrm{SU}(3)_C \times \mathrm{SU}(2)_L \times \mathrm{U}(1)_Y$ are identical to those of the SM.

The full Supersymmetric Lagrangian with all indices suppressed is given by [7]

$$\begin{aligned}\mathcal{L}_{\mathrm{SUSY}} = &-\frac{1}{4}F^2 + i\lambda^\dagger\bar{\boldsymbol{\sigma}}\mathrm{D}\lambda + i\psi^\dagger\bar{\boldsymbol{\sigma}}\mathrm{D}\psi - \frac{1}{2}\psi\boldsymbol{y}\psi\phi - \frac{1}{2}\psi\boldsymbol{M}\psi \\ &- \sqrt{2}g(\phi^*\boldsymbol{T}\psi)\lambda + |\mathrm{D}\phi|^2 - V(\phi,\phi^*) + \mathrm{h.c.},\end{aligned} \tag{2.8}$$

where ψ and ϕ indicate the Weyl fermion and scalar components of the chiral supermultiplets and λ the Weyl fermion gaugino fields describing the gluino, bino and wino. The gauge fields A again enter through F and D, just like in the SM. Additionally, the $\bar{\boldsymbol{\sigma}}$ matrices are defined by

$$\bar{\boldsymbol{\sigma}}^i = \begin{cases} \mathrm{diag}(1,1) & \text{if } i = 0 \\ -\boldsymbol{\sigma}^i & \text{if } i = 1,2,3, \end{cases}$$

with $\boldsymbol{\sigma}$ the Pauli matrices. The gamma matrices γ are defined as before, $\boldsymbol{M}$ are the symmetric mass matrices corresponding to the fermion fields ψ and $\boldsymbol{y}$ again quantify the Yukawa coupling. The $\boldsymbol{T}$ are the generators of the chiral supermultiplet gauge transformations given by $\boldsymbol{T} = \frac{1}{2}\boldsymbol{\sigma}$ [7]. The scalar potential $V(\phi,\phi^*)$ is given by

$$V(\phi,\phi^*) = |\boldsymbol{M}\phi|^2 + \frac{1}{2}\phi\boldsymbol{M}\boldsymbol{y}^*\phi^*\phi^* + \frac{1}{4}|\phi\phi\boldsymbol{y}|^2 + \frac{1}{2}g^2(\phi^*\boldsymbol{T}\phi)^2 + \mathrm{h.c.} \tag{2.9}$$

and describes the ϕ mass term as well as the ϕ self-interactions [7].

In the MSSM, electroweak symmetry breaking provides the two Higgs fields H_u and H_d with vacuum expectation values of $\langle H_u\rangle = \nu\sin\beta$ and $\langle H_d\rangle = \nu\cos\beta$, with $\nu \approx 174\,\mathrm{GeV}$ and β a free parameter of the theory [7]. This results in three neutral

Higgs bosons h, H^0 and A and two charged Higgs bosons H^+ and H^-. Here, h and H^0 are CP-even and A is CP-odd.[4]

Electroweak symmetry breaking also occurs in the Supersymmetric sector of the supermultiplets. The neutral bino $\tilde{B}$ and wino $\tilde{W}^0$ mix with the neutral Higgsinos $\tilde{H}_d^0$ and $\tilde{H}_u^0$, resulting in four fermionic neutralino mass eigenstates $\tilde{\chi}_i^0$, with $i = 1, 2, 3, 4$ ordered by mass ranging from lowest ($i = 1$) to highest ($i = 4$). Their masses are largely determined by the Bino, Wino and Higgsino mass parameters M_1, M_2 and μ [78]. The lightest neutralino $\tilde{\chi}_1^0$ is considered the LSP in many models. If the lightest neutralino has a mass of $m(\tilde{\chi}_1^0) = \mathcal{O}(100\,\text{GeV})$, such models naturally account for the correct quantity of Dark Matter, which is referred to as the 'Weakly Interacting Massive Particle (WIMP) miracle' [79–81].

Just as the charged components W^a mix to form the $W^\pm$-boson in the SM, the charged components of the $\tilde{W}^a$ first mix together to form the charged Winos $\tilde{W}^\pm$, which subsequently mix with the charged Higgsino components $\tilde{H}_u^+$, $\tilde{H}_d^-$ in forming the fermionic chargino mass eigenstates $\tilde{\chi}_i^\pm$, with $i = 1, 2$.[5] The reader is referred to Ref. [78] for more details on the mixing of charginos and neutralinos.

For the squarks and sleptons, mixing only occurs in the third generation sector, where the scalar superpartners of the left- and right-handed components of a fermion $(\tilde{f}_L, \tilde{f}_R)$ mix to $\tilde{f}_i$, with $i = 1, 2$. This happens for the stop $\tilde{t}$ and sbottom $\tilde{b}$ squarks as well as for the stau $\tilde{\tau}$. As the sfermion mixing is dominated by the Yukawa coupling and the Yukawa couplings of the first and second generation are negligible [7], the first and second generation squarks and sleptons are not expected to mix substantially. They are typically indicated with $\tilde{f}_L$ and $\tilde{f}_R$. A second consequence of the negligible Yukawa coupling is that pairs of masses of first and second generation sfermions are almost identical. This leads to seven almost mass-degenerate, unmixed pairs

[4] The neutral, CP-odd Higgs boson A is not to be confused with the gauge fields, for which the symbol A is also used.

[5] Since there are two charginos of opposite charge for each mass index i, the index can only take values of $i = 1, 2$.

of sfermions $(\tilde{e}_R, \tilde{\mu}_R)$, $(\tilde{e}_L, \tilde{\mu}_L)$, $(\tilde{\nu}_e, \tilde{\nu}_\mu)$, $(\tilde{u}_R, \tilde{c}_R)$, $(\tilde{u}_L, \tilde{c}_L)$, $(\tilde{d}_R, \tilde{s}_R)$, $(\tilde{d}_L, \tilde{s}_L)$, avoiding a possibly large Flavour-Changing Neutral Current (FCNC) [7, 82].

The precise values of all sparticle masses depend on the values of MSSM parameters. The reader is referred to Refs. [7] and [82] for a summary of the calculated masses. The MSSM therefore does not provide a precise prediction for the sparticle masses.

However, to address the hierarchy problem, all mass parameters are expected to be of the order of the soft SUSY scale m_{soft}, which is expected to be $\mathcal{O}(\text{TeV})$ at most [7]. Additionally, the mass of the Z-boson is directly related to the Higgsino mass parameter μ and the mass of the H_u boson with $m_Z^2 = -1/2(|\mu|^2 + m_{H_u}^2)$ at tree-level [83, 84]. Fine-tuning arguments therefore suggest Higgsino masses below the TeV range [85, 86], which is accessible by the LHC, as will be explored in more detail in chapter 5.

A common feature in many Supersymmetric models is the conservation of a quantum number referred to as R-parity with [7, 10]:

$$R = (-1)^{3(B-L)+2S} = \begin{cases} 1 & \text{for SM fields} \\ -1 & \text{for SUSY fields,} \end{cases} \tag{2.10}$$

where S indicates spin and B and L are baryon- and lepton-number, respectively. R-parity conservation has a handful of important consequences. Firstly, the Lightest Supersymmetric Particle (LSP) of a particular Supersymmetry model is always stable, since its decay is forbidden by R-parity conservation. This mechanism ensures that SUSY can provide a Dark Matter candidate, if the LSP is weakly coupled to the Standard Model particles. Secondly, it implies that the production of sparticles at colliders will always occur in pairs. Lastly, baryon-number violating decays, such as the decay of the proton $p \to \pi^0 e^+$, which is yet unobserved [87], are forbidden. The absence of empirical evidence for the decay of the proton forms one of the strongest constraints on GUTs [88, 89], which R-parity conserving SUSY is compatible with by construction.

In R-Parity Violating (RPV) SUSY models, the lightest neutralino is allowed to decay to e.g. three quarks [7]. If the corresponding coupling is sufficiently small, the

neutralino can nevertheless be a viable DM candidate [90]. The reader is referred to Ref. [90] for a detailed summary of RPV Supersymmetry. Searches for RPV SUSY have been performed by both ATLAS and CMS [91–97]. The $\gamma\gamma$bb search presented in chapter 5 considers R-parity conserving SUSY models. Hence, R-parity conservation is assumed throughout the remainder of this thesis.

2.2.2 Gauge-Mediated Supersymmetry Breaking

It is generally assumed that Supersymmetry should be an exact symmetry, which is broken spontaneously. To provide this breaking, Gauge-Mediated Supersymmetry Breaking (GMSB) extends the MSSM by introducing a new supermultiplet containing a massless Weyl fermion called the 'goldstino' as well as a vacuum expectation value $\langle F \rangle$.

Aditionally, GMSB requires the introduction of gravity into Supersymmetry by promoting SUSY to a local symmetry. The resulting theory of 'supergravity' introduces a spin-2 graviton, mediating the gravitational force, as well as its spin-$3/2$ superpartner the gravitino $\tilde{G}$, which are both massless before SUSY breaking [7, 98–105]. During SUSY breaking, the gravitino then obtains a mass by absorbing the goldstino, completely analogous to how the $W^{\pm}$ and Z bosons obtain their masses in the Higgs mechanism. The process of Supersymmetry breaking is therefore referred to as the 'super-Higgs' mechanism.

In this model, the breaking of Supersymmetry can be mediated either by gravitational or gauge interactions. In the first case, the gravitino only interacts through gravitation, putting it out of reach of collider experiments. Such models require a relatively heavy gravitino of at least $100\,\text{GeV}$, which easily over-produces Dark Matter [106, 107]. In Gauge-Mediated Supersymmetry Breaking models, the gravitino mass is expected to be much lower than the masses of other sparticles, implying that the gravitino naturally arises as LSP [7, 108]. Despite its low predicted mass, the gravitino can still be a viable DM candidate, for masses above the keV range, since gravitino Dark

Matter is not produced through the WIMP mechanism and instead depends on the reheating temperature of the universe after inflation [109–111].

If we assume the lightest neutralino $\tilde{\chi}_1^0$ to be the Next-to-Lightest Supersymmetric Particle (NLSP), there are three possible decay modes of the lightest neutralino [112], as illustrated in figure 2.3, where the $\tilde{\chi}_1^0$ decays to a γ, Z or h and a gravitino $\tilde{G}$. More details on searches for such GMSB models are presented in chapter 5. Other possibilities for NLSPs include the partners of the right-handed sleptons, predominantly the stau $\tilde{\tau}$ [108].

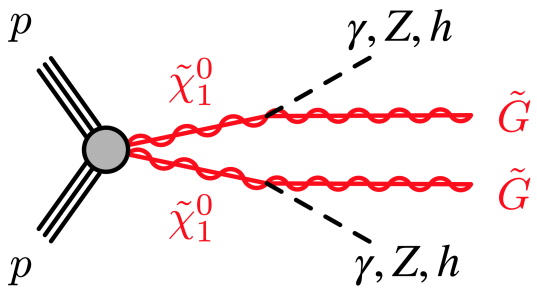

Figure 2.3: Feynman diagram for the GMSB model. Supersymmetric particles are indicated in red, while SM particles are indicated in black.

2.2.3 Current Experimental Limits

As no sparticles have been found yet, limits can be set on the masses of Supersymmetric particles. The current limits as measured by the ATLAS experiment are shown in figure 2.4. The presented are interpreted in the context of simplified models, assuming certain sparticle masses and branching fractions. While many searches for Supersymmetry have already been performed, a large fraction of the parameter space is still uncovered, even for masses well below the TeV range. One example for this are models assuming a decay of the lightest neutralino to a Higgs boson and a gravitino, which ATLAS can currently not provide limits for for neutralino masses of $m(\tilde{\chi}_1^0) \approx 250\,\text{GeV}$. The analysis presented in chapter 5 was designed to fill this gap in the experiment's sensitivity.

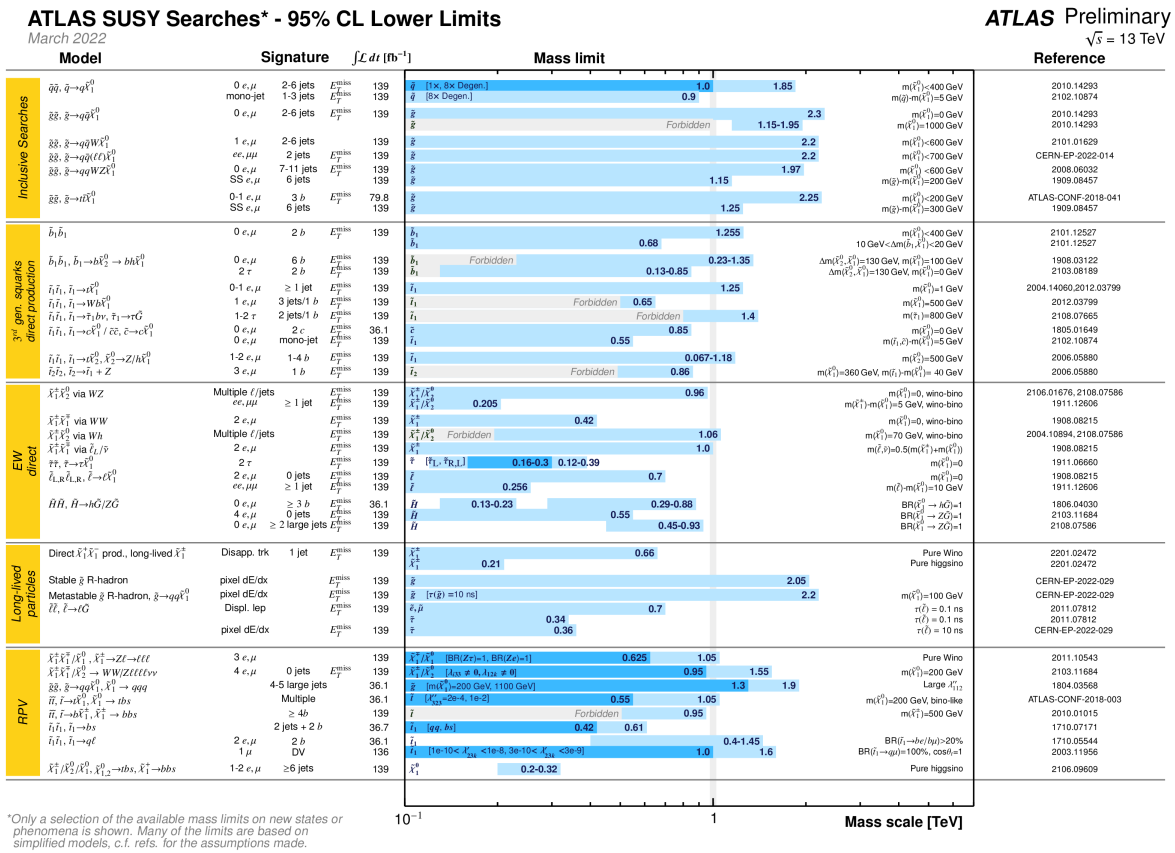

Figure 2.4: Mass reach of the ATLAS searches for Supersymmetry. A representative selection of the available search results is shown. Results are quoted for the nominal cross section in both a region of near-maximal mass reach and a demonstrative alternative scenario, in order to display the range in model space of search sensitivity. Some limits depend on additional assumptions on the mass of the intermediate states, as described in the references provided in the plot. In some cases these additional dependencies are indicated by darker bands showing different model parameters. Figure and caption taken from Ref. [113].

3

The LHC and ATLAS

Contents

3.1 Exploring the Microscopic World 28
3.2 Large Hadron Collider 31
3.3 ATLAS detector 35
3.3.1 Inner Detector 39
3.3.2 Calorimeter 42
3.3.3 Muon Spectrometer 44
3.3.4 Trigger and data acquisition 46

3.1 Exploring the Microscopic World

For all of recorded history, humans have been fascinated by the microscopic world. Greek philosophers Leucippus and Democritus postulated the existence of small indivisible particles called atoms already in the 5th century BC [114]. Their ideas could not be proven experimentally until 1808, when John Dalton published a book collecting experimental evidence on the matter, concluding that distilled water consists of hydrogen and oxygen, particles that have the same fundamental properties everywhere [115].

From an experimental standpoint, the exploration of the microscopic world began when Dutch businessman Anthonie van Leeuwenhoek polished and ground lenses, drastically improving upon the first microscope developed by Galileo Galilei in 1610 [116, 117].[1] Van Leeuwenhoek intended to inspect the quality of thread with his microscope and instead made a number of revolutionary scientific discoveries. In 1683, he discovered bacteria[2], founding the field of Microbiology [118].

The resolution of such microscopes can be expressed by [119]:

$$d = \frac{\lambda}{2\mathrm{N.A.}}, \tag{3.1}$$

with λ the wavelength of light and N.A. the objective numerical aperture, a constant describing the microscope. If smaller objects are to be studied, λ can be reduced or, like in van Leeuwenhoek's case, the numerical aperture N.A. can be increased.

The first insight into the sub-atomic structure was obtained by the Geiger-Marsden-Rutherford experiments, which proved the existence of a small, heavy core in the centre of the atom referred to as the nucleus. This discovery was made with the use of scattering experiments, scattering alpha particles with thin foils of metal [120–122].

[1] In 1610, Galilei was using a telescope at close range to inspect and magnify parts of insects. He did not refer to this device as a microscope yet, but used it as such.

[2] Van Leeuwenhoek referred to them as "dierkes", which is colloquial Dutch for "small animals".

At first glance, these experiments have little in common with van Leeuwenhoek's discoveries. However, the same fundamental principle for the resolution applies. Making use of the matter-wave duality, the wavelength λ in equation 3.1 can be expressed by the non-relativistic de Broglie wavelength $\lambda = \frac{h}{mv}$, with h the Planck constant and m and v the mass and velocity of the respective particle [123]. The resolution then becomes:

$$d = \frac{h}{2\mathrm{N.A.}mv}. \tag{3.2}$$

As h and m are constants, the most efficient way of improving the resolution is to increase the scattering particle's velocity (and consequentially its kinetic energy). This fundamental principle gave rise to the field of High Energy Physics and lead to the construction of increasingly large and powerful particle accelerators, reaching increasingly high energies, thus probing smaller length scales and producing increasingly heavy states. The key variable in this context is the energy of the colliding particles in the centre-of-mass frame $\sqrt{s}$, effectively describing the accessible energy in the collision.

Following this principle, electrons e^- and positrons e^+ were collided at $\sqrt{s}$ of up to $208\,\mathrm{GeV}$ at the Large Electron-Positron Collider (LEP) [124]. This, among other results, lead to the precise measurement of the Z-boson mass, its decay width and cross-sections [125–127]. Searches for Supersymmetric particles were also performed [128–130], setting limits on the Supersymmetric parameter space which are relevant to this day.

The first machine to reach the TeV scale was the Tevatron accelerator at the Fermi National Accelerator Laboratory in the US [131]. Collisions of protons p with anti-protons $\bar{p}$ at $\sqrt{s}$ of up to $1.92\,\mathrm{TeV}$, leading to the discovery of the top quark [132, 133].

The focus of this thesis, however, are searches for new physics performed with the ATLAS detector at the Large Hadron Collider (LHC), which is the most powerful particle accelerator to date, reaching centre-of-mass energies of $\sqrt{s} = 13\,\mathrm{TeV}$ [134, 135]. The most important discovery of the LHC era is the discovery of the Higgs boson

[136, 137]. The Large Hadron Collider is discussed in section 3.2. The ATLAS detector and its subsystems are explored in more detail in section 3.3. This chapter draws inspiration from the treatment in Refs. [8–10], which provide a very concise summary of the Large Hadron Collider as well as the ATLAS experiment.

3.2 Large Hadron Collider

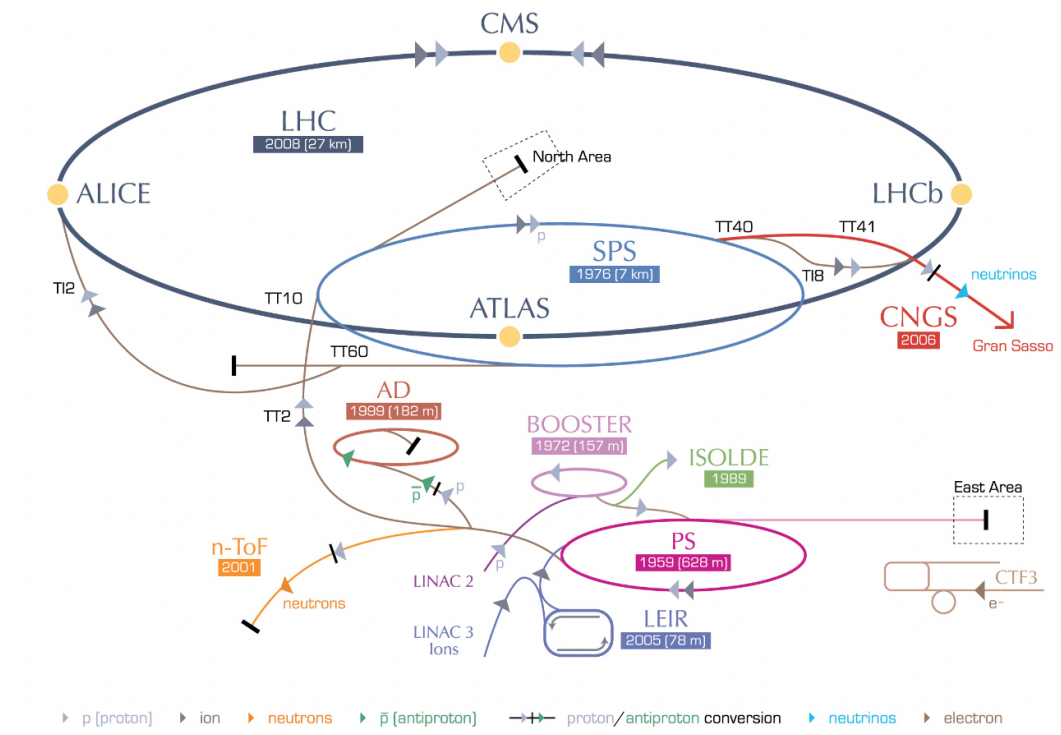

Figure 3.1: Schematic of the CERN accelerator complex. Figure adapted from Ref. [138].

The Large Hadron Collider (LHC) [135] is the largest particle accelerator complex to date. It is a synchrotron with a circumference of 27 km located at the CERN laboratory in Switzerland, approximately 100 m underground. At the LHC, collisions occur between two beams of protons (proton-proton or pp), as well as between beams of heavy ions. In proton-proton collisions, hydrogen gas is ionised and the resulting protons enter the CERN accelerator complex at the LINAC2 linear accelerator. The protons undergo several accelerations stages before being injected into the LHC, as is schematically illustrated in figure 3.1. The LHC makes use of Radio Frequency (RF) cavities for acceleration, dipole magnets for bending and quadrupole magnets for focusing the beams. At the moment when collisions take place at the LHC, two beams of up to 2544 bunches of about 10^{11} protons circulate in opposite directions. This thesis presents results from LHC Run 2, which lasted from 2015 until 2018,

during which protons collided at centre-of-mass energies of $\sqrt{s} = 13\,\text{TeV}$ [139]. The bunches are spaced in time-intervals of $25\,\text{ns}$.

The rate of relevant events for physics analysis at the LHC is often expressed by

$$\frac{\mathrm{d}N}{\mathrm{d}t} = \sigma L_{\text{inst.}}, \tag{3.3}$$

where σ is the cross-section of the respective process, as introduced in section 2.1 and $L_{\text{inst.}}$ is the instantaneous luminosity provided by the LHC. During Run 2, the LHC has reached a peak luminosity of $L_{\text{inst.}} = 2.1 \times 10^{34}\,\text{cm}^{-2}\text{s}^{-1}$ [140]. As protons are composite particles, consisting largely of quarks and gluons, the interaction occurs between the proton composites, also referred to as partons, where the knowledge of the proton composition is collected in a Parton Distribution Function (PDF). The PDF quantifies the probability of finding a specific parton, depending on the four-momentum transfer Q^2 and the fraction of the longitudinal proton momentum carried by the parton, also known as Bjorken-x [141]. The behaviour of the partons is dominated by non-perturbative QCD effects [142]. Hence, non-perturbative QCD plays a vital role in accurately describing a PDF. The proton does not only contain quarks and gluons, but antiquarks are also present, due to gluons splitting into quark-antiquark pairs. The reader is referred to Ref. [142] for a complete overview of PDFs.

The collisions relevant for physics analysis typically involve large momentum transfer between the two partons. Events resulting form such collisions are referred to in the following as hard-scatter events. As mentioned before in section 2.1, the cross-section is a measure for the probability of a hard-scatter event resulting in a particular final state of interest. It collects all dependencies on the underlying physical process. The instantaneous luminosity $L_{\text{inst.}}$ is a measure for the rate of hard-scatter events provided by the LHC. The integrated luminosity given by

$$L = \int L_{\text{inst.}}\,\mathrm{d}t \tag{3.4}$$

is used as a measure for the total amount of data collected. In total, the Run 2 luminosity relevant for physics analysis amounts to $L = 139\,\text{fb}^{-1}$, where $1\,\text{fb}^{-1} =$

$10^{-39}\,\mathrm{cm}^{-2}$. Figure 3.2a shows the evolution of the integrated luminosity recorded by the ATLAS experiment during Run 2.

As the proton bunches contain many protons and the detector readout time exceeds the time intervals between collisions (cf. section 3.3), the probability of a recorded event containing only a single hard-scatter interaction is very low. The additional interactions are referred to as pile-up $\langle\mu\rangle$. The pile-up distributions for the various years of Run 2 data recorded by ATLAS are shown in figure 3.2b. Pile-up can enter collisions from interactions occurring in the same bunch-crossing as the collision of interest (in-time pile-up), interactions occurring shortly before or after the collision of interest if the detector readout time is longer than the time between bunch-crossings (out-of-time pile-up) or from background events related to the LHC beam [143]. Pile-up is difficult to model and presents physics analyses with a serious challenge. It is especially challenging at the trigger level, as will be discussed in detail in chapter 4.

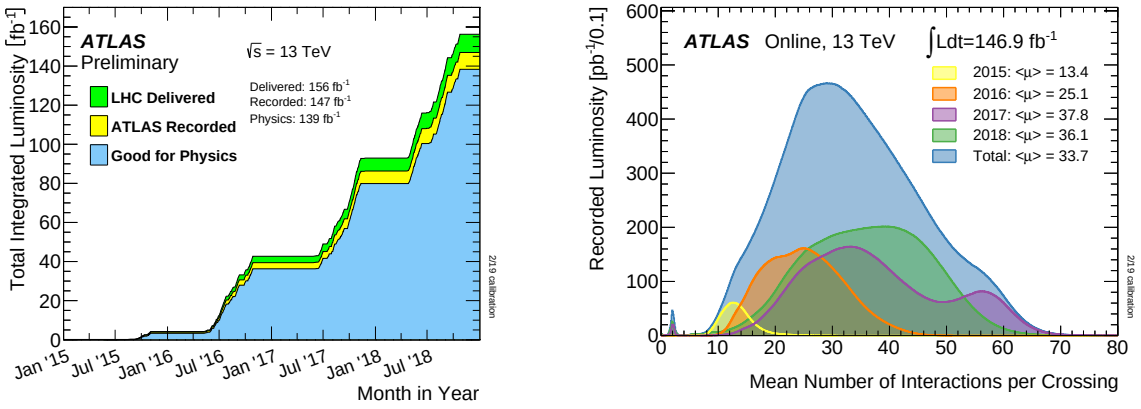

(a) **(b)**

Figure 3.2: Evolution of the integrated luminosity (3.2a) and mean number of interactions per bunch-crossing (3.2b) recorded by ATLAS during stable beams for pp collisions at $\sqrt{s} = 13$ TeV centre-of-mass energy in LHC Run 2. Figures taken from Ref. [140].

Collisions of the beams occur at four interaction points spread along the LHC ring, each corresponding to a major experiment. These are ATLAS [134], LHCb [144], CMS [145] and ALICE [146]. Of these four, the ATLAS and CMS detectors are so-called "general-purpose detectors", investigating a wide range of physics. The LHCb detector has been designed for flavour physics precision measurements and the

ALICE experiment focuses on heavy-ion collisions and measurements on the Quark-Gluon Plasma (QGP). The reader is referred to Ref. [147] for an introduction to flavour physics and Ref. [148] for a review of the phenomenology of the QGP. These topics will not be explored further here, as the focus of this thesis lies on searches for new physics with the ATLAS detector. The ATLAS detector design and its sub-systems will be explored in more detail in the next section.

3.3 ATLAS detector

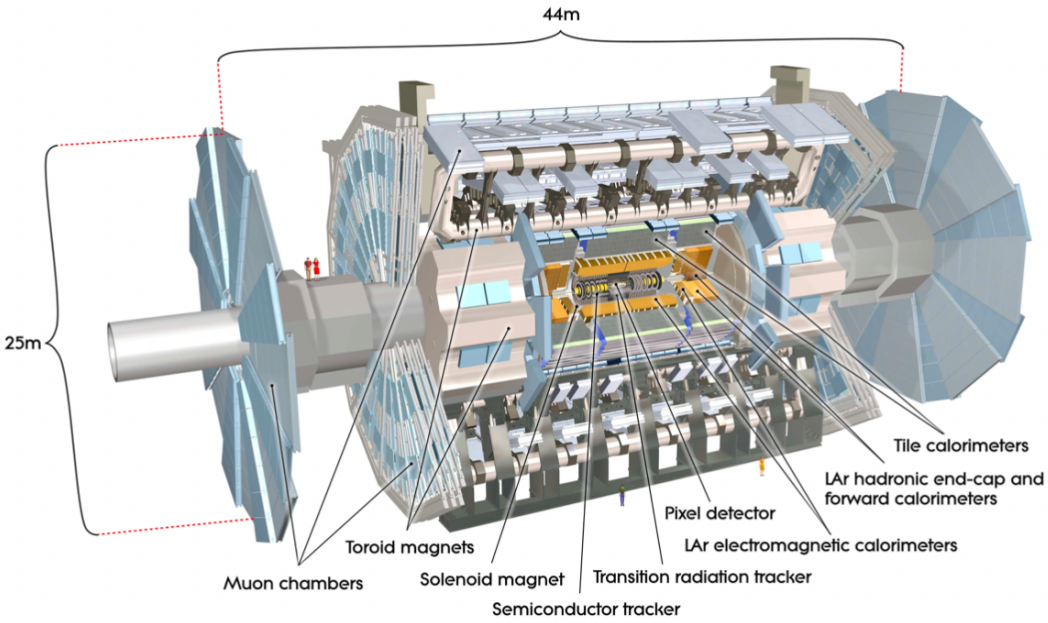

Figure 3.3: Cut-away view of the ATLAS detector. Two average size humans are included for reference. Figure taken from Ref. [134].

The ATLAS (**A** **T**oroidal **L**HC **A**pparatu**S**) detector [134] is a cylindrical detector located at the LHC. It is the largest-volume particle detector at the LHC. The general-purpose detector has been designed for a wide range of physics analyses, which demands excellent performance of the detector, its trigger system and reconstruction [149]. A particular focus in the design of the ATLAS detector was the Higgs boson, which ATLAS and CMS discovered in 2012 [136, 137].

The detector is roughly $44\,\text{m}$ long and $25\,\text{m}$ high and weighs about 7000 tons. A cut-away view of the detector is shown in figure 3.3. It uses a right-handed coordinate system, with:

- x-axis: Towards the centre of the LHC.
- y-axis: Upwards.
- z-axis: Along the LHC beam.

Most analyses make use of cylindrical coordinates (r, ϕ, z), where ϕ is the azimuthal angle, r the radial distance and z the distance along the beam with respect to the interaction point. To indicate the direction of the movement of a decay product inside the detector, the angle ϕ and the pseudorapidity $\eta = -\ln[\tan(\theta/2)]$ are used, where θ is the polar angle with respect to the beam axis z. As the polar angle approaches zero, pseudorapidity increases rapidly, making small differences in θ especially evident. The distance between two particles in the detector is given by $\Delta R = \sqrt{(\Delta\eta)^2 + (\Delta\phi)^2}$.

The detector is hermetic in ϕ, meaning that detection for all values of ϕ are possible. The detector achieves an overall good coverage in $|\eta|$ of up to 4.9, where only large values are inaccessible as the geometry approaches the beampipe at $\theta = 0$. The ATLAS detector consists of three major subsystems. The Inner Detector, used for tracking, the calorimeter, used for energy measurements and the muon spectrometer, used for muon detection. The $|\eta|$ coverage changes between these subsystems. The subsystems and the properties of the subsystem's components are listed in table 3.1.

Subsystem	$\lvert\eta\rvert$ coverage	Active material	Trigger	Object reconstruction
Inner detector				
Pixel	< 2.5	Silicon		Vertex, Q, $\vec{p}$
SCT	< 2.5	Silicon	ROI: μ, e, τ, b-jet	Vertex, Q, $\vec{p}$
TRT	< 2.0	Argon, xenon gas		Vertex, Q, $\vec{p}$, e PID
Calorimetry				
ECal	< 3.2	Liquid Argon		EM energy, e/γ PID
HCal Endcap	$[1.5, 3.2]$	Liquid Argon	$E_{\mathrm{T}}^{\mathrm{miss}}$, (b)-jet, e, γ	Hadronic energy
FCal	$[3.1, 4.9]$	Liquid Argon		EM & hadronic energy
HCal Barrel	< 1.7	Tile scintillator		Hadronic energy
Muon spectrometry				
RPCs	< 1.05	$C_2H_2F_4$ gas	μ	
TGCs	$[1.05, 2.4]$	CO_2, n-C_5H_{12} gas	μ	Q, $\vec{p}(\mu)$
MDTs	< 2.7	Ar, CO_2 gas	-	
CSCs	$[2.0, 2.7]$	Ar, CO_2 gas	-	

Table 3.1: Summary of the ATLAS detector subsystems and their components. For each component, the $|\eta|$ coverage, its active material and use of the trigger as well as the use in object reconstruction are indicated. Here, Q and $\vec{p}$ indicate charge and momentum reconstruction and PID the particle identification. Neutral particles such as photons or neutrons do not leave tracks in the Inner Detector. The detector can only detect particles which interact via either the strong or Electromagnetic (EM) forces. The Inner Detector is used in Region of Interest (ROI)-based triggers. Table adapted from Ref. [10].

A large fraction of the ATLAS physics program is aimed at collisions with very large momentum transfer. Such signal models typically involve collisions with very large transverse particle momenta (momenta in the plane orthogonal to the beam pipe) p_{T}. This is true for, for example, the Standard Model production of Higgs bosons [136, 137], as well as searches for new physics, including the search for gauge mediated Supersymmetry in final states of $\gamma\gamma b\bar{b} + E_{\mathrm{T}}^{\mathrm{miss}}$ presented in chapter 5.

Particle	Mass [GeV]	Stability	Detector Signature
Quarks			
Up u	2×10^{-3}	Unstable	ECal, HCal (jets)
Down d	5×10^{-3}	Unstable	ECal, HCal (jets)
Strange s	0.1	Unstable	ECal, HCal (jets)
Charm c	1.3	Metastable	ECal, HCal (jets), displaced vertex
Bottom b	24.2	Metastable	ECal, HCal (jets), displaced vertex
Top t	173	Unstable	m_t from e.g. $t \to bW \to$ jets
Leptons			
Neutrinos ν_e, ν_μ, ν_τ	$< 10^{-9}$	Stable	$E_{\mathrm{T}}^{\mathrm{miss}}$
Electron e	5×10^{-4}	Stable	Silicon/TRT hits, transition radiation, ECal
Muon μ	0.106	Stable	Silicon/TRT hits, muon spectrometer
Tau τ	1.78	Metastable	Jets, displaced vertex
Bosons			
Gluon g	0	Unstable	ECal, HCal (jets)
Photon γ	0	Stable	No tracks, ECal deposit
$W^{\pm}$-boson	80.3	Unstable	m_W from e.g. $W \to \mu\nu_\mu$
Z-boson	90.1	Unstable	m_Z from e.g. $Z \to \mu\mu$
Higgs boson h	125.1	Unstable	m_h from e.g. $h \to \gamma\gamma$

Table 3.2: Summary of the SM particles produced at the LHC, their masses, stability on the timescale resolvable by the detector and resulting signature in the detector. Section 2.1 includes more information on the properties of these particles. Masses are taken from the Particle Data Group [35]. Table adapted from Ref. [10].

To aid in the reconstruction and identification of different particles, the detector subsystems have been designed such that different particles result in different signatures in the detector. The different signatures of the Standard Model particles produced in LHC collisions are listed in table 3.2. Quarks and gluons are highly interactive, leading to hadronisation and the resulting formation of collimated streams of hadrons, referred to as jets in the following. Particles which produce jets typically deposit their entire energy in the hadronic calorimeter and are therefore considered unstable.

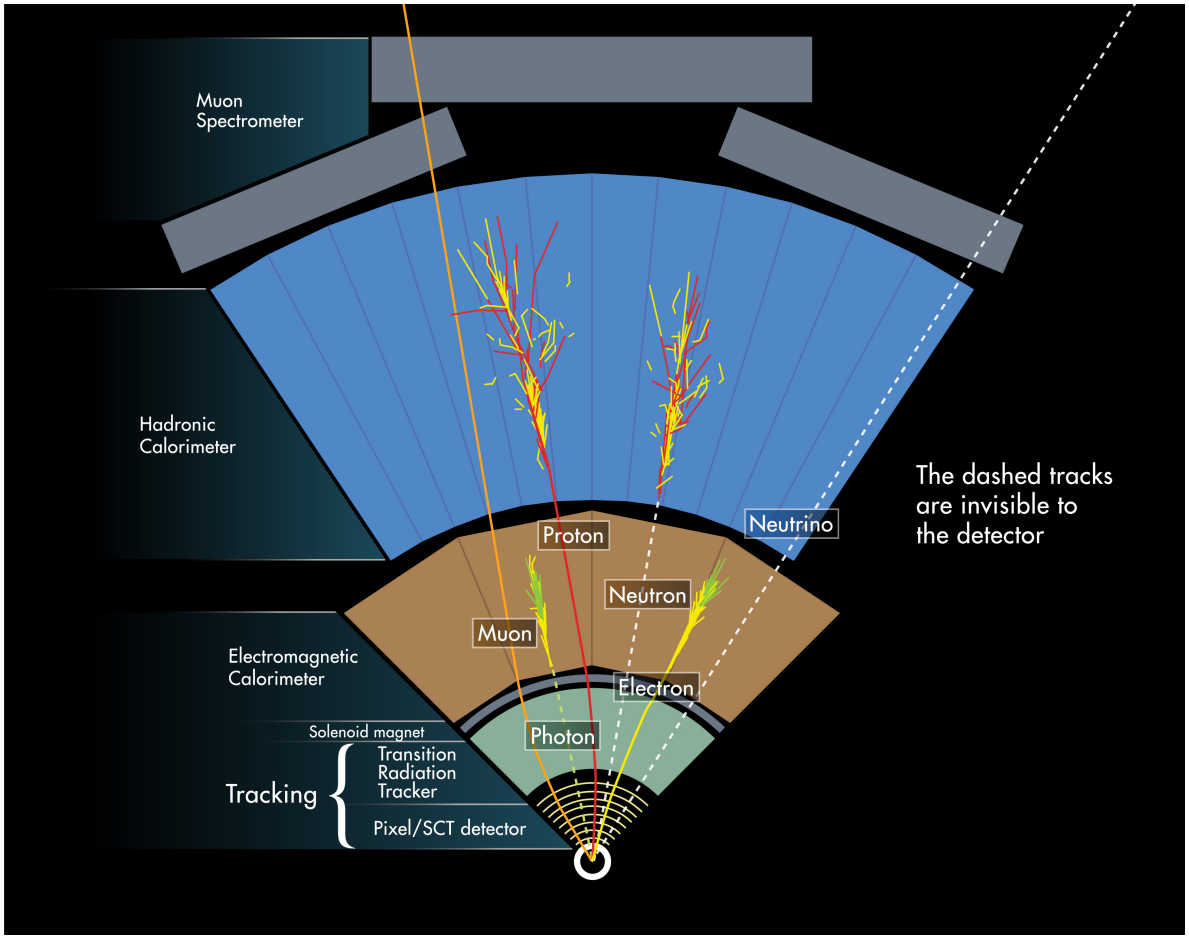

Figure 3.4: Schematic illustration of the detector signatures of different particles. Figure taken from Ref. [150].

Metastable particles typically have lifetimes such that they decay inside the detector volume, leading to displaced decay vertices in the tracker. Quarks can form composite states, which impact their stability. For example, kaons containing strange quarks have lifetimes of $\sim 10^{-8}\,\mathrm{s}$ [35]. The relatively long lifetimes cause them to pass through the tracker without decaying, where the kaon specific energy loss can be used in reconstructing them [151]. Kaons are therefore metastable on the timescale resolvable by ATLAS. Up- and down quarks can form charged or neutral pions, which undergo showering in the hadronic calorimeter.

Figure 3.4 shows a schematic illustration of the signatures which different particles leave in the detector. The top quark t, the $W^{\pm}$-, Z- and Higgs bosons have very short lifetimes, such that they decay before entering the detector. They can therefore

not be detected directly but can instead be reconstructed from their decay products. The main focus of chapter 5 lies in the reconstruction of Higgs bosons produced through Supersymmetric decays.

In the following, the detection techniques employed by the different ATLAS sub-detectors and the resulting signatures of different particles will be explored in more detail.

3.3.1 Inner Detector

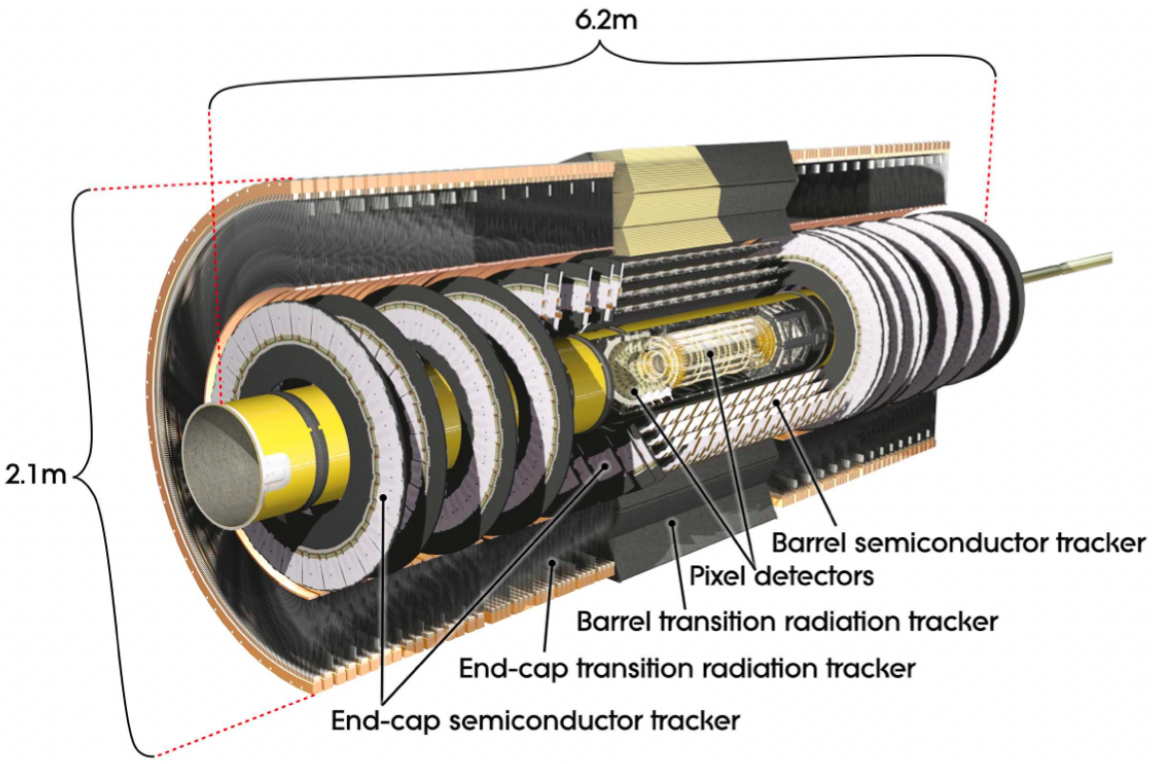

Figure 3.5: Schematic view of the ATLAS Inner Detector. Figure taken from Ref. [134].

The Inner Detector (ID) [152] is the innermost layer of the ATLAS detector, therefore located closest to the interaction point. A schematic view of the ID is shown in figure 3.5. The Inner Detector is enclosed in a homogeneous 2 T magnetic field, parallel to the beam pipe, produced by the ATLAS superconducting solenoid magnet [153]. This field bends the trajectory of charged particles. The Inner Detector has three sub-components: The Pixel detector, the SemiConductor Tracker (SCT) and the Transition

Radiation Tracker (TRT). The first two make use of silicon-based detection [154], while the TRT uses transition radiation [155]. In all three cases, charged particles deposit energy in the corresponding sensors, also referred to as hits. The hits are used for reconstructing tracks of charged particles, from which the primary interaction vertex [156], the particle's charge Q and its momentum $\vec{p}$ can be inferred, as indicated in table 3.1. The Inner Detector has been designed to provide a momentum resolution of $\sigma_{p_\mathrm{T}}/p_\mathrm{T} = 0.05\%\, p_\mathrm{T} \oplus 1\%$ [134].

The three sub-components of the Inner Detector are explored in the following.

Pixel Detector

The Run 2 ATLAS Pixel detector [157–160] consists of four barrel layers and three endcap layers on either side of the detector, with 1888 silicon modules in total, out of which 88 (5%) were non-operational after three years of operation in 2014 [161]. The four barrel layers are the Insertable Beam Layer (IBL), the B-layer, Layer-1 and Layer-2. The IBL was installed shortly before the beginning of LHC Run 2 to improve impact parameter resolution [159, 160, 162]. The barrel layers are located in concentric layers at $r = 33\,\mathrm{mm}$, $r = 50.5\,\mathrm{mm}$, $r = 88.5\,\mathrm{mm}$ and $r = 122.5\,\mathrm{mm}$ distance from the LHC beam, respectively, positioning them closest to the LHC beam out of all ATLAS detector elements.

In addition to the barrel region, three endcap layers were installed at $|z| = 495\,\mathrm{mm}$, $|z| = 580\,\mathrm{mm}$ and $|z| = 650\,\mathrm{mm}$ distance on either side from the interaction point. For the non-IBL layers, the size of the pixels is $50\,\mu\mathrm{m} \times 400\,\mu\mathrm{m}$ in the $\phi - z$ plane for the barrel region and the $\phi - r$ plane for the endcaps. The IBL has a reduced pixel size in the z direction with $250\,\mu\mathrm{m}$, leading to an improved intrinsic per module accuracy of $8\,\mu\mathrm{m}$ in $r - \phi$ and $115\,\mu\mathrm{m}$ in the z-direction (barrel) and in the r-direction (endcaps). The Run 2 Pixel detector, including the IBL, has a total number of 92 million channels.

SemiConductor Tracker (SCT)

The SemiConductor Tracker (SCT) [163, 164] consists of 4088 silicon-strip detector modules. It surrounds the pixel detector and is consists of four concentric barrel layers, as well as nine endcap disk layers on each side of the detector. The barrel modules [165] consist of four rectangular silicon-strip sensors [166]. Two sensors on each side are daisy-chained together, resulting in 768 strips per side. Every strip has a length of about $12\,\text{cm}$. The four barrel layers are located at $r = 299\,\text{mm}$, $r = 317\,\text{mm}$, $r = 443\,\text{mm}$ and $r = 514\,\text{mm}$, covering the region with $|\eta| < 1.5$. The nine disk layers are located in the region ranging of $853.8\,\text{mm} \leq |z| \leq 2720.2\,\text{mm}$ and cover pseudorapidity values of $|\eta| < 2.5$. The single plane position resolution per module in the SCT barrel layers amounts to $17\,\mu\text{m}$ in the transverse plane and $580\,\mu\text{m}$ in the z-direction along the beam pipe. The accuracy per module in the disks amounts to $17\,\mu\text{m}$ in the transverse plane and $580\,\mu\text{m}$ in the r-direction [134].

Transition Radiation Tracker (TRT)

The ATLAS Transition Radiation Tracker (TRT) [167] constitutes the outermost layer of the Inner Detector. It consists of about $350,000$ drift tubes, also referred to as straw tubes. Each tube has a diameter of $4\,\text{mm}$. The straws are arranged parallel to the beam pipe in the barrel and orthogonal to the beam direction in the two endcaps. The straws in the barrel are arranged in 73 layers, covering the region of $560\,\text{mm} \leq r \leq 1080\,\text{mm}$ and $|z| < 720\,\text{mm}$. In the endcaps, the covered region is $827\,\text{mm} \leq |z| \leq 2774\,\text{mm}$ and $617\,\text{mm} \leq r \leq 1106\,\text{mm}$, where the straws are arranged in 160 planes. This results in an accuracy of $130\,\mu\text{m}$ in $r - \phi$ plane per straw, for $|\eta| < 2$ and $p_{\text{T}} > 0.5\,\text{GeV}$. As shown in table 3.1, the TRT contributes to electron particle identification. Electrons can be distinguished from pions over for energies between 1 and $200\,\text{GeV}$ through the use of transition radiation [168].

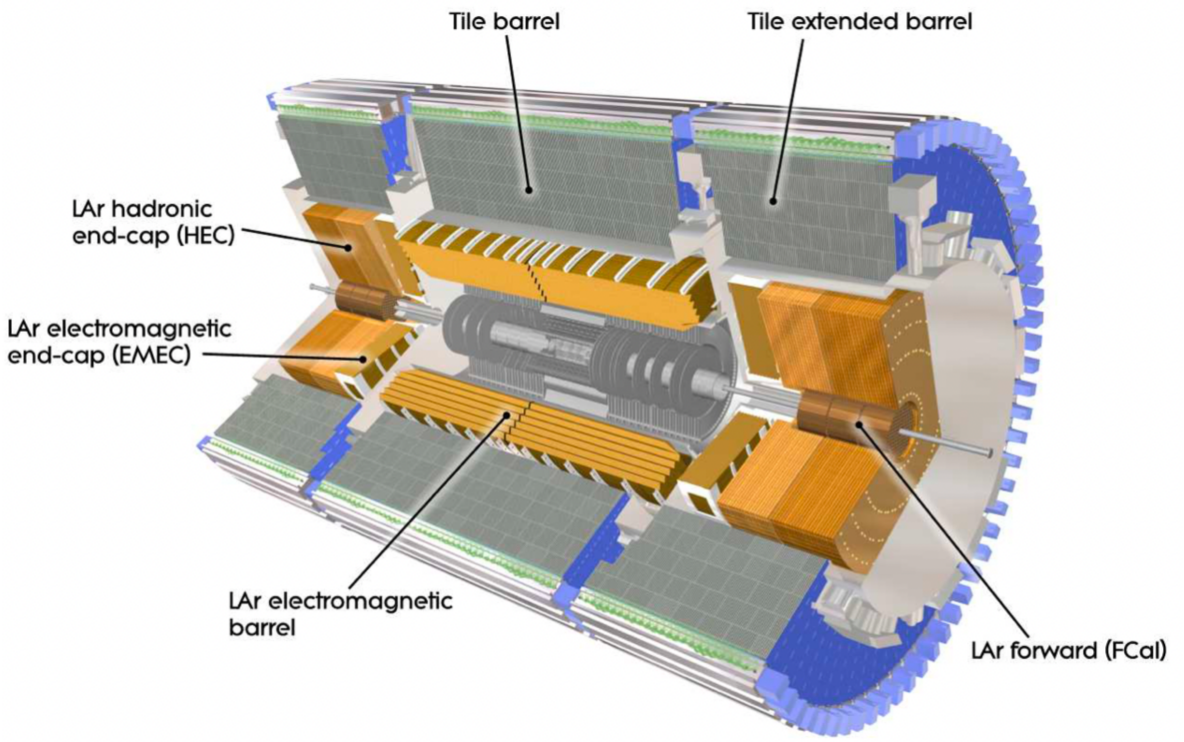

Figure 3.6: Schematic view of the ATLAS calorimeter system. Figure taken from Ref. [134].

3.3.2 Calorimeter

The ATLAS calorimeter system [169] consists of the Liquid Argon (LAr) [170] and the Tile [171] sampling calorimeters. Sampling calorimeters make use of alternating active and passive layers, where the active layer is used for detection and the passive layer consists of a dense material used to degrade the energy of any particle travelling through the calorimeter [172]. The LAr calorimeter makes use of Liquid Argon as an active sampling material, while the Tile calorimeter uses plastic scintillator tiles. A schematic view of the ATLAS calorimeter system is shown in figure 3.6.

As illustrated in figure 3.4, the interaction with the passive material of the ATLAS calorimeter system forces the interacting particle to split into particles with lower energy, i.e. create a "shower" of particles, until the particle's energy is low enough to be stopped. The exception between the particles with electromagnetic or strong inter-

actions is the muon, which is only minimally ionising to the calorimeter and therefore only deposits little energy [173]. The ATLAS calorimeter system has been designed to limit punch-through of produced showers into the muon spectrometer. The calorimeter was designed for a general target resolution of $\sigma_E/E = 10\%/\sqrt{E} \oplus 0.7\%$ [134].

The LAr and Tile calorimeters are explored in more detail in the following.

Liquid Argon calorimeter

The Liquid Argon calorimeter is used to measure energies of both electromagnetic and hadronic interactions [170, 174, 175]. In the LAr Electromagnetic Calorimeter (ECal) barrel ($|\eta| < 1.475$) and endcap ($1.375 < |\eta| < 3.2$), lead absorbers are arranged in an accordion geometry, where the gaps are filled with liquid argon which is ionised by incoming particles, allowing for precise energy measurements of photons and electrons. The barrel consist of two half-barrels and the endcaps each consist of two co-axial wheels. A thin LAr presampler, used to estimate energy losses in the ID, is included in the region with $|\eta| < 1.8$.

Two parallel-plate copper/LAr Hadronic Calorimeter (HCal) endcaps are installed, covering the region of $1.5 < |\eta| < 3.2$. The use of copper results in more efficient heat dissipation. Finally, the Forward Calorimeter (FCal) [176] is included, with an $|\eta|$ coverage of $3.1 < |\eta| < 4.9$. They consist of three cylindrical modules, where the innermost module uses copper as active material and the outer two mainly consist of tungsten. The use of tungsten instead of copper reduces the shower width and improves the overall containment of hadronic showers, thus minimising punch-through to the muon system. Copper is used for the innermost layer, as it is less expensive to work with than tungsten [170]. To withstand the large radiation in the forward region close to the beam, the LAr gaps are kept very narrow, thus avoiding ion buildup.

Tile calorimeter

In addition to the LAr HCal endcaps, the tile calorimeter also provides hadronic calorimetry [171]. Steel is used as the passive material in the tile calorimeter, while scintillators are used for detection [177–179]. It covers the region with $|\eta| < 1.7$ and has a radial depth of about 7.4 interaction lengths to minimise punch-through to the muon system. Interacting particles produce scintillation photons, while passing through the tile calorimeter. These are guided to photomultiplier tubes with the use of wavelength-shifting fibres.

3.3.3 Muon Spectrometer

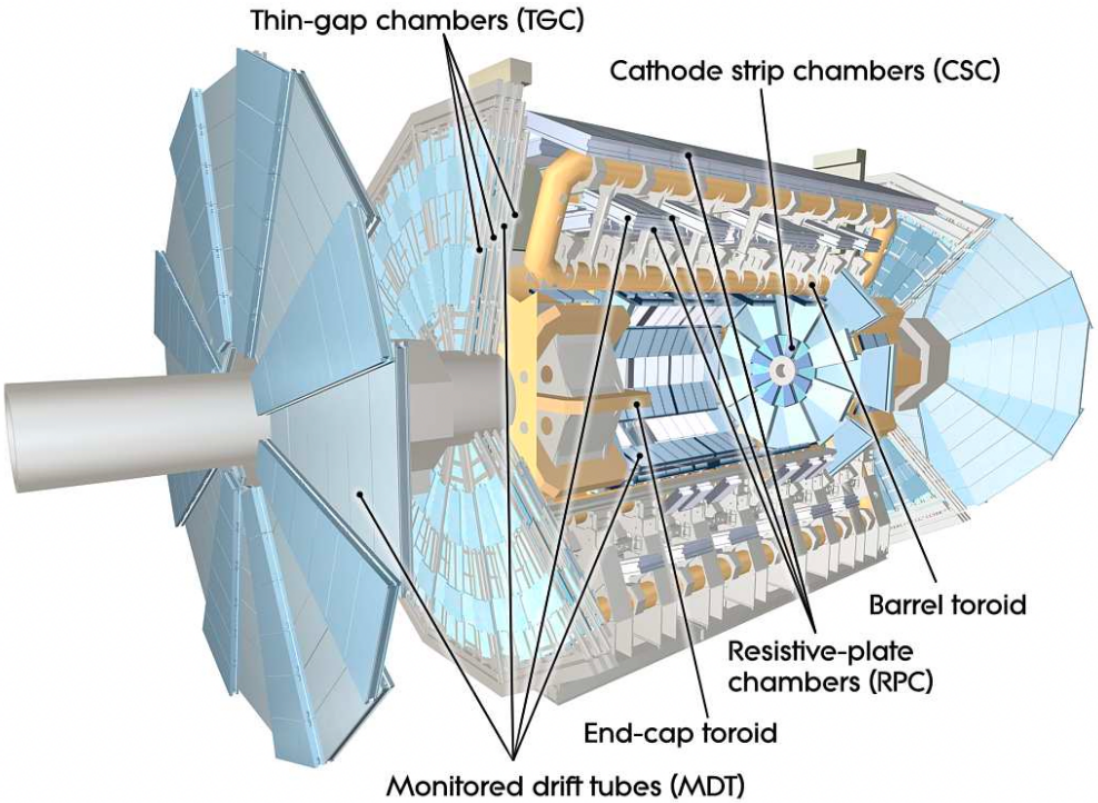

Figure 3.7: Cut-away view of the ATLAS muon spectrometer. Figure taken from Ref. [134].

As muons pass through most of the ATLAS detector without depositing a large fraction of their energy, the ATLAS muon spectrometer [180, 181] is used for triggering

on muons as well as measuring their momentum. A cut-away view of the muon system is shown in figure 3.7. The surrounding $0.5 - 1\,\mathrm{T}$ superconducting toroidal magnets bend muons in the $r - \eta$ plane, which allows for a momentum measurement in the muon spectrometer with a precision of $\sigma_{p_\mathrm{T}}/p_\mathrm{T} = 10\%$ at $p_\mathrm{T} = 1\,\mathrm{TeV}$ (4% at $p_\mathrm{T} = 100\,\mathrm{GeV}$).

Monitored Drift Tubes (MDTs) [182] are used for precision tracking in the $r - \eta$ plane in the region with $|\eta| < 2.7$. Tubes with a diameter of about $30\,\mathrm{mm}$ are stacked in three to eight layers. Each tube is filled with $\mathrm{Ar}/\mathrm{CO_2}/\mathrm{H_2O}$ gas, which is ionised by incoming muons and the resulting electrons are collected at a tungsten-rhenium wire located in the middle of the tube. In the forward region closest to the interaction point ($2 < \eta < 2.7$), the detector occupancy is too high for employing MDTs. In this region, Cathode Strip Chambers (CSCs) [183] instead provide precision measurements. The CSCs are multiwire proportional chambers, chambers in which $\mathrm{Ar}/\mathrm{CO_2}$ gas is ionised by muons and the resulting ions and electrons travel through the chamber, causing an avalanche of ionisation which is then detected by an array of wires [184].

To trigger on muons, Resistive Plate Chambers (RPCs) [185] and Thin Gap Chambers (TGCs) [186] are used in the barrel and endcaps respectively, leading to an overall coverage of $0 < \eta < 2.4$. The RPCs are chambers filled with gas which is again ionised by incoming muons. In contrast to the MDTs and CSCs, the ionisation is here detected by the surrounding plates, which serve as anode and cathode, leading to a significantly smaller detector readout time. The TGCs employ a similar strategy than the CSCs, but have a high electric field around an array of wires with a finer granularity, leading to excellent time resolution. The RPCs and TGCs are also used to identify the bunch-crossing due to their fast readout times of $15 - 25\,\mathrm{ns}$, as well as for measuring muons in the direction orthogonal to that determined by the MDTs and CSCs.

3.3.4 Trigger and data acquisition

The LHC has a collision rate of approximately $40\,\text{MHz}$. Every event requires about $1.3\,\text{MB}$ of storage space, leading to more than $50\,\text{TB/s}$ of data. Storing such large amounts of data is not feasible. Furthermore, the vast majority of the occurring collisions only involves small momentum transfer (cf. figure 2.2). While such collisions are part of the ATLAS physics programme, the focus of many measurements and especially searches lies on hard-scatter interactions with large momentum transfer, which have a much lower probability of occurring. Hence, a decision has to be made during collisions (online) on whether an event should be kept for later analysis or discarded. This decision is made by the ATLAS trigger system. Discarded events are forever lost and can not be recovered, so the trigger system has a responsibility for the entire physics program.

In Run 2, ATLAS employed a two-layer trigger system, with a hardware-based First Level (L1) trigger reducing the rate of events from the full collision rate of $40\,\text{MHz}$ to $100\,\text{kHz}$ and a software-based High Level Trigger (HLT) performing an additional reduction of the rate to $1\,\text{kHz}$ [187, 188]. The L1 trigger was therefore used to define a broad Region of Interest (ROI), in which the HLT trigger performed a more elaborate selection.

The broad physics programme of the ATLAS experiment is accompanied by a large variety of trigger signatures, including triggers for electrons and photons [189], muons [190], b-jets [191], triggers based on the Inner Detector [192] and triggers for missing transverse momentum [2]. The missing transverse momentum triggers during Run 2 and prospective Run 3 candidates are explored in more detail in chapter 4 of this thesis. The collection of all triggers is referred to as the trigger menu [188, 193].

Overall, the ATLAS trigger system has a pass fraction of about 2.5×10^{-5}, which still results in $\mathcal{O}(10^4)\,\text{TB}$ of data per year. To keep up with these demands, data is stored at the CERN Tier 0 (T0) data centre and processed at regional Tier 1 (T1) nodes using the `Athena` framework [194]. In the work presented in this thesis,

data analysis is performed using the ROOT data analysis framework [195] and the corresponding RooFit toolkit [196].

Despite the challenging environment, many searches and measurements have successfully been performed with the ATLAS detector. One such example is the measurement of the inclusive and differential cross section in the $H \to ZZ^* \to 4l$ decay channel in pp collisions at $\sqrt{s} = 13\,\text{TeV}$ [197], for which a candidate signal event is shown in figure 3.8. In this particular event, 25 additional pile-up vertices were reconstructed, significantly complicating the detection, triggering, reconstruction and analysis of such events. Despite these conditions, the $H \to ZZ^* \to 4l$ fiducial cross-section was successfully measured as $\sigma = 3.62 \pm 0.50\,(\text{stat})^{+0.25}_{-0.20}\,(\text{sys})\,\text{fb}$.

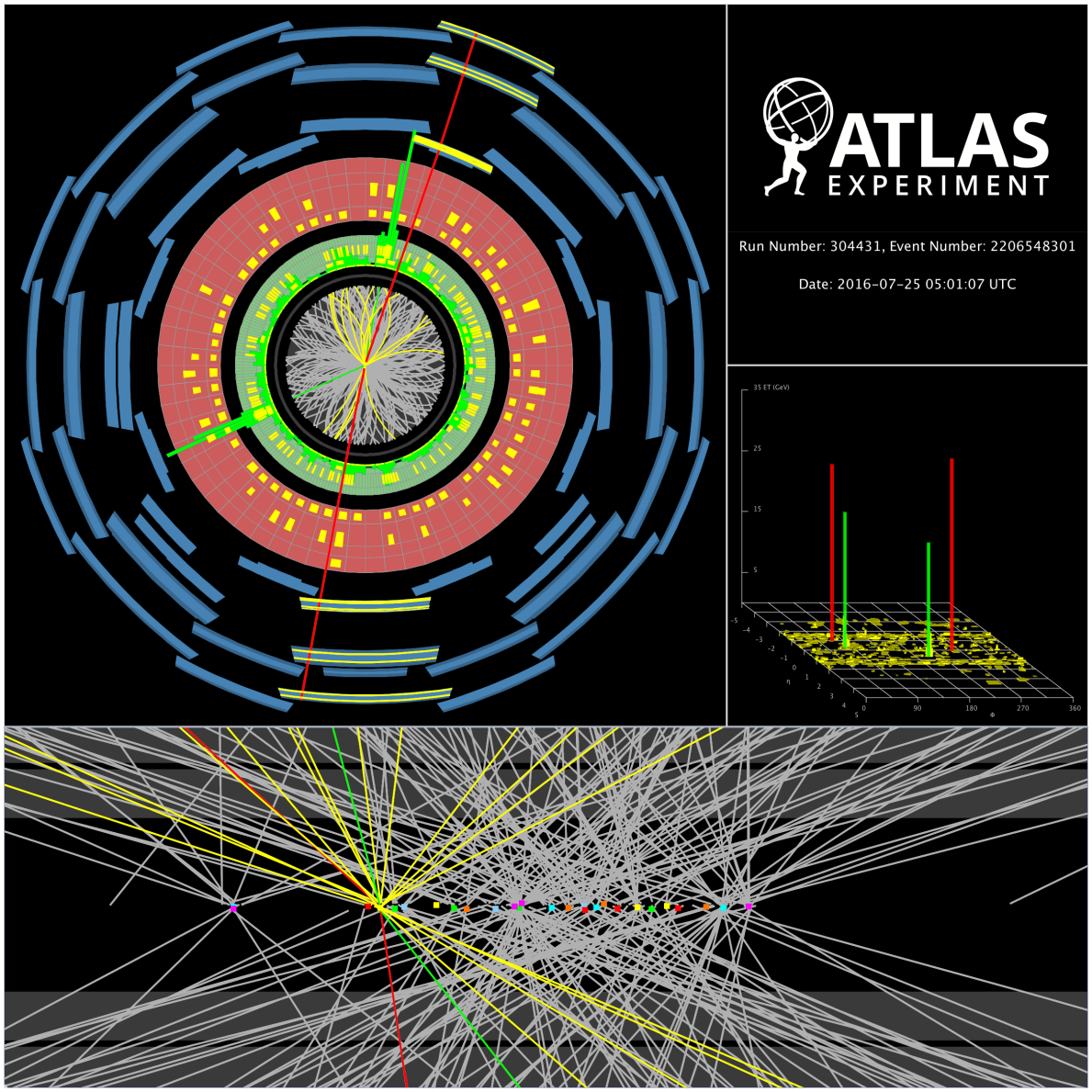

Figure 3.8: Event display associated to the measurement of the inclusive and differential cross section in the $H \to ZZ^* \to 4l$ decay channel in pp collisions at $\sqrt{s} = 13\,\text{TeV}$ [197]. The Higgs boson candidate is reconstructed in a beam crossing with 25 additionally reconstructed primary vertices from the minimum bias interactions. The candidate event is reconstructed in the $2\mu 2e$ final state. In the left display, the red lines show the path of the two muons including the hits in the muon spectrometer, the green lines show the paths of the two electrons together with the energy deposit in the Electromagnetic Calorimeter, and the yellow tracks are the remaining charged particles from the Higgs boson candidate vertex. No jet has been reconstructed with transverse momentum above $30\,\text{GeV}$. The grey tracks correspond to the charged particles from the 25 pile-up vertices with transverse momentum above $0.5\,\text{GeV}$ and the coloured squares in the lower display correspond to the position of the reconstructed vertices. This event falls within the standard mass selection window of 118 to $129\,\text{GeV}$ and has a Boosted Decision Tree discriminant response which gives a high probability that this event comes from a Higgs decay as opposed to a background $ZZ*$ decay. Figure and caption adapted from Ref. [198].

4

The $E_{\mathrm{T}}^{\mathrm{miss}}$ trigger

Contents

4.1 Introduction **50**
4.2 Run 2 performance **53**
4.2.1 $E_{\mathrm{T}}^{\mathrm{miss}}$ trigger algorithms 53
4.2.2 Trigger performance metrics 59
4.3 Run 3 tracking ideas **71**
4.3.1 The `trktc` algorithm 71
4.3.2 Performance of the `trktc` constituents 76

4.1 Introduction

The ATLAS trigger system is responsible for making a relatively quick decision on whether an events should be kept for later analysis or discarded, as explained in section 3.3.4. Different dedicated trigger strategies are employed for electrons, photons, muons, taus, jets, b-jets as well as $E_{\mathrm{T}}^{\mathrm{miss}}$. The hardware-based First Level (L1) $E_{\mathrm{T}}^{\mathrm{miss}}$ trigger takes inputs from the calorimeter detectors and then uses the custom made electronics of the Central Trigger Processor (CTP) to make a decision [188]. The L1 trigger's main tasks are rate reduction and the definition of ROIs which can be investigated in a second trigger stage. The event data is read out by the Front-End detector electronics for all detectors only if an event is accepted at L1. At the second stage of the trigger, the software-based High Level Trigger (HLT) makes a final decision on whether an event is kept or discarded. The HLT makes use of the `Athena` sofware framework [194] and runs on a farm of about $50,000$ processing units [2]. This chapter introduces the key concepts of the $E_{\mathrm{T}}^{\mathrm{miss}}$ trigger, specifically the HLT $E_{\mathrm{T}}^{\mathrm{miss}}$ trigger.

ATLAS is able to detect particles which interact with the detector through either strong or electromagnetic interactions. If a particle does not interact with the detector, it is considered 'invisible'. One example for such a particle is the neutrino, which interacts only via the weak force. Despite the detector's inability to detect them directly, invisible particles are an important part of the ATLAS physics program, in particular in searches for Dark Matter. Therefore, a strategy is necessary to detect these particles indirectly and select relevant events at the trigger level such that they can be kept for later analysis.

The main variable used in this context is $E_{\mathrm{T}}^{\mathrm{miss}}$. It is based on the conservation of momentum in the detector. The colliding partons' momenta along the direction of the beam are unknown, due the inherent uncertainty on their momentum caused by the parton distribution functions. Hence, the momenta along the direction of the beam can not be used in any momentum conservation calculation. However,

the momenta orthogonal to the direction of the beam (also: the 'transverse' plane) can be used. The incoming partons are assumed to have no momentum in this direction[1], so any collision only involving visible particles has no momentum in the transverse plane (within measurement uncertainties). Therefore, for a perfect hermetic detector we expect

$$\sum_{i}^{N} \vec{p_{\mathrm{T}i}} = \vec{0}, \tag{4.1}$$

where N is the total number of visible particles in the event and $\vec{p_{\mathrm{T}i}}$ are the visible particle momenta in the transverse plane (also: the transverse momenta).

If an invisible particle is present in the event, it can disrupt the balance in the visible transverse momentum and can therefore be indirectly detected by ATLAS through the 'missing' transverse momentum defined as:

$$\vec{p}_{\mathrm{T}}^{\,\mathrm{miss}} := -\sum_{i}^{N} \vec{p_{\mathrm{T}i}}, \tag{4.2}$$

From this, the missing transverse energy is then calculated as $E_{\mathrm{T}}^{\mathrm{miss}} = |\vec{p}_{\mathrm{T}}^{\,\mathrm{miss}}|$.

In the Standard Model, the presence of neutrinos in collisions causes events to have non-zero $E_{\mathrm{T}}^{\mathrm{miss}}$. In many models of BSM physics there can be additional sources of $E_{\mathrm{T}}^{\mathrm{miss}}$ such as Dark Matter. The precise properties of the invisible particle are strongly dependent on the considered model, implying that a model independent approach is necessary at the trigger level. Relevant data should be collected for further analysis to gain sensitivity to a broad range of such models.

Examples of searches in ATLAS that use the $E_{\mathrm{T}}^{\mathrm{miss}}$ trigger include searches for Higgs bosons decaying into invisible final states [199, 200], searches for charged Higgs boson decays into $\tau\nu$ [201], searches for Dark Matter produced by a heavy mediator recoiling against a high energy jet [202], searches involving a stable, massive Supersymmetric $\tilde{\chi}_1^0$ as Dark Matter candidate, both in strong [203] and electroweak [204] production modes, searches for Supersymmetric partners of the top quark [205], searches for

[1] The parton's p_{T} is $\mathcal{O}(\mathrm{MeV})$, which is negligible on the energy scales considered here.

stable long-lived particles [206] as well as the observation of Higgs decays into a pair of b-quarks, where the Higgs was produced in association with a Z boson decaying into neutrinos [207].

This chapter is structured as follows. Section 4.2 highlights the key developments that have lead to the successful operation of the $E_{\mathrm{T}}^{\mathrm{miss}}$ trigger during Run 2 and the increase in performance that these brought. It shows results reviewing the $E_{\mathrm{T}}^{\mathrm{miss}}$ trigger performance that I have produced as well as some results produced by collaborators[2]. All figures have been published in Ref. [2]. Section 4.3 contains a performance review of selected candidate algorithms involving tracking information that have been tested for Run 3. This section only considers the algorithms that I have investigated for my qualification task. Other algorithms have been considered by other members of the $E_{\mathrm{T}}^{\mathrm{miss}}$ trigger group.

[2]This has been noted in the corresponding figure caption wherever applicable.

4.2 Run 2 performance

In Run 2 of the LHC, collisions occurred with a rate of about $40\,\mathrm{MHz}$. Of these, events were accepted by the L1 $E_{\mathrm{T}}^{\mathrm{miss}}$ trigger with a rate of approximately 5 to $10\,\mathrm{kHz}$. The HLT $E_{\mathrm{T}}^{\mathrm{miss}}$ trigger accepted events at a rate of about $1200\,\mathrm{Hz}$ [208].

The large required reduction of the rate largely shapes the operational requirements of the trigger system. Firstly, a trigger has to reject a large majority of backgrounds in which fake $E_{\mathrm{T}}^{\mathrm{miss}}$ typically arises from mismeasurements in the detector [2]. This requirement reduces the trigger output rate of the HLT $E_{\mathrm{T}}^{\mathrm{miss}}$ trigger such that storage and later analysis of events are more manageable. Secondly, a trigger should have a high efficiency, meaning that if an events contains high true $E_{\mathrm{T}}^{\mathrm{miss}}$, the trigger should recognise it as such with a large probability. Lastly, the trigger should be robust towards changing external factors, such as the number of proton-proton interactions in a bunch-crossing (pile-up $\langle\mu\rangle$) or time. This concept is also referred to as trigger stability.

The requirements of high efficiency and low rate can be particularly difficult to combine, particularly in the LHC Run 2 environment with large pile-up which has the effect of degrading detector resolution. In Run 2, the average pile-up reached $\langle\mu\rangle = 37.8$ in 2017 and the tails of the distribution stretch until values of 70 (cf. figure 3.2b). To combat this issue, different $E_{\mathrm{T}}^{\mathrm{miss}}$ trigger algorithms have been developed. These will be further explored in the next section.

4.2.1 $E_{\mathrm{T}}^{\mathrm{miss}}$ trigger algorithms

At the trigger level, the $E_{\mathrm{T}}^{\mathrm{miss}}$ is is not calculated directly from the particle momenta in the event, as suggested in section 4.1. The main reason for this is that there is an operational requirement of the $E_{\mathrm{T}}^{\mathrm{miss}}$ trigger to not exceed $\mathcal{O}(100\,\mathrm{ms})$ of computation time per event. In order for the particle momenta to be accessible in the $E_{\mathrm{T}}^{\mathrm{miss}}$ calculation, all particles would need to be reconstructed as such. Full particle reconstruction requires

the use of tracking information, which typically is computationally expensive, leading to evaluation times of $\mathcal{O}(1-5\,\mathrm{s})$. To satisfy the requirement on the computation time, the ATLAS Run 2 trigger has only made use of calorimeter information. This is going to change with the introduction of Full-Scan tracking in LHC Run 3 [209], as explained in section 4.3.

Instead of full momenta, $E_{\mathrm{T}}^{\mathrm{miss}}$ is calculated from energy deposits in the calorimeter, also referred to as elements. A two-vector $\vec{E}_{\mathrm{T}}^{\mathrm{miss}}$ is calculated from these elements in the approximation of massless particles

$$E_x^{\mathrm{miss}} = -\sum_{i=1}^{|\mathrm{Elements}|} E_i \sin\theta_i \cos\phi_i, \tag{4.3}$$

$$E_y^{\mathrm{miss}} = -\sum_{i=1}^{|\mathrm{Elements}|} E_i \sin\theta_i \sin\phi_i, \tag{4.4}$$

with $|\mathrm{Elements}|$ indicating the total number of elements. From this, the $E_{\mathrm{T}}^{\mathrm{miss}}$ is calculated with $E_{\mathrm{T}}^{\mathrm{miss}} = \sqrt{(E_x^{\mathrm{miss}})^2 + (E_y^{\mathrm{miss}})^2}$ [2].

The algorithms differ in how the elements entering the $E_{\mathrm{T}}^{\mathrm{miss}}$ sum are defined. An event passes a trigger if the $E_{\mathrm{T}}^{\mathrm{miss}}$ calculated by the considered algorithm exceeds a predetermined value. This value is referred to as the ´trigger threshold'.

Level-1 trigger

The hardware-based L1 trigger calculates the $E_{\mathrm{T}}^{\mathrm{miss}}$ sum based on projective calorimeter towers [210]. The towers are formed from calorimeter cells with a granularity of approximately $\Delta\eta \times \Delta\phi = 0.1 \times 0.1$ for $|\eta| < 2.5$ (larger, less regular distances are used for $|\eta| > 2.5$). The analogue sums of the calorimeter cells are digitised to counts corresponding to approximately $1\,\mathrm{GeV}$ in E_{T}. To reduce noise, the energy of all towers below a fixed threshold, the value of which depends on η, is set to zero. These thresholds were optimised to simultaneously yield acceptable efficiency for $E_{\mathrm{T}}^{\mathrm{miss}} > 150\,\mathrm{GeV}$ as well as a fixed occupancy of 0.5-1%. With the increase in luminosity, the trigger's occupancy typically increased and thus the threshold had

to be raised. Thresholds ranged from $1-2\,\mathrm{GeV}$ for low $|\eta|$ and reached values of $10\,\mathrm{GeV}$ in the very forward region [211].

After applying the noise reduction, larger towers with a granularity of $\Delta\eta \times \Delta\phi = 0.2 \times 0.2$ are formed. These larger towers, also referred to as jet elements, are then used in equations 4.3 and 4.4 to determine the x- and y-contributions to the total $E_{\mathrm{T}}^{\mathrm{miss}}$.

As mentioned before, the L1 $E_{\mathrm{T}}^{\mathrm{miss}}$ trigger reduces the rate of considered events over many orders of magnitude from the full collision rate of $40\,\mathrm{MHz}$ to a much lower $5-10\,\mathrm{kHz}$. Hence, the trigger's main task is background rejection and identifying events potentially containing $E_{\mathrm{T}}^{\mathrm{miss}}$. After the L1 trigger's decision to accept an event, the HLT algorithms recalculate the $E_{\mathrm{T}}^{\mathrm{miss}}$ in different ways and a decision on whether the event should be kept for analysis is made.

The `cell` algorithm

The `cell` algorithm uses calorimeter cells to determine the $E_{\mathrm{T}}^{\mathrm{miss}}$. The x- and y-contributions to the $E_{\mathrm{T}}^{\mathrm{miss}}$ are determined by summing over all $188\,\mathrm{k}$ calorimeter cells. Pile-up suppression in this algorithm is limited. To suppress pile-up and noise, cells only enter the sum if $|E_i| > 2\sigma_i$ and $E_i > -5\sigma_i$, where σ_i is the expected energy-equivalent noise in cell i as described in Ref. [212]. Cell energies can be negative since the LAr electronics were designed such that energy deposits from pile-up in later bunch-crossings may appear as negative. These typically cancel against positive contributions from earlier bunch-crossings, improving robustness against pile-up [213]. The $E_i > -5\sigma_i$ requirement is include to exclude spurious large negative energy cells from the $E_{\mathrm{T}}^{\mathrm{miss}}$ sum.

The `cell` algorithm is the simplest of all HLT $E_{\mathrm{T}}^{\mathrm{miss}}$ algorithms. However, its simplicity has proven very useful to the trigger in both providing a benchmark in performance studies as well as in algorithm combinations (cf. section 4.2.2).

The `tc_lcw` algorithm

As described in section 3.3.2, particles can shower in the EM and hadronic calorimeters, leading to clusters of energy deposits. Topological clustering [212] can be useful in identifying these clusters and thus reconstructing the particles.

Topological clusters are reconstructed in an iterative process. First, the highest energy cells satisfying $|E_i| > 4\sigma_i$ are identified. These are referred to as 'seeds', meaning that clusters are formed around them. All cells neighbouring the seeding cell in three spacial dimensions are added to the cluster. Next, if any of the neighbouring cells satisfies $|E_i| > 2\sigma_i$, its neighbouring cells are in turn added to the cluster. This process continues until no more neighbours with $|E_i| > 2\sigma_i$ are found.

Clusters are split between their local energy maxima, defined as cells with $E_i > 500\,\text{MeV}$, by an additional algorithm described in Ref. [212]. Depending on whether clusters are identified as electromagnetic or hadronic in origin, a different energy correction is applied to the cluster [212].

The `tc_lcw` trigger algorithm forms the $E_{\text{T}}^{\text{miss}}$ sum directly from the topological clusters. The clusters are also used as inputs to the `mht` and `pufit` algorithms.

The `mht` algorithm

Jets play a vital role to the ATLAS physics program and thus the detector and the reconstruction algorithms have been designed such that jets can be calibrated to high accuracy [214]. The `mht` algorithm calculates the $E_{\text{T}}^{\text{miss}}$ from jets reconstructed at the trigger level.

Jets are reconstructed from the topological clusters explained in the previous section with the anti-k_t algorithm with $R = 0.4$ [215]. At the trigger level, the anti-k_t algorithm is implemented in the FastJet toolkit [216]. After jet reconstruction, pile-up

contributions to jets are removed using the jet-area-based pile-up suppression method [217, 218]. Finally, jets are calibrated using the procedure described in Ref. [219].

The `mht` $E_{\mathrm{T}}^{\mathrm{miss}}$ is calculated from the negative sum of the momenta of the calibrated jets. The energy deposits from non-jet particles (photons, electrons and hadronically decaying τ-leptons) are included in the jet reconstruction and therefore also enter the $E_{\mathrm{T}}^{\mathrm{miss}}$ sum.

The `pufit` algorithm

The `pufit` algorithm takes topological clusters as inputs and corrects them for pile-up by performing a χ^2-method fit. Topological clusters are grouped in $\eta - \phi$ patches corresponding roughly to a jet of radius $R = 0.4$. A threshold is then determined to split patches into high- and low-E_{T} patches corresponding to the hard-scatter collision and pile-up respectively. The threshold is given by:

$$E_{\mathrm{T}}^{\mathrm{thres}} = \langle E_{\mathrm{T}} \rangle_{\mathrm{patch}} + 5\sqrt{V_{\mathrm{patch}}}, \tag{4.5}$$

with $\langle E_{\mathrm{T}} \rangle_{\mathrm{patch}}$ the trimmed mean of all E_{T} values in the patch and V_{patch} the corresponding variance [2]. A typical value for $E_{\mathrm{T}}^{\mathrm{thres}}$ during LHC Run 2 was 30 GeV.

The χ^2-method fit is based on a number of key assumptions. Firstly, it assumes that high-E_{T} patches generally correspond to the hard-scatter collision, while low-E_{T} patches generally can be attributed to pile-up. Secondly, the method assumes that pile-up is approximately equally distributed around the detector. Lastly, the total $\vec{p}_{\mathrm{T}}^{\,\mathrm{miss}}$ caused by pile-up should be zero. The first assumption is used in the fit setup, while the other two assumptions are used to constrain the fit.

The pile-up contributions to E_x and E_y (cf. equations 4.3 and 4.4) are then constrained to zero within fluctuations by the fit. Fluctuations are allowed to allow for possible mismeasurements in energy. Finally, the `pufit` $E_{\mathrm{T}}^{\mathrm{miss}}$ is given by the negative sum over all pile-up corrected high-E_{T} patches entering E_x and E_y. More details on the `pufit` algorithm can be found in Ref. [2].

ATLAS trigger naming conventions

Within ATLAS, specific condensed naming conventions are used to refer to triggers, generally referred to 'trigger chains'. One such example is:

`HLT_xe70_mht_L1XE50`

Trigger chains indicate all algorithms and thresholds used on both trigger levels to make a decision. Events passing the trigger need to pass all algorithm selections, going from right to left. `L1` indicates a requirement on the Level-1 trigger, while `HLT` indicates a HLT level requirement. The trigger level is followed by a string indicating the signature considered by the trigger. In the case of the $E_{\mathrm{T}}^{\mathrm{miss}}$ trigger, this string is either `_xe` (for the HLT) or `XE` (for L1). The number following the string indicates the applied nominal threshold on the algorithm $E_{\mathrm{T}}^{\mathrm{miss}}$ in GeV. Therefore, `L1XE50` implies that events pass the trigger if the corresponding $E_{\mathrm{T}}^{\mathrm{miss}}$ at the L1 trigger level satisfies $E_{\mathrm{T}}^{\mathrm{miss}}(\mathrm{L1}) \geq 50\,\mathrm{GeV}$.

Since multiple algorithms exist at the HLT, the threshold is followed by another string indicating which algorithm is used to calculate the $E_{\mathrm{T}}^{\mathrm{miss}}$. In this example, `HLT_xe70_mht` therefore implies that the $E_{\mathrm{T}}^{\mathrm{miss}}$ determined with the `mht` algorithm has to satisfy $E_{\mathrm{T}}^{\mathrm{miss}}(\mathtt{mht}) \geq 70\,\mathrm{GeV}$. If no algorithm name is provided, the $E_{\mathrm{T}}^{\mathrm{miss}}$ is determined with the `cell` algorithm.

Overall, the trigger chain of `HLT_xe70_mht_L1XE50` therefore requires $E_{\mathrm{T}}^{\mathrm{miss}}(\mathrm{L1}) \geq 50\,\mathrm{GeV}$ and $E_{\mathrm{T}}^{\mathrm{miss}}(\mathtt{mht}) \geq 70\,\mathrm{GeV}$.

In some trigger chains such as `HLT_xe110_pufit_xe65_L1XE50`, multiple HLT algorithms are applied. Events then have to satisfy all requirements applied to the different algorithms, again starting from the requirements on the right. For this specific chain, events need to satisfy $E_{\mathrm{T}}^{\mathrm{miss}}(\mathrm{L1}) \geq 50\,\mathrm{GeV}$, $E_{\mathrm{T}}^{\mathrm{miss}}(\mathtt{cell}) \geq 65\,\mathrm{GeV}$ and $E_{\mathrm{T}}^{\mathrm{miss}}(\mathtt{pufit}) \geq 110\,\mathrm{GeV}$.

4.2.2 Trigger performance metrics

This section explains the most relevant trigger performance metrics while providing examples of the $E_{\mathrm{T}}^{\mathrm{miss}}$ trigger performance in LHC Run 2. All results shown in this section have been published in Ref. [2]. The maintenance and development of the algorithms introduced in the previous section with using these performance metrics have lead to the successful operation of the ATLAS $E_{\mathrm{T}}^{\mathrm{miss}}$ trigger during Run 2.

This section focuses on the performance of the ATLAS HLT trigger, the performance of the L1 trigger is studied in more detail in Ref. [2].

Background acceptance and signal efficiency

As mentioned before, two important features to the trigger's performance are the trigger rate and its efficiency in selecting signal. As the trigger rate can be nontrivial to determine, the fraction of accepted background events (also: background acceptance) is sometimes considered instead. Here, the signal efficiency and background acceptance are defined as:

$$\varepsilon(X_i) = \frac{N(\text{trigger}|X_i)}{N(X_i)}, \tag{4.6}$$

where X_i is a selection of signal or background events respectively and N is the number of events passing the corresponding selection.

As the trigger threshold increases, more background is rejected and the trigger rate is thus reduced. However, in doing so, the trigger efficiency is also reduced as fewer events containing real $E_{\mathrm{T}}^{\mathrm{miss}}$ can pass the trigger. Thus, an optimal trigger threshold has to be determined using both the background acceptance and the signal efficiency simultaneously.

In this study, background events were selected with an unbiased trigger, also referred to as zero bias trigger, which saves random events. As the zero bias trigger yields only limited statistics at high values of $E_{\mathrm{T}}^{\mathrm{miss}}$, additional events collected with the

HLT_noalg_L1XE30 and HLT_noalg_L1XE50 triggers were collected, which require thresholds of $E_{\mathrm{T}}^{\mathrm{miss}}(\mathrm{L1}) > 30\,\mathrm{GeV}$ and $50\,\mathrm{GeV}$, as well as no HLT requirement. To keep the rate of these triggers manageable, they were prescaled at rates of the order of $10^4 - 10^5$ for the trigger seeded by L1XE30 and 10^3 for the trigger seeded by L1XE50. A prescale of 10^x implies that only one out of 10^x events passing the trigger selection are accepted. Background events dominate the rate of these triggers, hence the probability of a random event having large $E_{\mathrm{T}}^{\mathrm{miss}}$ is quite low and the sample produced by this trigger has low enough contamination of events with real $E_{\mathrm{T}}^{\mathrm{miss}}$.

The trigger efficiency is determined using $Z \to \mu\mu$ events. Muons deposit only very small quantities of energy in the calorimeter and are therefore considered invisible to the calorimeter (cf. section 3.3.2). Hence, the transverse momentum of the di-muon system $p_{\mathrm{T}}(\mu\mu)$ can be considered as 'missing' and is a good approximation of the real $E_{\mathrm{T}}^{\mathrm{miss}}$ in the event. Events with two muons were selected using di-muon triggers requiring either both muons to satisfy $p_{\mathrm{T}}(\mu) > 14\,\mathrm{GeV}$ or the leading muon to have $p_{\mathrm{T}}(\mu) > 22\,\mathrm{GeV}$ and the sub-leading muon $p_{\mathrm{T}}(\mu) > 8\,\mathrm{GeV}$. After reconstruction, both muons are required to have $p_{\mathrm{T}}(\mu) > 25\,\mathrm{GeV}$ and $66.6\,\mathrm{GeV} < m(\mu\mu) < 116.6\,\mathrm{GeV}$, where the former requirement aims to select muons of good quality and the latter aims to select muons originating from decays of a Z boson. A preselection of $E_{\mathrm{T}}^{\mathrm{miss}}(L1) > 50\,\mathrm{GeV}$ is included for both the background and the signal to eliminate any bias originating from the L1 trigger.

A requirement of $p_{\mathrm{T}}(\mu\mu) > 175\,\mathrm{GeV}$ is included in the signal sample preselection since the trigger is expected to be sufficiently efficient for these values of $E_{\mathrm{T}}^{\mathrm{miss}}$ to be relevant for many analyses [2]. The resulting performance of all HLT $E_{\mathrm{T}}^{\mathrm{miss}}$ algorithms for data collected in 2017 is shown in figure 4.1. Results are grouped by pile-up $\langle\mu\rangle$, with the range of $0 \leq \langle\mu\rangle < 20$, $20 \leq \langle\mu\rangle < 30$, $30 \leq \langle\mu\rangle < 40$ and $40 \leq \langle\mu\rangle$ in figures 4.1a, 4.1b, 4.1c, 4.1d respectively. A marker is included to mark the performance of the trigger HLT_xe110_pufit_L1XE50, accepting background with a probability of about 9.2×10^{-3} while keeping an efficiency on selecting $Z \to \mu\mu$ candidate events with an efficiency of about 99.5% for low values of pile-up ($0 \leq \langle\mu\rangle < 20$).

An ideal trigger combines low background acceptance with high signal efficiency. At low $\langle\mu\rangle$, the `cell` algorithm performs worst, followed by the `mht` and `tc_lcw` algorithms. As pile-up increases, the performance of all four algorithms degrades. With the increase of pile-up, the detector resolution degrades and larger fake $E_{\mathrm{T}}^{\mathrm{miss}}$ enters collisions. Hence, distinguishing between $E_{\mathrm{T}}^{\mathrm{miss}}$ originating from pile-up and a possible signal becomes increasingly difficult as pile-up increases. The `mht` and `tc_lcw` algorithms are most affected by this degradation, which can be attributed to the lack of pile-up mitigation strategy in the algorithms. Although it is not the most efficient algorithm at low $\langle\mu\rangle$, `cell` retains most of its performance throughout the $\langle\mu\rangle$ range. The `cell` algorithm is relatively robust with respect to pile-up as it includes a noise cut of $E_i > 2\sigma_i$ for every cell. All other algorithms are instead based on topoclusters, which do not include any noise cuts for the lowest energy neighbouring cells added to the cluster. Topocluster-based algorithms are therefore more susceptible to pile-up than `cell`. Despite the `cell` algorithm's stability with increasing pile-up, `pufit` is the best performing algorithm across all pile-up ranges. The `pufit` algorithm was designed to be robust against pile-up and thus retains the most performance out of the four algorithms.

An additional improvement to the performance of the standalone `pufit` algorithm can be made by combining it with a different algorithm. During LHC Run 2, the `cell` algorithm was chosen for this combination due to its simple nature and relative robustness towards pile-up. At a given efficiency, the background acceptance (and thus the trigger rate) can be reduced by such a combination. Background events are largely dominated by $E_{\mathrm{T}}^{\mathrm{miss}}$ mismeasurements. At the trigger level, this means that events with little-to-no real $E_{\mathrm{T}}^{\mathrm{miss}}$ can be reconstructed as having large $E_{\mathrm{T}}^{\mathrm{miss}}$ by one of the algorithms. Since the details of the $E_{\mathrm{T}}^{\mathrm{miss}}$ calculation differ between all algorithms, it is less likely for an event with little-to-no real $E_{\mathrm{T}}^{\mathrm{miss}}$ to pass multiple algorithms and background can be reduced by requiring events to pass two algorithms thresholds. Events with true $E_{\mathrm{T}}^{\mathrm{miss}}$, on the other hand, are more likely to have large $E_{\mathrm{T}}^{\mathrm{miss}}$ in more than one algorithm, meaning that the signal efficiency is mostly unaffected.

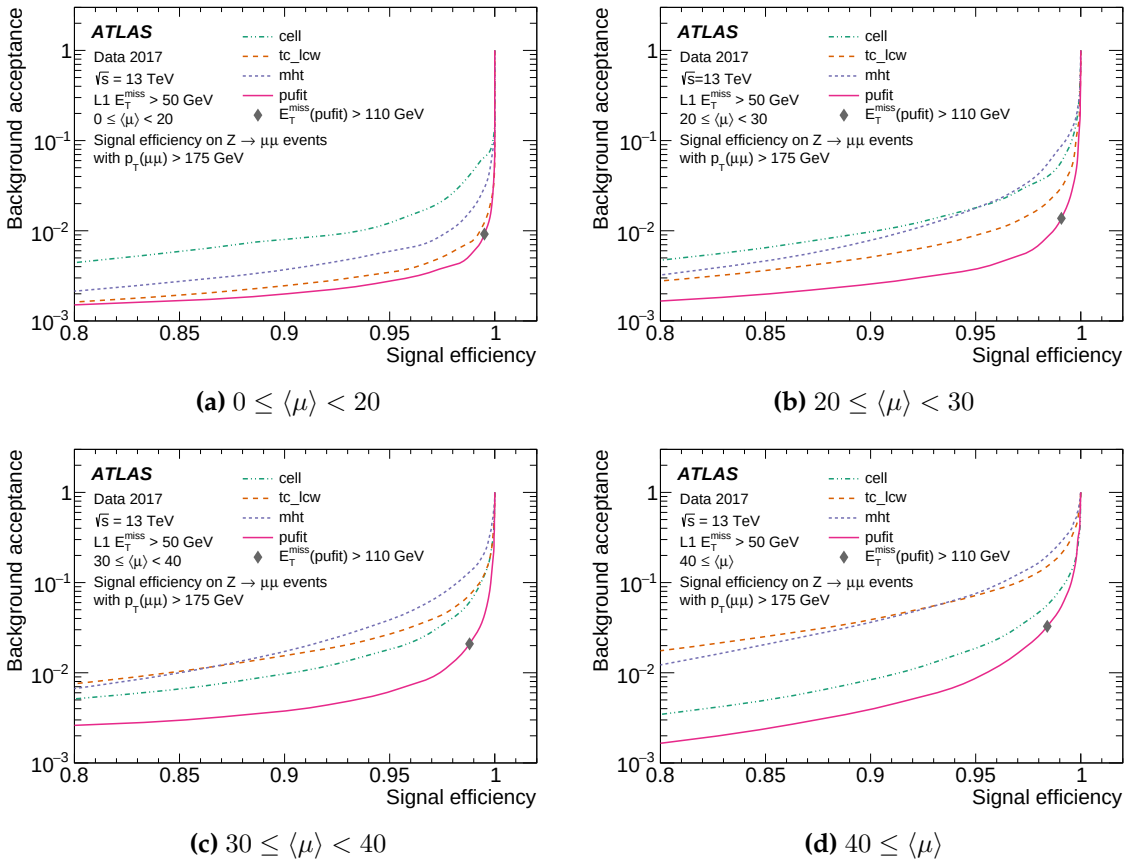

(a) $0 \leq \langle\mu\rangle < 20$ **(b)** $20 \leq \langle\mu\rangle < 30$

(c) $30 \leq \langle\mu\rangle < 40$ **(d)** $40 \leq \langle\mu\rangle$

Figure 4.1: Background acceptance against signal efficiency for all four HLT $E_{\mathrm{T}}^{\mathrm{miss}}$ algorithms for data collected in 2017. Signal events with $Z \to \mu\mu$ and $p_{\mathrm{T}}(\mu\mu) > 175\,\mathrm{GeV}$ are considered. A preselection of $E_{\mathrm{T}}^{\mathrm{miss}}(\mathtt{L1}) > 50\,\mathrm{GeV}$ was included for signal and background. Results are grouped by pile-up ranges.

The impact of the combination of the `pufit` and `cell` algorithms in Run 2 is shown in figure 4.2. The performance of both individual algorithms is shown, as well as the performance of the `pufit` algorithm with additional selections of $E_{\mathrm{T}}^{\mathrm{miss}}(\mathtt{cell}) > 65\,\mathrm{GeV}$ and $E_{\mathrm{T}}^{\mathrm{miss}}(\mathtt{cell}) > 70\,\mathrm{GeV}$. Both the background acceptance and the signal efficiency have been normalised with respect to $E_{\mathrm{T}}^{\mathrm{miss}}(\mathtt{pufit}) > 110\,\mathrm{GeV}$. A second marker is included for $E_{\mathrm{T}}^{\mathrm{miss}}(\mathtt{cell}) > 65\,\mathrm{GeV}$, $E_{\mathrm{T}}^{\mathrm{miss}}(\mathtt{pufit}) > 110\,\mathrm{GeV}$, which was one of the primary triggers during data taking in 2018. While the additional `cell` requirement reduces the relative efficiency by about 1%, the relative background acceptance is reduced by about 30%, greatly reducing the rate and thus the strain on and cost of the HLT readout bandwidth.

The improvement in performance is shown for a less (more) stringent signal selection

in figure 4.2a (4.2b) with $p_{\mathrm{T}}(\mu\mu) > 150\,(175)\,\mathrm{GeV}$. The additional reduction in the background acceptance remains constant between the two figures. However, the loss in signal efficiency is reduced to about 0.05% when considering figure 4.2b. The increased requirement on the true $E_{\mathrm{T}}^{\mathrm{miss}}$ makes it more likely for a considered event to pass both algorithm selections, which increases the trigger efficiency.

By choosing the applied threshold for both triggers appropriately, it is possible to reach similar efficiency to the individual `pufit` algorithm, while still reducing the rate significantly.

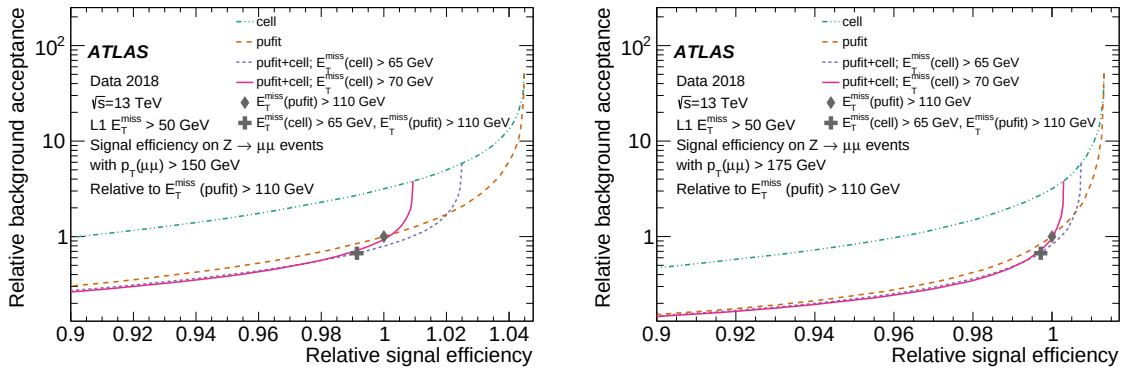

(a) $p_{\mathrm{T}}(\mu\mu) > 150\,\mathrm{GeV}$ **(b)** $p_{\mathrm{T}}(\mu\mu) > 175\,\mathrm{GeV}$

Figure 4.2: Background acceptance against signal efficiency for the single `cell` and `pufit` algorithms, the `pufit` algorithm with an additional requirement of $E_{\mathrm{T}}^{\mathrm{miss}}(\mathtt{cell}) > 65\,\mathrm{GeV}$ and the the `pufit` algorithm with an additional requirement of $E_{\mathrm{T}}^{\mathrm{miss}}(\mathtt{cell}) > 70\,\mathrm{GeV}$. A preselection of $E_{\mathrm{T}}^{\mathrm{miss}}(\mathtt{L1}) > 50\,\mathrm{GeV}$ was included for signal and background. Events with $Z \to \mu\mu$ are selected.

Efficiency Turn-On

As the trigger algorithms can only provide an approximation of the true $E_{\mathrm{T}}^{\mathrm{miss}}$, they can not reach an efficiency of 100%. How likely it is for an event to pass a certain trigger depends on the particular final state and on the chosen trigger threshold and algorithm. If the algorithm $E_{\mathrm{T}}^{\mathrm{miss}}$ were equal to the true $E_{\mathrm{T}}^{\mathrm{miss}}$, and with an algorithm trigger threshold of X, the efficiency as a function of the true $E_{\mathrm{T}}^{\mathrm{miss}}$ would

be a step function with:

$$f(E_{\mathrm{T}}^{\mathrm{miss}}) = \begin{cases} 0 & \text{if } E_{\mathrm{T}}^{\mathrm{miss}} < X \\ 1 & \text{if } X \leq E_{\mathrm{T}}^{\mathrm{miss}}. \end{cases}$$

However, as the trigger $E_{\mathrm{T}}^{\mathrm{miss}}$ can only form an approximation of the true $E_{\mathrm{T}}^{\mathrm{miss}}$, the edges of this function are smeared out. This function is referred to as the trigger turn-on curve. A better agreement between trigger algorithm and true $E_{\mathrm{T}}^{\mathrm{miss}}$ leads to a sharper turn-on curve.

The turn-on curves for the `cell` and `pufit` algorithms as well as their combination are shown in figure 4.3 for $Z \to \mu\mu$ candidate events in 2018 data. Here, the efficiency is plotted against (a) the reconstructed $E_{\mathrm{T}}^{\mathrm{miss}}$ while considering muons to be invisible or (b) $p_{\mathrm{T}}(\mu\mu)$. The results are compatible between the two plots, indicating that using the transverse momentum of the di-muon system as an approximation for the true $E_{\mathrm{T}}^{\mathrm{miss}}$ is a valid assumption. Choosing the thresholds for all algorithms

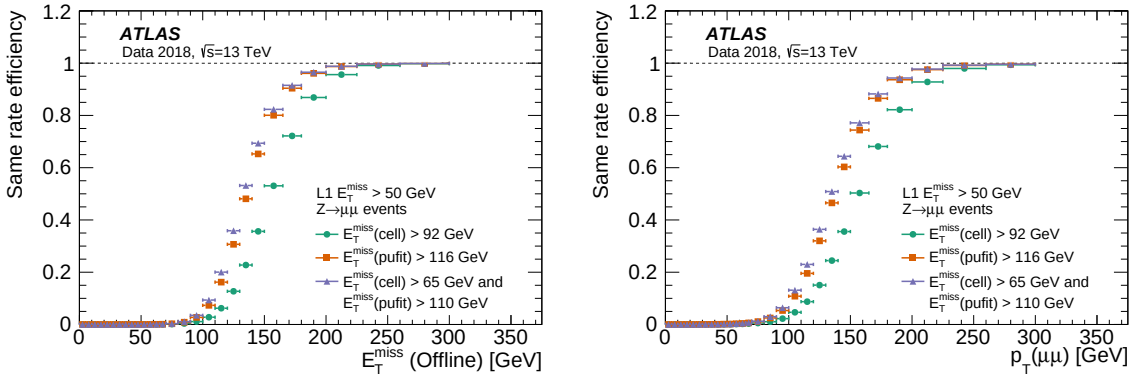

Figure 4.3: Efficiency turn-on curves for $Z \to \mu\mu$ events in 2018 data for the `cell` algorithm, the `pufit` algorithm as well as the `pufit` + `cell` combination. A preselection of $E_{\mathrm{T}}^{\mathrm{miss}}(\mathtt{L1}) > 50\,\mathrm{GeV}$ was included for signal and background. The algorithm thresholds were chosen such that all triggers produce equal rates. The same-rate efficiency is plotted against $E_{\mathrm{T}}^{\mathrm{miss}}(\mathrm{Offline})$ while treating muons as invisible (4.3a) and $p_{\mathrm{T}}(\mu\mu)$ (4.3b).

such that they yield an equal rate, the `cell` algorithm has a lower overall efficiency than both `pufit` and the `pufit` combination with `cell`. The `cell` algorithm also shows a slower efficiency turn-on. The `pufit` + `cell` combination reaches the plateau at about 25 GeV below standalone `cell` in $p_{\mathrm{T}}(\mu\mu)$. Consequentially, the use

of the pufit + cell combination allows about a 25 GeV reduction in the offline $E_{\mathrm{T}}^{\mathrm{miss}}$ selection used by analyses.

Reducing the offline $E_{\mathrm{T}}^{\mathrm{miss}}$ selection can greatly increase an analysis' acceptance. One such example is the search for Higgs boson decays to b-quarks associated with a $Z \to \nu\nu$ decay [207]. For this analysis, moving the offline $E_{\mathrm{T}}^{\mathrm{miss}}$ selection from $E_{\mathrm{T}}^{\mathrm{miss}} > 200$ GeV to 225 GeV would reduce the acceptance from 5% to only 3.5% [2, 220].

Efficiency Stability

An additional requirement for the performance of a good trigger is that it should be stable with respect to pile-up and data period. This is true both for L1 and for the HLT trigger.

Figure 4.4 shows the efficiency of a trigger requiring $E_{\mathrm{T}}^{\mathrm{miss}}(\mathtt{L1}) > 50$ GeV, $E_{\mathrm{T}}^{\mathrm{miss}}(\mathtt{cell}) > 65$ GeV and $E_{\mathrm{T}}^{\mathrm{miss}}(\mathtt{pufit}) > 110$ GeV as well as the efficiency of the $E_{\mathrm{T}}^{\mathrm{miss}}(\mathtt{L1}) > 50$ GeV trigger against pile-up $\langle\mu\rangle$ for $Z \to \mu\mu$ candidate events in 2018 data. Results are separated by the additional signal selection, with figures 4.4a and 4.4b requiring a selection on the offline $E_{\mathrm{T}}^{\mathrm{miss}}$ and figures 4.4c and 4.4d requiring a selection on $p_{\mathrm{T}}(\mu\mu)$.

There is no material drop in efficiency when requiring a selection on $p_{\mathrm{T}}(\mu\mu)$ for pile-up values of up to $\langle\mu\rangle = 60$ for both the L1 as well as the L1+HLT triggers, indicating that both triggers are stable with respect to pile-up below these values. In contrast, the efficiency of both triggers drops with increasing pile-up while selecting signal with the offline $E_{\mathrm{T}}^{\mathrm{miss}}$. The difference between the online (trigger) and offline $E_{\mathrm{T}}^{\mathrm{miss}}$ definitions therefore becomes increasingly relevant with larger values of $\langle\mu\rangle$.

The $E_{\mathrm{T}}^{\mathrm{miss}}$ trigger is used by a large variety of analyses considering a broad range of different signals. Hence, it should yield high, stable efficiencies for all possible signals. The pile-up dependence of the $E_{\mathrm{T}}^{\mathrm{miss}}(\mathtt{L1}) > 50$ GeV, $E_{\mathrm{T}}^{\mathrm{miss}}(\mathtt{cell}) > 65$ GeV and $E_{\mathrm{T}}^{\mathrm{miss}}(\mathtt{pufit}) > 110$ GeV trigger as well as the $E_{\mathrm{T}}^{\mathrm{miss}}(\mathtt{L1}) > 50$ GeV trigger for different signals are shown in figure 4.5. Table 4.1 lists the different selections used

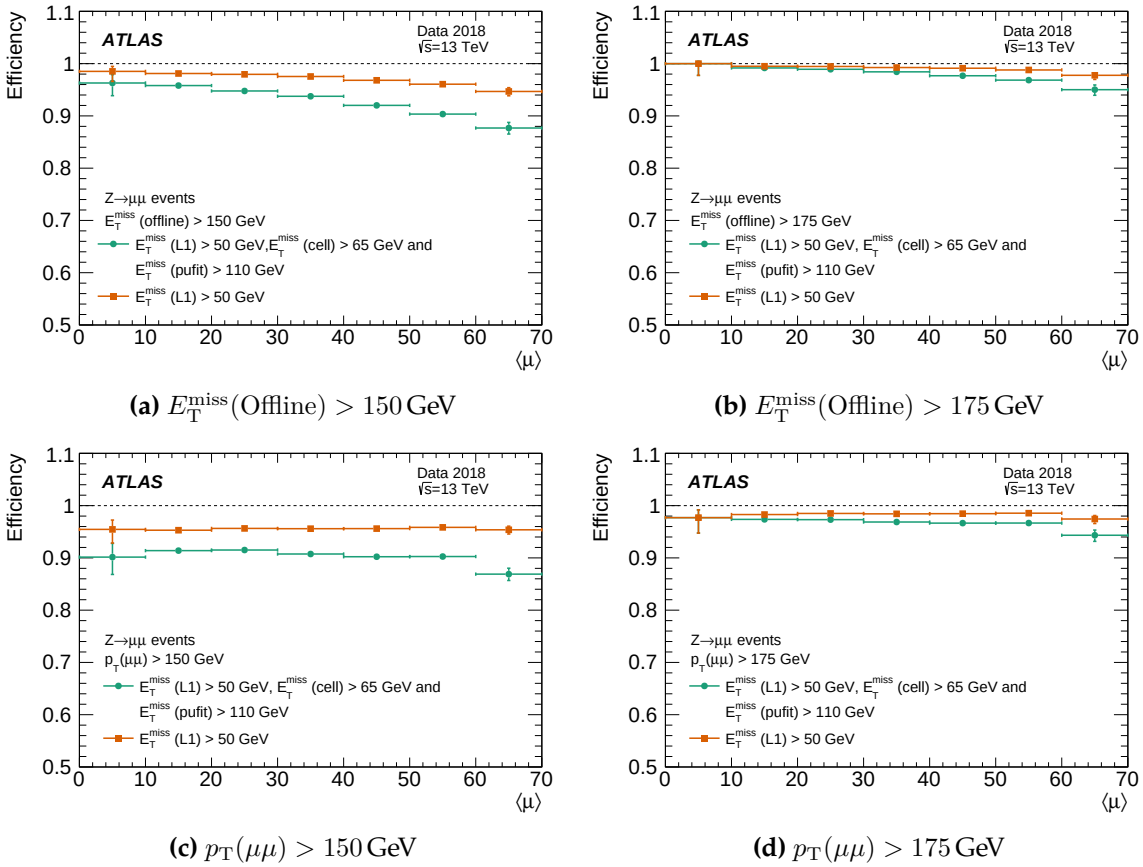

(a) $E_{\mathrm{T}}^{\mathrm{miss}}(\mathrm{Offline}) > 150\,\mathrm{GeV}$ **(b)** $E_{\mathrm{T}}^{\mathrm{miss}}(\mathrm{Offline}) > 175\,\mathrm{GeV}$

(c) $p_{\mathrm{T}}(\mu\mu) > 150\,\mathrm{GeV}$ **(d)** $p_{\mathrm{T}}(\mu\mu) > 175\,\mathrm{GeV}$

Figure 4.4: Efficiency of the `HLT_xe110_pufit_xe65_L1XE50` and `L1XE50` triggers against pile-up $\langle\mu\rangle$ for $Z \to \mu\mu$ candidate events in 2018 data. Results include a signal selection on $E_{\mathrm{T}}^{\mathrm{miss}}(\mathrm{Offline})$ (4.4a and 4.4b) or on $p_{\mathrm{T}}(\mu\mu)$ (4.4c and 4.4d). Statistical uncertainties are included.

for the different signal processes. The overall efficiency for selecting $W \to e\nu$ events is lower than the efficiency for selecting $Z \to \mu\mu$. The selection efficiency for signals including electrons is not expected to be the same as the efficiency for selecting events including muons, as muons are not included in the calculation of the visible momentum, while electrons are. Including a kinematic requirement on the number of jets in events also has an impact on the behaviour of the efficiency. The efficiencies for Vector Boson Fusion (VBF) and $t\bar{t}$ signal events behave differently than the efficiencies for selecting signals without jet requirements as the jet multiplicity and jet kinematics impact the $E_{\mathrm{T}}^{\mathrm{miss}}$ resolution, depending on where in the calorimeter the jets are found. There is some signal dependence in the $E_{\mathrm{T}}^{\mathrm{miss}}$ trigger efficiency. However, a sufficiently high and stable efficiency of the $E_{\mathrm{T}}^{\mathrm{miss}}(\mathtt{L1}) > 50\,\mathrm{GeV}$, $E_{\mathrm{T}}^{\mathrm{miss}}(\mathtt{cell}) > 65\,\mathrm{GeV}$ and

$E_{\mathrm{T}}^{\mathrm{miss}}(\texttt{pufit}) > 110\,\mathrm{GeV}$ trigger is found for all considered signal selections.

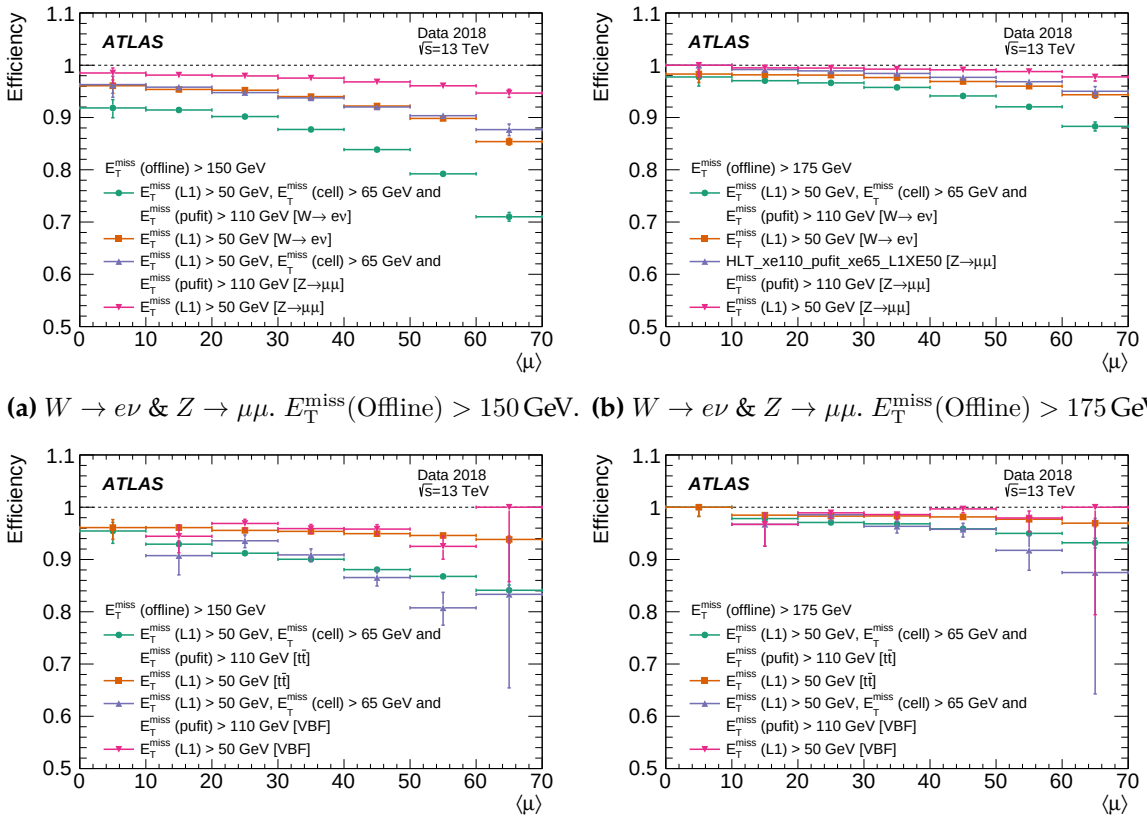

(a) $W \to e\nu$ & $Z \to \mu\mu$. $E_{\mathrm{T}}^{\mathrm{miss}}(\mathrm{Offline}) > 150\,\mathrm{GeV}$. **(b)** $W \to e\nu$ & $Z \to \mu\mu$. $E_{\mathrm{T}}^{\mathrm{miss}}(\mathrm{Offline}) > 175\,\mathrm{GeV}$.

(c) $t\bar{t}$ & VBF. $E_{\mathrm{T}}^{\mathrm{miss}}(\mathrm{Offline}) > 150\,\mathrm{GeV}$. **(d)** $t\bar{t}$ & VBF. $E_{\mathrm{T}}^{\mathrm{miss}}(\mathrm{Offline}) > 175\,\mathrm{GeV}$.

Figure 4.5: Efficiency of the `HLT_xe110_pufit_xe65_L1XE50` and `L1XE50` triggers against pile-up $\langle\mu\rangle$ in 2018 data. Results are grouped by signal selection and $E_{\mathrm{T}}^{\mathrm{miss}}(\mathrm{Offline})$ selection. Statistical uncertainties are included.

Physics process	Offline $E_{\mathrm{T}}^{\mathrm{miss}}$ definition	Leptons	Kinematics
$Z \to \mu\mu$	$p_{\mathrm{T}}(\mu\mu)$	$\mu\mu$	$66.6 < m(\mu\mu) < 116.6\,\mathrm{GeV}$
W $\to e\nu$	Tight	e	-
VBF	Tight	μ, $p_{\mathrm{T}} > 30\,\mathrm{GeV}$	Exactly two jets, $p_{\mathrm{T}} > 80\,(50)\,\mathrm{GeV}$, $\lvert\Delta\phi(\mathrm{jj})\rvert < 1.8$, $\lvert\Delta\eta(\mathrm{jj})\rvert > 4.9$
$t\bar{t}$	Tight	e, μ, $e^{\pm}\mu^{\mp}$	≥ 2 b-tagged jets

Table 4.1: Definition of offline analysis selections used for efficiency measurements, labelled by the physics process being examined. All indicated lepton requirements implicitly require $p_{\mathrm{T}}(l) > 25\,\mathrm{GeV}$ unless specified. The offline $E_{\mathrm{T}}^{\mathrm{miss}}$ definitions correspond to different working points. When multiple jets are required with different p_{T} thresholds, the threshold for the sub-leading jet is listed in parentheses, e.g. 80 (50) GeV. Table adapted from Ref. [2].

Rate and Evolution of the $E_{\mathrm{T}}^{\mathrm{miss}}$ Trigger

The introduction of the `pufit` algorithm and its combination with `cell` enabled the maintenance of an acceptable rate throughout all of Run 2.

The evolution of the primary $E_{\mathrm{T}}^{\mathrm{miss}}$ triggers and the dependence of the corresponding trigger rates on pile-up $\langle\mu\rangle$ are shown in figure 4.6a. As the instantaneous luminosity increased, so did the average pile-up $\langle\mu\rangle$. The resulting exponential increase in the trigger rate demanded the introduction of more robust pile-up mitigation techniques. In 2016, the `mht` trigger threshold had to be raised from to 90 to $110\,\mathrm{GeV}$ to keep trigger rates manageable.

Trigger rates lowered from about $300\,\mathrm{Hz}$ to about $40\,\mathrm{Hz}$ at moderate pile-up values of 40 when the `cell` + `pufit` combination was first employed as the primary $E_{\mathrm{T}}^{\mathrm{miss}}$ trigger, despite the increase of $\langle\mu\rangle$. Figure 4.6b shows the rate evolution of the $E_{\mathrm{T}}^{\mathrm{miss}}(\mathtt{L1}) > 50\,\mathrm{GeV}$ and $E_{\mathrm{T}}^{\mathrm{miss}}(\mathtt{pufit}) > 110\,\mathrm{GeV}$ trigger for data taken during run number 336832 in 2017. This trigger effectively corresponds to the pure `pufit` component of the `pufit` + `cell` triggers shown in figure 4.6a. The pure `pufit` trigger shows a rate of about $120\,\mathrm{Hz}$ at high pile-up values of $\langle\mu\rangle = 55$, which is reduced to about $100\,\mathrm{Hz}$ by the `pufit` + `cell` combination. The combination of the `pufit` and `cell` algorithms thus offers a reduction of about $20\,\mathrm{Hz}$ at high values of pile-up. The reduction in rate is less significant at lower $\langle\mu\rangle$. At pile-up values of $\langle\mu\rangle = 40$, both the `pufit` + `cell` combination and the pure `pufit` trigger show a rate of about $40\,\mathrm{Hz}$.

The evolution of the efficiency of the lowest, unprescaled $E_{\mathrm{T}}^{\mathrm{miss}}$ triggers is shown in figure 4.7. The overall efficiency was highest in 2015 due to the ideal low pile-up conditions. A similar efficiency was maintained with the introduction of the `pufit` + `cell` combination, despite the significant reduction in the trigger rate, indicating a significant improvement in background rejection. While some expected dependence of the trigger efficiency on pile-up and the considered signal selection was found,

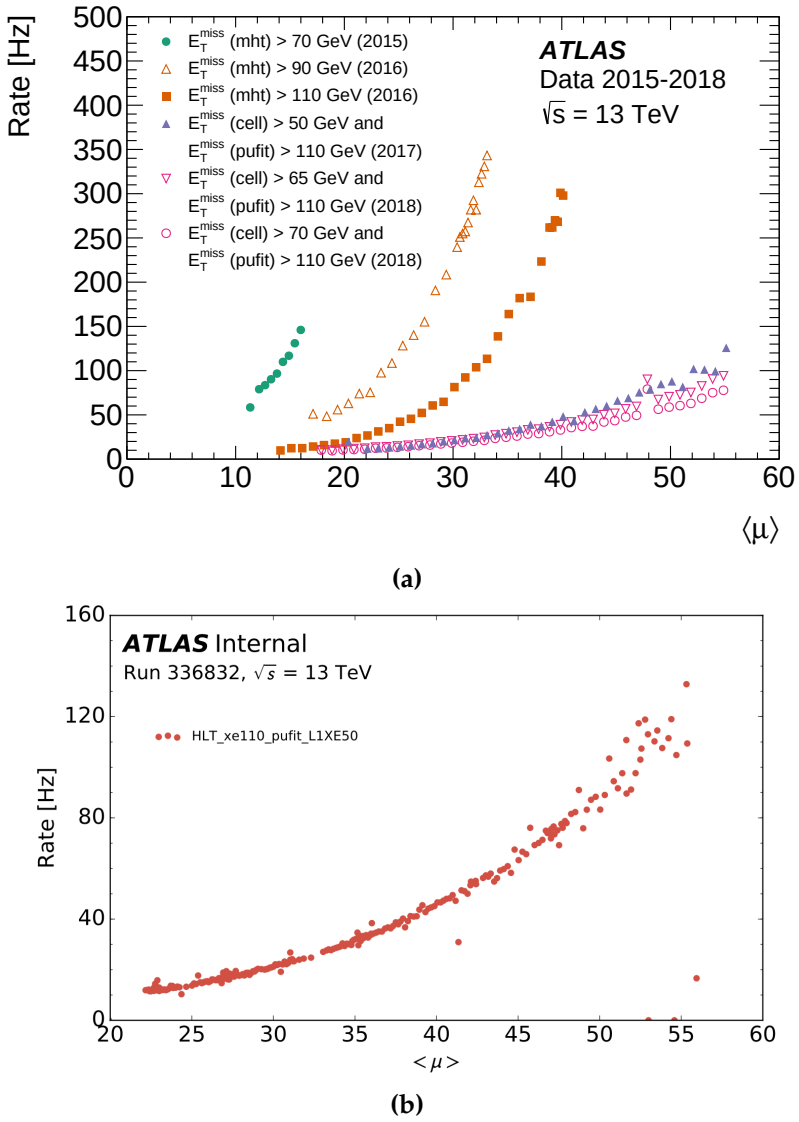

Figure 4.6: Rate dependence of the $E_{\mathrm{T}}^{\mathrm{miss}}$ triggers against $\langle\mu\rangle$ during Run 2. Figure 4.6a shows the rate evolution of the primary $E_{\mathrm{T}}^{\mathrm{miss}}$ triggers for the different years during Run 2. Figure 4.6b shows the rate evolution of the `HLT_xe110_pufit_L1XE50` trigger for data taken during run number 336832 in September 2017. These figures were produced by collaborators. Figures 4.6a and 4.6b taken from Refs. [2] and [1], respectively.

an overall stable, high efficiency with a sufficiently sharp turn-on was maintained throughout all years of Run 2 data-taking.

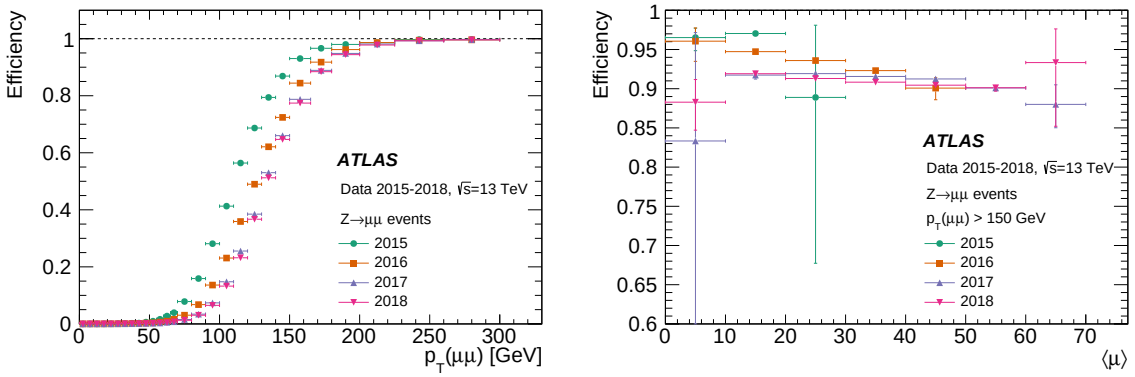

(a) **(b)**

Figure 4.7: Full-chain trigger efficiencies of the lowest unprescaled trigger for the different years of Run 2 data-taking for $Z \to \mu\mu$ candidate events against $p_{\mathrm{T}}(\mu\mu)$ (4.7a) and against $\langle\mu\rangle$ (4.7b) for $p_{\mathrm{T}}(\mu\mu) > 150\,\mathrm{GeV}$. Statistical uncertainties are included. These figures were produced by a collaborator. Figures taken from Ref. [2].

4.3 Run 3 tracking ideas

With the ability to run tracking at the trigger level comes a unique opportunity to construct new $E_{\mathrm{T}}^{\mathrm{miss}}$ trigger algorithms and thus greatly improve trigger performance [221]. In particular, tracking information can be of excellent use in mitigating pile-up, which helps in reducing trigger rates. Pile-up originates from additional pp interactions in the collision, which are associated to a different vertex than the hard scatter interaction. Tracking information can be used to identify tracks associated to pile-up vertices and thus remove pile-up from the event. This will be especially relevant during the High-Luminosity LHC era, when the average pile-up will increase to $\langle\mu\rangle = 200$ [222].

In this chapter, the `trktc` algorithm (one of the algorithms considered as candidates for the primary Run 3 $E_{\mathrm{T}}^{\mathrm{miss}}$ trigger) will be introduced and the performance of the algorithm and its constituents compared in detail to the existing $E_{\mathrm{T}}^{\mathrm{miss}}$ trigger algorithms developed during Run 2. The presented results were produced for my ATLAS authorship qualification task.

This section is structured as follows: First, the `trktc` algorithm and its constituents are introduced in section 4.3.1. The performance of the constituents is then explored in detail in section 4.3.2.

4.3.1 The `trktc` algorithm

The `trktc` algorithm closely follows constituent-level pile-up mitigation techniques employed in offline jet reconstruction [223, 224]. It uses the topological clusters defined in the `tc_lcw` algorithm as well as tracks as inputs and combines four different constituents in constructing the $E_{\mathrm{T}}^{\mathrm{miss}}$. The different constituents introduced in the following are executed in the presented order.

Voronoi Spreading

Voronoi Spreading (VS) uses information on the spacial distribution of topological clusters in the $\eta - \phi$ plane to suppress pile-up [224]. This is done in three steps:

Firstly, Voronoi areas are formed from topological clusters. These areas collect all points in the $\eta - \phi$ plane closer to a cluster than to any other cluster [225]. The area of the resulting polygons is referred to as A^{Vor} in the following. An example for an event display with the constructed Voronoi areas is shown in figure 4.8a.

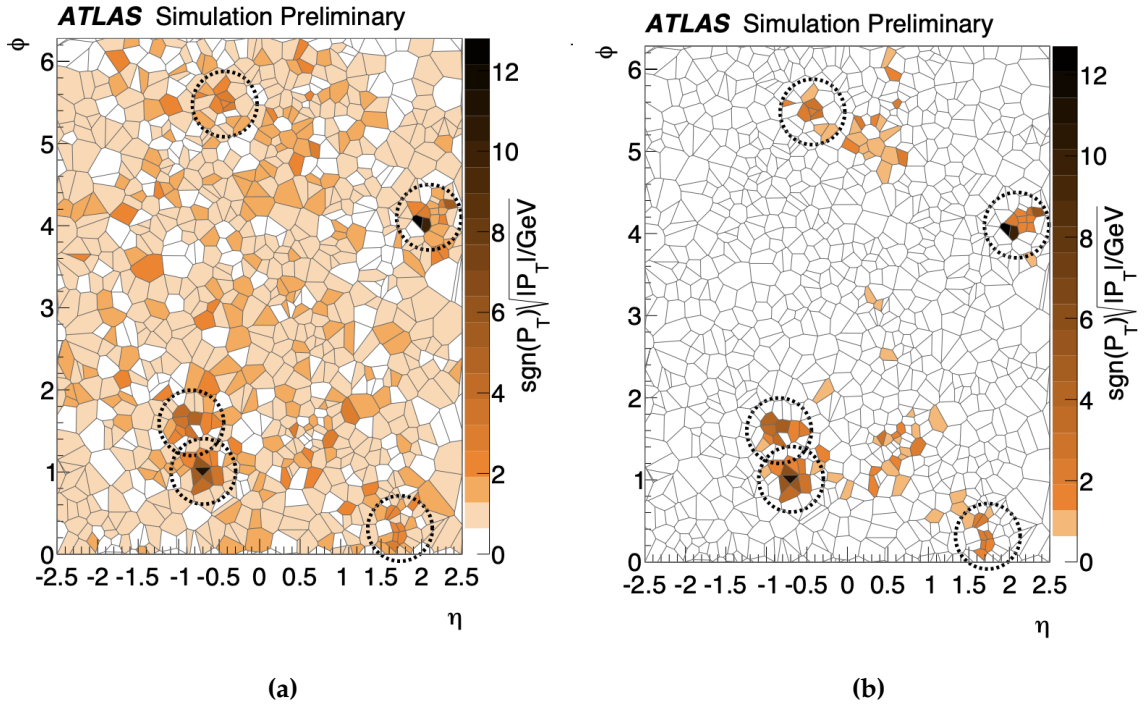

Figure 4.8: Event displays at $\mu = 20$ before (4.8a) and after (4.8b) applying Voronoi spreading, where the polygonal regions are Voronoi areas and the black dotted circles indicate truth jets with $p_{\text{T}} > 20\,\text{GeV}$. Figures taken from Ref. [224].

In the second step, pile-up is suppressed by removing the product of the median energy density ρ and the Voronoi area from the p_{T} of each cluster:

$$p_{\text{T}}^{\text{corr}} = p_{\text{T}}^{\text{cl}} - \rho A^{\text{Vor}} \tag{4.7}$$

If the original cluster p_{T}^{cl} is small, the cluster can have negative corrected values of $p_{\text{T}}^{\text{corr}}$. Such clusters are very likely to originate from pile-up. The third step spreads the

negative $p_{\mathrm{T}}^{\mathrm{corr}}$ to surrounding clusters with positive $p_{\mathrm{T}}^{\mathrm{corr}}$. This allows the suppression of positive fluctuations in pile-up energy deposits.

The $p_{\mathrm{T},i}^{\mathrm{corr}} < 0\,\mathrm{GeV}$ for each cluster i is spread to surrounding clusters as follows [224]:

1. Find all clusters j with $\Delta R_{ij} < 0.4$, $p_{\mathrm{T},j}^{\mathrm{corr}} > 0\,\mathrm{GeV}$
2. Calculate a weight w_{ij} per cluster such that $\sum w_{ij} = 1$:
$$w_{ij} = \frac{1}{N\Delta R_{ij}}, N = \sum 1/\Delta R_{ij} \tag{4.8}$$
3. Spread the negative $p_{\mathrm{T},i}^{\mathrm{corr}}$:
$$p_{\mathrm{T},j}^{\mathrm{corr}} \mapsto \begin{cases} 0\,\mathrm{GeV} & \text{if } |w_{ij}p_{\mathrm{T},i}^{\mathrm{corr}}| > p_{\mathrm{T},j}^{\mathrm{corr}} \\ p_{\mathrm{T},j}^{\mathrm{corr}} + w_{ij}p_{\mathrm{T},i}^{\mathrm{corr}} & \text{if } |w_{ij}p_{\mathrm{T},i}^{\mathrm{corr}}| < p_{\mathrm{T},j}^{\mathrm{corr}} \end{cases}$$
4. Set $p_{\mathrm{T},i}^{\mathrm{corr}} = 0\,\mathrm{GeV}$.

After the spreading is completed, all values of $p_{\mathrm{T}}^{\mathrm{corr}}$ are positive and can therefore be used in jet reconstruction or, in the case of the `trktc` algorithm, for the calculation of $E_{\mathrm{T}}^{\mathrm{miss}}$. An event display after applying Voronoi spreading is shown in figure 4.8b, where the black circles indicate truth jets with $p_{\mathrm{T}} > 20\,\mathrm{GeV}$. The Voronoi spreading algorithm is able to suppress a large fraction of the pile-up in the event, while keeping all truth jets with $p_{\mathrm{T}} > 20\,\mathrm{GeV}$.

The SoftKiller Algorithm

Instead of modifying the momenta of individual clusters, the SoftKiller (SK) algorithm introduces an event-level approach by removing the softest particles from the event [226]. This is done by placing clusters in an $\eta - \phi$ grid of 0.6×0.6 and removing all clusters with a p_{T} below a certain threshold $p_{\mathrm{T}}^{\mathrm{cut}}$. The threshold is chosen such that exactly half of the $\eta - \phi$ grid spaces are empty after it is applied. An illustration of the algorithm is given in figure 4.9. The SoftKiller algorithm has proven especially effective when combined with Voronoi spreading [224]. Therefore, only the combination of the two algorithms is considered in this study.

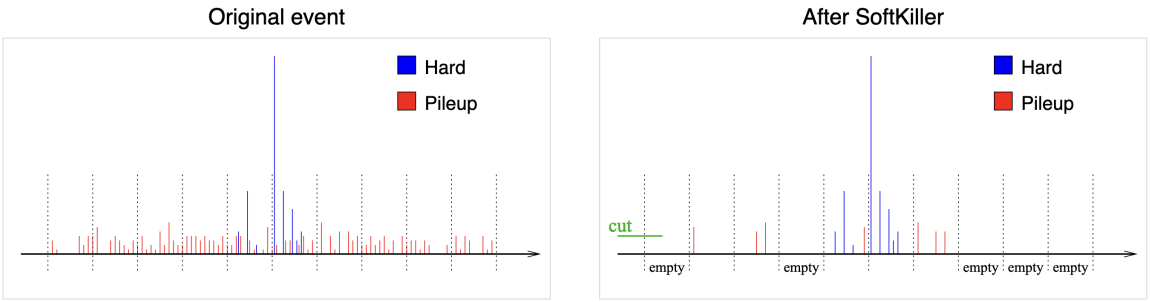

Figure 4.9: An illustration of the SOFTKILLER algorithm. The left panel demonstrates the original event, with hard-scatter particles in blue and pile-up in red. Removing all cells below the cut threshold (green) yields the right panel with substantially reduced pile-up. Figure taken from Ref. [226].

Cluster-Vertex-Fraction

Like SOFTKILLER, the Cluster Vertex Fraction (CVF) approach aims to reject clusters originating from pile-up. In the case of CVF, this is done by taking tracking information into account.

First, all tracks associated with a particular cluster are identified, by requiring that they be within $\Delta R < 0.1$ of the cluster and have $p_{\mathrm{T},i}^{\mathrm{trk}} > 0.5\,\mathrm{GeV}$ [223]. After this, the CVF is calculated from the tracks originating from the primary vertex and pile-up, determining the fraction of track p_{T} originating from the primary vertex [224]:

$$\mathrm{CVF} = \frac{\sum_{\mathrm{HS}} p_{\mathrm{T},i}^{\mathrm{trk}}}{\sum_{\mathrm{HS}} p_{\mathrm{T},i}^{\mathrm{trk}} + \sum_{\mathrm{PU}} p_{\mathrm{T},i}^{\mathrm{trk}}} \tag{4.9}$$

The reader is referred to Ref [227] for more information on how tracks are associated with vertices and how both are reconstructed in ATLAS. If no tracks are associated with the cluster, the CVF takes a value of -1. The CVF can therefore only take values of either -1 or between 0 and 1. Clusters without any hard-scatter contribution, i.e. with $\mathrm{CVF} = 0$, are removed. To avoid the removal of high-p_{T} neutral particles without tracks, clusters are only removed if they have $p_{\mathrm{T}}^{\mathrm{cluster}} < 1\,\mathrm{GeV}$. Figure 4.10 shows an illustration of the CVF method.

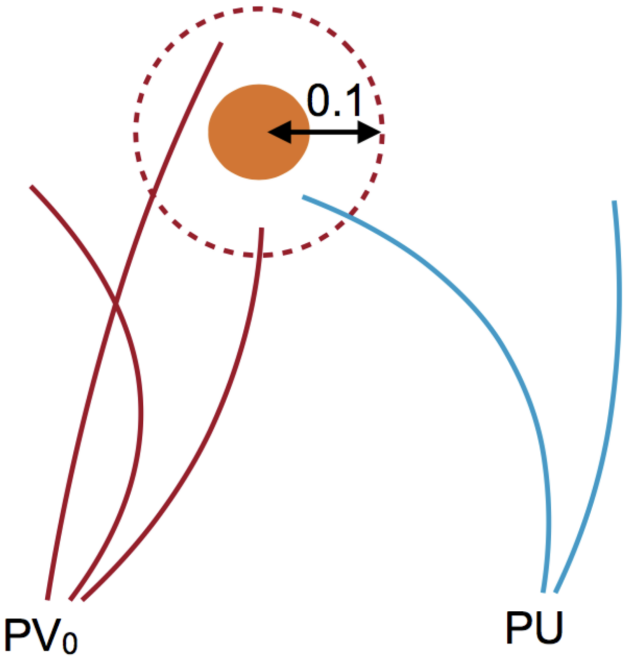

Figure 4.10: An illustration of the CVF approach. Tracks within $\Delta R < 0.1$ of the cluster (orange) are considered. Tracks are separated into originating from the primary vertex PV_0 or pile-up PU. Figure taken from Ref. [223].

Track Soft Term

The Track Soft Term (TST) offers an additional correction to the $E_{\mathrm{T}}^{\mathrm{miss}}$ by collecting all soft tracks originating from the primary vertex that are not associated with high-p_{T} objects in a single term. In offline $E_{\mathrm{T}}^{\mathrm{miss}}$ construction, the TST term is added to the negative sum over all reconstructed objects, thereby removing the soft tracks from the $E_{\mathrm{T}}^{\mathrm{miss}}$ and thus yielding a more accurate prediction for it [214]. At the trigger level, full object reconstruction is not available. Instead, the TST is formed from all tracks not associated with the primary vertex, if they satisfy $p_{\mathrm{T}}^{\mathrm{trk}} \leq 20\,\mathrm{GeV}$. This requirement prevents high-p_{T} muons from entering the sum over the visible momentum, ensuring that they remain invisible to the trigger. This is necessary as some analyses involving muons use this feature in selecting events with the $E_{\mathrm{T}}^{\mathrm{miss}}$ triggers, such as the observation of VH production, where the Higgs boson is produced in association with a Z-boson which decays to muons or a W-boson which decays to $\mu\nu$ [207]. To avoid any negative impact of the physics reach of

such analyses, the decision was made that any new $E_{\mathrm{T}}^{\mathrm{miss}}$ trigger algorithm should also treat muons as invisible.

The final $E_{\mathrm{T}}^{\mathrm{miss}}$ is calculated from the negative sum over all CVF corrected clusters and the track soft term. In this study, the track soft term is seen as an optional addition to CVF and is therefore only studied in combination with CVF.

4.3.2 Performance of the `trktc` constituents

This section explores the performance of the `trktc` algorithm and its constituents in more detail. The considered combinations of constituents are shown in table 4.2.

VS + SK	CVF	TST	algo. name
✓	-	-	`sktc`
✓	✓	-	`sktc_cvf`
✓	✓	✓	`trktc`
-	✓	-	`tc_cvf`
-	✓	✓	`tc_cvf_tst`

Table 4.2: Combinations of `trktc` constituents considered in the performance study. VS, TST, CVF and TST indicate Voronoi spreading, SOFTKILLER, Cluster Vertex Fraction and Track Soft Term, respectively.

The background rejection of the `trktc` algorithms is evaluated on reprocessed enhanced-bias data collected in 2018 which is collected by a combination of L1 triggers such that roughly similar rates are allocated to all events, regardless of their $E_{\mathrm{T}}^{\mathrm{miss}}$ and the trigger phase space is thus roughly uniformly populated [228, 229].

The signal efficiency is calculated using simulated VBF and $W \to \mu\nu$ events. Higgs boson production via VBF was simulated in the decay channel of $H \to ZZ$, where each Z-boson decays to a pair of neutrinos. Events were generated using POWHEG BOX V2 [230–232], interfaced with PYTHIA 8 using the AZNLO PYTHIA 8 tune [233]. The POWHEG prediction is accurate to Next-to-Leading Order (NLO) and uses the PDF4LHC15 NLO PDF set [234]. An additional requirement on the true missing transverse momentum of $E_{\mathrm{T}}^{\mathrm{miss}} > 125\,\mathrm{GeV}$ was applied.

The simulation of $W \to \mu\nu$ events was performed with with SHERPA 2.2 [235], using the NNPDF 3.0 NNLO PDF set [236]. A veto of b- and c-quarks was applied, as well as a selection requiring $140\,\mathrm{GeV} < p_{\mathrm{T}}^{W} < 280\,\mathrm{GeV}$.

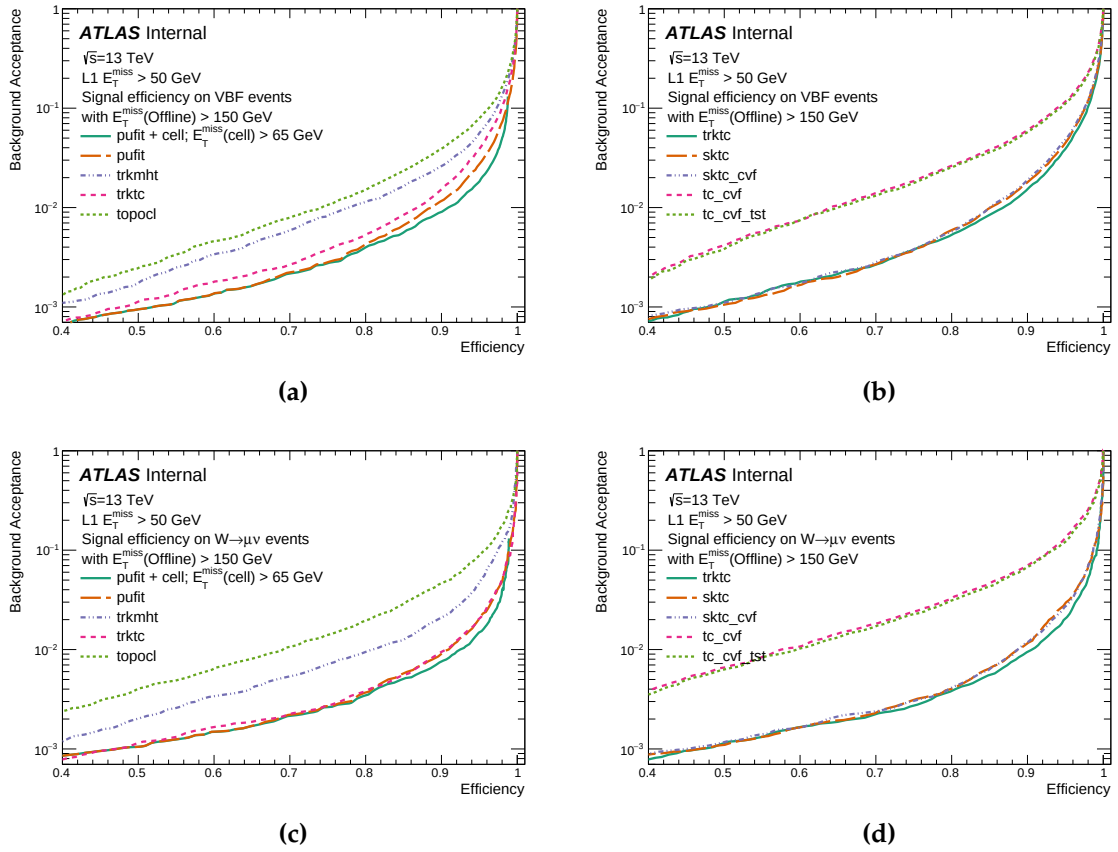

Figure 4.11: Background acceptance against signal efficiency for the `trktc` algorithm variants compared to other algorithms. Signal events with an offline $E_{\mathrm{T}}^{\mathrm{miss}} > 150\,\mathrm{GeV}$ are considered. Results are grouped by signal sample with the top plots (4.11a, 4.11b) showing results for the VBF signal sample and the bottom plots (4.11c, 4.11d) showing results for the $W \to \mu\nu$ signal sample. The left plots (4.11a, 4.11c) compare the performance of the proposed `trktc` and `trkmht` algorithms to existing algorithms developed in Run 2, while the right plots (4.11b, 4.11d) compare the performance of the `trktc` constituents. A preselection of $E_{\mathrm{T}}^{\mathrm{miss}}(\mathtt{L1}) > 50\,\mathrm{GeV}$ was required for signal and background.

The performance of the `trktc` algorithm is compared against several different algorithms in figures 4.11a and 4.11c. As a reference point, the performance of the `trkmht` algorithm is included in figures 4.11a and 4.11c. This Run 3 candidate algorithm combines the `mht` algorithm with tracking information by only including jet-vertex-tagged jets in the $E_{\mathrm{T}}^{\mathrm{miss}}$ sum [221]. The reader is referred to Ref. [237] for details concerning jet-vertex-tagging.

The pufit + cell trigger rejects more background for a fixed efficiency than both tracking algorithms. The trkmht algorithm performs only slightly better than tc_lcw and the performance of trktc is similar to that of standalone pufit. Results are consistent between the VBF and $W \to \mu\nu$ signal samples.

The trktc variant algorithms largely fall into two categories in terms of their performance, where tc_cvf and tc_cvf_tst perform poorer than sktc, sktc_cvf and trktc (cf. figures 4.11b and 4.11d). A large fraction of the performance of the trktc algorithm therefore comes from Voronoi spreading and the SoftKiller algorithm and adding the CVF and track soft term algorithms has only little effect on the algorithm performance.

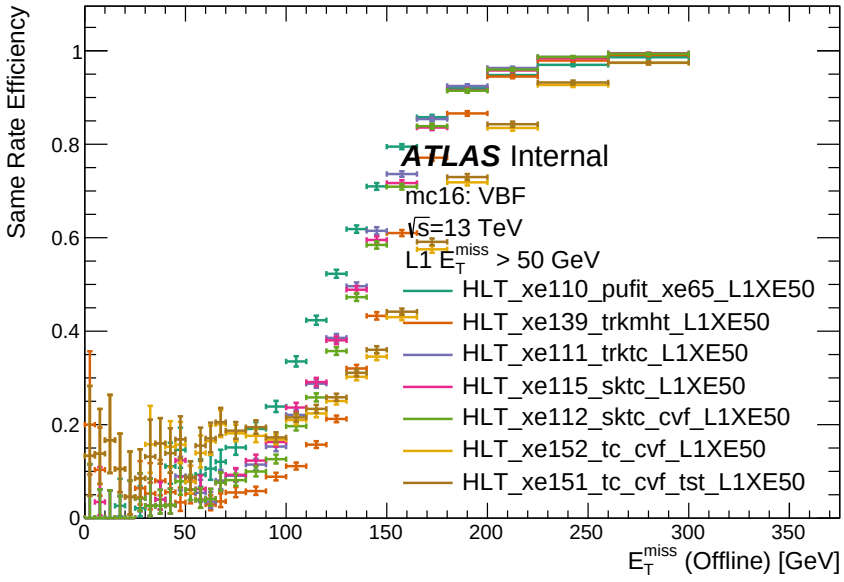

Figure 4.12: Same-rate efficiency for selecting VBF signal events for the trktc algorithm variants compared to the $E_{\mathrm{T}}^{\mathrm{miss}}(\mathtt{L1}) > 50\,\mathrm{GeV}$, $E_{\mathrm{T}}^{\mathrm{miss}}(\mathtt{cell}) > 65\,\mathrm{GeV}$ and $E_{\mathrm{T}}^{\mathrm{miss}}(\mathtt{pufit}) > 110\,\mathrm{GeV}$ trigger. A preselection of $E_{\mathrm{T}}^{\mathrm{miss}}(\mathtt{L1}) > 50\,\mathrm{GeV}$ was included. The trigger thresholds for the trktc variants were chosen to match the rates of the pufit + cell trigger.

This is confirmed by the same-rate efficiency turn-on curve shown in figure 4.12. The $E_{\mathrm{T}}^{\mathrm{miss}}(\mathtt{L1}) > 50\,\mathrm{GeV}$, $E_{\mathrm{T}}^{\mathrm{miss}}(\mathtt{cell}) > 65\,\mathrm{GeV}$ and $E_{\mathrm{T}}^{\mathrm{miss}}(\mathtt{pufit}) > 110\,\mathrm{GeV}$ trigger yields higher efficiencies and a sharper turn-on than all trktc variants, and the constituents employing Voronoi spreading and SoftKiller yield a sharper turn-on curve than the constituents without. These results were unexpected, as the additional

tracking information added by the CVF algorithm was expected to contribute significantly to the overall performance of the `trktc` algorithm. Instead, the CVF algorithm offers only a limited improvement to the overall performance. This implies that the CVF algorithm is less efficient in mitigating pile-up than the Voronoi spreading and SOFTKILLER algorithms, while the Voronoi spreading and SOFTKILLER algorithms are less efficient in mitigating pile-up than the `pufit + cell` combination. These results motivate the use of non-CVF tracking information in the `pufit` algorithm in constructing a primary trigger for Run 3.

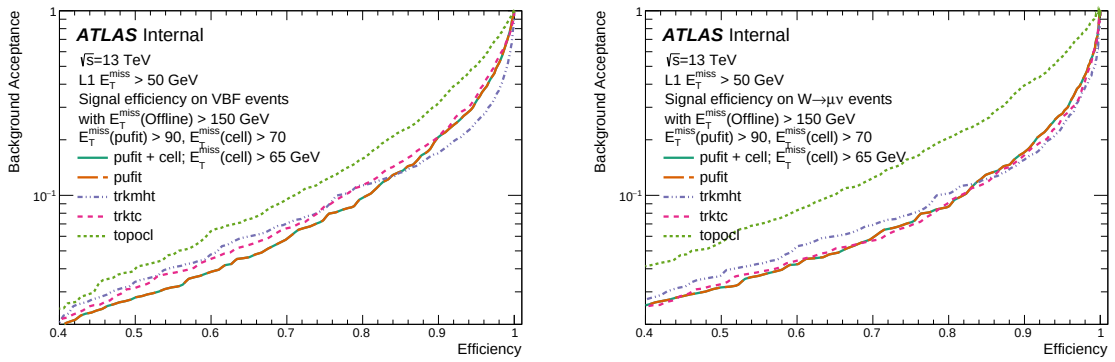

(a) VBF signal events **(b)** $W \to \mu\nu$ signal events

Figure 4.13: Background acceptance against signal efficiency. Signal events with an offline $E_{\mathrm{T}}^{\mathrm{miss}} > 150\,\mathrm{GeV}$ are considered. A preselection of $E_{\mathrm{T}}^{\mathrm{miss}}(\mathtt{L1}) > 50\,\mathrm{GeV}$, $E_{\mathrm{T}}^{\mathrm{miss}}(\mathtt{cell}) > 70\,\mathrm{GeV}$ and $E_{\mathrm{T}}^{\mathrm{miss}}(\mathtt{pufit}) > 90\,\mathrm{GeV}$ was included for signal and background. Results are grouped by signal events.

The performance of the `trktc` algorithm when combined with Run 2 $E_{\mathrm{T}}^{\mathrm{miss}}$ trigger algorithms needs to be investigated to further explore the potential increase of the algorithm performance through the use of tracking information. While the `trktc` algorithm performs poorer than the `pufit + cell` combination, it is possible that a combination of all three algorithms results in a significant improvement in the reduction of pile-up. Figure 4.13 shows the impact of applying a preselection of $E_{\mathrm{T}}^{\mathrm{miss}}(\mathtt{cell}) > 70\,\mathrm{GeV}$ and $E_{\mathrm{T}}^{\mathrm{miss}}(\mathtt{pufit}) > 90\,\mathrm{GeV}$ on the performance of the `trktc` algorithm variants. The `trkmht` algorithm performs much better when this preselection is included, yielding a better performance in the region of high efficiency ($> 85\%$) than both the `pufit + cell` combination and the `trktc` algorithm for

the VBF signal sample (cf. figure 4.13a). All three algorithms yield a comparable performance for the $W \rightarrow \mu\nu$ signal sample (cf. figure 4.13b).

The `trktc` algorithm does not offer a significant improvement over the performance of the already existing `pufit` algorithm or its combination with `cell`. Furthermore, adding tracking information in the form of CVF and TST offers only a minimal improvement over the performance of the `sktc` algorithm, which uses Voronoi spreading and SoftKiller. Tracking information is only able to remove pile-up originating from charged particles, as neutral particles do not leave tracks in the ID. Neutral pile-up can therefore not be removed by the added CVF and TST requirements. The limited performance gain when CVF and TST are added therefore indicates that most pile-up which remains after running Voronoi spreading and SoftKiller is neutral. A solution to this problem is to incorporate tracking information into the inputs of the `pufit` algorithm, as the `pufit` algorithm would then only need to reduce neutral pile-up in the χ^2-method fit, thus potentially improving its performance with the use of tracking.

Motivated by this unexpected lack of improvement of the `trktc` algorithm when tracking information is added, other $E_{\mathrm{T}}^{\mathrm{miss}}$ trigger candidate algorithms were studied for Run 3. Studies performed by collaborators have identified algorithms for which adding tracking information does result in a significant improvement of the algorithm performance [238]. Therefore, the `trktc` algorithm is not chosen as one of the Run 3 primary $E_{\mathrm{T}}^{\mathrm{miss}}$ triggers. Instead, the current primary $E_{\mathrm{T}}^{\mathrm{miss}}$ trigger for Run 3 involves a combination of `cell` with the `pfopufit` algorithm, a `pufit` variant which builds towers from particle flow objects instead of calorimeter cells while using particle flow vertex information to remove charged pile-up before the fit [221]. Thus improving the `pufit` algorithm following the reasoning outlined above. The studies presented in this thesis have aided the development of this primary trigger in further motivating the use of both a `pufit` variant algorithm as well as a trigger combination of the Run 3 primary algorithm with at least one of the existing algorithms developed in Run 2.

5

The $\gamma\gamma$bb analysis

Contents

5.1 Gauge-Mediated Supersymmetry breaking at the LHC 82
5.2 Data and Simulation Samples 86
5.2.1 Background Samples 86
5.2.2 Signal Samples 88
5.3 Event Reconstruction, Selection & Categorisation 91
5.3.1 Event Reconstruction 91
5.3.2 Event Selection 93
5.3.3 Signal Region Optimisation 95
5.3.4 Event Categorisation 101
5.4 Background Estimation Techniques 103
5.4.1 2x2D Sideband Method 104
5.4.2 Modified ABCD Method - used for SR2 only 114
5.4.3 Validation of Background Modelling 119
5.5 Signal Region Sensitivity 125
5.6 Systematic Uncertainties 128
5.7 Results 131
5.8 Conclusions 137

5.1 Gauge-Mediated Supersymmetry breaking at the LHC

From the absence of direct evidence for physics beyond the Standard Model, we know that Supersymmetry, if realised in nature, has to be a broken symmetry. One well motivated way of realising Supersymmetry breaking is Gauge-Mediated Supersymmetry Breaking (GMSB) [108, 112]. In this model, the breaking is mediated through gauge interactions, naturally leading to scenarios with the gravitino $\tilde{G}$ (the super partner of the graviton) as the Lightest Supersymmetric Particle (LSP). If the lightest neutralino $\tilde{\chi}_1^0$ is assumed to be the NLSP, this results in a decay of the lightest neutralino $\tilde{\chi}_1^0$ to a γ, Z or h and a $\tilde{G}$, as seen in figure 5.1a. The exact

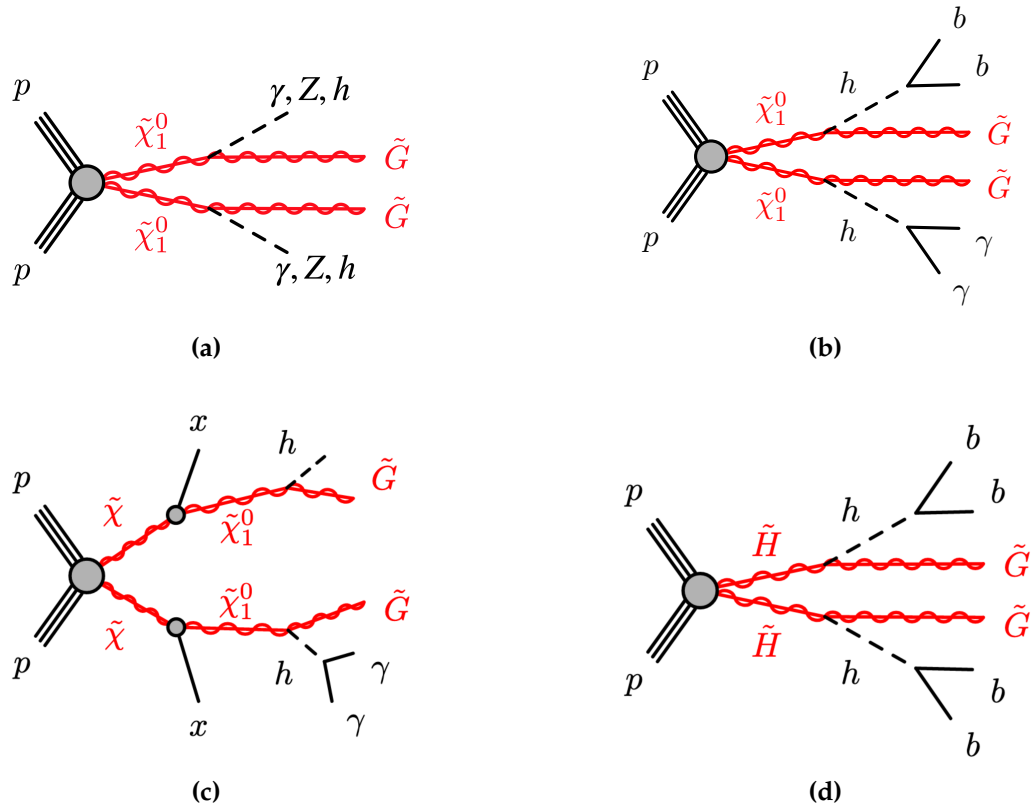

Figure 5.1: Feynman diagrams for the GMSB model (5.1a), the final state considered in the $\gamma\gamma$bb analysis (5.1b), the WHphoton search [239] (5.1c) and the multi-b search [240] (5.1d). Supersymmetric particles are indicated in red, while SM particles are indicated in black.

branching fractions for the neutralino in this decay depend on its mixing. Here, we are considering a pure Higgsino-type $\tilde{\chi}_1^0$ (also denoted as $\tilde{H}$), with the possible decay modes being $\tilde{\chi}_1^0 \to h\tilde{G}$ and $\tilde{\chi}_1^0 \to Z\tilde{G}$. The $\tilde{G}$ is expected to be stable and nearly

massless ($\mathcal{O}(\mathrm{MeV})$). It does not interact with the detector and can therefore only be detected as Missing Transverse Momentum ($E_{\mathrm{T}}^{\mathrm{miss}}$), calculated by the sum of all transverse momenta in the collision (see section 5.3.2). If R-parity conservation is assumed, the gravitino $\tilde{G}$ is stable and therefore a viable Dark Matter candidate.

Two previous searches for GMSB models have been performed in related final states with the ATLAS detector. The "WHphoton" search [239] considers decays of one Higgs boson to a pair of photons on one leg of the diagram and an inclusive decay on the other leg of the diagram, as illustrated in figure 5.1c, while the "multi-b" analysis [240] considers decay of both Higgs bosons to a pair of b-quarks, as illustrated in figure 5.1d. Neither of these searches directly targets the $\gamma\gamma b\bar{b} + E_{\mathrm{T}}^{\mathrm{miss}}$ final state.

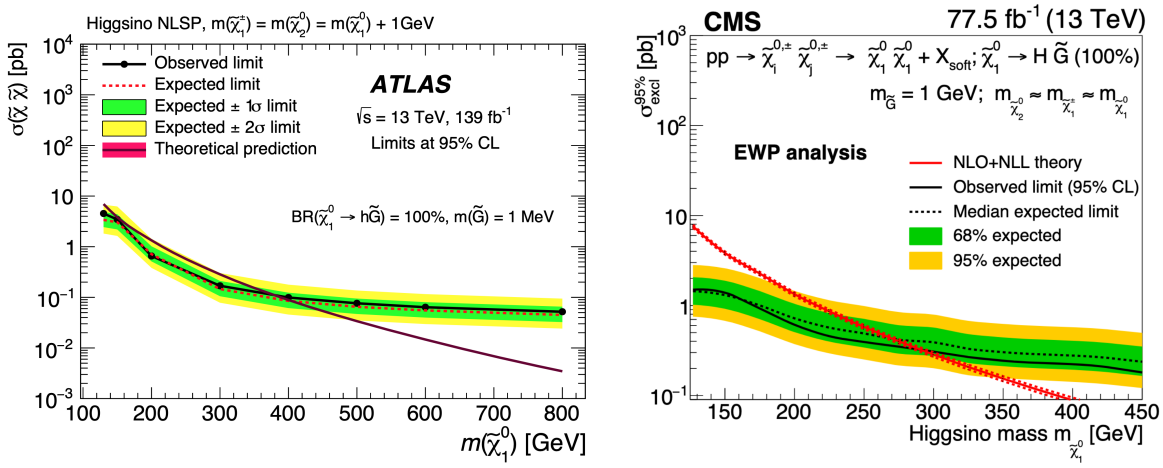

(a) **(b)**

Figure 5.2: Observed exclusion by the ATLAS WHphoton search [239] (5.2a) and a related search by CMS [241] (5.2b).

The WHphoton search excludes models with neutralino $\tilde{\chi}_1^0$ masses of up to $\sim 350\,\mathrm{GeV}$, assuming a branching ratio of $\mathrm{BR}(\tilde{\chi}_1^0 \to h\tilde{G}) = 100\%$ and using the full Run 2 luminosity of $139\,\mathrm{fb}^{-1}$, as shown in figure 5.2a. It has been optimised for pure Higgsino type neutralinos and is expected to lose sensitivity with other branching ratios. A related search by CMS [241] is able to exclude models with pure-Higgsino cross sections as low as $1.5\,\mathrm{pb}$ for a neutralino mass of $m(\tilde{\chi}_1^0) = 130\,\mathrm{GeV}$ (see figure 5.2b), while the WHphoton exclusion only reaches cross sections of $4.5\,\mathrm{pb}$ at the same

mass. The difference in sensitivity occurs despite the search by CMS using only roughly half of the luminosity of the ATLAS WHphoton search with $77.5\,\mathrm{fb}^{-1}$.

One of the key differences between the two analyses is in the preselection. The WHphoton search aims to select events with a Higgs boson decaying into two photons on one leg of the Feynman diagram, while remaining remaining agnostic to the decays of the Higgs boson on the other leg of the Feynman diagram (see fig. 5.1c). The search by CMS aims to select events with one Higgs decaying to a pair of photons and the other to a pair of b-quarks (see fig. 5.1b). This selection combines the advantages of the large branching fraction of the Higgs boson to two b-quarks with the distinct signature of two photons in an environment where most backgrounds involve QCD particles. It should be noted that events with two pairs of photons and b-quarks are included in the dataset of both analyses. However, the added explicit requirement of two b-quarks originating from the decay of a Higgs boson in the search by CMS enhances the sensitivity.

The $\gamma\gamma$bb analysis presented in this thesis aims to use a similar selection of a final state with two photons and two b-quarks both with an invariant mass close to the mass of the Higgs to enhance the overall sensitivity with ATLAS, especially to models with low $\tilde{\chi}_1^0$ masses. The $\gamma\gamma$bb and WHphoton analyses are not orthogonal due to the inclusive Higgs boson decay considered by the WHphoton search, significantly complicating a potential combination of the two analyses. The two searches should therefore be considered separately.

In the next section, we will introduce all of the data and simulated samples used by this analysis. Section 5.3 provides a detailed description of the employed event reconstruction and selection. Furthermore, three signal regions with narrow selections on the invariant di-photon mass $m_{\gamma\gamma}$ will be defined, separated by the invariant di-b mass m_{bb} as well as $E_{\mathrm{T}}^{\mathrm{miss}}$. Two fully data-driven background estimation techniques will be introduced and validated in detail in section 5.4. The background in this analysis is dominated by the non-resonant di-photon and fake-photon backgrounds.

The "2x2D sideband method" makes use of simulated data as well as data in the $m_{\gamma\gamma}$ sidebands in estimating the the non-resonant backgrounds in the control regions. The obtained background estimation will then also be applied directly to the low-$E_{\mathrm{T}}^{\mathrm{miss}}$ signal regions. A "modified ABCD method" will be used to extrapolate background estimation results to the high-$E_{\mathrm{T}}^{\mathrm{miss}}$ signal region. The sensitivity of the individual signal regions will be discussed in section 5.5. Results will be provided in section 5.7. As no significant excess is found in any signal region, limits on the production cross-section $\sigma(\tilde{\chi}\tilde{\chi})$ and accepted ranges of $m(\tilde{\chi}_1^0)$ and $\mathrm{BF}(\tilde{\chi}_1^0 \to h\tilde{G})$ will be drawn.

The contents of this chapter are adapted from original contributions to Ref. [3].

5.2 Data and Simulation Samples

This analysis considers pp collision data collected with the ATLAS detector between 2015 and 2018. During this period, the LHC was operating with a bunch crossing interval of 25 ns at $\sqrt{s} = 13\,\text{TeV}$. All considered events were recorded under stable beam conditions in which the ATLAS trigger, tracking and calorimeter systems were operational. The events pass the *Loose* and *Medium* di-photon triggers (cf. section 5.3.2) as well as additional data quality criteria [242]. The full dataset adds to an integrated luminosity of $139\,\text{fb}^{-1}$.

5.2.1 Background Samples

The background samples used in this analysis are listed in table 5.1. A detailed account of the simulation of the background samples can be found in Refs. [3, 243]. We will summarise them as follows. The non-resonant di-photon background was simulated with SHERPA 2.2 [235], using a dedicated tune developed by the SHERPA authors. Matrix elements were calculated at Next-to-Leading Order (NLO) for up to one parton and at Leading Order (LO) for up to three partons with the COMIX [244] and OPENLOOPS [245–247] libraries. The the NNPDF3.0 NNLO PDF set [236] was used.

Events containing a Higgs boson produced in association with a top quark and other quarks (tHq or tHjb) were generated with MADGRAPH5_AMC@NLO 2.3.3 [248], using the NNPDF 3.0 NLO PDF set [236], interfaced with PYTHIA 8.230 [249], using the A14 tune [250] and the NNPDF 2.3 LO PDF set [236]. The production of tWH events was modelled using MADGRAPH5_AMC@NLO 2.3.3 with PYTHIA 8.235 [249] and the A14 tune.

The production of other backgrounds containing SM Higgs bosons is simulated at NLO using POWHEG BOX V2 [230–232], interfaced with PYTHIA 8.230. In the case of Higgs boson production in association with a vector boson (ZH, WpH, WmH, ggZH), the PDF4LHC15 NLO PDF set [234] and the AZNLO PYTHIA 8 tune [233] were used.

The same configuration was used to simulate Higgs boson production via Vector Boson Fusion (VBF). The generation of events containing Higgs boson production via two b-quarks (bbH) used the NNPDF 2.3 LO PDF set and the AZNLO PYTHIA 8 tune. Events containing a Higgs boson produced in association with two top quarks (ttH) were generated using POWHEG BOX V2 with the NNPDF 3.0 NLO PDF set interfaced with PYTHIA 8.230 using the A14 tune and the NNPDF 2.3 LO PDF set. Higgs boson production via gluon-gluon fusion (ggH) achieved Next-to-Next-to-Leading Order (NNLO) accuracy in the simulation with POWHEG BOX V2 by re-weighting the Higgs boson rapidity spectrum as calculated in HNNLO [251]. The PDF4LHC15 NNLO PDF set [234] and the AZNLO tune of PYTHIA 8 were used in the generation.

All SM Higgs backgrounds are normalised according to the cross-section as determined by Ref. [252].

The ATLAS detector response is simulated with a full detector simulation for all background samples, with the exception of the non-resonant di-photon background, for which the detector response is simulated with ATLFAST-II (AFII) [253, 254]. Full simulation mostly improves the modelling of detector resolution effects with respect to AFII, causing potential inaccuracies in the width of resonances. Hence, detector resolution effects are not expected to have a large impact in the non-resonant di-photon background, justifying the use of AFII. The non-resonant $\gamma\gamma$ background MC sample is used together with the fake-photon data to estimate the total non-resonant background using the 2x2D sideband method in section 5.4.1. This data-driven technique can compensate for some potential inaccuracies in the $\gamma\gamma$ MC sample. During the 2x2D sideband method, photon isolation and identification efficiencies are calculated using the di-photon background. Studies have shown that the difference in photon efficiencies between full simulation and AFII is below the percent level [255]. As the efficiencies can only be determined to the percent level in this analysis, the simulation with AFII therefore provides sufficient accuracy.

Process	Matrix element	Parton Shower	PDF set	Cross-section
$\gamma\gamma$+jets	SHERPA 2.2		NNPDF 3.0 NNLO	Generator NLO
tHjb	MADGRAPH_AMC 2.3.3	PYTHIA 8.230	NNPDF 3.0 NLO + NNPDF 2.3 LO	[252]
tWH	MADGRAPH_AMC 2.3.3	PYTHIA 8.235	NNPDF 2.3 LO	[252]
ZH	POWHEG BOX V2 [230–232, 256]	PYTHIA 8.230	PDF4LHC15 NLO	[252]
WpH	POWHEG BOX V2 [230–232, 256]	PYTHIA 8.230	PDF4LHC15 NLO	[252]
WmH	POWHEG BOX V2 [230–232, 256]	PYTHIA 8.230	PDF4LHC15 NLO	[252]
ggZH	POWHEG BOX V2 [230–232, 256]	PYTHIA 8.230	PDF4LHC15 NLO	[252]
VBF	POWHEG BOX V2 [230–232, 257]	PYTHIA 8.230	PDF4LHC15 NLO	[252]
bbH	POWHEG BOX V2 [230–232, 256]	PYTHIA 8.230	NNPDF 2.3 LO	[252]
ttH	POWHEG BOX V2 [230–232, 258, 259]	PYTHIA 8.230	NNPDF 3.0 NLO + NNPDF 2.3 LO	[252]
ggH	POWHEG BOX V2 [230–232, 260, 261]	PYTHIA 8.230	PDF4LHC15 NNLO	[252]

Table 5.1: Background MC Samples used in this analysis. The first category are non-resonant samples used in the data-driven background estimation (see section 5.4), the others are resonant Higgs processes. The resonant Higgs samples are generated considering 100% BR to $\gamma\gamma$ and therefore $\sigma \times \mathrm{BR}[\mathrm{pb}]$ is considered.

5.2.2 Signal Samples

The signal samples considered in this analysis are generated using MADGRAPH5_AMC@NLO 2.9.3 with the NNPDF 3.0 NLO PDF, interfaced with PYTHIA 8 using the A14 tune and the NNPDF 2.3 LO PDF. All signal samples consider the production of a Higgsino neutralino $\tilde{\chi}_1^0$ through $\tilde{\chi}_1^\pm - \tilde{\chi}_1^\pm$, $\tilde{\chi}_1^\pm - \tilde{\chi}_1^0$, $\tilde{\chi}_1^\pm - \tilde{\chi}_2^0$ and $\tilde{\chi}_1^0 - \tilde{\chi}_2^0$ production. The production cross sections are computed at NLO plus Next-to-Leading-Log (NLL) precision, where the lightest chargino $\tilde{\chi}_1^\pm$ and the second lightest neutralino $\tilde{\chi}_2^0$ are assumed to be roughly mass degenerate to the lightest neutralino, i.e. we set $m(\tilde{\chi}_1^\pm) = m(\tilde{\chi}_2^0) = m(\tilde{\chi}_1^0) + 1\,\mathrm{GeV}$. Following the arguments presented in section 2.2.2, the mass of the gravitino is assumed to be $m(\tilde{G}) = 1\,\mathrm{MeV}$, while all other sparticles are assumed to be heavy and decoupled, with masses of $4.5 \times 10^9\,\mathrm{GeV}$ [262, 263]. The considered signal samples cover $\tilde{\chi}_1^0$ masses of $m(\tilde{\chi}_1^0) = 130, 150, 200, 300, 400, 500, 600, 800\,\mathrm{GeV}$.

The detector simulation of all signal samples is performed with AFII. The impact of this is discussed in detail in Ref. [3]. From this study, it was concluded that the AFII signal samples are sufficient to determine the analysis' sensitivity to the

considered models. To increase the number of relevant events in the signal samples, the decays of the neutralino $\tilde{\chi}_1^0$ are fixed to:

- $\mathrm{BF}\left(\tilde{\chi}_1^0 \to h\tilde{G}\right) = 50\%$, where h is the SM Higgs
- $\mathrm{BF}\left(\tilde{\chi}_1^0 \to h'\tilde{G}\right) = 50\%$, where h' is the SM Higgs with $\mathrm{BF}\left(h' \to \gamma\gamma\right) = 100\%$

Consequentially, the signal sample cross-section needs to be re-weighted to account for Higgs boson branching ratios. The corresponding re-weighting factor is calculated in appendix A.1. It amounts to approximately 0.0091. These samples will be referred to as 'hh signal samples' in the following.

To account for $\tilde{\chi}_1^0 \to Z\tilde{G}$, with $Z \to b\bar{b}$ decays, a second class of signal samples is generated with the same setup but assuming:

- $\mathrm{BF}\left(\tilde{\chi}_1^0 \to Z\tilde{G}\right) = 50\%$, where Z is the SM Z
- $\mathrm{BF}\left(\tilde{\chi}_1^0 \to h'\tilde{G}\right) = 50\%$, where h' is the SM Higgs with $\mathrm{BF}\left(h' \to \gamma\gamma\right) = 100\%$.

In the following, these will be referred to as 'Zh signal samples'. Again, a re-weighting factor needs to be applied. This re-weighting factor is also calculated in app. A.1 and amounts to 2.270×10^{-3}. To simplify the use of these samples, only events with exactly one neutralino decaying to a Z-boson and one decaying to a Higgs boson are considered.

Signal samples with arbitrary values of the neutralino branching fraction can be obtained by adding the yields for the two classes of signal samples with appropriate weights, i.e.:

$$N_{\mathrm{tot.}} = \mathrm{BF}\left(\tilde{\chi}_1^0 \to h\tilde{G}\right)^2 N_{hh} + 4\,\mathrm{BF}\left(\tilde{\chi}_1^0 \to h\tilde{G}\right)\mathrm{BF}\left(\tilde{\chi}_1^0 \to Z\tilde{G}\right) N_{Zh}. \tag{5.1}$$

Here, the Zh samples only include events with exactly one neutralino decay to Higgs and one to a Z-boson. Events with $\mathrm{BF}(\tilde{\chi}_1^0 \to Z\tilde{G}) = 100\%$ need not be considered as

the Z-boson does not decay to photons. The rationale for the factor of 4 can be seen by considering the scenario where $\mathrm{BF}\left(\tilde{\chi}_1^0 \to h\tilde{G}\right) = 0.5$, for which events from the Zh sample are taken without applying any additional re-weighting factor.

In summary, two sets of signal samples for a Higgsino neutralino scenario are generated. The first set is re-weighted to a Higgsino scenario with $\mathrm{BR}(\tilde{\chi}_1^0 \to h\tilde{G}) = 1$, while the second set is re-weighted to a Higgsino scenario with $\mathrm{BR}(\tilde{\chi}_1^0 \to h\tilde{G}) = \mathrm{BR}(\tilde{\chi}_1^0 \to Z\tilde{G}) = 0.5$. A signal sample for arbitrary values of of $\mathrm{BR}(\tilde{\chi}_1^0 \to h\tilde{G})$ can then be obtained from these two sets by re-weighting and combining the two using equation 5.1.

5.3 Event Reconstruction, Selection & Categorisation

This section summarises the analysis strategy of the $\gamma\gamma$bb analysis in detail, structured as follows. First, section 5.3.1 will give a detailed account of the event reconstruction and object definition. After events are reconstructed, a preselection is applied as summarised in section 5.3.2. An account of the optimisation of the three signal regions is provided in section 5.3.3. Lastly, the full event categorisation and employed region strategy of the $\gamma\gamma$bb analysis including all defined signal, control and validation regions will be summarised in section 5.3.4.

5.3.1 Event Reconstruction

Photons: Photons are reconstructed with $|\eta| < 2.37$, while applying a veto on the ECal transition region $1.37 < |\eta| < 1.52$. In overlap removal (explained below), photons are given priority. We distinguish between baseline and signal photons. The former are used to model backgrounds while the latter enter the signal regions. Baseline photons are required to pass *Loose'3* selection requirements, while signal photons are required to pass *Tight* selection and isolation requirements [264]. Photons are only considered if they satisfy $p_T^\gamma > 25\,\text{GeV}$ in both cases. This ensures a high photon reconstruction efficiency of $\gtrsim 85\%$ [264].

The *Loose'N* working points select photons that pass *Loose* selection criteria as well as $11-N$ out of the 11 *Tight* selection criteria, meaning that N of the *Tight* selection criteria are not applied. In the case of *Loose'3*, the three requirements that are not applied are: a selection on the lateral shower width w_{s3}, the energy fraction outside the core of three central cells f_{side}, and the energy difference between the second maximum cell and the cell with the smallest value found between first and second maximum ΔE_s. For further details on the *Loose'N* working points, the reader is referred to Ref. [264].

The *Loose'3* working point is used for two reasons: Firstly, it is tighter than the trigger *Medium* identification working point, reducing the trigger bias of the considered

events. Secondly, there is a non-negligible correlation between the photon isolation energy E_T^{iso} and some shower shape variables used in the *Tight* photon identification. The *Loose'3* preselection requires photons to pass the selections using correlated variables, ensuring that there is only a negligible correlation between applying *Tight* isolation and identification after the preselection [3, 265]. This is relevant for the 2x2D background estimation technique described later in section 5.4.1. The 2x2D sideband method separates photon candidates using the photon isolation and identification variables, which is complicated by the potential presence of significant correlations between the two. Due to the use of the *Loose'3* preselection, only negligible correlations between photon isolation and identification enter the dataset used in the 2x2D sideband method, which significantly simplifies the background estimation.

Jets: The analysis uses PFlow jets, which are reconstructed using the particle flow algorithm [266], combining both calorimeter and tracking information. Jets are accepted if they pass $p_{\text{T}} > 30\,\text{GeV}$ and $\eta < 2.5$. From the selected jets, b-jets are identified using the DL1 tagger at the fixed 77% efficiency working point [267], as calculated on $t\bar{t}$ events. Default working points are used for jet-vertex-tagging and jet cleaning.

Leptons: Electrons are required to have: $|\eta| < 2.47$, as well as a transverse momentum of $p_{\text{T}} > 4.5\,\text{GeV}$. The *LooseAndBLayerLLH* identification working point is used for baseline electrons [268]. No veto on the EM Calorimeter transition region is applied.

Muons are required to have: $|\eta| < 2.7$, as well as $p_{\text{T}} > 4\,\text{GeV}$. For baseline muons, the *Medium* working point is used [269].

All electrons and muons need to satisfy a requirement on the longitudinal impact parameter of $|z_0|\sin(\theta) < 0.5\,\text{mm}$.

Missing Transverse Momentum: The $E_{\text{T}}^{\text{miss}}$ is constructed from the vector sum of all transverse momenta of all reconstructed objects in the collision (photons, jets,

muons and electrons), as well as a 'track-soft-term' (tst) including the transverse momenta of all tracks associated with the primary vertex that are not reconstructed as one of the particles listed before:

$$E_{\mathrm{T}}^{\mathrm{miss}} = \left| \sum_{\mathrm{objects}} -\vec{p}_{\mathrm{T}} + \sum_{\mathrm{tst}} -\vec{p}_{\mathrm{T}} \right| \tag{5.2}$$

The default $E_{\mathrm{T}}^{\mathrm{miss}}$ working point is used [270]. In contrast to the trigger-level $E_{\mathrm{T}}^{\mathrm{miss}}$, which is calculated from lower level objects such as calorimeter towers, depending on the algorithms introduced in section 4.2, the definition of $E_{\mathrm{T}}^{\mathrm{miss}}$ used in this analysis relies on full object reconstruction.

Overlap removal: Reconstructed objects located in close vicinity to other objects are removed to avoid double counting. The ATLAS overlap removal strategy for analyses involving photons is used in this analysis. Electrons, muons and jets are removed from events if they are within $\Delta R = 0.4$ of any photon.

5.3.2 Event Selection

After reconstruction, events are selected using an *OR* of the four loose and medium di-photon triggers listed in table 5.2. The triggers were active during different years of data-taking as shown in table 5.3.

All signal, control and validation regions consider events with exactly two signal photons. Events with two *Loose'3* photons are used to estimate the non-resonant backgrounds in the control regions, as described in section 5.4.1. All events are required to satisfy a selection on the invariant mass of the di-photon system with $100\,\mathrm{GeV} \leq m_{\gamma\gamma} \leq 160\,\mathrm{GeV}$, with the additional requirement that $p_T^{\gamma}/m_{\gamma\gamma} > 0.2$, which was introduced to reduce the contribution from fake photons and to enhance the signal to background ratio. To reduce the effect of the trigger thresholds, the leading (highest p_{T}) photon is required to have $p_T^{\gamma} > 35\,\mathrm{GeV}$.

Events with two or fewer b-quarks ($n_b \leq 2$) are selected. This ensures orthogonality to the multi-b analysis. To reduce $\gamma\gamma Z$, $\gamma\gamma W^{\pm}$ and leptonic $t\bar{t}$ backgrounds, a veto

HLT_g35_loose_L1EM15_g25_loose_L1EM15	
leading γ	sub-leading γ
L1: $p_{\mathrm{T}} > 15\,\mathrm{GeV}$	**L1**: $p_{\mathrm{T}} > 15\,\mathrm{GeV}$
HLT: `Loose`, $p_{\mathrm{T}} > 35\,\mathrm{GeV}$	**HLT**: `Loose`, $p_{\mathrm{T}} > 25\,\mathrm{GeV}$
HLT_g35_loose_g25_loose_L12EM15VH	
leading γ	sub-leading γ
L1: $p_{\mathrm{T}} > 15\,\mathrm{GeV}$, VH	**L1**: $p_{\mathrm{T}} > 15\,\mathrm{GeV}$, VH
HLT: `Loose`, $p_{\mathrm{T}} > 35\,\mathrm{GeV}$	**HLT**: `Loose`, $p_{\mathrm{T}} > 25\,\mathrm{GeV}$
HLT_g35_medium_g25_medium_L12EM20VH	
leading γ	sub-leading γ
L1: $p_{\mathrm{T}} > 20\,\mathrm{GeV}$, VH	**L1**: $p_{\mathrm{T}} > 20\,\mathrm{GeV}$, VH
HLT: `Medium`, $p_{\mathrm{T}} > 35\,\mathrm{GeV}$	**HLT**: `Medium`, $p_{\mathrm{T}} > 25\,\mathrm{GeV}$
HLT_2g50_loose_L12EM20VH	
leading γ	sub-leading γ
L1: $p_{\mathrm{T}} > 20\,\mathrm{GeV}$, VH	**L1**: $p_{\mathrm{T}} > 20\,\mathrm{GeV}$, VH
HLT: `Loose`, $p_{\mathrm{T}} > 50\,\mathrm{GeV}$	**HLT**: `Loose`, $p_{\mathrm{T}} > 50\,\mathrm{GeV}$

Table 5.2: The triggers used in this analysis. **L1** refers to the selection applied at the hardware based first-level trigger, while **HLT** refers to the requirements applied at the software based high-level trigger. *Loose* and *Medium* refer to the applied photon identification working point. A 'V' appended to the trigger name indicates an η-dependent E_{T} threshold at **L1**, 'H' denotes a hadronic activity veto at **L1**. Events are required to pass at least one trigger. All triggers are fully unprescaled for Run 2 [189]. The baseline *Loose'3* photon identification Working Point is tighter than the trigger *Medium* photon identification Working Point, so the trigger bias entering the selected events in minimised.

Trigger	2015	2016	2017	2018
HLT_g35_loose_L1EM15_g25_loose_L1EM15	✓	-	-	-
HLT_g35_loose_g25_loose_L12EM15VH	✓	✓	-	-
HLT_g35_medium_g25_medium_L12EM20VH	-	-	✓	✓
HLT_2g50_loose_L12EM20VH	-	-	✓	✓

Table 5.3: Overview of the triggers used in this analysis per year of data-taking.

on any event containing one or more loose leptons is applied. Events with two or more jets are selected to reduce the overall number of events used in the background estimation, reducing both the data sample's size as well as the time and computation power required in handling them. No signal events are lost due to this cut, since a selection of exactly two b-jets is later applied in both signal regions. In the following, applying the selections listed above will be referred to as *preselection level*, while $n_b = 2$ *preselection level* refers to the above selections with the added requirements

of exactly 2 b-jets in all events.

5.3.3 Signal Region Optimisation

This section repeats the evaluation of the expected significance under the signal + background hypothesis and an optimisation of each discovery Signal Region (SR). SR1 and SR1Z are optimised for low $m(\tilde{\chi}_1^0)$ ($\lesssim 150\,\text{GeV}$) while SR2 is optimised for more intermediate values of $m(\tilde{\chi}_1^0)$ ($\sim 200 - 300\,\text{GeV}$). The sensitivity is calculated with [271]:

$$Z_N = \sqrt{2\left(n\ln\left(\frac{n(b+\sigma^2)}{b^2+n\sigma^2}\right) - \frac{b^2}{\sigma^2}\ln\left(\frac{b^2+n\sigma^2}{b(b+\sigma^2)}\right)\right)}, \tag{5.3}$$

where b is the number of background events, s the number of signal events, $n = b + s$ is the number of total expected events and σ the systematic uncertainty on the background. A detailed account of the uncertainty on all backgrounds will be provided later in section 5.6. The background uncertainty is later found to be of the order of 15% (39%) for the low-$E_{\text{T}}^{\text{miss}}$ (high-$E_{\text{T}}^{\text{miss}}$) signal regions. Equation 5.3 leads to a single significance value for each $\tilde{\chi}_1^0$ mass point in each of the three signal regions.

The significance obtained by a simple cut on the most relevant variables are shown in figure 5.3 and 5.4 for SR1, 5.5 for SR1Z and figure 5.6 for SR2. These figures display "N-1 plots" where all signal region selections are applied, except for the selection on the plotted variable. Markers are included in all three figures, indicating the value and direction of the selection. The cumulative significance is calculated using the same indicated direction. In short, all three signal regions select events with an invariant di-photon mass $m_{\gamma\gamma}$ close to the mass of the Higgs boson. The low-$E_{\text{T}}^{\text{miss}}$ signal regions SR1 and SR1Z select the Higgs and Z-boson peaks in the invariant di-b mass m_{bb} respectively, while the high-$E_{\text{T}}^{\text{miss}}$ signal region SR2 makes use of a wide m_{bb} window to increase acceptance. A choice was made to use background estimation techniques that improve the modelling of $m_{\gamma\gamma}$ by a large margin. This makes it possible to select events close to the Higgs mass in $m_{\gamma\gamma}$, while keeping a looser selection on m_{bb}. The low-$E_{\text{T}}^{\text{miss}}$ signal regions SR1 and SR1Z have been

optimised using the $m(\tilde{\chi}_1^0) = 130\,\text{GeV}$ mass point, while the high-$E_{\text{T}}^{\text{miss}}$ SR2 has been optimised using the $m(\tilde{\chi}_1^0) = 200\,\text{GeV}$ mass point.

Figures 5.4a, 5.5a and 5.6a show the cumulative significance for a varying upper limit on $|m_{\gamma\gamma} - 125\,\text{GeV}|$. As indicated in these figures, an optimal upper limit of $|m_{\gamma\gamma} - 125\,\text{GeV}| < 5\,\text{GeV}$ was chosen in all three signal regions to simplify the categorisation of control and validation regions. While a tighter selection would yield a slightly stronger significance, the expected number of background events would shrink significantly (in particular below the 2-event mark in SR2), implying that large fluctuations on the observed numbers of events in the signal regions would be expected.

The cumulative significance for an upper limit selection on m_{bb} is shown in figures 5.3 for SR1 and figure 5.6b for SR2. As the signal is asymmetric around the Higgs boson mass peak, these plots were used to motivate the initial values used in a further optimisation of an asymmetric m_{bb} selection, as explored in appendix A.2. SR1Z was added at lower m_{bb} values after SR1 was optimised. The technique used to determine the lower limit used in SR1Z is also explored in appendix A.2.

All signal regions include a lower limit on $p_{\text{T}}^{\gamma_2}/m_{\gamma\gamma}$ to increase the signal to background ratio, as indicated in figures 5.4b, 5.5b and 5.6c for SR1, SR1Z and SR2, respectively. Additionally, a selection of $p_{\text{T}}^{\gamma\gamma} > 90\,\text{GeV}$ was found for both SR1 and SR1Z. No $p_{\text{T}}^{\gamma\gamma}$ selection is included for SR2 due to the low numbers of events. The selections on $p_{\text{T}}^{\gamma_2}/m_{\gamma\gamma}$ and $p_{\text{T}}^{\gamma\gamma}$ were optimised independently for all signal regions.

Lastly, a $E_{\text{T}}^{\text{miss}}$ selection is included for all signal regions, where it serves as an upper limit for SR1 (figure 5.4d) and SR1Z (figure 5.5d) and as a lower limit for SR2 (figure 5.6d). This selection makes it possible to optimise SR2 for intermediate neutralino masses of $m(\tilde{\chi}_1^0) \approx 200\,\text{GeV}$. All three signal regions are orthogonal due to the employed $E_{\text{T}}^{\text{miss}}$ selection and can therefore be used in a statistical combination to enhance sensitivity (see secion 5.7).

Based on this optimisation, three signal regions are defined as follows:

SR1: $n_b = 2$; $E_{\mathrm{T}}^{\mathrm{miss}} \leq 100\,\mathrm{GeV}$; $|m_{\gamma\gamma} - 125| < 5\,\mathrm{GeV}$; $100\,\mathrm{GeV} < m_{bb} < 140\,\mathrm{GeV}$
$p_T^{\gamma}/m_{\gamma\gamma} > 0.4$; $p_{\mathrm{T}}^{\gamma\gamma} > 90\,\mathrm{GeV}$

SR1Z: $n_b = 2$; $E_{\mathrm{T}}^{\mathrm{miss}} \leq 100\,\mathrm{GeV}$; $|m_{\gamma\gamma} - 125| < 5\,\mathrm{GeV}$; $60\,\mathrm{GeV} < m_{bb} \leq 100\,\mathrm{GeV}$
$p_T^{\gamma}/m_{\gamma\gamma} > 0.4$; $p_{\mathrm{T}}^{\gamma\gamma} > 90\,\mathrm{GeV}$

SR2: $n_b = 2$; $E_{\mathrm{T}}^{\mathrm{miss}} > 100\,\mathrm{GeV}$; $|m_{\gamma\gamma} - 125| < 5\,\mathrm{GeV}$; $35\,\mathrm{GeV} < m_{bb} \leq 145\,\mathrm{GeV}$
$p_T^{\gamma}/m_{\gamma\gamma} > 0.2$

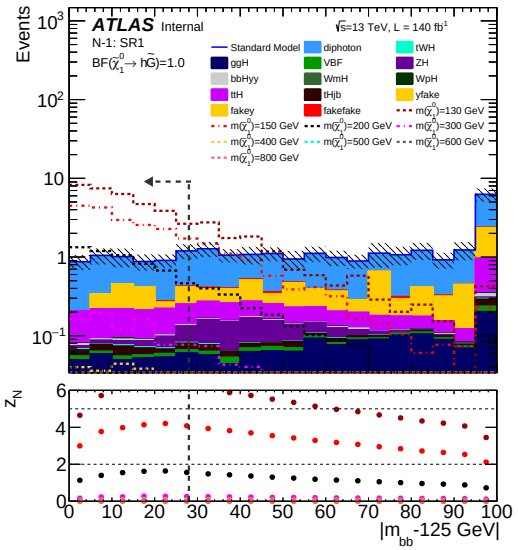

Figure 5.3: Distributions of the discriminating variable $|m_{bb} - 125\,\mathrm{GeV}|$ for signal and backgrounds, with all the selections of SR1 applied, except for the selection on the plotted variable. The lower pad shows the cumulative significance obtained by applying a upper or lower limit on the plotted variable at the indicated value. A marker is included, indicating the central value used for further optimisation in appendix A.2. The signal benchmarks in this set of figures assume $\mathrm{BF}(\tilde{\chi}_1^0 \to h\tilde{G}) = 100\%$.

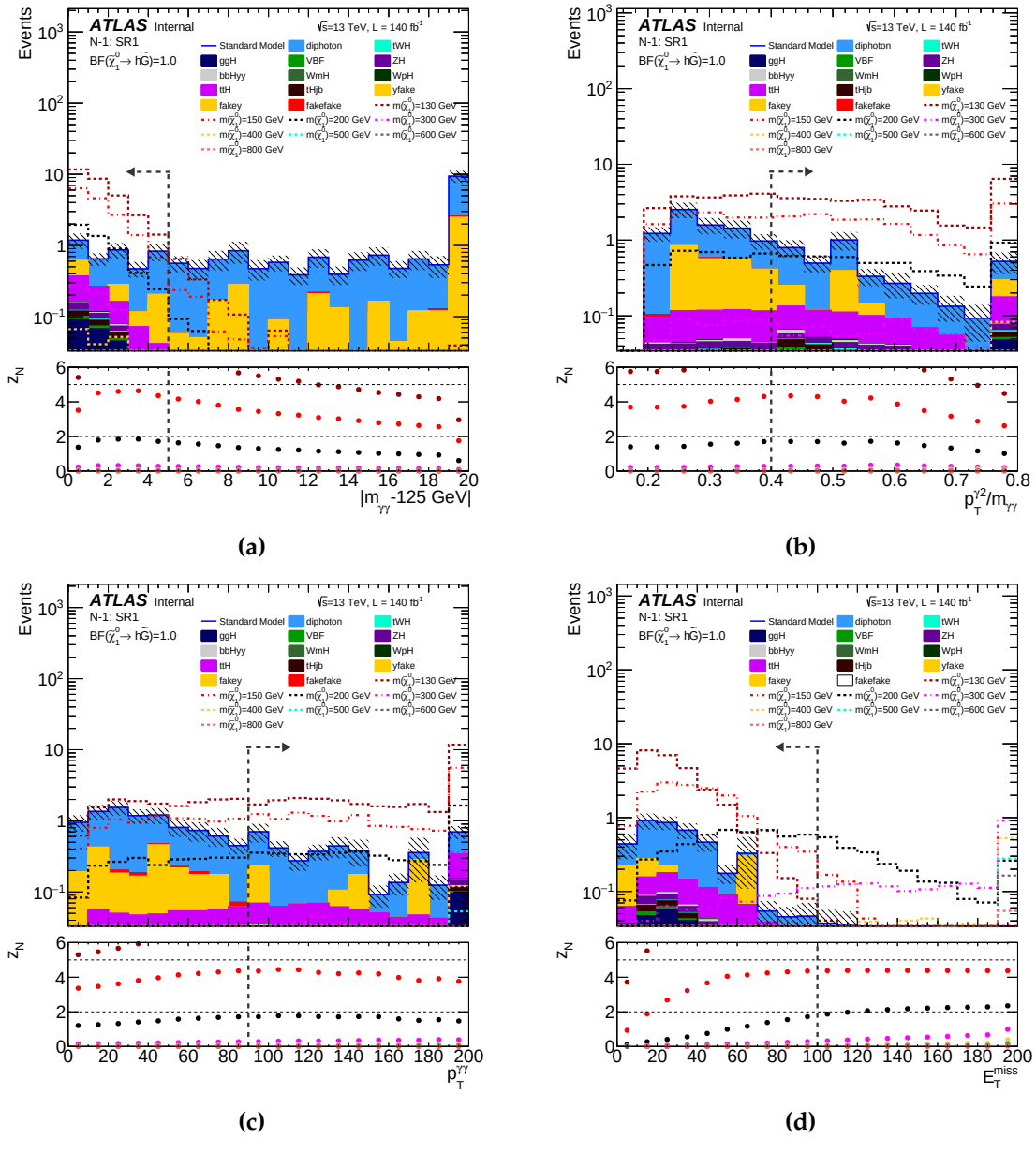

Figure 5.4: Distributions of the main discriminating variables for signal and backgrounds, with all the selections of SR1 applied, except for the selection on the plotted variable. The lower pad shows the cumulative significance obtained by applying a upper or lower limit on the plotted variable at the indicated value. A marker is included, indicating the value and direction of the selection applied in the signal region. The signal benchmarks in this set of figures assume $\mathrm{BF}(\tilde{\chi}_1^0 \to h\tilde{G}) = 100\%$.

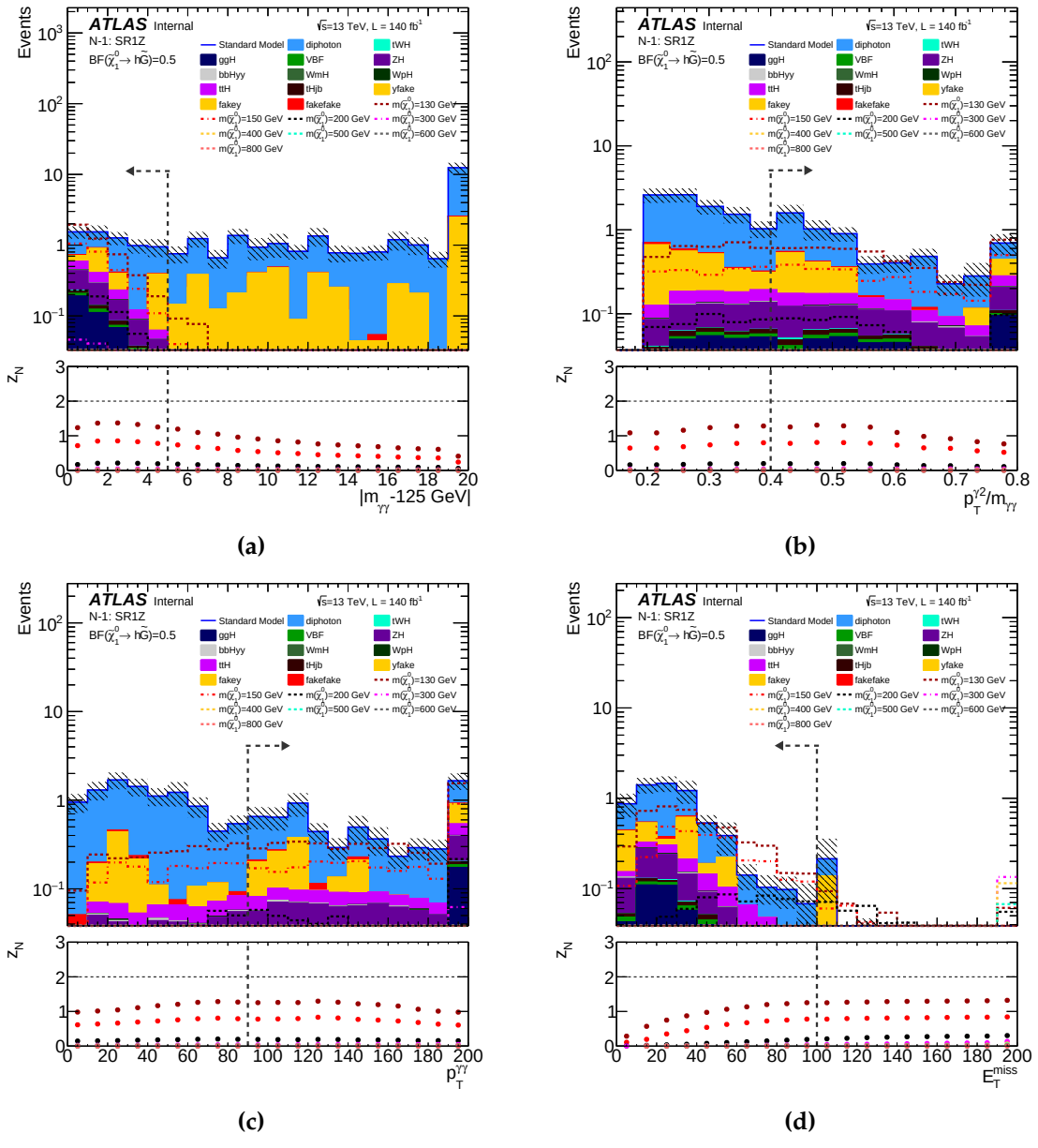

Figure 5.5: Distributions of the main discriminating variables for signal and backgrounds, with all the selections of SR1Z applied, except for the selection on the plotted variable. The lower pad shows the cumulative significance obtained by applying a upper or lower limit on the plotted variable at the indicated value. A marker is included, indicating the value and direction of the selection applied in the signal region. The signal benchmarks in this set of figures assume $\mathrm{BF}(\tilde{\chi}_1^0 \to Z\tilde{G}) = 50\%$.

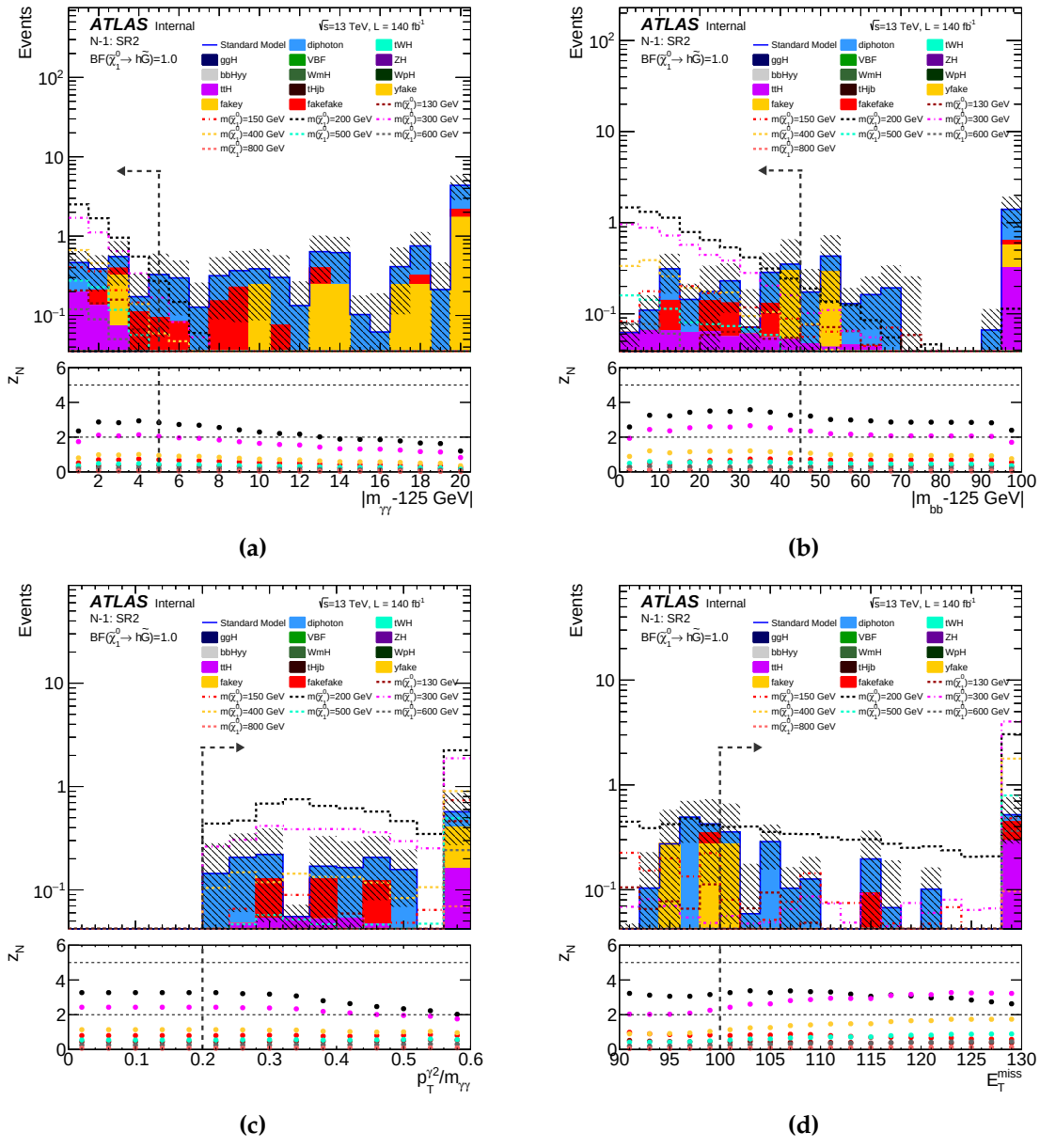

Figure 5.6: Distributions of the main discriminating variables for signal and backgrounds, with all the selections of SR2 applied, except for the selection on the plotted variable. The lower pad shows the cumulative significance obtained by applying a upper or lower limit on the plotted variable at the indicated value. A marker is included, indicating the value and direction of the selection applied in the signal region. The marker for $|m_{bb} - 125\,\text{GeV}|$ (figure 5.6b) indicates the central value used for further optimisation in appendix A.2. The signal benchmarks in this set of figures assume $\text{BF}(\tilde{\chi}_1^0 \to h\tilde{G}) = 100\%$.

5.3.4 Event Categorisation

With three signal regions defined in the previous section, events need to be categorised in control and validation regions to estimate backgrounds and validate the background estimations.

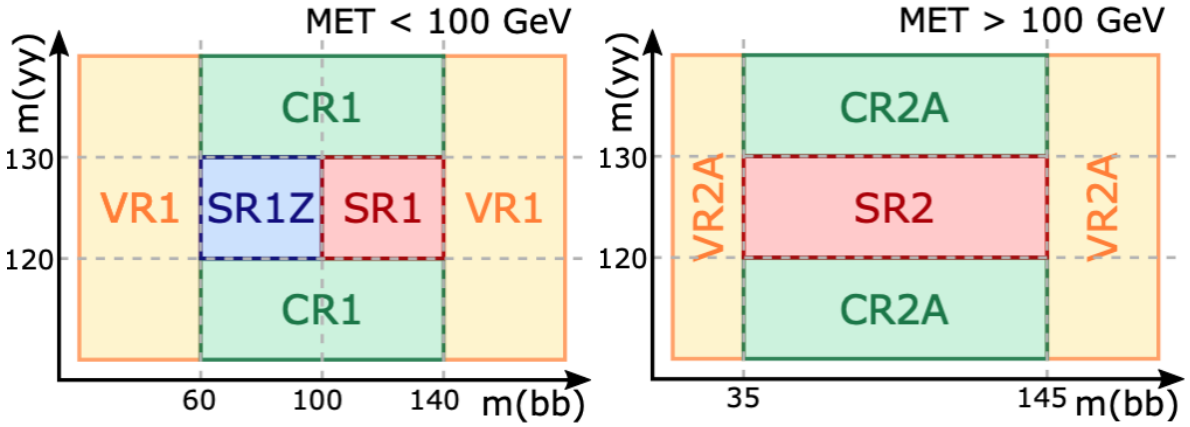

Figure 5.7: Schematic overview of the event categorisation in this analysis. The control regions (CR) are used to estimate backgrounds. This estimation is applied to both the validation regions (VR) and the signal regions (SR). The validation regions are used to validate the background estimation methods. This figure was produced by a collaborator.

region	selection		
CR1	$n_b = 2$; $E_{\mathrm{T}}^{\mathrm{miss}} \leq 100\,\mathrm{GeV}$;	$\lvert m_{\gamma\gamma} - 125\rvert \geq 5\,\mathrm{GeV}$;	$60\,\mathrm{GeV} < m_{bb} < 140\,\mathrm{GeV}$
CR2A	$n_b = 2$; $E_{\mathrm{T}}^{\mathrm{miss}} > 100\,\mathrm{GeV}$;	$\lvert m_{\gamma\gamma} - 125\rvert \geq 5\,\mathrm{GeV}$;	$35\,\mathrm{GeV} < m_{bb} < 145\,\mathrm{GeV}$
CR2B	$n_b < 2$; $E_{\mathrm{T}}^{\mathrm{miss}} > 100\,\mathrm{GeV}$		
CR2C	$n_b = 2$; $E_{\mathrm{T}}^{\mathrm{miss}} \leq 100\,\mathrm{GeV}$;	$\lvert m_{\gamma\gamma} - 125\rvert \geq 5\,\mathrm{GeV}$;	$35\,\mathrm{GeV} < m_{bb} < 145\,\mathrm{GeV}$
CR2D	$n_b < 2$; $E_{\mathrm{T}}^{\mathrm{miss}} \leq 100\,\mathrm{GeV}$		
VR1	$n_b = 2$; $E_{\mathrm{T}}^{\mathrm{miss}} \leq 100\,\mathrm{GeV}$;		$m_{bb} \leq 60\,\mathrm{GeV} \lvert\rvert m_{bb} \geq 140\,\mathrm{GeV}$
VR2A	$n_b = 2$; $E_{\mathrm{T}}^{\mathrm{miss}} > 100\,\mathrm{GeV}$;		$m_{bb} \leq 35\,\mathrm{GeV} \lvert\rvert m_{bb} \leq 145\,\mathrm{GeV}$
SR1	$n_b = 2$; $E_{\mathrm{T}}^{\mathrm{miss}} \leq 100\,\mathrm{GeV}$; $p_T^{\gamma}/m_{\gamma\gamma} > 0.4$; $p_{\mathrm{T}}^{\gamma\gamma} > 90\,\mathrm{GeV}$	$\lvert m_{\gamma\gamma} - 125\rvert < 5\,\mathrm{GeV}$;	$100\,\mathrm{GeV} < m_{bb} < 140\,\mathrm{GeV}$;
SR1Z	$n_b = 2$; $E_{\mathrm{T}}^{\mathrm{miss}} \leq 100\,\mathrm{GeV}$; $p_T^{\gamma}/m_{\gamma\gamma} > 0.4$; $p_{\mathrm{T}}^{\gamma\gamma} > 90\,\mathrm{GeV}$	$\lvert m_{\gamma\gamma} - 125\rvert < 5\,\mathrm{GeV}$;	$60\,\mathrm{GeV} < m_{bb} \leq 100\,\mathrm{GeV}$;
SR2	$n_b = 2$; $E_{\mathrm{T}}^{\mathrm{miss}} > 100\,\mathrm{GeV}$; $p_T^{\gamma}/m_{\gamma\gamma} > 0.2$	$\lvert m_{\gamma\gamma} - 125\rvert < 5\,\mathrm{GeV}$;	$35\,\mathrm{GeV} < m_{bb} < 145\,\mathrm{GeV}$;

Table 5.4: Selections used in the various regions. SR indicates a signal region, CR a control region and VR a validation region.

A schematic view of the event categorisation can be seen in figure 5.7, while a precise definition is given in table 5.4. Three signal regions are defined, with SR1 and SR1Z

defined with adjecent, nonoverlapping m_{bb} selections at low $E_{\mathrm{T}}^{\mathrm{miss}}$ and SR2 defined at high $E_{\mathrm{T}}^{\mathrm{miss}}$. The dominant backgrounds for each signal region are estimated in a corresponding control region close to the Higgs boson mass peak in the invariant mass of the di-b system m_{bb}, but off peak in the sidebands of the invariant mass of the di-photon system $m_{\gamma\gamma}$. This ensures kinematics that are close to the signal region while maintaining a small signal contamination. For each signal region, results are validated in a corresponding validation region off peak in the sidebands of m_{bb}. Backgrounds in SR1 and SR1Z are estimated using CR1, while the background estimation method is validated in VR1. Control regions CR2A, CR2B, CR2C and CR2D are needed to estimate backgrounds in SR2. The corresponding background estimation method is validated in VR2A.

Due to the opposing selections in $E_{\mathrm{T}}^{\mathrm{miss}}$ and m_{bb}, the signal regions are statistically orthogonal by construction and can be combined to enhance sensitivity (see section 5.5). There is minimal overlap between control regions CR1 and CR2C. However, the background estimation in SR2 is taken from CR2A and CR2C is only used to extrapolate the background estimation to CR2A. The overlap between CR1 and CR2C is therefore not expected to introduce any bias in a combination of the signal regions.

The details of the employed background estimation techniques will be explored in detail in the next section.

5.4 Background Estimation Techniques

The dominant background in each signal region is from non-resonant di-photon ($\gamma\gamma$) events. This background is difficult to model to high precision without the use of data-driven techniques. Events with only one or no real photons can enter the signal region if one or more particles (mostly jets) are falsely identified as photons and therefore pass photon selection requirements. This can happen in under a few different circumstances: if a jet is reconstructed as the leading photon and the sub-leading photon is real (jet-γ events); if the leading photon is real and a jet is reconstructed as the sub-leading photon (γ-jet events); or if jets are reconstructed as both the leading and the sub-leading photons (jet-jet events). In the following, these will together be referred to as "fake" backgrounds. The method developed in this section is agnostic to the type of particle which is falsely identified as a photon. Data-driven techniques are needed as there are many possible sources of mis-measurements which can contribute. The $\gamma\gamma$ background template is taken from MC to enhance statistics while the fake backgrounds are taken from fake-enriched data.

This analysis makes use of two data-driven background estimation techniques. The contributions of all four types of non-resonant background events ($\gamma\gamma$, γ-jet, jet-γ and jet-jet events) are estimated with the use of the "2x2D sideband method" fit described in section 5.4.1. The photon identification and isolation variables form the basis of this fit. The contributions to SR1, SR1Z and VR1 are taken from the fit to CR1, while the contributions to SR2 and VR2A are taken from a separate fit to CR2A. The underlying assumption is that the signal and validation regions contain the same fraction of $\gamma\gamma$, γ-jet, jet-γ and jet-jet events as the corresponding control region[1]. The separate treatment of γ-jet and jet-γ events in the 2x2D sideband fit has been validated elsewhere as described in Ref. [3].

[1] More precisely, SR1 and SR1Z are assumed to contain the same fraction of $\gamma\gamma$, γ-jet, jet-γ and jet-jet events as CR1 and VR1, while SR2 is assumed to have the same fraction as CR2A and VR2A.

Due to the low event yields in CR2A, the 2x2D fit can not be performed in this region directly. Therefore, the 2x2D sideband method fit is performed in CR2B, CR2C and CR2D and the results are then extrapolated to CR2A using a "modified ABCD method" as described in section 5.4.2.

The background estimation results in a separate weight for each of the four types of non-resonant backgrounds in CR1 and CR2A. The weights determined for CR1 are also applied to VR1 and SR1, while the weights determined for CR2A are also applied in VR2A and SR2. These weights force the respective numbers of each type of non-resonant background events in the control regions to match the prediction.

Section 5.4.3 shows the validation of all applied background estimation techniques. Further validation is provided in Ref. [3].

5.4.1 2x2D Sideband Method

The 2x2D sideband method [265] serves as a data-driven technique to estimate the contributions from di-photon and fake backgrounds to the signal regions. Events with two photons passing a *Loose'* working point [264] are selected, here the *Loose'3* working point is used.

Figure 5.8 shows the photon isolation and identification efficiencies for the various *Loose'N* working points in di-photon Monte Carlo corresponding to 2017 data-taking conditions versus the p_{T} of the respective photon. Since the *Loose'N* working points determine the photon identification, there is no strong dependence of the isolation efficiencies on N. For the photon identification, however, N has a significant impact. The *Loose'3* working point was chosen since it is the loosest of the *Loose'N* working points that is tighter than trigger *Medium*, thereby eliminating a potential trigger bias.

During the 2x2D sideband method, the two highest p_{T} photons are each partitioned into four categories, according to whether or not they satisfy:

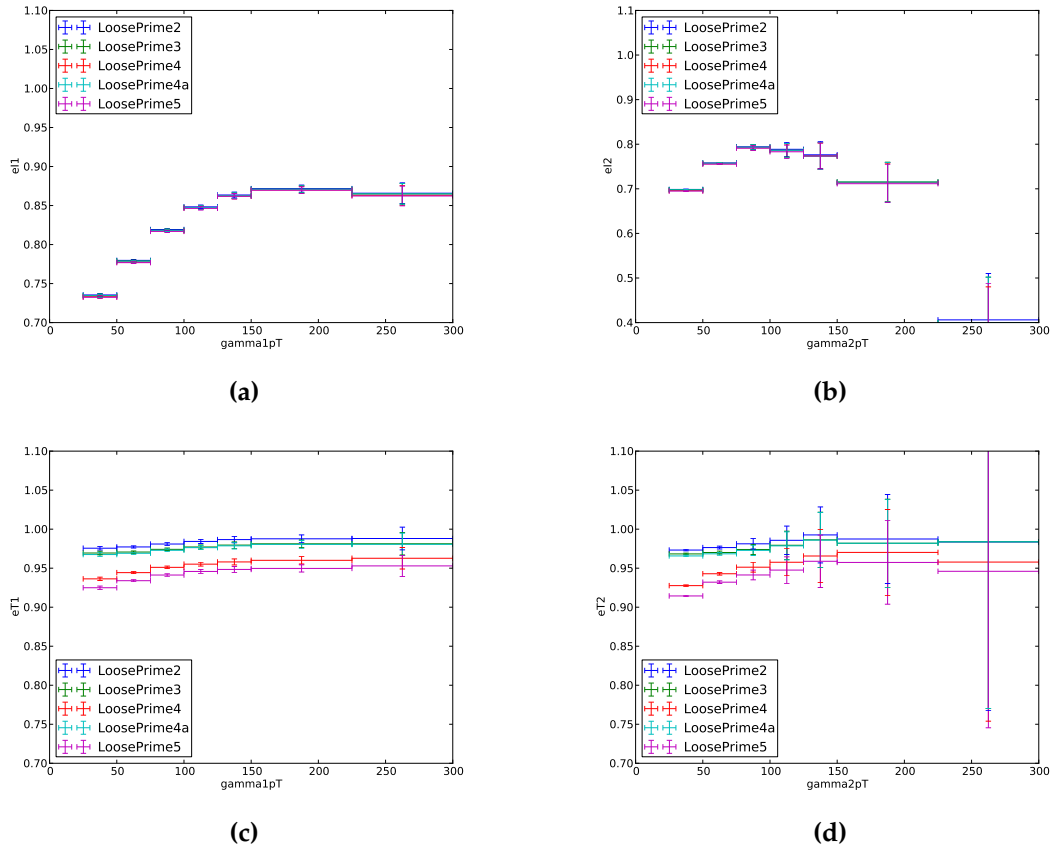

Figure 5.8: Tight efficiencies for the isolation of the leading (5.8a) and sub-leading (5.8b) photon and for the identification of the leading (5.8c) and sub-leading (5.8d) photon as measured in the di-photon MC corresponding to 2017 data-taking conditions for the various *Loose'N* working point preselecions. Preselection-level selections have been applied.

(a) *Tight* **isolation** requirements

(b) *Tight* **identification** requirements

This results in four categories per photon and 16 categories overall. A schematic view of the categories can be seen in figure 5.9. The 2x2D fit is used to estimate the background yields in multiple control regions. The **AA** category, where both photons pass *Tight* identification and isolation requirements, corresponds to the respective control region.

The number of events in each of the 16 categories can be calculated from the *Loose'3* yields, efficiencies and the appropriate correlations as well as fake-factors. A fake-factor is given by the fraction of fake background events passing a certain selection.

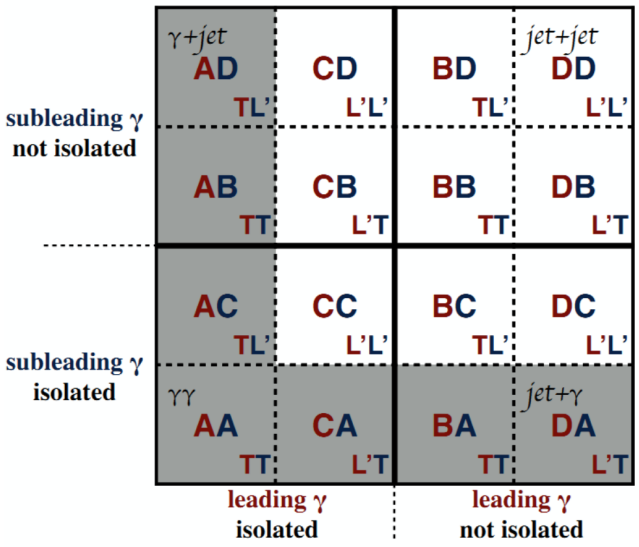

Figure 5.9: The 16 categories as defined in the 2x2D sideband method. **T** indicates a *Tight* selection and **L'** indicates *Loose'3* selection. Figure taken from Ref. [272].

In this case, the fraction of fake-photon events passing *Tight* photon isolation or identification requirements after passing the *Loose'3* selection.

This method assumes that any photon-photon efficiency correlations, photon-jet efficiency correlations or fake-factor correlations are negligible [265]. No correlation between photon isolation and identification needs to be taken into account as the correlated selections are applied as part of the *Loose'3* preselection (see section 5.3.1). The yields in the **AA** category for example can then be expressed by:

$$\begin{aligned} N_{AA} &= W_{\gamma\gamma}\varepsilon_{I1}\varepsilon_{T1}\varepsilon_{I2}\varepsilon_{T2} \\ &+ W_{\gamma j}\varepsilon_{I1}\varepsilon_{T1}f_{I2}f_{T2}\xi_{j2} \\ &+ W_{j\gamma}f_{I1}f_{T1}\varepsilon_{I2}\varepsilon_{T2}\xi_{j1} \\ &+ W_{jj}f'_{I1}f'_{T1}f'_{I2}f'_{T2}\xi_{j1}\xi_{j2}\xi_{Ijj}, \end{aligned} \tag{5.4}$$

where:

- $W_{\gamma\gamma}$, $W_{\gamma j}$, $W_{j\gamma}$ and W_{jj} are the yields from $\gamma\gamma$, γ-jet, jet-γ and jet-jet events after *Loose'3* preselection.

- ε_{I1} and ε_{I2} are the *Tight* isolation efficiencies for the leading and sub-leading photon respectively.
- ε_{T1} and ε_{T2} are the *Tight* identification efficiencies for the leading and sub-leading photon respectively.
- f_{I1} and f_{I2} are the fake-factors for jets passing the *Tight* isolation requirements for the leading and sub-leading photon respectively, in jet-γ and γ-jet events.
- f'_{I1} and f'_{I2} are the fake-factors for jets passing the *Tight* isolation requirements for the leading and sub-leading photon respectively, in jet-jet events.
- f_{T1} and f_{T2} are the fake-factors for jets passing the *Tight* identification requirements for the leading and sub-leading photon respectively, in jet-γ and γ-jet events.
- f'_{T1} and f'_{T2} are the fake-factors for jets passing the *Tight* identification requirements for the leading and sub-leading photon respectively, in jet-jet events.
- ξ_{j1} and ξ_{j2} are the correlation between f_{T1} and f_{I1} and the correlation between f_{T2} and f_{I2} respectively.
- ξ_{Ijj} is the correlation between the isolation of jets in jet-jet events.

In this equation, the terms including $W_{\gamma\gamma}$, $W_{\gamma j}$, $W_{j\gamma}$ and W_{jj} indicate the contributions to the respective category from $\gamma\gamma$, γ-jet, jet-γ and jet-jet events. Equations for the other 15 categories are provided in appendix A.3.

Using the 16 equations, a simultaneous fit is performed. For this fit, the number of events in each category (i.e. N_{AA}, N_{AB}, N_{AC}, etc.) is measured in data, the *Tight* isolation and identification efficiencies for both photons (ε_{I1}, ε_{I2}, ε_{T1} and ε_{T2}) are determined using di-photon MC and the correlations ξ_{j1} and ξ_{j2} are fixed to 1 ± 0.01. The correlations can be fixed since the *Loose'3* working point is used specifically to remove this correlation. A range is permitted to allow for checking for any systematic effect [265].

Therefore, the 13 unknowns determined by the fit are: $W_{\gamma\gamma}$, $W_{\gamma j}$, $W_{j\gamma}$, W_{jj}, f_{I1}, f_{I2}, f'_{I1}, f'_{I2}, f_{T1}, f_{T2}, f'_{T1}, f'_{T2} and ξ_{Ijj}. It should be noted that since there are 16 equations and 13 unknowns, the fit is over-constrained, which reduces the uncertainty on the fit result.

As a result of the 2x2D fit, a prediction of the fraction of each of the $\gamma\gamma$, γ-jet, jet-γ and jet-jet event categories can be made for the signal region, given by:

$$c_{\gamma\gamma} = \frac{W_{\gamma\gamma}\varepsilon_{I1}\varepsilon_{T1}\varepsilon_{I2}\varepsilon_{T2}}{N_{AA}^{\text{fit}}}, \tag{5.5}$$

$$c_{\gamma j} = \frac{W_{\gamma j}\varepsilon_{I1}\varepsilon_{T1}f_{I2}f_{T2}\xi_{j2}}{N_{AA}^{\text{fit}}}, \tag{5.6}$$

$$c_{j\gamma} = \frac{W_{j\gamma}f_{I1}f_{T1}\varepsilon_{I2}\varepsilon_{T2}\xi_{j1}}{N_{AA}^{\text{fit}}}, \text{ and} \tag{5.7}$$

$$c_{jj} = \frac{W_{jj}f'_{I1}f'_{T1}f'_{I2}f'_{T2}\xi_{j1}\xi_{j2}\xi_{Ijj}}{N_{AA}^{\text{fit}}}, \tag{5.8}$$

where N_{AA}^{fit} is the number of events in the **AA** category as predicted by the fit (cf. equation 5.4).

In the control regions in which the 2x2D fit is applied, each non-resonant background is weighted separately to match the 2x2D fit prediction. The weights for events of each category is given by

$$w_{ik} = \frac{1}{N_{ik}^{\text{templ.}}}N_{ik}^{\text{pred.}}, \tag{5.9}$$

where the $N_{ik}^{\text{templ.}}$ are the overall numbers of events in each of the $\gamma\gamma$, γ-jet, jet-γ and jet-jet templates and $N_{ik}^{\text{pred.}} = c_{ik}N_{AA}^{\text{fit}}$ the predicted numbers of $\gamma\gamma$, γ-jet, jet-γ and jet-jet events in the control region. Hence, the w_{ik} force the templates to match the 2x2D prediction for the numbers of events of each of the non-resonant backgrounds in the CR by first normalising the template to 1 ($1/N_{ik}^{\text{templ.}}$), and then multiplying by the predicted number of events in the CR $N_{ik}^{\text{pred.}}$. Both the normalisation and the predicted number of events vary between the non-resonant backgrounds. It should be noted that due to the weighting the w_{ik} do not sum to unity by design. The w_{ik} weight the $\gamma\gamma$, γ-jet, jet-γ and jet-jet backgrounds separately to match the prediction for both the overall number of events as well as the the fraction of events predicted in the 2x2D fit.

The w_{ik} derived in the control regions are also applied to the validation and signal regions. They capture the assumption that the fraction of events of each of the four types of non-resonant backgrounds are the same between the control region and the corresponding signal and validation regions.

2x2D method results

After selecting events with exactly two photons passing the *Loose'3* selection, the 2x2D fit is applied to estimate the contributions from $\gamma\gamma$, γ-jet, jet-γ and jet-jet events. The $\gamma\gamma$ sample is selected from the di-photon MC while requiring both photons to pass `Tight` identification and isolation, while fake-photon data are selected by requiring both photons to pass the `Loose'3` working point and at least one photon to fail the `Tight` isolation or identification requirements, i.e.:

- γj: the leading photon γ_1 passes both *Tight* isolation and *Tight* identification; the sub-leading photon γ_2 fails either *Tight* isolation or *Tight* identification or both
- $j\gamma$: the leading photon γ_1 fails either *Tight* isolation or *Tight* identification or both; the sub-leading photon γ_2 passes both *Tight* isolation and *Tight* identification
- jj: the leading photon γ_1 fails either *Tight* isolation or *Tight* identification or both; the sub-leading photon γ_2 fails either *Tight* isolation or *Tight* identification or both

All parameters determined in the 2x2D fit are given in table 5.5. The block "efficiencies" gives the efficiencies as determined in the $\gamma\gamma$ MC, "fit parameters" indicates the parameters determined in the fit and "fit quality" lists parameters used to determine the fit quality. In the last category, N_{AA}^{ratio} indicates the ratio of the fit prediction for N_{AA} and the observed value. The prediction of this value needs to be correct, since N_{AA} corresponds to the overall number of events in the respective control region.

The quality labelled χ^2 indicates the reduced $\chi^2/\mathrm{d.o.f.}$, where $\mathrm{d.o.f.} = 3$ indicates the number of degrees of freedom of the fit. Additional measures of the fit quality are r_{max} and $r_{\mathrm{tot.}}$, the maximum and total normalised residual of the 16 categories respectively, i.e.:

$$r_{\mathrm{max}} = \max\left(\frac{N_{ik}^{\mathrm{obs.}} - N_{ik}^{\mathrm{fit.}}}{N_{ik}^{\mathrm{obs.}}}\right), \tag{5.10}$$

$$r_{\mathrm{tot.}} = \sum_{ik=DD}^{AA} \frac{N_{ik}^{\mathrm{obs.}} - N_{ik}^{\mathrm{fit.}}}{N_{ik}^{\mathrm{obs.}}}, \tag{5.11}$$

where $N_{ik}^{\mathrm{fit.}}$ and $N_{ik}^{\mathrm{obs.}}$ are the predicted and observed numbers of events in the ik category, respectively.

Since the background composition is expected to change between the signal regions, the 2x2D fit is performed separately for the low- and high-$E_{\mathrm{T}}^{\mathrm{miss}}$ signal regions. For SR1 and SR1Z, the fit is performed with $n_b = 2$ while excluding $m_{\gamma\gamma}$ between $120\,\mathrm{GeV}$ and $130\,\mathrm{GeV}$ (CR1). This ensures that CR1 is close to both signal regions in kinematics and also ensures a small signal contamination in the background estimation. The fits to control regions CR2B, CR2C and CR2D are used to estimate backgrounds in CR2A and thus in SR2 using the modified ABCD technique described in the next section.

The overall fit quality is sufficiently precise to estimate the backgrounds in the analysis. We find that the 2x2D fit is less accurate in CR2B, which contains events with larger $E_{\mathrm{T}}^{\mathrm{miss}}$ and no b-jets, indicating that such events are more challenging to model correctly. The fit in CR2B arrives at a prediction of $W_{j\gamma} = 0 \pm 793$, which explains both the difference in other parameters such as f_{I1} as well as the larger χ^2 value and hence the poorer fit performance. As CR2B is only used in the extrapolation of the modelled backgrounds to CR2A, the observed modelling in the corresponding validation region VR2A is still satisfactory (see section 5.4.3). The fit arrives at uncertainties at the percent level for ξ_{j1} and ξ_{j2} in all control regions, indicating that fixing these parameters to an interval of $[0.99, 1.01]$ is justified.

Using equations 5.5 - 5.8, a prediction is made for the control region composition in terms of $\gamma\gamma$, γ-jet, jet-γ and jet-jet events. The fraction of background events as

predicted in the fit are listed in table 5.6.

To match the composition observed by the 2x2D fit, a separate weight is calculated for each sample from the fit results (equation 5.9). A template for the fake-photon backgrounds is calculated by filling a histogram with events passing the selections above. This histogram is then weighted to match the number of events predicted by the fit and the weight saved. The observed weights are given in table 5.6. The predicted background compositions largely agree between the different control regions, with $\gamma\gamma$ events the dominant background followed by γ-jet events. The weights required to match the background composition to the 2x2D prediction in the high-$E_{\mathrm{T}}^{\mathrm{miss}}$ control region CR2B are substantially different than in the other control regions, confirming that a separate 2x2D fit is required. The background estimation in SR2 is derived from CR2A, which contains high-$E_{\mathrm{T}}^{\mathrm{miss}}$ and low event yields. The dedicated technique developed eliminate the problem of low event yields in estimating backgrounds in SR2 will be explored in the next section.

		presel.	2b-presel.	CR1	CR2D	CR2C	CR2B
efficiencies	ε_{I1}	0.84 ± 0.00	0.83 ± 0.00	0.83 ± 0.01	0.84 ± 0.00	0.83 ± 0.01	0.78 ± 0.01
	ε_{I2}	0.75 ± 0.00	0.75 ± 0.00	0.75 ± 0.01	0.75 ± 0.00	0.75 ± 0.01	0.70 ± 0.01
	ε_{T1}	0.97 ± 0.00	0.97 ± 0.01	0.97 ± 0.01	0.97 ± 0.00	0.97 ± 0.01	0.97 ± 0.01
	ε_{T2}	0.97 ± 0.00	0.97 ± 0.01	0.97 ± 0.01	0.97 ± 0.00	0.97 ± 0.01	0.97 ± 0.01
fit parameters	$W_{\gamma\gamma}$	210328 ± 2436	2055 ± 108	686 ± 73	206815 ± 2631	932 ± 75	942 ± 40
	$W_{\gamma j}$	162444 ± 4027	1784 ± 106	745 ± 71	159402 ± 3500	930 ± 74	723 ± 39
	$W_{j\gamma}$	120121 ± 2444	1356 ± 85	523 ± 55	118322 ± 2403	716 ± 61	0 ± 793
	W_{jj}	223380 ± 4063	1604 ± 86	526 ± 52	221831 ± 3739	819 ± 60	1461 ± 125
	f_{I1}	0.11 ± 0.01	0.08 ± 0.03	0.09 ± 0.05	0.12 ± 0.01	0.07 ± 0.04	0.83 ± 0.56
	f_{I2}	0.14 ± 0.00	0.16 ± 0.03	0.19 ± 0.05	0.14 ± 0.00	0.19 ± 0.04	0.12 ± 0.03
	f_{T1}	0.66 ± 0.01	0.66 ± 0.02	0.68 ± 0.03	0.66 ± 0.01	0.67 ± 0.02	0.00 ± 1.00
	f_{T2}	0.68 ± 0.00	0.71 ± 0.02	0.71 ± 0.03	0.68 ± 0.00	0.71 ± 0.02	0.60 ± 0.02
	f'_{I1}	0.12 ± 0.01	0.11 ± 0.02	0.11 ± 0.04	0.12 ± 0.01	0.09 ± 0.03	0.11 ± 0.07
	f'_{I2}	0.14 ± 0.00	0.10 ± 0.03	0.11 ± 0.05	0.14 ± 0.00	0.11 ± 0.04	0.37 ± 0.03
	f'_{T1}	0.65 ± 0.01	0.64 ± 0.02	0.62 ± 0.03	0.65 ± 0.01	0.62 ± 0.02	0.63 ± 0.02
	f'_{T2}	0.69 ± 0.00	0.67 ± 0.02	0.66 ± 0.03	0.69 ± 0.00	0.67 ± 0.02	0.82 ± 0.01
	ξ_{Ijj}	1.33 ± 0.06	1.44 ± 1.00	2.69 ± 1.36	1.32 ± 0.05	2.72 ± 1.21	0.93 ± 0.51
	ξ_{j1}	1.00 ± 0.01	0.99 ± 0.01	0.99 ± 0.01	1.01 ± 0.01	0.99 ± 0.00	0.99 ± 0.00
	ξ_{j2}	0.99 ± 0.01	0.99 ± 0.01	1.01 ± 0.02	1.00 ± 0.00	0.99 ± 0.01	1.01 ± 0.00
fit quality	N_{AA}^{ratio}	1.00	1.00	1.00	1.00	1.00	1.01
	χ^2	0.02	0.38	1.06	0.02	0.01	2.78
	$r_{\max}$	0.00	0.09	0.57	0.00	0.02	1.19
	$r_{\text{tot.}}$	0.02	2.08	1.18	0.01	0.08	2.77

Table 5.5: Table with photon isolation and identification efficiencies, results of the 2x2D fit and fit quality measures for preselection, 2b-preselection and all relevant control regions.

	presel.	2b-presel.	CR1	CR2D	CR2C	CR2B	CR2A
	relative composition c_{ik}						
$\gamma\gamma$	0.854 ± 0.014	0.827 ± 0.132	0.780 ± 0.114	0.852 ± 0.015	0.806 ± 0.091	0.872 ± 0.068	-
γj	0.086 ± 0.003	0.117 ± 0.040	0.162 ± 0.045	0.086 ± 0.003	0.144 ± 0.034	0.075 ± 0.017	-
$j\gamma$	0.044 ± 0.005	0.056 ± 0.028	0.044 ± 0.027	0.046 ± 0.006	0.037 ± 0.022	0.000 ± 0.001	-
jj	0.015 ± 0.002	0.000 ± 0.006	0.014 ± 0.011	0.016 ± 0.002	0.013 ± 0.009	0.053 ± 0.044	-
	applied weight w_{ik} to match composition to 2x2D prediction						
$\gamma\gamma$	0.870 ± 0.018	0.914 ± 0.177	0.891 ± 0.157	0.865 ± 0.019	0.924 ± 0.127	1.348 ± 0.135	2.201 ± 0.454
γj	0.068 ± 0.003	0.083 ± 0.030	0.119 ± 0.035	0.068 ± 0.002	0.108 ± 0.027	0.052 ± 0.012	0.243 ± 0.110
$j\gamma$	0.048 ± 0.006	0.058 ± 0.029	0.044 ± 0.027	0.050 ± 0.007	0.034 ± 0.021	0.000 ± 0.001	0.000 ± 0.001
jj	0.009 ± 0.001	0.000 ± 0.005	0.009 ± 0.007	0.009 ± 0.001	0.008 ± 0.005	0.025 ± 0.021	0.075 ± 0.001

Table 5.6: Background composition and the corresponding weights to match the background composition to the prediction as determined by the 2x2D sideband fit for the different control regions and for preselection and 2b-preselection. The weights in CR2A are calculated with the modified ABCD method (cf. section 5.4.2, equation 5.14).

5.4.2 Modified ABCD Method - used for SR2 only

The ABCD method can be used to extrapolate the number of background events for data-driven background techniques to regions that are inaccessible. Usually this is due to large signal contamination. In this analysis, however, the limiting factor is the low yield of events in CR2A. SR2 requires $E_{\mathrm{T}}^{\mathrm{miss}} \geq 100\,\mathrm{GeV}$, removing a large number of events. As a result, the overall yield is not large enough to perform the 2x2D sideband fit. Hence, the 2x2D fit is performed in CR2D, CR2C and CR2B, and the signal region composition is extrapolated from these regions to SR2 using the modified ABCD method described as described in this section.

During the ABCD method, events are separated into four regions of high/low values of two observables. Here the extrapolation is performed in variables $E_{\mathrm{T}}^{\mathrm{miss}}$ and b-jet multiplicity n_b. The ABCD method is applied to CR2D, CR2C, CR2B and CR2A, where CR2A is kinematically closest to SR2 so the results are extrapolated to this region. The control regions allocate events according to:

- CR2D: $E_{\mathrm{T}}^{\mathrm{miss}} \leq 100\,\mathrm{GeV}$, $n_b < 2$
- CR2C: $E_{\mathrm{T}}^{\mathrm{miss}} \leq 100\,\mathrm{GeV}$, $n_b = 2$
- CR2B: $E_{\mathrm{T}}^{\mathrm{miss}} > 100\,\mathrm{GeV}$, $n_b < 2$
- CR2A: $E_{\mathrm{T}}^{\mathrm{miss}} > 100\,\mathrm{GeV}$, $n_b = 2$

In the remainder of this section, the names of these regions are shortened for simplicity. We refer to CR2D, CR2C, CR2B and CR2A as D, C, B and A respectively.

Assuming that the two variables are uncorrelated implies that $N_A/N_B = N_C/N_D$, where N_i are the number of events in region i. The number of events of each of the four non-resonant backgrounds in region A can then be expressed by

$$N_{A,ik}^{\mathrm{ABCD}} = \frac{N_{B,ik} N_{C,ik}}{N_{D,ik}}, \tag{5.12}$$

where the indices ik again indicate the different background categories ($\gamma\gamma$, γ-jet, jet-γ and jet-jet). In this analysis, the ABCD method is used to extrapolate the background weights w_{ik} (see equation 5.9) of $\gamma\gamma$, γ-jet, jet-γ and jet-jet events as calculated with the 2x2D sideband method in regions B, C and D into region A with

$$w_{A,ik}^{\mathrm{ABCD}} = \frac{w_{B,ik} w_{C,ik}}{w_{D,ik}}. \tag{5.13}$$

Hence, the same extrapolation procedure applies to weights and to predicted numbers of events.

The basic ABCD method assumes that the two variables ($E_{\mathrm{T}}^{\mathrm{miss}}$ and n_b) are uncorrelated for each type of non-resonant background. When that is not the case, there will be a disagreement between the predicted and real values of $N_{A,ik}$ and $w_{A,ik}$. However, since the same extrapolation procedure is used for numbers of events and weights, we can assume that $N_{A,ik}^{\mathrm{ABCD}}/N_{A,ik}^{\mathrm{templ.}} = w_{A,ik}^{\mathrm{ABCD}}/w_{A,ik}$, where $N_{A,ik}^{\mathrm{templ.}}$ and $w_{A,ik}$ are the number of template events and correct weights for each non-resonant background in the A region respectively. Therefore, the basic ABCD method is modified by expressing the total weight for each non-resonant background by

$$\begin{aligned} w_{A,ik} &= w_{A,ik}^{\mathrm{ABCD}} \frac{N_{A,ik}^{\mathrm{templ.}}}{N_{A,ik}^{\mathrm{ABCD}}} \\ &= \frac{w_{B,ik} w_{C,ik}}{w_{D,ik}} \frac{N_{A,ik}^{\mathrm{templ.}}}{N_{A,ik}^{\mathrm{ABCD}}} \\ &= \frac{w_{B,ik} w_{C,ik}}{w_{D,ik}} \frac{N_{A,ik}^{\mathrm{templ.}} N_{D,ik}}{N_{B,ik} N_{C,ik}}. \end{aligned} \tag{5.14}$$

This modification corrects for the mis-modelling in the ABCD weight extrapolation caused by the correlation of $E_{\mathrm{T}}^{\mathrm{miss}}$ and n_b using the measured mis-modelling in the number of events.

In summary, the modified ABCD method makes use of the high number of background events in CR2D, CR2C and CR2B to determine the weights of events applied to CR2A, VR2A and SR2, where CR2A and VR2A are kinematically close to the signal region. VR2A is used to validate the modified ABCD extrapolation technique in section 5.4.3.

The modification introduces additional sources of uncertainty on the predicted number of background events. The statistical uncertainty on the number of events in CR2A is the biggest added uncertainty, since the number of events in CR2A is small. However, unlike the basic ABCD method, this method does not require the use of uncorrelated variables, since the mis-modelling caused by a potential correlation is corrected for. This modification is necessary, since the two variables $E_{\mathrm{T}}^{\mathrm{miss}}$ and n_b are correlated, as will be shown in the next section.

$E_{\mathrm{T}}^{\mathrm{miss}}$ – n_b correlation

Figure 5.10 shows the ratio of the number of events with two b-jets to that of events with either no or one b-jet for the different non-resonant backgrounds as a function of $E_{\mathrm{T}}^{\mathrm{miss}}$. The blue line shows a linear fit to the ratio. Since this ratio is not flat, there is a correlation between $E_{\mathrm{T}}^{\mathrm{miss}}$ and b-jet multiplicity, implying that the basic ABCD method cannot be used and the modification derived above is indeed needed. The ratio behaves differently between the different non-resonant backgrounds, indicating that individual correction factors are required.[2]

[2] A modification using the linear fit was attempted, but since the ratio for the fake-backgrounds does not follow this linear fit, the analysis uses the inclusive modification described in this section.

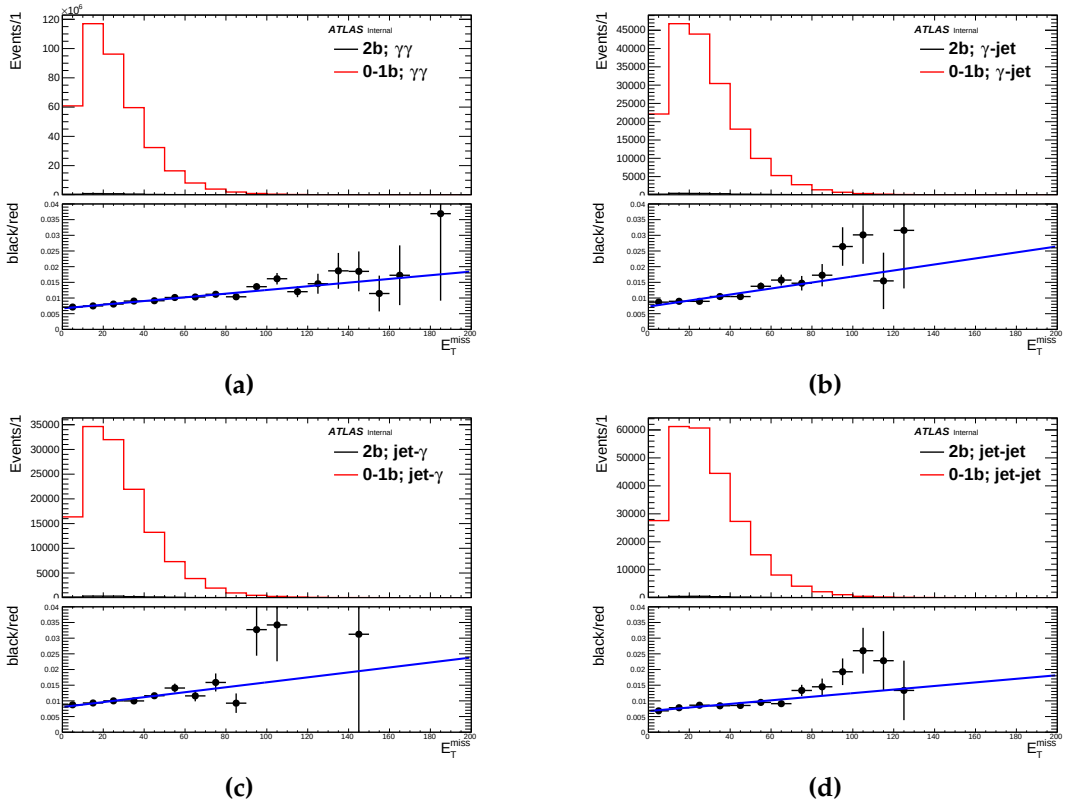

Figure 5.10: $E_{\mathrm{T}}^{\mathrm{miss}}$ distributions for events containing two b-jets ($n_b = 2$) and events containing no or one b-jet ($n_b \leq 1$) for the $\gamma\gamma$ MC (5.10a), γ-jet (5.10b), jet-γ (5.10c) and jet-jet (5.10d) background samples. The bottom panel shows the ratio of $n_b = 2$ events with $n_b \leq 1$ events. The ratio has been fitted with a linear curve. Preselection-level selections are applied.

Modified ABCD method results

	$N_D^{\text{templ.}}$	$N_C^{\text{templ.}}$	$N_B^{\text{templ.}}$	$N_A^{\text{templ.}}$
$\gamma\gamma$	140964.91 ± 68.07	4588.62 ± 4.49	359.81 ± 3.61	2.30 ± 0.26
γj	181399.00 ± 425.91	903.00 ± 30.05	812.00 ± 28.5	12.00 ± 3.46
$j\gamma$	132745.00 ± 364.34	718.00 ± 26.80	617.00 ± 24.84	14.00 ± 3.74
jj	252080.00 ± 502.08	1118.00 ± 33.44	1148.00 ± 33.88	17.00 ± 4.12
	N_A^{ABCD}	$N_A^{\text{templ.}}/N_A^{\text{ABCD}}$	w_A^{ABCD}	
$\gamma\gamma$	1.50 ± 0.02	1.53 ± 0.18	1.440 ± 0.247	
γj	4.04 ± 0.20	2.97 ± 0.87	0.082 ± 0.028	
$j\gamma$	3.34 ± 0.18	4.20 ± 1.14	0.000 ± 0.001	
jj	5.09 ± 0.21	3.34 ± 0.82	0.022 ± 0.024	

Table 5.7: Ingredients used for the modified ABCD method. $N_i^{\text{templ.}}$ indicates the number of template events in the corresponding region for the respective sample without applying any 2x2D weights, while N_A^{ABCD} indicates the pure ABCD prediction for N_A. $N_A^{\text{templ.}}/N_A^{\text{ABCD}}$ is the correction factor applied to the pure ABCD method prediction of the weights w_A^{ABCD}.

Table 5.7 summarises the results of the modified ABCD method. Since the correlation between $E_{\mathrm{T}}^{\mathrm{miss}}$ and b-jet multiplicity n_b is especially strong for the fake backgrounds, the corresponding correction faction is relatively large. The weights for CR2A in table 5.6 is the product of $N_A^{\mathrm{templ.}}/N_A^{\mathrm{ABCD}}$ and w_A^{ABCD}. One of the limiting factors of the modified ABCD method are the low event yields in CR2A shown in column $N_A^{\mathrm{templ.}}$. However, the largest source of uncertainty in weights in CR2A is the uncertainty on the weights of events in CR2C and CR2B, which have limited event yields, complicating the 2x2D sideband method fit.

As the observed background composition in table 5.6 does not change substantially between the different the control regions, the results are mostly compatible. The same is true for most of the weights, with the exception of CR2A, which shows much larger w_{ik} than the other regions. This can be explained by the correlation between the two observables used in the modified ABCD method, $E_{\mathrm{T}}^{\mathrm{miss}}$ and n_b. Events with two b-jets are much more likely to have $E_{\mathrm{T}}^{\mathrm{miss}}$ of $100\,\mathrm{GeV}$ or more than events with no or one b-jet (see figure 5.10). The correlation likely originates from electroweak decays of b mesons to final states including neutrinos. This confirms the necessity for the modification of the ABCD method, since the un-modified version assumes uncorrelated variables.

The uncertainty on the w_{ik} takes into account the uncertainties on the 2x2D fit result as well as the statistical uncertainties of the modified ABCD method, wherever it is applied. The total uncertainty on the weights in CR2A is relatively large compared to the other control regions. This is mainly caused by the large relative uncertainties on the fraction of signal region events determined by the 2x2D fit in CR2C and CR2B in combination with the low event yields in CR2A, which in turn causes large uncertainties on the weights in this control region.

5.4.3 Validation of Background Modelling

Having estimated the backgrounds in the previous sections, this section explores the agreement between the data and the Standard Model prediction for relevant variables in the control and validation regions. Most importantly, the agreement in validation regions VR1 and VR2A will be studied. These are designed to be close in kinematics to the signal regions. The observed and expected yields in all regions are summarised in appendix A.4.

This section only includes selected validation techniques used in the final analysis. Other techniques, including a background estimation based on a $m_{\gamma\gamma}$ shape fit, are discussed in detail in Ref. [3].

CR1/VR1

Figure 5.11 shows the agreement between data and prediction for a collection of relevant variables in CR1 and VR1.

All plots in this section share the background estimation derived in CR1 (see table 5.6). This background estimation is also applied to SR1, which is closer in kinematics to CR1 than VR1. Since the background estimation is derived in CR1 and applied to both CR1 and VR1, the agreement between data and the SM prediction in VR1 is expected to be worse than in CR1. However, good agreement is observed for both regions.

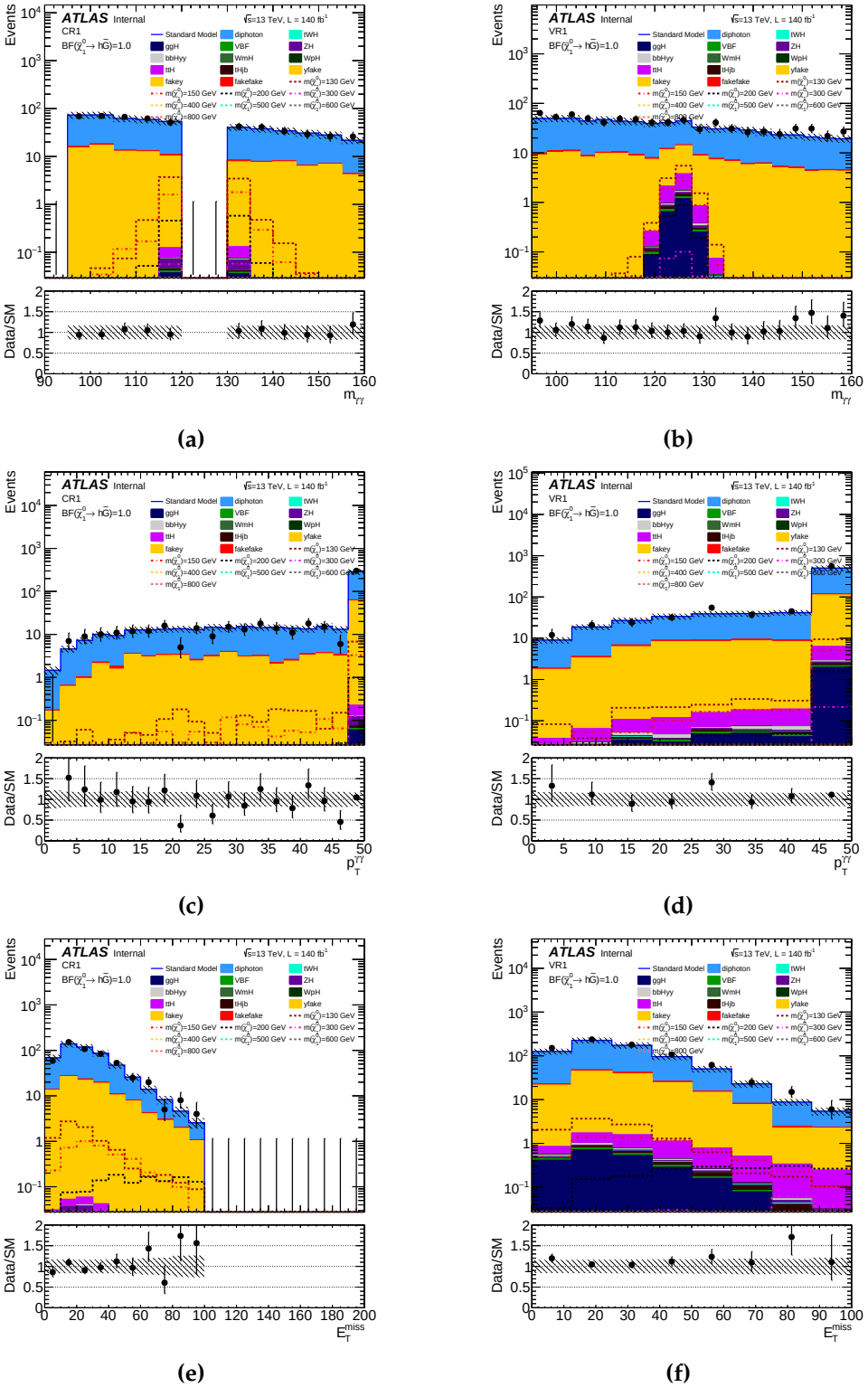

Figure 5.11: Distribution of relevant variables for signal and backgrounds in CR1 (left) and VR1 (right). Distributions are shown for $m_{\gamma\gamma}$ (top), $p_{\mathrm{T}}^{\gamma\gamma}$ (middle) and $E_{\mathrm{T}}^{\mathrm{miss}}$ (bottom). The 2x2D background estimation technique has been applied. Full treatment of the systematic uncertainties is included in this set of figures, resulting in a systematic uncertainty indicated by the shaded area. The lower panel shows the data/SM prediction ratio for the respective bin. These signal benchmarks in this set of figures assume $\mathrm{BF}(\tilde{\chi}_1^0 \to h\tilde{G}) = 100\%$.

CR2A/VR2A

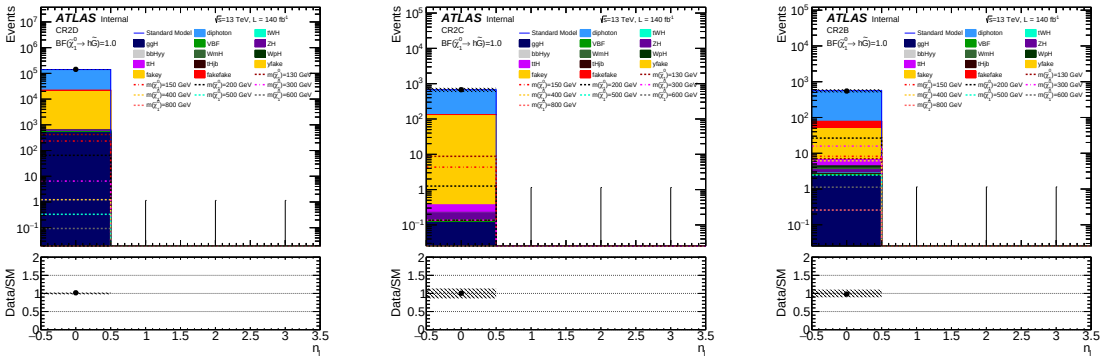

(a) (b) (c)

Figure 5.12: Distribution of lepton multiplicity for signal and backgrounds in CR2D (5.12a), CR2C (5.12b) and CR2B (5.12c), indicating the overall agreement in a single bin. The 2x2D background estimation technique has been applied. Full treatment of the systematic uncertainties is included in this set of figures, resulting in a systematic uncertainty indicated by the shaded area. The lower panel shows the data/SM prediction ratio for the respective bin. The signal benchmarks in this set of figures assume $\mathrm{BF}(\tilde{\chi}_1^0 \to h\tilde{G}) = 100\%$.

The background estimation fits for CR2D, CR2C and CR2B result in an excellent overall agreement between data and estimated backgrounds by construction, as shown in figure 5.12, indicating that the results of the three fits can be used to perform the background estimation with the modified ABCD method in SR2. For each of these control regions, a separate background estimation from table 5.6 is used.

Figure 5.13 shows the agreement between data and backgrounds in CR2A and VR2A as a result of the modified ABCD method weight extrapolation. All plots presented in this figure use the background estimation listed under CR2A in table 5.6. Considering the extreme nature of the considered area of phase space, excellent agreement is observed between the data and the background prediction. The background estimation is derived in CR2A and applied to CR2A, VR2A and SR2. Hence, data/MC agreement is expected to be worse for VR2A. Still, good agreement is observed. Just like in the case of CR1 and VR1, CR2A is closer in kinematics to SR2 than VR2. Therefore, the modelling in SR2 is expected to be better than for VR2A.

Some mis-modelling in CR2A and VR2A is expected due to the difficult modelling of

gluon splitting into pairs of b-quarks in Monte Carlo. Figure 5.14 shows an "N-1" plot of the b-jet multiplicity in VR2A, in which all selections of VR2A are applied, with the exception of the b-jet multiplicity. The background estimation technique is only applied to events with $n_b = 2$, hence the disagreement for $n_b = 0, 1$ is entirely expected. The strong difference between the modelling for the different b-jet multiplicities in this plot indicates the challenge of modelling events with large b-jet multiplicities to high precision. The combination of 2x2D sideband method and the modified ABCD method applied here is only able to partially compensate for this effect, causing a minor disagreement between data and SM prediction in VR2A, which is covered by the systematic uncertainties caused by the 2x2D and ABCD methods.

In conclusion, the employed background estimation techniques of the 2x2D sideband method and modified ABCD extrapolation technique model the backgrounds in all control and validation regions to sufficient accuracy, giving us confidence in the background modelling in the three signal regions.

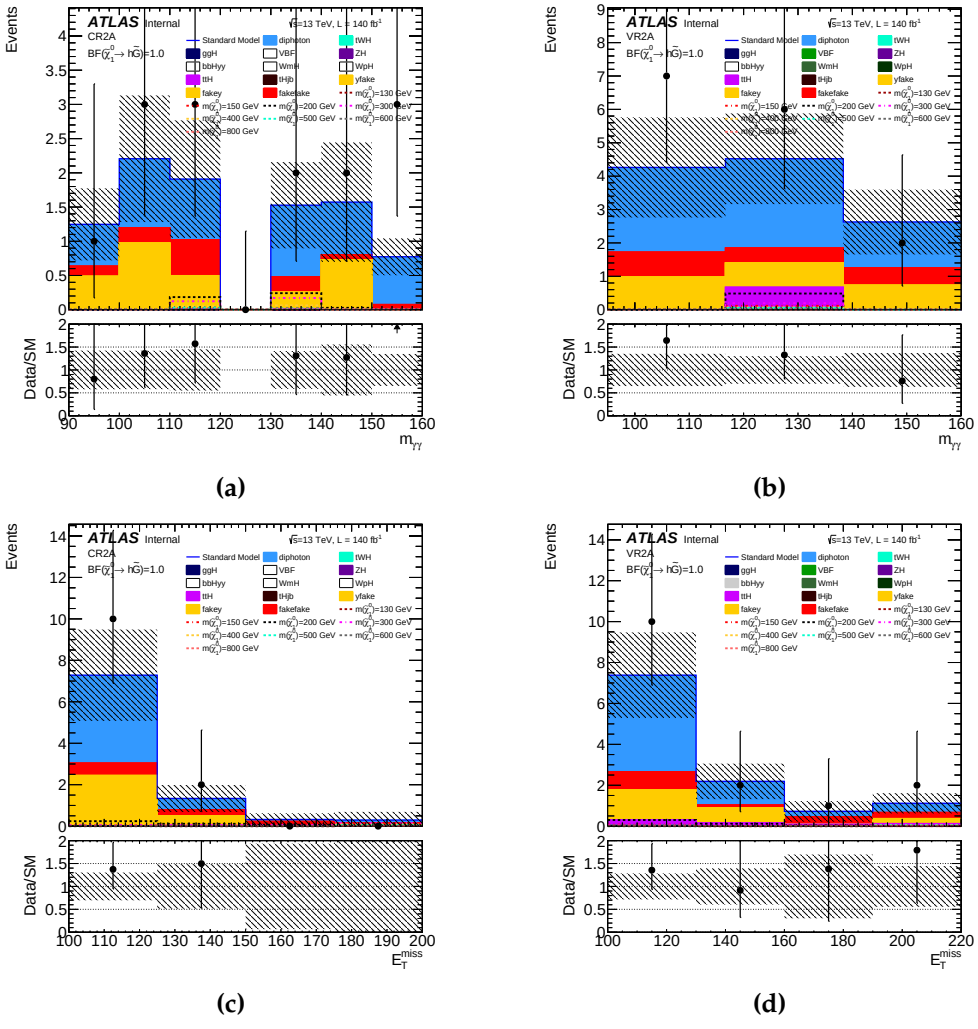

Figure 5.13: Distribution of relevant variables for signal and backgrounds in CR2A (left) and VR2A (right). Distributions are shown for $m_{\gamma\gamma}$ (top) and $E_{\mathrm{T}}^{\mathrm{miss}}$ (bottom). The 2x2D and modified ABCD background estimation techniques have been applied. Full treatment of the systematic uncertainties is included in this set of figures, resulting in a systematic uncertainty indicated by the shaded area. The lower panel shows the data/SM prediction ratio for the respective bin. The signal benchmarks in this set of figures assume $\mathrm{BF}(\tilde{\chi}_1^0 \to h\tilde{G}) = 100\%$.

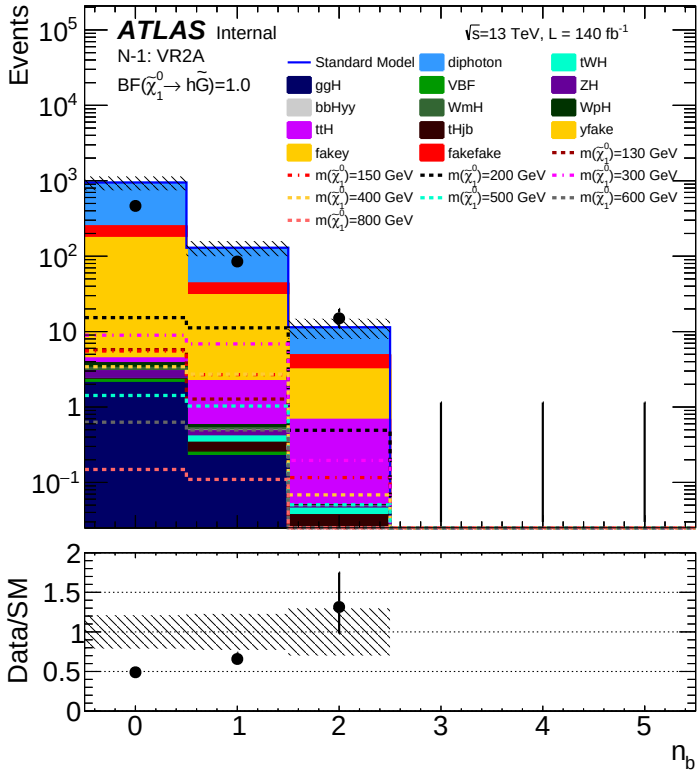

Figure 5.14: Distributions of the b-jet multiplicity n_b for signal and backgrounds, with all the selections of VR2A applied, except for the selection on n_b. The 2x2D and modified ABCD background estimation techniques have been applied. Full treatment of the systematic uncertainties is included in this figure, resulting in a systematic uncertainty indicated by the shaded area. The lower pad shows the data/SM prediction ratio for the respective bin. The mismodelling in $n_b = 0, 1$ is expected, as explained in the text.

5.5 Signal Region Sensitivity

In the previous sections, the object definition and event selection have been introduced, signal, control and validation regions have been defined, and techniques to estimate the backgrounds in the three signal regions have been developed and validated. In this section, we will explore the sensitivity reach of the individual signal regions.

The estimated significance calculated with equation 5.3 along with expected numbers of events for all backgrounds and signal mass points are given in Figure 5.15, assuming a 30% systematic uncertainty on all backgrounds. SR1 and SR1Z are optimised for low values of $m(\tilde{\chi}_1^0)$, covering the Higgs and Z boson peaks in the m_{bb} distributions respectively. SR1 reaches a significance of up to 6σ for low $m(\tilde{\chi}_1^0)$ assuming $\mathrm{BF}(\tilde{\chi}_1^0 \to h\tilde{G}) = 100\%$, indicating discovery potential. This is supported by an additional $\sim 1.2\sigma$ for $\mathrm{BF}(\tilde{\chi}_1^0 \to h\tilde{G}) = 50\%$ in SR1Z. It should be noted that while SR1Z does not offer discovery or exclusion potential by itself, it should be considered an extension of the search strategy of this analysis. The number of predicted signal events in both low-$E_{\mathrm{T}}^{\mathrm{miss}}$ signal regions falls approximately exponentially with increasing $\tilde{\chi}_1^0$ mass, so SR1 does not show significance to values of $m(\tilde{\chi}_1^0)$ of above about $180\,\mathrm{GeV}$.

Therefore, SR2 was optimised for $m(\tilde{\chi}_1^0) = 200\,\mathrm{GeV}$; it features the selection of $E_{\mathrm{T}}^{\mathrm{miss}} \geq 100\,\mathrm{GeV}$, which leads to sensitivity to the two intermediate $m(\tilde{\chi}_1^0)$ mass points of $200\,\mathrm{GeV}$ and $300\,\mathrm{GeV}$.

In the absence of any evidence for Supersymmetry, limits can be set on the model cross section. Blinded limits on the pure Higgsino cross section with $\mathrm{BF}(\tilde{\chi}_1^0 \to h\tilde{G}) = 100\%$, assuming perfect agreement between observed data and the SM hypothesis, are shown in figure 5.16. Full treatment of all systematic uncertainties is included in this set of figures. Individual limits are drawn for all three signal regions. As the uncertainty on the background estimate is smaller than 30% in SR1, this signal region shows stronger sensitivity for low neutralino masses of up to $200\,\mathrm{GeV}$ than indicated in figure 5.15a. If $\mathrm{BF}(\tilde{\chi}_1^0 \to h\tilde{G}) = 100\%$ is assumed, SR1Z is sensitive to

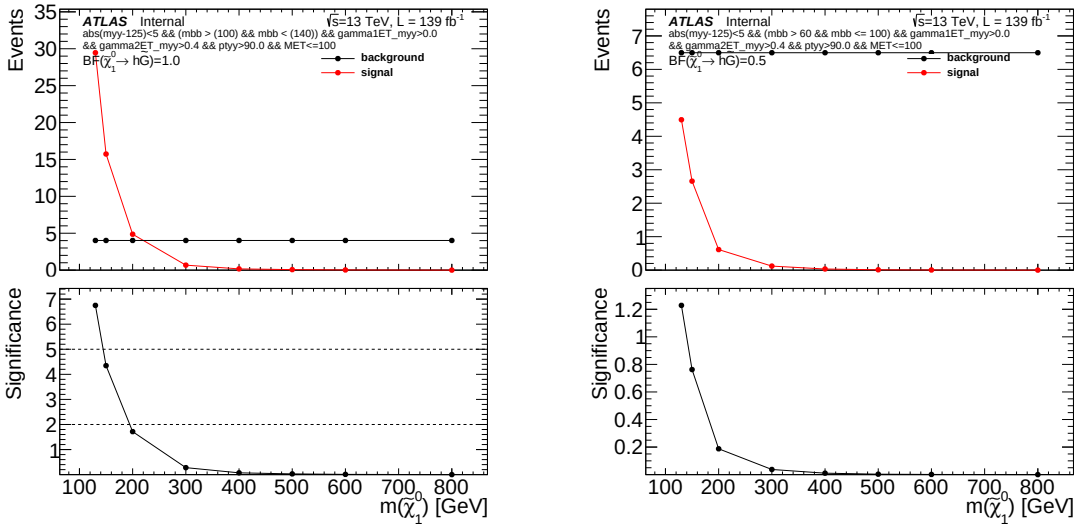

(a) SR1 **(b)** SR1Z

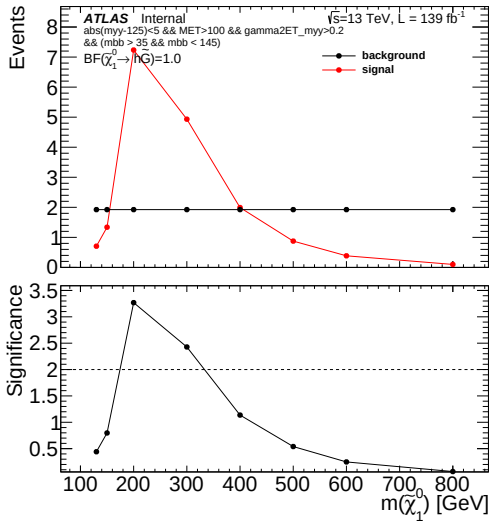

(c) SR2

Figure 5.15: Expected numbers of events for all considered signal $\tilde{\chi}_1^0$ mass points as well as the number of background events for SR1 (5.15a) at $\mathrm{BF}(\tilde{\chi}_1^0 \to h\tilde{G}) = 100\%$, SR1Z (5.15b) at $\mathrm{BF}(\tilde{\chi}_1^0 \to h\tilde{G}) = 50\%$ and SR2 (5.15c) at $\mathrm{BF}(\tilde{\chi}_1^0 \to h\tilde{G}) = 100\%$. The lower panel shows the signal region sensitivity to the respective mass point. These figures assume a 30% systematic uncertainty on all backgrounds.

models with very low neutralino masses of $\sim 130\,\mathrm{GeV}$. The limits obtained by SR2 show sensitivity to intermediate masses of $200 - 300\,\mathrm{GeV}$, largely in agreement with figure 5.15c. Limits are slightly weaker in figure 5.16c since the overall uncertainty is closer to 40% than 30%. The treatment of the systematic uncertainties will be discussed in the next section.

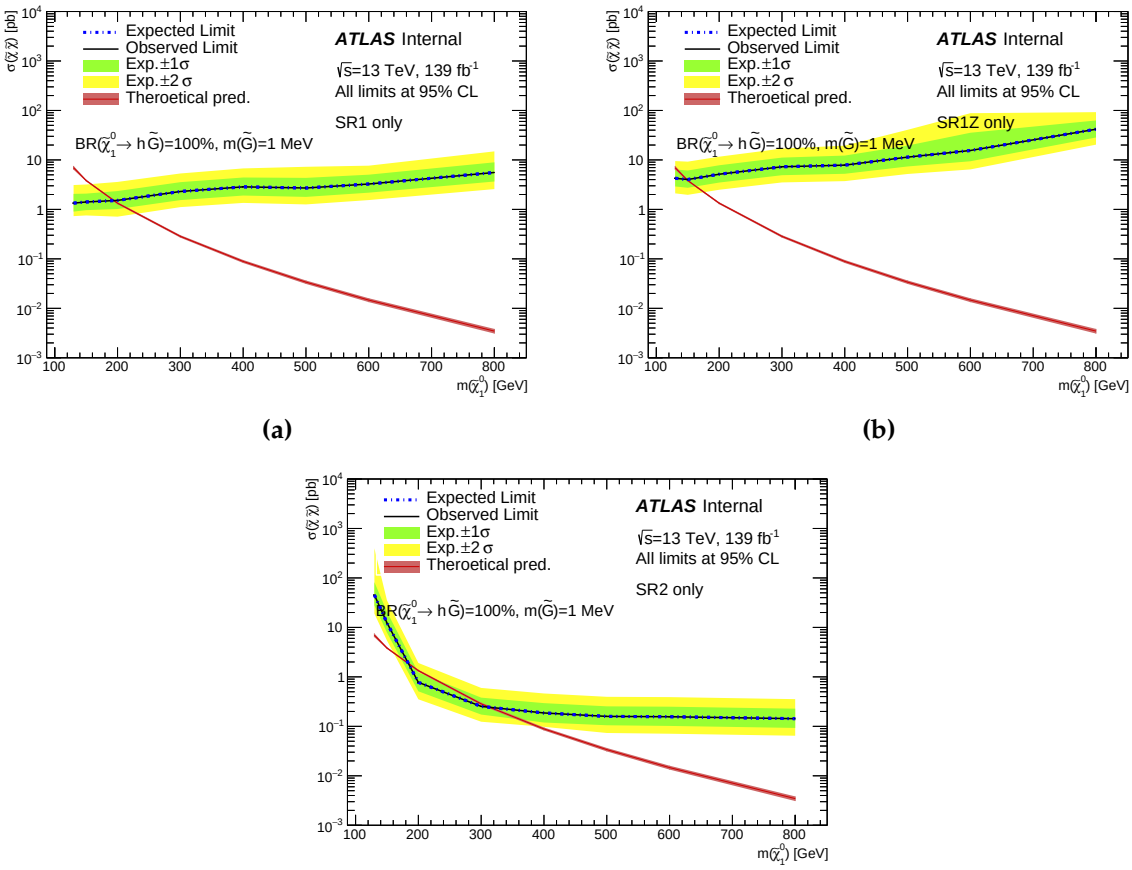

Figure 5.16: Expected limit on the pure Higgsino cross-section assuming $\mathrm{BF}(\tilde{\chi}_1^0 \to h\tilde{G}) = 100\%$ for different $\tilde{\chi}_1^0$ masses, obtained using the individual signal regions SR1 (5.16a), SR1Z (5.16b) and SR2 (5.16c). These figures are blinded, meaning that the observed number of events has been set to equal the background estimation exactly. The green and yellow bands indicate the 1σ and 2σ variation on the expected limit respectively. Full treatment of the systematic uncertainties is included in this set of figures.

5.6 Systematic Uncertainties

The background estimation techniques presented in the previous sections are all associated with a systematic uncertainty on the total estimated background yield. There are three classes of uncertainties: Uncertainties associated with the data-driven methods developed in the previous sections, uncertainties associated with modelling of the detector response and associated with theoretical modelling of different processes. The latter two are only relevant for simulated backgrounds, while the uncertainty on the data-driven methods is applied to the dominant $\gamma\gamma$, γ-jet, jet-γ and jet-jet backgrounds.

The systematic uncertainties in this analysis are shown in table 5.8. The systematic uncertainties on the non-resonant background estimation caused by the 2x2D and modified ABCD methods are included. Here, $\alpha(w_{\gamma\gamma,\gamma j,j\gamma,jj})$ indicate the systematic uncertainty on the weights calculated with the 2x2D sideband method (see section 5.4.1) and applied respectively to the $\gamma\gamma$, γ-jet, jet-γ and jet-jet samples. These uncertainties are calculated by propagating the uncertainties on the obtained 2x2D fit parameters as well as the statistical uncertainties in the 2x2D categories. Any unexpected correlations between (fake) photon isolation and identification would degrade the modelling in the 2x2D fit, thereby degrading the fit performance and thus the uncertainty on the fit result. This, in turn, would increase the uncertainty on the 2x2D weights $\alpha(w_{\gamma\gamma,\gamma j,j\gamma,jj})$ and is therefore accounted for in the analysis.

The $\alpha(w_{ik}^{\mathrm{ABCD}})$ indicate the systematic uncertainty on the the weights calculated with the modified ABCD method (see section 5.4.2) and applied to the $\gamma\gamma$, γ-jet, jet-γ and jet-jet samples in SR2. These are calculated from the statistical uncertainties in the control regions used in the modified ABCD method (CR2A/B/C/D).

Full treatment of the systematic uncertainties on the dominant resonant Higgs boson background MC (ttH) is included, following standard ATLAS procedures [273, 274]. This includes the full systematic treatment of the detector uncertainties ($\alpha(\mathrm{ttH}^{\mathrm{detec.}})$)

and theoretical uncertainties ($\alpha(\mathrm{ttH}^{\mathrm{theo.}})$). A flat 30% uncertainty on the remaining minor resonant backgrounds ($\alpha(h)$) is considered. The full treatment of the systematic detector uncertainties relating to the signal yields is also included.

As the non-resonant $\gamma\gamma$ background dominates at low $E_{\mathrm{T}}^{\mathrm{miss}}$, the largest systematic uncertainty in both SR1 and SR1Z is the uncertainty associated to the 2x2D sideband method weight applied to the di-photon background $\alpha(w_{\gamma\gamma})$ at the level of $\sim 10\%$, followed by statistical uncertainties on the background templates ($\alpha(\mathrm{stat.})$).

Due to the more challenging phase space in SR2 with high $E_{\mathrm{T}}^{\mathrm{miss}}$ and low event yields, the overall background systematic in SR2 amounts to 38.8%, more than twice the contribution in the low-$E_{\mathrm{T}}^{\mathrm{miss}}$ signal regions. While the uncertainty in the non-resonant $\gamma\gamma$ background amounts to roughly the same contribution as for SR1 and SR1Z, the dominant uncertainties are the statistical uncertainty on the background template $\gamma(\mathrm{stat.})$ of $\sim 20\%$ and the uncertainty on the jet-γ background of size $\sim 30\%$.

The uncertainty on the jet-γ background takes a larger value for SR2 since it is fitted to almost zero in the modified ABCD method, as shown in table 5.6. The uncertainties originating from the modification of the ABCD extrapolation ($\alpha(w_{ik}^{\mathrm{ABCD}})$) are all relatively minor, where $\alpha(w_{\gamma\gamma}^{\mathrm{ABCD}})$ is the largest uncertainty with $\sim 6\%$. Uncertainties on the resonant Higgs backgrounds are at the percent level in all signal regions. No closure systematics are included as the systematic uncertainties cover the disagreement in the validation regions.

The statistical uncertainties for all signal regions exceed the total systematic uncertainties by at least a factor of two. The analysis is therefore limited by statistics and not by the systematic uncertainties originating from the modelling of the backgrounds. This is essential in enhancing the analysis' sensitivity to Supersymmetric models and therefore serves as further confirmation of a successful modelling of the backgrounds, despite the challenging considered phase space.

Uncertainty of channel	SR1	SR1Z	SR2
Total background expectation	3.97	6.43	1.71
Total statistical ($\sqrt{N_{\text{exp}}}$)	$\pm$1.99	$\pm$2.54	$\pm$1.31
Total background systematic	$\pm$0.63 [15.9%]	$\pm$0.99 [15.3%]	$\pm$0.66 [38.8%]
$\alpha(w_{\gamma\gamma})$	$\pm$0.43 [10.9%]	$\pm$0.63 [9.8%]	$\pm$0.15 [8.7%]
$\alpha(w_{\gamma j})$	$\pm$0.27 [6.8%]	$\pm$0.48 [7.4%]	$\pm$0.12 [7.0%]
$\alpha(w_{j\gamma})$	$\pm$0.01 [0.28%]	$\pm$0.03 [0.52%]	$\pm$0.47 [27.4%]
$\alpha(w_{jj})$	$\pm$0.00 [0.00%]	$\pm$0.05 [0.81%]	$\pm$0.23 [13.3%]
$\alpha(\text{stat.})$	$\pm$0.35 [8.7%]	$\pm$0.45 [7.0%]	$\pm$0.33 [19.3%]
$\alpha(w_{\gamma\gamma}^{\text{ABCD}})$	-	-	$\pm$0.10 [5.9%]
$\alpha(w_{\gamma j}^{\text{ABCD}})$	-	-	$\pm$0.07 [4.1%]
$\alpha(w_{j\gamma}^{\text{ABCD}})$	-	-	$\pm$0.01 [0.31%]
$\alpha(w_{jj}^{\text{ABCD}})$	-	-	$\pm$0.05 [3.2%]
$\alpha(h)$	$\pm$0.13 [3.2%]	$\pm$0.37 [5.8%]	$\pm$0.02 [1.1%]
$\alpha(\text{ttH}^{\text{detec.}})$	$\pm$0.04 [1.0%]	$\pm$0.02 [0.3%]	$\pm$0.06 [3.5%]
$\alpha(\text{ttH}^{\text{theo.}})$	$\pm$0.03 [0.8%]	$\pm$0.02 [0.3%]	$\pm$0.02 [1.2%]

Table 5.8: Breakdown of the dominant systematic uncertainties on background estimates in the various signal regions. The percentages show the size of the uncertainty relative to the total expected background. It should be noted that uncertainties may correlate and therefore can not necessarily be added in quadrature to obtain the total value.

5.7 Results

This section summarises the results of the analysis. The unblinded $m_{\gamma\gamma}$ distributions for all signal regions are shown in figure 5.17, where all signal region selections are applied, except that on $m_{\gamma\gamma}$. Markers are included to indicate the respective signal region. In these figures, the regions with $m_{\gamma\gamma} < 120\,\text{GeV}$ and $m_{\gamma\gamma} > 130\,\text{GeV}$ correspond to slices of the respective control regions (CR1 for SR1 and SR1Z and CR2A for SR2). The observed numbers of events in all signal regions are consistent with the SM prediction, with small under-fluctuations in signal regions SR1 and SR1Z.

The deviations from the Standard Model prediction are investigated in more detail in figure 5.18. The under-fluctuations in both SR1 and SR2 amount to approximately 0.5σ. The observed numbers of events are therefore entirely consistent with the SM and no tension with the Standard Model prediction is observed in this analysis.

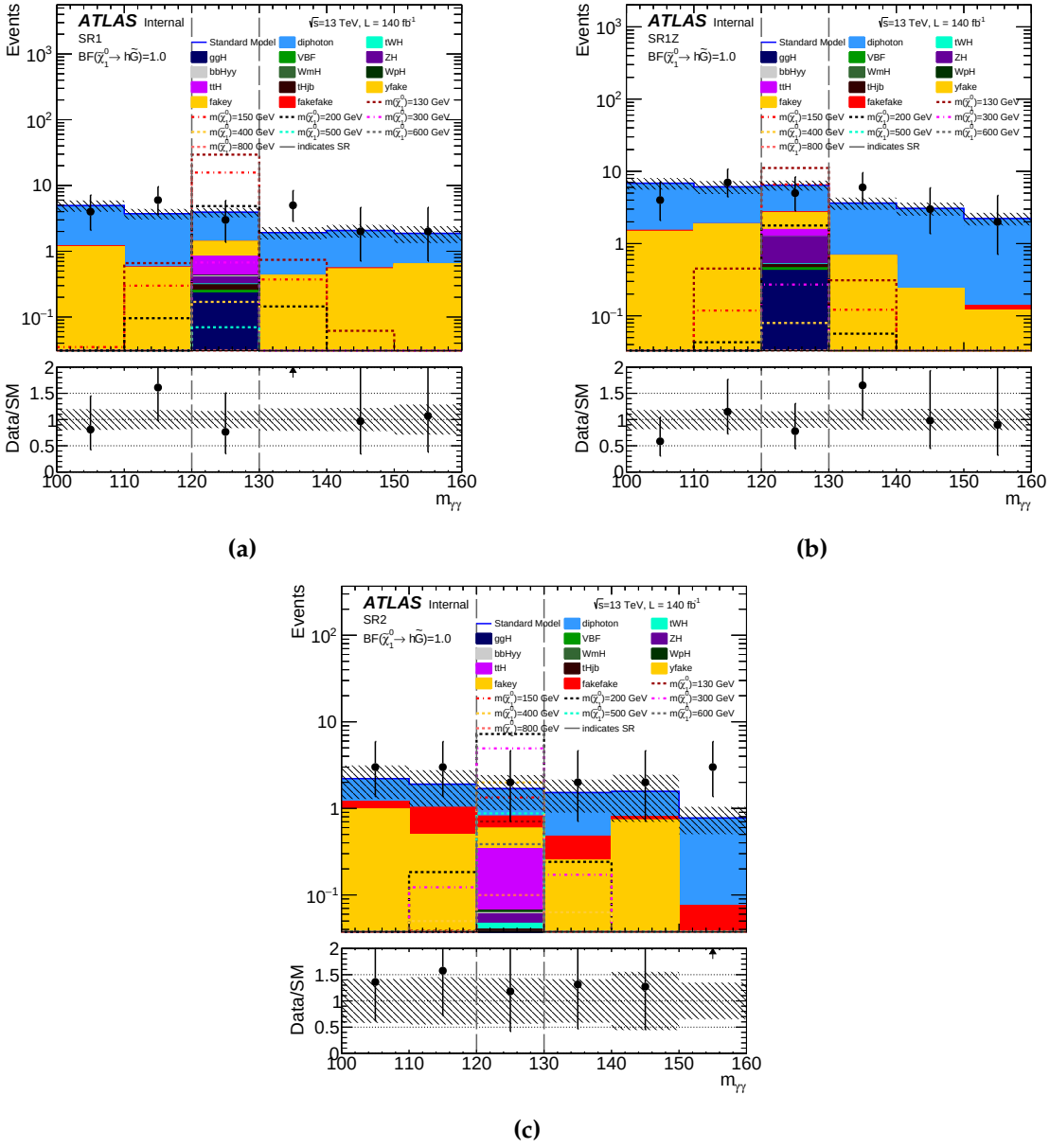

Figure 5.17: Distribution of the invariant di-photon mass $m_{\gamma\gamma}$ for signal and backgrounds with all selections of the signal regions applied, except for the selection on $m_{\gamma\gamma}$. The respective background estimation techniques are applied. Full treatment of the systematic uncertainties is included in this set of figures, resulting in a systematic uncertainty indicated by the shaded area. The lower panel shows the data/SM prediction ratio for the respective bin. Markers are included, indicating the borders of the signal region. Events outside of the marked area correspond to slices of the respective control region. The signal benchmarks in this set of figures assume $\mathrm{BF}(\tilde{\chi}_1^0 \to h\tilde{G}) = 100\%$. Distributions are shown for SR1 (5.17a), SR1Z (5.17a) and SR2 (5.17a).

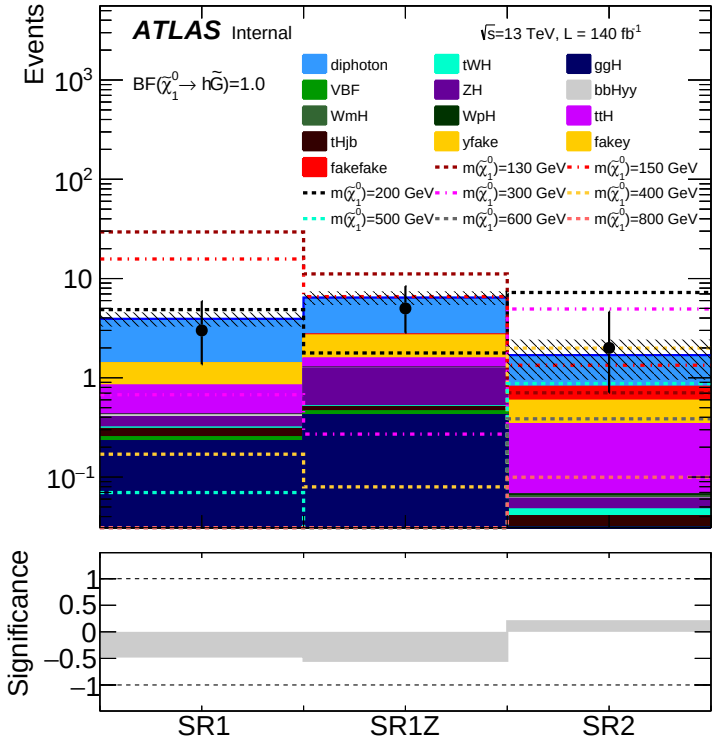

Figure 5.18: Numbers of signal and background events in the signal regions. The respective background estimation techniques are applied. Full treatment of the systematic uncertainties is included in this figure, resulting in a systematic uncertainty indicated by the shaded area in the top plot. The shaded area in the lower panel shows the significance in the deviation of the observed number of events from the SM prediction for the respective bin. The signal benchmarks in this set of figures assume $\mathrm{BF}(\tilde{\chi}_1^0 \to h\tilde{G}) = 100\%$. Distributions are shown for SR1 (5.17a), SR1Z (5.17a) and SR2 (5.17a).

A statistical combination of the three signal regions was performed and a limit on the predicted Higgsino cross-section of $\tilde{\chi}_1^0$ pair-production formed, assuming $\mathrm{BF}(\tilde{\chi}_1^0 \to h\tilde{G}) = 100\%$. The results of this statistical combination are shown in figure 5.19.

Due to the slight under-fluctuations in both low-$E_{\mathrm{T}}^{\mathrm{miss}}$ signal regions, limits for low neutralino masses exceed the expectation. Assuming $\mathrm{BF}(\tilde{\chi}_1^0 \to h\tilde{G}) = 100\%$, this analysis excludes cross sections above $\sigma(\tilde{\chi}\tilde{\chi}) \sim 1\,\mathrm{pb}$ for low masses of $m(\tilde{\chi}_1^0) = 130\,\mathrm{GeV}$. Under the same assumption on the neutralino branching fraction, the analysis excludes the theoretical prediction for the pure Higgsino cross section for neutralino masses below $\sim 300\,\mathrm{GeV}$. Due to the optimisation presented in earlier sections, this analysis has excellent sensitivity to the low and intermediate neutralino masses below this value. The tight selection on $m_{\gamma\gamma}$ of $|m_{\gamma\gamma} - 125\,\mathrm{GeV}| < 5\,\mathrm{GeV}$ included in all signal regions in combination with the the decreasing value of $\sigma \times \mathrm{BF}$ limit sensitivity to models with higher neutralino masses.

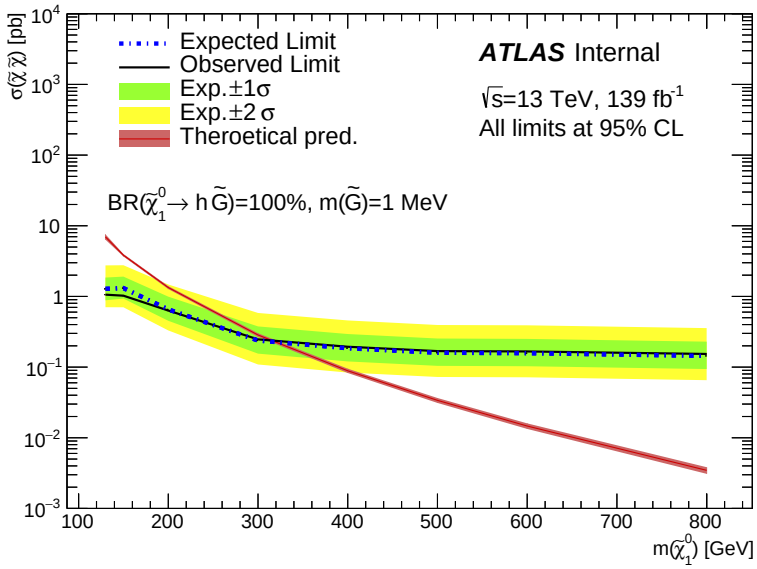

Figure 5.19: Observed and expected limits on the pure Higgsino cross-section assuming $\mathrm{BF}(\tilde{\chi}_1^0 \to h\tilde{G}) = 100\%$ for different $\tilde{\chi}_1^0$ masses, obtained by a statistical combination of the three signal regions SR1, SR1Z and SR2. The green and yellow bands indicate the 1σ and 2σ variation on the expected limit respectively. Full treatment of the systematic uncertainties is included in this figure.

Assuming $\tilde{\chi}_1^0 \to h\tilde{G}$ or $\tilde{\chi}_1^0 \to Z\tilde{G}$, limits are set for variable neutrino branching ratios in a statistical combination of the three signal regions and the results shown in figure

5.20. The analysis shows sensitivity to models where the CLs is lower than 0.05 [275], which occurs in the top left corner of the plot. Due to the requirement of two photons close to the Higgs boson peak in $m_{\gamma\gamma}$ in all signal regions, sensitivity decreases with decreasing $\mathrm{BF}(\tilde{\chi}_1^0 \to h\tilde{G})$ (increasing $\mathrm{BF}(\tilde{\chi}_1^0 \to Z\tilde{G})$). Despite this tight selection, the analysis is able to exclude GMSB models with branching fractions as low as $\mathrm{BF}(\tilde{\chi}_1^0 \to h\tilde{G}) = 40\%$ for low neutralino masses of 130 GeV. As the neutralino mass increases, the sensitivity decreases due to the reduction in the production cross-section of the neutralino.

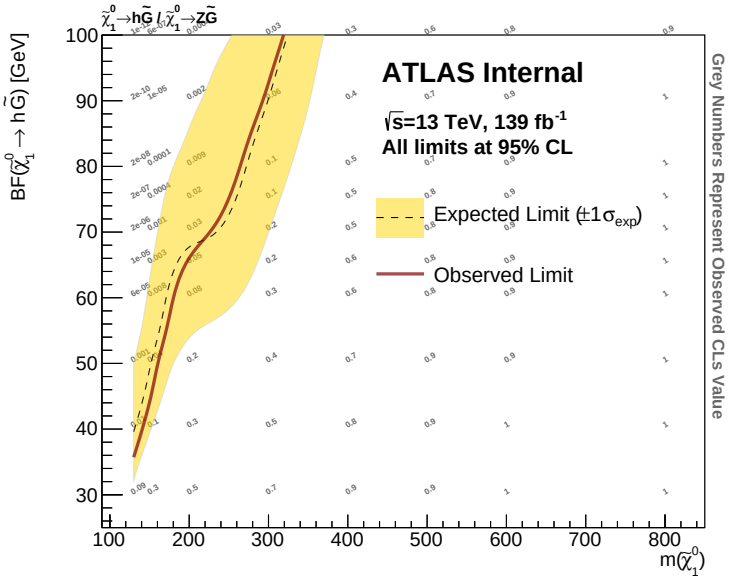

Figure 5.20: Observed and expected limits on the pure Higgsino cross-section assuming $\tilde{\chi}_1^0 \to h\tilde{G}/\tilde{\chi}_1^0 \to Z\tilde{G}$ for different $\tilde{\chi}_1^0$ masses, obtained by a statistical combination of the three signal regions SR1, SR1Z and SR2. The yellow band indicates the 1σ variation on the expected limit. Gray numbers indicate the observed CLs value at each point. A point is excluded at 95% confidence level if $\mathrm{CLs} < 0.05$. Full treatment of the systematic uncertainties is included in this figure.

The limit on models with variable $\mathrm{BF}(\tilde{\chi}_1^0 \to h\tilde{G})$ obtained by the $\gamma\gamma$bb analysis presented here is compared to different searches for Gauge-Mediated SUSY Breaking in figure 5.21. Previous searches for GMSB have been performed performed by the ATLAS collaboration in final states with at least three b-tagged jets (multi-b or 4b [240]), four or more charged leptons (4L [276]), two hadronically decaying bosons and $E_{\mathrm{T}}^{\mathrm{miss}}$ (0L [277]) and two leptons, jets and $E_{\mathrm{T}}^{\mathrm{miss}}$ (2L [278]). The 0L, 2L and 4L searches have been optimised for decays of the NLSP to the LSP as well as $W^{\pm}$ or Z-bosons

and therefore show excellent sensitivity to large values of $\mathrm{BF}(\tilde{\chi}_1^0 \to Z\tilde{G})$, covering the area with $\mathrm{BF}(\tilde{\chi}_1^0 \to h\tilde{G}) \lesssim 50\%$ for neutralino masses of up to $m(\tilde{\chi}_1^0) \approx 900\,\mathrm{GeV}$.

The multi-b search introduced in section 5.1 was optimised for the decay of $\tilde{\chi}_1^0 \to h\tilde{G}$, where the Higgs boson decays to a pair of b-quarks. This search is therefore most sensitive to larger branching fractions of the lightest neutralino to Higgs bosons. The multi-b search observed a $\sim 2\sigma$ excess for neutralino masses of $\sim 250\,\mathrm{GeV}$ [240], causing a gap in the observed limit. Due to the orthogonal final state considered between the multi-b and $\gamma\gamma$bb analyses, the $\gamma\gamma$bb analysis presented in this chapter contributes significantly to closing the gap in the ATLAS experiment's sensitivity to GMSB models containing neutralinos with low masses and a large branching fraction to Higgs bosons.[3]

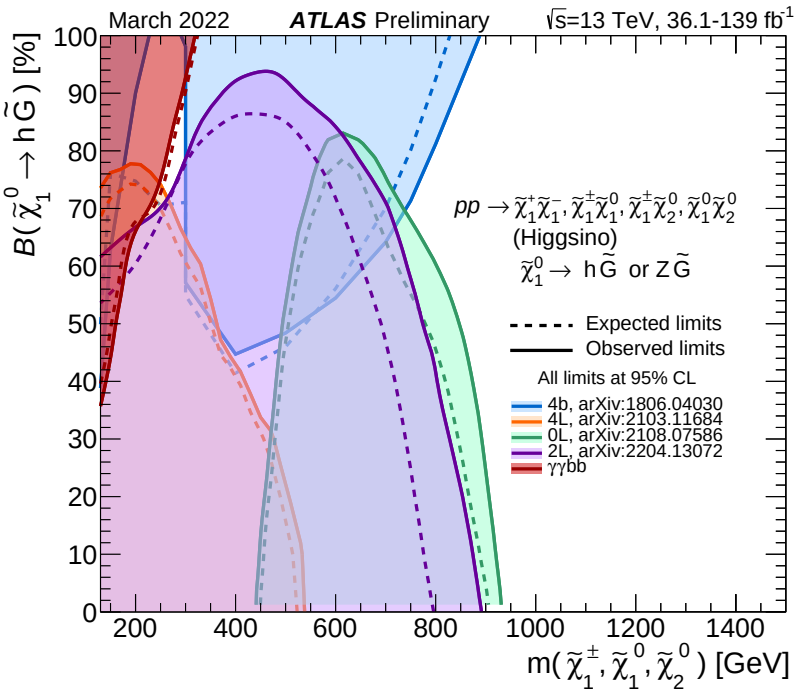

Figure 5.21: Observed and expected limits of different ATLAS analyses on the pure Higgsino cross-section assuming $\tilde{\chi}_1^0 \to h\tilde{G}/\tilde{\chi}_1^0 \to Z\tilde{G}$ for different $\tilde{\chi}_1^0$ masses. The included analyses are: multi-b (4b) [240], 4L [276], 0L [277], 2L [278] and the $\gamma\gamma$bb analysis presented in this thesis. Figure adapted from Ref. [113].

[3] It should be noted that a new, yet unpublished, rendition of the multi-b analysis is expected to also contribute to closing the gap in sensitivity.

5.8 Conclusions

This chapter has presented a search for Gauge-Mediated Supersymmetry Breaking models in final states of $\gamma\gamma b\bar{b}$ in $139\,\text{fb}^{-1}$ of pp collision data with $\sqrt{s} = 13\,\text{TeV}$ collected in LHC Run 2 by the ATLAS experiment. Three signal regions have been defined, where two require low missing transverse momentum ($E_{\text{T}}^{\text{miss}} \leq 100\,\text{GeV}$) and one requires high missing transverse momentum ($E_{\text{T}}^{\text{miss}} > 100\,\text{GeV}$). All signal regions include a tight selection around the Higgs boson mass in the invariant di-photon mass $m_{\gamma\gamma}$. A varying selection was applied on the invariant di-b mass m_{bb}, where SR1 included a selection around the Higgs boson mass, SR1Z included a selection around the Z-boson mass and SR2 included a wide m_{bb} selection window. The final state of $\gamma\gamma b\bar{b} + E_{\text{T}}^{\text{miss}}$ covered by SR2 was previously unexplored by the ATLAS experiment.

Control and validation regions were defined in the $m_{\gamma\gamma}$ and m_{bb} sidebands, respectively. Two dedicated data-driven techniques were used to estimate the non-resonant di-photon and fake-photon backgrounds. A simultaneous 16-dimensional fit (2x2D sideband method) was performed in control regions CR1, CR2D, CR2C and CR2B to determine the composition of the non-resonant background. The background composition in CR1 was assumed to be equal to the composition in VR1, SR1 and SR1Z, since these regions were designed to have similar kinematics. A modified ABCD extrapolation technique was developed to extrapolate the background estimation from control regions while correcting for a mis-modelling originating from a correlation of the b-jet multiplicity and missing transverse momentum. The obtained background estimate was then applied to validation and signal regions. The validation regions VR1 and VR2A were used in validating these background estimation techniques. It was shown that the presented analysis is limited by statistical uncertainties rather than systematic uncertainties arising from the background estimation.

The observed numbers of events agree with the Standard Model expectation in all signal regions. Hence, no evidence for physics beyond the Standard Model was found. Limits were set on the pair-production cross section of Higgsino neutralinos,

assuming a neutralino decay of $\tilde{\chi}_1^0 \to h\tilde{G}$ or $\tilde{\chi}_1^0 \to Z\tilde{G}$. Models with neutralino masses of up to 300 GeV were excluded for $\mathrm{BF}(\tilde{\chi}_1^0 \to h\tilde{G}) = 100\%$. While sensitivity overall decreases with $\mathrm{BF}(\tilde{\chi}_1^0 \to h\tilde{G})$, excluded neutralino masses reach ~ 250 GeV in scenarios with mixed neutralino decays with 75% branching fractions to Higgs bosons. Models with $m(\tilde{\chi}_1^0) = 130$ GeV are excluded for branching fractions as low as $\mathrm{BF}(\tilde{\chi}_1^0 \to h\tilde{G}) = 40\%$. The $\gamma\gamma$bb analysis almost completely closes a previous gap in the ATLAS experiment's sensitivity to GMSB models at large $\mathrm{BF}(\tilde{\chi}_1^0 \to h\tilde{G})$.

The presented analysis was designed to improve upon the sensitivity to low masses observed by a previous search in final states involving Higgs boson decays to $\gamma\gamma$ and $E_{\mathrm{T}}^{\mathrm{miss}}$ [239]. The cross-section limit to models with $m(\tilde{\chi}_1^0) = 130$ GeV is improved by a factor of ~ 5. As neither of these two searches was optimised for decays of the lightest neutralino to Z-bosons, a similar improvement is expected in excluded values of $\mathrm{BF}(\tilde{\chi}_1^0 \to Z\tilde{G})$ for this mass point. Due to the optimisation for low neutralino masses, no significant improvement is found for larger values of $m(\tilde{\chi}_1^0) \gtrsim 300$ GeV. The overall sensitivity of the $\gamma\gamma$bb analysis is comparable to the CMS analysis presented in section 5.1. The CMS analysis makes use of many highly optimised signal regions [241], while this search only defines three, to maintain more general model independence

The ATLAS multi-b search offers sensitivity to mostly intermediate to higher values of $m(\tilde{\chi}_1^0)$ [240]. As the analysis presented in this thesis is orthogonal to the multi-b search by construction, the two analyses are ideal candidates for a statistical combination, which can potentially improve sensitivity. A re-interpretation in a general Dark Matter model with a heavy mediator decaying to light Dark Matter in association with a Higgs or Z-boson would also be possible. Additional data taken during Run 3 is expected to increase the sensitivity of the ATLAS experiment to new physics in the final state of $\gamma\gamma b\bar{b} + E_{\mathrm{T}}^{\mathrm{miss}}$, as this analysis is limited by statistical uncertainties rather than systematic uncertainties. A $m_{\gamma\gamma}$ shape fit is expected to further improve sensitivity if event yields in the signal regions are larger.

6

In Summary

The hunt for Dark Matter is one of the biggest challenges in the history of Physics. This thesis has summarised a contribution to the search for DM using the ATLAS experiment.

Chapter 4 has summarised original research in the context of the ATLAS $E_{\mathrm{T}}^{\mathrm{miss}}$ trigger. The trigger was used by several analyses during LHC Run 2, including many searches for Dark Matter. The algorithms employed by the $E_{\mathrm{T}}^{\mathrm{miss}}$ trigger and their performance were discussed. The introduction of the `pufit` algorithm as well as its combination with the `cell` algorithm have allowed the maintenance of relatively low trigger thresholds, while providing high trigger efficiencies and keeping manageable rates despite the substantial increase of pile-up $\langle\mu\rangle$ over the years and the exponential rate dependence on $\langle\mu\rangle$.

The `trktc` algorithm, one of the candidate algorithms for the primary $E_{\mathrm{T}}^{\mathrm{miss}}$ trigger during Run 3, was introduced in section 4.3. The algorithm was separated by its constituents and the performance of the individual constituents and their combinations were evaluated. Contrary to expectations, the added use of tracking information through a selection on the Cluster Vertex Fraction and the use of Track Soft Term offered only a minimal improvement to the overall performance of the algorithm. Additionally, it was shown that the `trkmht` and `trktc` algorithms substantially benefit from a combination with the Run 2 algorithms, thereby motivating that a Run 3 primary trigger be formed by a combination of an algorithm using tracking with one or more Run 2 algorithms. These findings motivated studies performed by other members of the $E_{\mathrm{T}}^{\mathrm{miss}}$ trigger group which have lead to the use of the `pfopufit` algorithm in combination with `cell` in the primary $E_{\mathrm{T}}^{\mathrm{miss}}$ trigger for Run 3.

Chapter 5 discussed a search for new physics in final states of $\gamma\gamma b\bar{b} + E_{\mathrm{T}}^{\mathrm{miss}}$ in $139\,\mathrm{fb}^{-1}$ of pp collisions at $\sqrt{s} = 13\,\mathrm{TeV}$ with the ATLAS detector. Events in which one Higgs boson decays to $\gamma\gamma$ and one Higgs boson to $b\bar{b}$ where considered. Particular care has gone into the fully data-driven estimation of the non-resonant di-photon and fake-photon backgrounds. No significant deviations from the SM expectation

were observed in any of the three signal regions. Results were interpreted in the context of Gauge-Mediated Supersymmetry Breaking models. In the scenario with $\mathrm{BF}(\tilde{\chi}_1^0 \to h\tilde{G}) = 100\%$, GMSB models were excluded for neutralino masses below $m(\tilde{\chi}_1^0) \leq 300\,\mathrm{GeV}$. Due to the selection of two photons close to the Higgs mass in $m_{\gamma\gamma}$ in all signal regions, the analysis loses sensitivity as $\mathrm{BF}(\tilde{\chi}_1^0 \to h\tilde{G})$ decreases. Still, the analysis excludes models with branching fractions as low as $\mathrm{BF}(\tilde{\chi}_1^0 \to h\tilde{G}) = 40\%$ for low neutralino masses $m(\tilde{\chi}_1^0) = 130\,\mathrm{GeV}$. The presented $\gamma\gamma$bb analysis therefore contributes significantly to closing the ATLAS experiments gap in sensitivity to GMSB models with large $\mathrm{BF}(\tilde{\chi}_1^0 \to h\tilde{G})$ for $m(\tilde{\chi}_1^0) \approx 250\,\mathrm{GeV}$. Due the orthogonal final states between the $\gamma\gamma$bb and multi-b analyses, the two form ideal candidates for a statistical combination, which could further enhance sensitivity. A general DM re-interpretation of the $\gamma\gamma$bb analysis is also possible.

The lack of evidence for physics BSM does not demonstrate the failure, but rather the success of the $\gamma\gamma$bb analysis. It has shown that it is possible to make accurate predictions in extreme areas of phase space, thereby enabling us to gather more information on the nature of possible models for physics beyond the Standard Model. There are numerous searches performed both by the ATLAS collaboration and others which have set limits on Supersymmetry and other theories, thereby increasing our knowledge of what BSM physics scenarios are possible, as well as several measurements which deviate from the SM, further constraining theories for new physics. With the start of LHC Run 3 and the following High-Luminosity era of the LHC, new data will be collected, which will provide new opportunities in the search for BSM physics. This is, in a small part, made possible by the work on the $E_{\mathrm{T}}^{\mathrm{miss}}$ trigger presented in this thesis. Only when lessons learnt from past measurements and searches as well as theoretical motivations are carefully considered when defining new search strategies, will we be able to find new physics and the true nature of Dark Matter.

References

[1] Kenji Hamano et al. *Performance of the ATLAS missing transverse energy trigger at* $\sqrt{s} = 13\,\text{TeV}$. Tech. rep. Geneva: CERN, May 2018. URL: https://cds.cern.ch/record/2636374.

[2] ATLAS Collaboration. "Performance of the missing transverse momentum triggers for the ATLAS detector during Run-2 data taking". In: *JHEP* 08 (2020), p. 080. arXiv: 2005.09554 [hep-ex].

[3] Jonas Wurzinger, Claudia Merlassino, and Alan Barr. *Search for new physics in a final state of* $\gamma\gamma bb$+E_T^{miss} *in* $139\,\text{fb}^{-1}$ *of pp collisions at* $\sqrt{s} = 13\,\text{TeV}$ *with the ATLAS detector*. Tech. rep. Geneva: CERN, Sept. 2021. URL: https://cds.cern.ch/record/2781257.

[4] Muon $g-2$ Collaboration. "Final report of the E821 muon anomalous magnetic moment measurement at BNL". In: *Phys. Rev. D* 73 (7 Apr. 2006), p. 072003. URL: https://link.aps.org/doi/10.1103/PhysRevD.73.072003.

[5] Rosa Simoniello et al. *SUSY Summary Plots June 2021*. Tech. rep. All figures including auxiliary figures are available at https://atlas.web.cern.ch/Atlas/GROUPS/PHYSICS/PUBNOTES/ATL-PHYS-PUB-2021-019. Geneva: CERN, May 2021. URL: https://cds.cern.ch/record/2770591.

[6] WMAP Collaboration. "Seven-Year Wilkinson Microwave Anisotropy Probe (WMAP) Observations: Cosmological Interpretation". In: *The Astrophysical Journal Supplement Series* 192.2 (Jan. 2011), p. 18. arXiv: 1001.4538 [astro-ph.CO].

[7] Stephen P. Martin. "A Supersymmetry primer". In: *Adv. Ser. Direct. High Energy Phys.* 18 (1998). Ed. by Gordon L. Kane, pp. 1–98. arXiv: hep-ph/9709356.

[8] Aaron O'Neill. "The search for supersymmetry in complex hadronic states using the ATLAS detector". PhD thesis. Christ Church College, University of Oxford, 2021.

[9] Gabriel Gallardo. "Searches for new physics with leptons and invisible particles at the ATLAS experiment at the LHC". PhD thesis. St Edmund Hall, University of Oxford, 2021.

[10] Jesse Lui. "Discovery strategies for dark matter and Higgsinos at the LHC". PhD thesis. St Catherine's College, University of Oxford, 2019.

[11] Andrew Purcell. "Go on a particle quest at the first CERN webfest. Le premier webfest du CERN se lance à la conquête des particules". In: (Aug. 2012), p. 10. URL: https://cds.cern.ch/record/1473657.

[12] M.E. Peskin and Schroeder D.V. *An Introduction to Quantum Field Theory*. 1995.

[13] P.W. Higgs. "Broken symmetries, massless particles and gauge fields". In: *Physics Letters* 12.2 (1964), pp. 132–133. URL: https://www.sciencedirect.com/science/article/pii/0031916364911369.

[14] F. Englert and R. Brout. "Broken Symmetry and the Mass of Gauge Vector Mesons". In: *Phys. Rev. Lett.* 13 (9 Aug. 1964), pp. 321–323. URL: https://link.aps.org/doi/10.1103/PhysRevLett.13.321.

[15] Chris Quigg. "Electroweak Symmetry Breaking in Historical Perspective". In: *Annual Review of Nuclear and Particle Science* 65.1 (2015), pp. 25–42. eprint: https://doi.org/10.1146/annurev-nucl-102313-025537.

[16] A.N. Schellekens. *Beyond the Standard Model*. Vol. 1. Nikhef, 2017.

[17] Julia Woithe, Gerfried J Wiener, and Frederik F Van der Veken. "Let's have a coffee with the Standard Model of particle physics!" In: *Physics Education* 52.3 (Mar. 2017), p. 034001. URL: https://doi.org/10.1088/1361-6552/aa5b25.

[18] Cliff Burgess and Guy Moore. *The standard model: A primer*. Cambridge University Press, 2007.

[19] R. D. Peccei and Helen R. Quinn. "CP Conservation in the Presence of Pseudoparticles". In: *Phys. Rev. Lett.* 38 (25 June 1977), pp. 1440–1443. URL: https://link.aps.org/doi/10.1103/PhysRevLett.38.1440.

[20] Dan-di Wu. "A brief introduction to the strong CP problem". In: *Zeitschrift für Naturforschung A* 52.1-2 (1997), pp. 179–182.

[21] C. A. Baker et al. "An Improved experimental limit on the electric dipole moment of the neutron". In: *Phys. Rev. Lett.* 97 (2006), p. 131801. arXiv: hep-ex/0602020.

[22] Guido Altarelli. "Collider Physics within the Standard Model: a Primer". In: (Mar. 2013). arXiv: 1303.2842 [hep-ph].

[23] Matthew D. Schwartz. *Quantum Field Theory and the Standard Model*. Cambridge University Press, Mar. 2014.

[24] Jose Bernabeu. "On the history of the PMNS Matrix... with today's perspective". In: *Nuovo Cim. C* 037.03 (2014), pp. 145–154. arXiv: 1312.7451 [hep-ph].

[25] ATLAS Collaboration. *Standard Model Summary Plots February 2022*. Tech. rep. All figures including auxiliary figures are available at https://atlas.web.cern.ch/Atlas/GROUPS/PHYSICS/PUBNOTES/ATL-PHYS-PUB-2022-009. Geneva: CERN, Mar. 2022. URL: https://cds.cern.ch/record/2804061.

[26] H. Georgi and S. L. Glashow. "Unity of All Elementary Particle Forces". In: *Phys. Rev. Lett.* 32 (1974), pp. 438–441.

[27] S. Dimopoulos, S. Raby, and Frank Wilczek. "Supersymmetry and the scale of unification". In: *Phys. Rev. D* 24 (6 Sept. 1981), pp. 1681–1683. URL: https://link.aps.org/doi/10.1103/PhysRevD.24.1681.

[28] Savas Dimopoulos and Howard Georgi. "Softly broken supersymmetry and SU(5)". In: *Nuclear Physics B* 193.1 (1981), pp. 150–162. URL: https://www.sciencedirect.com/science/article/pii/0550321381905228.

[29] A.J. Buras et al. "Aspects of the grand unification of strong, weak and electromagnetic interactions". In: *Nuclear Physics B* 135.1 (1978), pp. 66–92. URL: https://www.sciencedirect.com/science/article/pii/0550321378902146.

[30] Steven Weinberg. "Implications of dynamical symmetry breaking". In: *Phys. Rev. D* 13 (4 Feb. 1976), pp. 974–996. URL: https://link.aps.org/doi/10.1103/PhysRevD.13.974.

[31] S. Weinberg. "Implications of dynamical symmetry breaking: An addendum". In: *Phys. Rev. D* 19 (4 Feb. 1979), pp. 1277–1280. URL: https://link.aps.org/doi/10.1103/PhysRevD.19.1277.

[32] Steven Weinberg. "Gauge Theories of Weak, Electromagnetic and Strong Interactions". In: *8th International Symposium on Lepton and Photon Interactions at High Energies*. Oct. 1977, p. 619.

[33] Leonard Susskind. "Dynamics of Spontaneous Symmetry Breaking in the Weinberg-Salam Theory". In: *Phys. Rev. D* 20 (1979), pp. 2619–2625.

[34] Eldad Gildener. "Gauge-symmetry hierarchies". In: *Phys. Rev. D* 14 (6 Sept. 1976), pp. 1667–1672. URL: https://link.aps.org/doi/10.1103/PhysRevD.14.1667.

[35] Particle Data Group et al. "Review of Particle Physics". In: *Progress of Theoretical and Experimental Physics* 2020.8 (Aug. 2020). 083C01. URL: https://doi.org/10.1093/ptep/ptaa104.

[36] Super-Kamiokande Collaboration. "Evidence for oscillation of atmospheric neutrinos". In: *Phys. Rev. Lett.* 81 (1998), pp. 1562–1567. arXiv: hep-ex/9807003.

[37] SNO Collaboration. "Measurement of the rate of $\nu_e + d \rightarrow p + p + e^-$ interactions produced by ^{8}B solar neutrinos at the Sudbury Neutrino Observatory". In: *Phys. Rev. Lett.* 87 (2001), p. 071301. arXiv: nucl-ex/0106015.

[38] M Magg and C Wetterich. "Neutrino mass problem and gauge hierarchy". In: *Phys. Lett. B* 94 (Mar. 1980), 61–64. 10 p. URL: https://cds.cern.ch/record/133759.

[39] LSND Collaboration. "Evidence for neutrino oscillations from the observation of $\bar{\nu}_e$ appearance in a $\bar{\nu}_\mu$ beam". In: *Phys. Rev. D* 64 (2001), p. 112007. arXiv: hep-ex/0104049.

[40] G. Mention et al. "The Reactor Antineutrino Anomaly". In: *Phys. Rev. D* 83 (2011), p. 073006. arXiv: 1101.2755 [hep-ex].

[41] MiniBooNE Collaboration. "Significant Excess of ElectronLike Events in the MiniBooNE Short-Baseline Neutrino Experiment". In: *Phys. Rev. Lett.* 121.22 (2018), p. 221801. arXiv: 1805.12028 [hep-ex].

[42] MiniBooNE Collaboration. "Updated MiniBooNE neutrino oscillation results with increased data and new background studies". In: *Phys. Rev. D* 103.5 (2021), p. 052002. arXiv: 2006.16883 [hep-ex].

[43] Sacha Davidson, Enrico Nardi, and Yosef Nir. "Leptogenesis". In: *Phys. Rept.* 466 (2008), pp. 105–177. arXiv: 0802.2962 [hep-ph].

[44] James M. Cline. "Baryogenesis". In: *Les Houches Summer School - Session 86: Particle Physics and Cosmology: The Fabric of Spacetime*. Sept. 2006. arXiv: hep-ph/0609145.

[45] R. D. Peccei. "The Strong CP problem and axions". In: *Lect. Notes Phys.* 741 (2008). Ed. by Markus Kuster, Georg Raffelt, and Berta Beltran, pp. 3–17. arXiv: hep-ph/0607268.

[46] LHCb Collaboration. "Test of lepton universality using $B^+ \to K^+\ell^+\ell^-$ decays". In: *Phys. Rev. Lett.* 113 (2014), p. 151601. arXiv: 1406.6482 [hep-ex].

[47] Gregory Ciezarek et al. "A Challenge to Lepton Universality in B Meson Decays". In: *Nature* 546 (2017), pp. 227–233. arXiv: 1703.01766 [hep-ex].

[48] F Archilli et al. "Flavour-changing neutral currents making and breaking the standard model". In: *Nature* 546.7657 (2017), pp. 221–226.

[49] LHCb Collaboration. "Test of lepton universality with $B^0 \to K^{*0}\ell^+\ell^-$ decays". In: *JHEP* 08 (2017), p. 055. arXiv: 1705.05802 [hep-ex].

[50] LHCb Collaboration. "Test of Lepton Flavor Universality by the measurement of the $B^0 \to D^{*-}\tau^+\nu_\tau$ branching fraction using three-prong τ decays". In: *Phys. Rev. D* 97.7 (2018), p. 072013. arXiv: 1711.02505 [hep-ex].

[51] LHCb Collaboration. "Test of lepton universality in beauty-quark decays". In: *Nature Phys.* 18.3 (2022), pp. 277–282. arXiv: 2103.11769 [hep-ex].

[52] Andreas Crivellin, Benjamin Fuks, and Luc Schnell. "Explaining the hints for lepton flavour universality violation with three S_2 leptoquark generations". In: *JHEP* 06 (2022), p. 169. arXiv: 2203.10111 [hep-ph].

[53] Muon $g-2$ Collaboration. "Measurement of the Positive Muon Anomalous Magnetic Moment to 0.46 ppm". In: *Phys. Rev. Lett.* 126 (14 Apr. 2021), p. 141801. URL: https://link.aps.org/doi/10.1103/PhysRevLett.126.141801.

[54] Sz. Borsanyi et al. "Leading hadronic contribution to the muon magnetic moment from lattice QCD". In: *Nature* 593.7857 (2021), pp. 51–55. arXiv: 2002.12347 [hep-lat].

[55] Glennys R. Farrar. "The muon g-2 and lattice QCD hadronic vacuum polarization may point to new, long-lived neutral hadrons". In: (June 2022). arXiv: 2206.13460 [hep-ph].

[56] CDF Collaboration. "High-precision measurement of the W boson mass with the CDF II detector". In: *Science* 376.6589 (2022), pp. 170–176. eprint: https://www.science.org/doi/pdf/10.1126/science.abk1781.

[57] A.A. Starobinsky. "A new type of isotropic cosmological models without singularity". In: *Physics Letters B* 91.1 (1980), pp. 99–102. URL: https://www.sciencedirect.com/science/article/pii/037026938090670X.

[58] Daniel Baumann. "Inflation". In: *Theoretical Advanced Study Institute in Elementary Particle Physics: Physics of the Large and the Small*. 2011, pp. 523–686. arXiv: 0907.5424 [hep-th].

[59] Andrei Linde. "Inflationary Cosmology after Planck 2013". In: *100e Ecole d'Ete de Physique: Post-Planck Cosmology*. 2015, pp. 231–316. arXiv: 1402.0526 [hep-th].

[60] Jérôme Martin et al. "The Best Inflationary Models After Planck". In: *JCAP* 03 (2014), p. 039. arXiv: 1312.3529 [astro-ph.CO].

[61] Jerome Martin, Christophe Ringeval, and Vincent Vennin. "Encyclopædia Inflationaris". In: *Phys. Dark Univ.* 5-6 (2014), pp. 75–235. arXiv: 1303.3787 [astro-ph.CO].

[62] J. C. Kapteyn. "First Attempt at a Theory of the Arrangement and Motion of the Sidereal System". In: *Astrophys. J.* 55 (1922), pp. 302–328.

[63] Vera C Rubin and W Kent Ford Jr. "Rotation of the Andromeda nebula from a spectroscopic survey of emission regions". In: *The Astrophysical Journal* 159 (1970), p. 379.

[64] Vera C Rubin, W Kent Ford Jr, and Norbert Thonnard. "Rotational properties of 21 SC galaxies with a large range of luminosities and radii, from NGC 4605/R= 4kpc/to UGC 2885/R= 122 kpc". In: *The Astrophysical Journal* 238 (1980), pp. 471–487.

[65] Alexandre Refregier. "Weak gravitational lensing by large scale structure". In: *Ann. Rev. Astron. Astrophys.* 41 (2003), pp. 645–668. arXiv: astro-ph/0307212.

[66] J. Anthony Tyson, Greg P. Kochanski, and Ian P. Dell'Antonio. "Detailed mass map of CL0024+1654 from strong lensing". In: *Astrophys. J. Lett.* 498 (1998), p. L107. arXiv: astro-ph/9801193.

[67] Benoit Famaey and Stacy McGaugh. "Modified Newtonian Dynamics (MOND): Observational Phenomenology and Relativistic Extensions". In: *Living Rev. Rel.* 15 (2012), p. 10. arXiv: 1112.3960 [astro-ph.CO].

[68] Planck Collaboration. "Planck 2015 results. XIII. Cosmological parameters". In: *Astron. Astrophys.* 594 (2016), A13. arXiv: 1502.01589 [astro-ph.CO].

[69] Lerh Feng Low. *Constraints on the composite photon theory*. Nov. 2016. URL: https://doi.org/10.1142/s021773231675002x.

[70] SDSS Collaboration. "Cosmological parameters from SDSS and WMAP". In: *Phys. Rev. D* 69 (2004), p. 103501. arXiv: astro-ph/0310723.

[71] Douglas Clowe et al. "A direct empirical proof of the existence of dark matter". In: *Astrophys. J. Lett.* 648 (2006), pp. L109–L113. arXiv: astro-ph/0608407.

[72] Pieter Van Dokkum et al. "A galaxy lacking dark matter". In: *Nature* 555.7698 (2018), pp. 629–632.

[73] Steven Weinberg. "The cosmological constant problem". In: *Rev. Mod. Phys.* 61 (1 Jan. 1989), pp. 1–23. URL: https://link.aps.org/doi/10.1103/RevModPhys.61.1.

[74] Supernova Search Team. "Observational evidence from supernovae for an accelerating universe and a cosmological constant". In: *Astron. J.* 116 (1998), pp. 1009–1038. arXiv: astro-ph/9805201.

[75] Supernova Cosmology Project. "Measurements of Ω and Λ from 42 high redshift supernovae". In: *Astrophys. J.* 517 (1999), pp. 565–586. arXiv: astro-ph/9812133.

[76] Jerome Martin. "Everything You Always Wanted To Know About The Cosmological Constant Problem (But Were Afraid To Ask)". In: *Comptes Rendus Physique* 13 (2012), pp. 566–665. arXiv: 1205.3365 [astro-ph.CO].

[77] Manimala Chakraborti, Sven Heinemeyer, and Ipsita Saha. "The new "MUON G-2" result and supersymmetry". In: *Eur. Phys. J. C* 81.12 (2021), p. 1114. arXiv: 2104.03287 [hep-ph].

[78] Peter Z. Skands et al. "SUSY Les Houches accord: Interfacing SUSY spectrum calculators, decay packages, and event generators". In: *JHEP* 07 (2004), p. 036. arXiv: hep-ph/0311123.

[79] Annika H. G. Peter. *Dark Matter: A Brief Review*. 2012. arXiv: 1201.3942 [astro-ph].

[80] John R. Ellis et al. "Supersymmetric Relics from the Big Bang". In: *Nucl. Phys. B* 238 (1984). Ed. by M. A. Srednicki, pp. 453–476.

[81] H. Goldberg. "Constraint on the Photino Mass from Cosmology". In: *Phys. Rev. Lett.* 50 (19 May 1983), pp. 1419–1422. URL: https://link.aps.org/doi/10.1103/PhysRevLett.50.1419.

[82] Ian J. R. Aitchison. "Supersymmetry and the MSSM: An Elementary introduction". In: (May 2005). arXiv: hep-ph/0505105.

[83] Michele Papucci, Joshua T. Ruderman, and Andreas Weiler. "Natural SUSY Endures". In: *JHEP* 09 (2012), p. 035. arXiv: 1110.6926 [hep-ph].

[84] Riccardo Barbieri and Duccio Pappadopulo. "S-particles at their naturalness limits". In: *JHEP* 10 (2009), p. 061. arXiv: 0906.4546 [hep-ph].

[85] Riccardo Barbieri and Gian Francesco Giudice. "Upper bounds on supersymmetric particle masses". In: *Nucl. Phys. B* 306 (Aug. 1987), 63–76. 19 p. URL: https://cds.cern.ch/record/180560.

[86] B. de Carlos and J. A. Casas. "One loop analysis of the electroweak breaking in supersymmetric models and the fine tuning problem". In: *Phys. Lett. B* 309 (1993), pp. 320–328. arXiv: hep-ph/9303291.

[87] Super-Kamiokande. "Search for Proton Decay via p —> e+ pi0 and p —> mu+ pi0 in a Large Water Cherenkov Detector". In: *Phys. Rev. Lett.* 102 (2009), p. 141801. arXiv: 0903.0676 [hep-ex].

[88] Sören Wiesenfeldt. "Proton decay in supersymmetric GUT models". In: *Modern Physics Letters A* 19.29 (2004), pp. 2155–2169.

[89] Paul Langacker. "Grand unified theories and proton decay". In: *Physics Reports* 72.4 (1981), pp. 185–385. URL: https://www.sciencedirect.com/science/article/pii/0370157381900594.

[90] R. Barbier et al. "R-parity violating supersymmetry". In: *Phys. Rept.* 420 (2005), pp. 1–202. arXiv: hep-ph/0406039.

[91] ATLAS Collaboration. "Search for R-parity-violating supersymmetry in a final state containing leptons and many jets with the ATLAS experiment using $\sqrt{s} = 13TeV$ proton-proton collision data". In: *Eur. Phys. J. C* 81.11 (2021), p. 1023. arXiv: 2106.09609 [hep-ex].

[92] ATLAS Collaboration. "Search for supersymmetry in events with four or more charged leptons in 139 fb^{-1} of $\sqrt{s}$ = 13 TeV pp collisions with the ATLAS detector". In: *JHEP* 07 (2021), p. 167. arXiv: 2103.11684 [hep-ex].

[93] ATLAS Collaboration. "Search for trilepton resonances from chargino and neutralino pair production in $\sqrt{s}$ = 13 TeV pp collisions with the ATLAS detector". In: *Phys. Rev. D* 103.11 (2021), p. 112003. arXiv: 2011.10543 [hep-ex].

[94] ATLAS Collaboration. "Search for R-parity-violating supersymmetric particles in multi-jet final states produced in p-p collisions at $\sqrt{s} = 13$ TeV using the ATLAS detector at the LHC". In: *Phys. Lett. B* 785 (2018), pp. 136–158. arXiv: 1804.03568 [hep-ex].

[95] CMS Collaboration. "Search for top squarks in final states with two top quarks and several light-flavor jets in proton-proton collisions at $\sqrt{s}$ = 13 TeV". In: *Phys. Rev. D* 104.3 (2021), p. 032006. arXiv: 2102.06976 [hep-ex].

[96] CMS Collaboration. "Search for resonant production of second-generation sleptons with same-sign dimuon events in proton-proton collisions at $\sqrt{s} = 13$ TeV". In: *Eur. Phys. J. C* 79.4 (2019), p. 305. arXiv: 1811.09760 [hep-ex].

[97] CMS Collaboration. "Search for R-parity violating supersymmetry in pp collisions at $\sqrt{s} = 13$ TeV using b jets in a final state with a single lepton, many jets, and high sum of large-radius jet masses". In: *Phys. Lett. B* 783 (2018), pp. 114–139. arXiv: 1712.08920 [hep-ex].

[98] E. Cremmer et al. "Yang-Mills theories with local supersymmetry: Lagrangian, transformation laws and super-Higgs effect". In: *Nuclear Physics B* 212.3 (1983), pp. 413–442. URL: https://www.sciencedirect.com/science/article/pii/055032138390679X.

[99] Pran Nath and R Arnowitt. "Generalized super-gauge symmetry as a new framework for unified gauge theories". In: *Physics Letters B* 56.2 (1975), pp. 177–180.

[100] R Arnowitt, Pran Nath, and B Zumino. "Superfield densities and action principle in curved superspace". In: *Physics Letters B* 56.1 (1975), pp. 81–84.

[101] Daniel Z Freedman and P Van Nieuwenhuizen. "Properties of supergravity theory". In: *Physical Review D* 14.4 (1976), p. 912.

[102] Stanley D Deser and Bruno Zumino. "Consistent supergravity". In: *Phys. Lett. B* 62.CERN-TH-2164 (1976), pp. 335–337.

[103] Daniel Z Freedman and P Van Nieuwenhuizen. "Properties of supergravity theory". In: *Physical Review D* 14.4 (1976), p. 912.

[104] E Cremmer et al. "Spontaneous symmetry breaking and Higgs effect in supergravity without cosmological constant". In: *Nuclear Physics B* 147.1-2 (1979), pp. 105–131.

[105] Jonathan A Bagger. "Coupling the gauge-invariant supersymmetric non-linear sigma model to supergravity". In: *Nuclear Physics B* 211.2 (1983), pp. 302–316.

[106] Heinz Pagels and Joel R Primack. "Supersymmetry, cosmology, and new physics at teraelectronvolt energies". In: *Physical Review Letters* 48.4 (1982), p. 223.

[107] T Moroi, H Murayama, and Masahiro Yamaguchi. "Cosmological constraints on the light stable gravitino". In: *Physics Letters B* 303.3-4 (1993), pp. 289–294.

[108] Christopher F. Kolda. "Gauge mediated supersymmetry breaking: Introduction, review and update". In: *Nucl. Phys. B Proc. Suppl.* 62 (1998). Ed. by M. Cvetic and P. Langacker, pp. 266–275. arXiv: hep-ph/9707450.

[109] Alexandre Arbey et al. "LHC constraints on Gravitino Dark Matter". In: *Phys. Rev. D* 92.11 (2015), p. 115008. arXiv: 1505.04595 [hep-ph].

[110] M. Bolz, A. Brandenburg, and W. Buchmuller. "Thermal production of gravitinos". In: *Nucl. Phys. B* 606 (2001). [Erratum: Nucl.Phys.B 790, 336–337 (2008)], pp. 518–544. arXiv: hep-ph/0012052.

[111] Josef Pradler and Frank Daniel Steffen. "Thermal gravitino production and collider tests of leptogenesis". In: *Phys. Rev. D* 75 (2007), p. 023509. arXiv: hep-ph/0608344.

[112] Savas Dimopoulos et al. "Experimental signatures of low-energy gauge mediated supersymmetry breaking". In: *Phys. Rev. Lett.* 76 (1996), pp. 3494–3497. arXiv: hep-ph/9601367.

[113] ATLAS Collaboration. *SUSY Summary Plots March 2022*. Tech. rep. All figures including auxiliary figures are available at https://atlas.web.cern.ch/Atlas/GROUPS/PHYSICS/PUBNOTES/ATL-PHYS-PUB-2022-013. Geneva: CERN, Apr. 2022. URL: https://cds.cern.ch/record/2805985.

[114] Christopher Charles Whiston Taylor et al. *The atomists, Leucippus and Democritus: fragments: a text and translation with a commentary*. Vol. 5. University of Toronto Press, 2010.

[115] John Dalton. *A new system of chemical philosophy*. Vol. 1. Cambridge University Press, 2010.

[116] Michael W. Davidson. "Leeuwenhoek Microscope". In: *Molecular Expressions, Optical Microscopy Primer* (2015). Available at: https://micro.magnet.fsu.edu.

[117] Stillman Drake. *Galileo at work: His scientific biography*. Courier Corporation, 2003.

[118] Jeffrey C Pommerville. *Fundamentals of microbiology*. Jones & Bartlett Publishers, 2013.

[119] Rudi Rottenfusser, Erin E. Wilson, and Michael W. Davidson. *Numerical Aperture and Resolution*. Available at: https://zeiss-campus.magnet.fsu.edu.

[120] H. Gegier and E. Marsden. "On a diffuse reflection of the α-particles". In: *Proc. R. Soc. Lond. A* 82 (1909), pp. 495–500.

[121] E. Rutherford. "The scattering of alpha and beta particles by matter and the structure of the atom". In: *Phil. Mag. Ser. 6* 21 (1911), pp. 669–688.

[122] H. Geiger and E. Marsden. "LXI. The laws of deflexion of a particles through large angles". In: *The London, Edinburgh, and Dublin Philosophical Magazine and Journal of Science* 25.148 (1913), pp. 604–623. URL: https://doi.org/10.1080/14786440408634197.

[123] Louis De Broglie. "Recherches sur la théorie des quanta". PhD thesis. Migration-université en cours d'affectation, 1924.

[124] *LEP design report*. Copies shelved as reports in LEP, PS and SPS libraries. Geneva: CERN, 1984. URL: https://cds.cern.ch/record/102083.

[125] "Measurement of the mass of the Z boson and the energy calibration of LEP". In: *Physics Letters B* 307.1 (1993), pp. 187–193. URL: https://www.sciencedirect.com/science/article/pii/0370269393902109.

[126] S. Schael et al. "Precision electroweak measurements on the Z resonance". In: *Phys. Rept.* 427 (2006), pp. 257–454. arXiv: hep-ex/0509008.

[127] Enrique Fernandez. "Physics at LEP-1 and LEP-2". In: *PoS* silafae-III (2000). Ed. by E. Nardi, p. 008.

[128] ALEPH, DELPHI, L3, OPAL Experiments. *Combined LEP Chargino Results, up to 208 GeV for large m0*. LEPSUSYWG/01-03.1. 2001.

[129] ALEPH, DELPHI, L3, OPAL Experiments. *Combined LEP Chargino Results, up to 208 GeV for low DM*. LEPSUSYWG/02-04.1. 2002.

[130] ALEPH, DELPHI, L3, OPAL Experiments. *Combined LEP Selectron/Smuon/Stau Results, 183-208 GeV*. LEPSUSYWG/04-01.1. 2004.

[131] *Design Report Tevatron 1 project*. Tech. rep. 1984. URL: https://cds.cern.ch/record/1478620.

[132] D0 Collaboration. "Observation of the top quark". In: *Phys. Rev. Lett.* 74 (1995), pp. 2632–2637. arXiv: hep-ex/9503003.

[133] CDF Collaboration. "Observation of top quark production in $\bar{p}p$ collisions". In: *Phys. Rev. Lett.* 74 (1995), pp. 2626–2631. arXiv: hep-ex/9503002.

[134] ATLAS Collaboration. "The ATLAS Experiment at the CERN Large Hadron Collider". In: *JINST* 3 (2008), S08003.

[135] Lyndon Evans and Philip Bryant. "LHC Machine". In: *Journal of Instrumentation* 3.08 (Aug. 2008), S08001–S08001. URL: https://doi.org/10.1088/1748-0221/3/08/s08001.

[136] ATLAS Collaboration. "Observation of a new particle in the search for the Standard Model Higgs boson with the ATLAS detector at the LHC". In: *Phys. Lett. B* 716 (2012), pp. 1–29. arXiv: 1207.7214 [hep-ex].

[137] CMS Collaboration. "Observation of a New Boson at a Mass of 125 GeV with the CMS Experiment at the LHC". In: *Phys. Lett. B* 716 (2012), pp. 30–61. arXiv: 1207.7235 [hep-ex].

[138] Christiane Lefèvre. "The CERN accelerator complex. Complexe des accélérateurs du CERN". Dec. 2008. URL: https://cds.cern.ch/record/1260465.

[139] Rende Steerenberg et al. "Operation and performance of the CERN Large Hadron Collider during proton Run 2". In: (2019), MOPMP031. 4 p. URL: https://cds.cern.ch/record/2696126.

[140] ATLAS Collaboration. "Public ATLAS Luminosity Results for Run-2 of the LHC". In: *tech. rep.* (2018). All figures including auxiliary figures are available at LuminosityPublicResultsRun2.

[141] ATLAS Collaboration. "Determination of the parton distribution functions of the proton from ATLAS measurements of differential $W^{\pm}$ and Z boson production in association with jets". In: *JHEP* 07 (2021), p. 223. arXiv: 2101.05095 [hep-ex].

[142] Davison E. Soper. "Parton distribution functions". In: *Nucl. Phys. B Proc. Suppl.* 53 (1997). Ed. by C. Bernard et al., pp. 69–80. arXiv: hep-lat/9609018.

[143] Zachary Marshall and. "Simulation of Pile-up in the ATLAS Experiment". In: *Journal of Physics: Conference Series* 513.2 (June 2014), p. 022024. URL: https://doi.org/10.1088/1742-6596/513/2/022024.

[144] LHCb Collaboration. "The LHCb Detector at the LHC". In: *JINST* 3 (2008), S08005.

[145] CMS Collaboration. "The CMS Experiment at the CERN LHC". In: *JINST* 3 (2008), S08004.

[146] ALICE Collaboration. "The ALICE experiment at the CERN LHC". In: *JINST* 3 (2008), S08002.

[147] Jure Zupan. "Introduction to flavour physics". In: *CERN Yellow Rep. School Proc.* 6 (2019). Ed. by M. Mulders and C. Duhr, pp. 181–212. arXiv: 1903.05062 [hep-ph].

[148] Roman Pasechnik and Michal Šumbera. "Phenomenological Review on Quark–Gluon Plasma: Concepts vs. Observations". In: *Universe* 3.1 (2017), p. 7. arXiv: 1611.01533 [hep-ph].

[149] ATLAS Collaboration. "Expected Performance of the ATLAS Experiment - Detector, Trigger and Physics". In: (Jan. 2009). arXiv: 0901.0512 [hep-ex].

[150] Joao Pequenao and Paul Schaffner. "How ATLAS detects particles: diagram of particle paths in the detector". Jan. 2013. URL: https://cds.cern.ch/record/1505342.

[151] ATLAS Collaboration. "The differential production cross section of the ϕ (1020) meson in $\sqrt{s}$ = 7 TeV pp collisions measured with the ATLAS detector". In: *Eur. Phys. J. C* 74.7 (2014), p. 2895. arXiv: 1402.6162 [hep-ex].

[152] ATLAS Collaboration. *ATLAS inner detector: Technical Design Report, 1*. Technical design report. ATLAS. Geneva: CERN, 1997. URL: https://cds.cern.ch/record/331063.

[153] H.H.J. ten Kate on behalf of the ATLAS Collaboration. "ATLAS superconducting toroids and solenoid". In: *IEEE Trans. Appl. Supercond.* 15 (2005), 1267–1270. 4 p. URL: http://cds.cern.ch/record/912244.

[154] Andrei Nomerotski. "Silicon detectors for tracking and vertexing". In: *Nuclear Instruments and Methods in Physics Research Section A: Accelerators, Spectrometers, Detectors and Associated Equipment* 598.1 (2009). Instrumentation for Collding Beam Physics, pp. 33–40. URL: https://www.sciencedirect.com/science/article/pii/S0168900208011856.

[155] V. L. Ginzburg and I. M. Frank. "Radiation of a uniformly moving electron due to its transition from one medium into another". In: *J. Phys. (USSR)* 9 (1945), pp. 353–362.

[156] F. Meloni on behalf of the ATLAS Collaboration. *Primary vertex reconstruction with the ATLAS detector*. Tech. rep. Geneva: CERN, Oct. 2016. URL: https://cds.cern.ch/record/2222390.

[157] ATLAS Collaboration. "ATLAS pixel detector electronics and sensors". In: *Journal of Instrumentation* 3.07 (July 2008), P07007–P07007. URL: https://doi.org/10.1088/1748-0221/3/07/p07007.

[158] M. Backhaus on behalf of the ATLAS Collaboration. "The upgraded Pixel Detector of the ATLAS Experiment for Run 2 at the Large Hadron Collider". In: *Nuclear Instruments and Methods in Physics Research Section A: Accelerators, Spectrometers, Detectors and Associated Equipment* 831 (Jan. 2015).

[159] M Capeans et al. on behalf of the ATLAS Collaboration. *ATLAS Insertable B-Layer Technical Design Report*. Tech. rep. Sept. 2010. URL: https://cds.cern.ch/record/1291633.

[160] B. Abbott et al. on behalf of the ATLAS Collaboration. "Production and Integration of the ATLAS Insertable B-Layer". In: *JINST* 13.05 (2018), T05008. arXiv: 1803.00844 [physics.ins-det].

[161] Timon Heim, ATLAS Collaboration, et al. "Status and performance of the ATLAS Pixel Detector after 3 years of operation". In: *Nuclear Instruments and Methods in Physics Research Section A: Accelerators, Spectrometers, Detectors and Associated Equipment* 765 (2014), pp. 227–231.

[162] Karolos Potamianos. "The upgraded Pixel detector and the commissioning of the Inner Detector tracking of the ATLAS experiment for Run-2 at the Large Hadron Collider". In: *PoS* EPS-HEP2015 (2015), p. 261. arXiv: 1608.07850 [physics.ins-det].

[163] A. Ahmad et al. "The silicon microstrip sensors of the ATLAS semiconductor tracker". In: *Nuclear Instruments and Methods in Physics Research Section A: Accelerators, Spectrometers, Detectors and Associated Equipment* 578.1 (2007), pp. 98–118. URL: https://www.sciencedirect.com/science/article/pii/S0168900207007644.

[164] ATLAS Collaboration. "Operation and performance of the ATLAS semiconductor tracker". In: *JINST* 9 (2014), P08009. arXiv: 1404.7473 [hep-ex].

[165] Abdesselam Abdelouahab et al. "The barrel modules of the ATLAS semiconductor tracker". In: (Dec. 2006).

[166] A Ahmad et al. *The Silicon Microstrip Sensors of the ATLAS SemiConductor Tracker*. Tech. rep. Geneva: CERN, Mar. 2007. URL: https://cds.cern.ch/record/1019885.

[167] B. Mindur on behalf of the ATLAS Collaboration. "ATLAS Transition Radiation Tracker (TRT): Straw tubes for tracking and particle identification at the Large Hadron Collider". In: *Nucl. Instrum. Meth. A* 845 (2017). Ed. by G. Badurek et al., pp. 257–261.

[168] ATLAS Collaboration. *Particle Identification Performance of the ATLAS Transition Radiation Tracker*. Tech. rep. All figures including auxiliary figures are available at https://atlas.web.cern.ch/Atlas/GROUPS/PHYSICS/CONFNOTES/ATLAS-CONF-2011-128. Geneva: CERN, Sept. 2011. URL: https://cds.cern.ch/record/1383793.

[169] ATLAS Collaboration. "ATLAS calorimeter performance Technical Design Report". In: (Dec. 1996).

[170] ATLAS Collaboration. *ATLAS liquid-argon calorimeter: Technical Design Report*. Technical design report. ATLAS. Geneva: CERN, 1996. URL: https://cds.cern.ch/record/331061.

[171] ATLAS Collaboration. *ATLAS tile calorimeter: Technical Design Report*. Technical design report. ATLAS. Geneva: CERN, 1996. URL: https://cds.cern.ch/record/331062.

[172] Christian Wolfgang Fabjan and F Gianotti. "Calorimetry for Particle Physics". In: *Rev. Mod. Phys.* 75 (Oct. 2003), 1243–1286. 96 p. URL: https://cds.cern.ch/record/692252.

[173] Jonathan Burr. "Searches for new physics involving massive invisible particles". Presented 18 Sep 2018. July 2018. URL: https://cds.cern.ch/record/2648475.

[174] ATLAS Collaboration. "Readiness of the ATLAS Liquid Argon Calorimeter for LHC Collisions". In: *Eur. Phys. J. C* 70 (2010), pp. 723–753. arXiv: 0912.2642 [physics.ins-det].

[175] N. Nikiforou on behalf of the ATLAS Collaboration. "Performance of the ATLAS Liquid Argon Calorimeter after three years of LHC operation and plans for a future upgrade". In: *3rd International Conference on Advancements in Nuclear Instrumentation Measurement Methods and their Applications*. June 2013. arXiv: 1306.6756 [physics.ins-det].

[176] ATLAS Collaboration. "The ATLAS forward calorimeters". In: *JINST* 3 (2008), P02010.

[177] ATLAS Collaboration. "Readiness of the ATLAS Tile Calorimeter for LHC collisions". In: *Eur. Phys. J. C* 70 (2010), pp. 1193–1236. arXiv: 1007.5423 [physics.ins-det].

[178] A. Hrynevich on behalf of the ATLAS Collaboration. *Performance of the ATLAS Tile Calorimeter*. Tech. rep. Geneva: CERN, May 2017. URL: https://cds.cern.ch/record/2263799.

[179] Michaela Mlynarikova. "Performance of the ATLAS hadronic Tile calorimeter". In: *5th Large Hadron Collider Physics Conference*. Aug. 2017. arXiv: 1709.00100 [physics.ins-det].

[180] ATLAS Collaboration. *ATLAS muon spectrometer: Technical Design Report*. Technical design report. ATLAS. Geneva: CERN, 1997. URL: https://cds.cern.ch/record/331068.

[181] E. Diehl on behalf of the ATLAS Collaboration. "Calibration and Performance of the ATLAS Muon Spectrometer". In: *Meeting of the APS Division of Particles and Fields*. Sept. 2011. arXiv: 1109.6933 [physics.ins-det].

[182] F. Bauer et al. "Construction and Test of MDT Chambers for the ATLAS Muon Spectrometer". In: *Nucl. Instrum. Meth. A* 461 (2001). Ed. by G. Batignani, F. Cervelli, G. Chiarelli and A. Scribano on behalf of the ATLAS Collaboraion, pp. 17–20. arXiv: 1604.02000 [physics.ins-det].

[183] Theodoros Argyropoulos et al. "Cathode Strip Chambers in ATLAS: Installation, Commissioning and in Situ Performance". In: *Nuclear Science, IEEE Transactions on* 56 (July 2009), pp. 1568–1574.

[184] Fabio Sauli. *Principles of operation of multiwire proportional and drift chambers*. Tech. rep. Cern, 1977.

[185] G Aielli, M Bindi, and A Polini. "Performance, operation and detector studies with the ATLAS Resistive Plate Chambers". In: *Journal of Instrumentation* 8.02 (Feb. 2013), P02020–P02020. URL: https://doi.org/10.1088/1748-0221/8/02/p02020.

[186] Koichi Nagai. "Thin gap chambers in ATLAS". In: *Nuclear Instruments and Methods in Physics Research Section A: Accelerators, Spectrometers, Detectors and Associated Equipment* 384.1 (1996). BEAUTY '96, pp. 219–221. URL: https://www.sciencedirect.com/science/article/pii/S0168900296010650.

[187] ATLAS Collaboration. "Performance of the ATLAS Trigger System in 2015". In: *Eur. Phys. J. C* 77.5 (2017), p. 317. arXiv: 1611.09661 [hep-ex].

[188] ATLAS Collaboration. "Operation of the ATLAS trigger system in Run 2". In: *JINST* 15.10 (2020), P10004. arXiv: 2007.12539 [physics.ins-det].

[189] ATLAS Collaboration. "Performance of electron and photon triggers in ATLAS during LHC Run 2". In: *Eur. Phys. J. C* 80.1 (2020), p. 47. arXiv: 1909.00761 [hep-ex].

[190] ATLAS Collaboration. "Performance of the ATLAS muon triggers in Run 2". In: *JINST* 15.09 (2020), P09015. arXiv: 2004.13447 [physics.ins-det].

[191] ATLAS Collaboration. "Configuration and performance of the ATLAS b-jet triggers in Run 2". In: *Eur. Phys. J. C* 81.12 (2021), p. 1087. arXiv: 2106.03584 [hep-ex].

[192] ATLAS Collaboration. "The ATLAS inner detector trigger performance in pp collisions at 13 TeV during LHC Run 2". In: *Eur. Phys. J. C* 82.3 (2022), p. 206. arXiv: 2107.02485 [hep-ex].

[193] M. Rybar on behalf of the ATLAS Collaboration. "The ATLAS Run-2 Trigger Menu". In: (June 2019). URL: https://cds.cern.ch/record/2677532.

[194] ATLAS Collaboration. *ATLAS Computing: technical design report*. Technical design report. ATLAS. Geneva: CERN, 2005. URL: https://cds.cern.ch/record/837738.

[195] R. Brun and F. Rademakers. "ROOT: An object oriented data analysis framework". In: *Nucl. Instrum. Meth. A* 389 (1997). Ed. by M. Werlen and D. Perret-Gallix, pp. 81–86.

[196] Wouter Verkerke and David Kirkby. *The RooFit toolkit for data modeling*. 2003. URL: https://arxiv.org/abs/physics/0306116.

[197] ATLAS Collaboration. "Measurement of inclusive and differential cross sections in the $H \to ZZ^* \to 4\ell$ decay channel in pp collisions at $\sqrt{s} = 13$ TeV with the ATLAS detector". In: *JHEP* 10 (2017), p. 132. arXiv: 1708.02810 [hep-ex].

[198] ATLAS Collaboration. "Event Displays from Run 2 physics analyses not included in publications". In: *tech. rep.* (2017). All figures including auxiliary figures are available at EventDisplayRun2Physics.

[199] ATLAS Collaboration. "Search for invisible Higgs boson decays in vector boson fusion at $\sqrt{s} = 13$ TeV with the ATLAS detector". In: *Phys. Lett. B* 793 (2019), pp. 499–519. arXiv: 1809.06682 [hep-ex].

[200] ATLAS Collaboration. "Combination of searches for invisible Higgs boson decays with the ATLAS experiment". In: *Phys. Rev. Lett.* 122.23 (2019), p. 231801. arXiv: 1904.05105 [hep-ex].

[201] ATLAS Collaboration. "Search for charged Higgs bosons decaying via $H^\pm \to \tau^\pm \nu_\tau$ in the τ+jets and τ+lepton final states with 36 fb^{-1} of pp collision data recorded at $\sqrt{s} = 13$ TeV with the ATLAS experiment". In: *JHEP* 09 (2018), p. 139. arXiv: 1807.07915 [hep-ex].

[202] ATLAS Collaboration. "Search for dark matter and other new phenomena in events with an energetic jet and large missing transverse momentum using the ATLAS detector". In: *JHEP* 01 (2018), p. 126. arXiv: 1711.03301 [hep-ex].

[203] ATLAS Collaboration. "Search for squarks and gluinos in final states with hadronically decaying τ-leptons, jets, and missing transverse momentum using pp collisions at $\sqrt{s}$ = 13 TeV with the ATLAS detector". In: *Phys. Rev. D* 99.1 (2019), p. 012009. arXiv: 1808.06358 [hep-ex].

[204] ATLAS Collaboration. "Searches for electroweak production of supersymmetric particles with compressed mass spectra in $\sqrt{s} = 13$ TeV pp collisions with the ATLAS detector". In: *Phys. Rev. D* 101.5 (2020), p. 052005. arXiv: 1911.12606 [hep-ex].

[205] ATLAS Collaboration. "Search for new phenomena using the invariant mass distribution of same-flavour opposite-sign dilepton pairs in events with missing transverse momentum in $\sqrt{s} = 13$ TeV pp collisions with the ATLAS detector". In: *Eur. Phys. J. C* 78.8 (2018), p. 625. arXiv: 1805.11381 [hep-ex].

[206] ATLAS Collaboration. "Search for heavy charged long-lived particles in the ATLAS detector in 36.1 fb^{-1} of proton-proton collision data at $\sqrt{s} = 13$ TeV". In: *Phys. Rev. D* 99.9 (2019), p. 092007. arXiv: 1902.01636 [hep-ex].

[207] ATLAS Collaboration. "Observation of $H \to b\bar{b}$ decays and VH production with the ATLAS detector". In: *Phys. Lett. B* 786 (2018), pp. 59–86. arXiv: 1808.08238 [hep-ex].

[208] ATLAS Collaboration. *Trigger menu in 2018*. Tech. rep. All figures including auxiliary figures are available at https://atlas.web.cern.ch/Atlas/GROUPS/PHYSICS/PUBNOTES/ATL-DAQ-PUB-2019-001. Geneva: CERN, Oct. 2019. URL: https://cds.cern.ch/record/2693402.

[209] J. Long on behalf of the ATLAS Collaboration. *The ATLAS Inner Detector tracking trigger at 13 TeV in LHC Run-2 and new developments on standard and unconventional tracking signatures for the upcoming LHC Run-3*. Tech. rep. Geneva: CERN, June 2022. URL: https://cds.cern.ch/record/2813981.

[210] R Achenbach et al. "The ATLAS Level-1 Calorimeter Trigger". In: *Journal of Instrumentation* 3.03 (Mar. 2008), P03001–P03001. URL: https://doi.org/10.1088/1748-0221/3/03/p03001.

[211] ATLAS Collaboration. "Performance of the upgraded PreProcessor of the ATLAS Level-1 Calorimeter Trigger". In: *JINST* 15.11 (2020), P11016. arXiv: 2005.04179 [physics.ins-det].

[212] ATLAS Collaboration. "Topological cell clustering in the ATLAS calorimeters and its performance in LHC Run 1". In: *Eur. Phys. J. C* 77 (2017), p. 490. arXiv: 1603.02934 [hep-ex].

[213] ATLAS Collaboration. "Readiness of the ATLAS Liquid Argon Calorimeter for LHC Collisions". In: *Eur. Phys. J. C* 70 (2010), pp. 723–753. arXiv: 0912.2642 [physics.ins-det].

[214] ATLAS Collaboration. "Performance of algorithms that reconstruct missing transverse momentum in $\sqrt{s} = 8$ TeV proton-proton collisions in the ATLAS detector". In: *Eur. Phys. J. C* 77.4 (2017), p. 241. arXiv: 1609.09324 [hep-ex].

[215] Matteo Cacciari, Gavin P. Salam, and Gregory Soyez. "The anti-k_t jet clustering algorithm". In: *JHEP* 04 (2008), p. 063. arXiv: 0802.1189 [hep-ph].

[216] Matteo Cacciari, Gavin P. Salam, and Gregory Soyez. "FastJet User Manual". In: *Eur. Phys. J. C* 72 (2012), p. 1896. arXiv: 1111.6097 [hep-ph].

[217] Matteo Cacciari, Gavin P. Salam, and Gregory Soyez. "The Catchment Area of Jets". In: *JHEP* 04 (2008), p. 005. arXiv: 0802.1188 [hep-ph].

[218] ATLAS Collaboration. "Performance of pile-up mitigation techniques for jets in pp collisions at $\sqrt{s} = 8$ TeV using the ATLAS detector". In: *Eur. Phys. J. C* 76.11 (2016), p. 581. arXiv: 1510.03823 [hep-ex].

[219] ATLAS Collaboration. "Jet energy scale measurements and their systematic uncertainties in proton-proton collisions at $\sqrt{s} = 13$ TeV with the ATLAS detector". In: *Phys. Rev. D* 96.7 (2017), p. 072002. arXiv: 1703.09665 [hep-ex].

[220] ATLAS Collaboration. *Technical Design Report for the Phase-II Upgrade of the ATLAS TDAQ System*. Tech. rep. Geneva: CERN, Sept. 2017. URL: https://cds.cern.ch/record/2285584.

[221] Aranzazu Ruiz-Martinez et al. *Run 3 trigger menu design*. Tech. rep. Geneva: CERN, July 2019. URL: https://cds.cern.ch/record/2683881.

[222] O. Aberle et al. *High-Luminosity Large Hadron Collider (HL-LHC): Technical design report*. CERN Yellow Reports: Monographs. Geneva: CERN, 2020. URL: https://cds.cern.ch/record/2749422.

[223] J. Roloff on behalf of the ATLAS Collaboration. "Pileup Mitigation". In: (Aug. 2017). URL: https://cds.cern.ch/record/2276691.

[224] ATLAS Collaboration. *Constituent-level pile-up mitigation techniques in ATLAS*. Tech. rep. All figures including auxiliary figures are available at https://atlas.web.cern.ch/Atlas/GROUPS/PHYSICS/CONFNOTES/ATLAS-CONF-2017-065. Geneva: CERN, Aug. 2017. URL: https://cds.cern.ch/record/2281055.

[225] Zekai Sen. *Spatial modeling principles in earth sciences*. Vol. 10. Springer, 2016.

[226] Matteo Cacciari, Gavin P. Salam, and Gregory Soyez. "SoftKiller, a particle-level pileup removal method". In: *Eur. Phys. J. C* 75.2 (2015), p. 59. arXiv: 1407.0408 [hep-ph].

[227] ATLAS Collaboration. *Performance of the ATLAS Inner Detector Track and Vertex Reconstruction in the High Pile-Up LHC Environment*. Tech. rep. All figures including auxiliary figures are available at https://atlas.web.cern.ch/Atlas/GROUPS/PHYSICS/CONFNOTES/ATLAS-CONF-2012-042. Geneva: CERN, Mar. 2012. URL: https://cds.cern.ch/record/1435196.

[228] ATLAS Collaboration. *Trigger monitoring and rate predictions using Enhanced Bias data from the ATLAS Detector at the LHC*. Tech. rep. All figures including auxiliary figures are available at https://atlas.web.cern.ch/Atlas/GROUPS/PHYSICS/PUBNOTES/ATL-DAQ-PUB-2016-002. Geneva: CERN, Oct. 2016. URL: https://cds.cern.ch/record/2223498.

[229] Robert Keyes and. "Development, Validation and Integration of the ATLAS Trigger System Software in Run 2". In: *Journal of Physics: Conference Series* 898 (Oct. 2017), p. 032008. URL: https://doi.org/10.1088/1742-6596/898/3/032008.

[230] Simone Alioli et al. "A general framework for implementing NLO calculations in shower Monte Carlo programs: the POWHEG BOX". In: *JHEP* 06 (2010), p. 043. arXiv: 1002.2581 [hep-ph].

[231] Stefano Frixione, Paolo Nason, and Carlo Oleari. "Matching NLO QCD computations with Parton Shower simulations: the POWHEG method". In: *JHEP* 11 (2007), p. 070. arXiv: 0709.2092 [hep-ph].

[232] Paolo Nason. "A New method for combining NLO QCD with shower Monte Carlo algorithms". In: *JHEP* 11 (2004), p. 040. arXiv: hep-ph/0409146.

[233] G. Aad et al. "Measurement of the Z/γ * boson transverse momentum distribution in pp collisions at $\sqrt{s} = 7$ TeV with the ATLAS detector". In: *Journal of High Energy Physics* 2014.9 (Sept. 2014). URL: http://dx.doi.org/10.1007/JHEP09(2014)145.

[234] Jon Butterworth et al. "PDF4LHC recommendations for LHC Run II". In: *Journal of Physics G: Nuclear and Particle Physics* 43.2 (Jan. 2016), p. 023001. URL: http://dx.doi.org/10.1088/0954-3899/43/2/023001.

[235] Enrico Bothmann et al. "Event generation with Sherpa 2.2". In: *SciPost Physics* 7.3 (Sept. 2019). URL: http://dx.doi.org/10.21468/SciPostPhys.7.3.034.

[236] Richard D. Ball et al. "Parton distributions for the LHC run II". In: *Journal of High Energy Physics* 2015.4 (Apr. 2015). URL: http://dx.doi.org/10.1007/JHEP04(2015)040.

[237] K G Tomiwa. "Performance of Jet Vertex Tagger in suppression of pileup jets and $E_{\mathrm{T}}^{\mathrm{miss}}$ in ATLAS detector". In: *Journal of Physics: Conference Series* 802 (Jan. 2017), p. 012012. URL: https://doi.org/10.1088/1742-6596/802/1/012012.

[238] ATLAS Collaboration. "Missing Energy Trigger Public Results". In: *TWiki* (Apr. 2021). All figures including auxiliary figures are available at https://twiki.cern.ch/twiki/bin/view/AtlasPublic/MissingEtTriggerPublicResults.

[239] ATLAS Collaboration. "Search for direct production of electroweakinos in final states with missing transverse momentum and a Higgs boson decaying into photons in pp collisions at $\sqrt{s}$ = 13 TeV with the ATLAS detector". In: *JHEP* 10 (2020), p. 005. arXiv: 2004.10894 [hep-ex].

[240] ATLAS Collaboration. "Search for pair production of higgsinos in final states with at least three b-tagged jets in $\sqrt{s} = 13$ TeV pp collisions using the ATLAS detector". In: *Phys. Rev. D* 98.9 (2018), p. 092002. arXiv: 1806.04030 [hep-ex].

[241] CMS Collaboration. "Search for supersymmetry using Higgs boson to diphoton decays at $\sqrt{s}$ = 13 TeV". In: *JHEP* 11 (2019), p. 109. arXiv: 1908.08500 [hep-ex].

[242] G. Aad et al. "ATLAS data quality operations and performance for 2015–2018 data-taking". In: *Journal of Instrumentation* 15.04 (Apr. 2020), P04003–P04003. URL: http://dx.doi.org/10.1088/1748-0221/15/04/P04003.

[243] Simone Amoroso et al. *PMG references document*. Tech. rep. Geneva: CERN, June 2019. URL: https://cds.cern.ch/record/2678867.

[244] Tanju Gleisberg and Stefan Höche. "Comix, a new matrix element generator". In: *Journal of High Energy Physics* 2008.12 (Dec. 2008), pp. 039–039. URL: http://dx.doi.org/10.1088/1126-6708/2008/12/039.

[245] Federico Buccioni et al. "OpenLoops 2". In: *The European Physical Journal C* 79.10 (Oct. 2019). URL: http://dx.doi.org/10.1140/epjc/s10052-019-7306-2.

[246] F. Cascioli, P. Maierhöfer, and S. Pozzorini. "Scattering Amplitudes with Open Loops". In: *Physical Review Letters* 108.11 (Mar. 2012). URL: http://dx.doi.org/10.1103/PhysRevLett.108.111601.

[247] Ansgar Denner, Stefan Dittmaier, and Lars Hofer. "Collier: A fortran-based complex one-loop library in extended regularizations". In: *Computer Physics Communications* 212 (Mar. 2017), pp. 220–238. URL: http://dx.doi.org/10.1016/j.cpc.2016.10.013.

[248] J. Alwall et al. "The automated computation of tree-level and next-to-leading order differential cross sections, and their matching to parton shower simulations". In: *Journal of High Energy Physics* 2014.7 (July 2014). URL: http://dx.doi.org/10.1007/JHEP07(2014)079.

[249] Torbjörn Sjöstrand et al. "An introduction to PYTHIA 8.2". In: *Computer Physics Communications* 191 (June 2015), pp. 159–177. URL: http://dx.doi.org/10.1016/j.cpc.2015.01.024.

[250] *ATLAS Pythia 8 tunes to 7 TeV data*. Tech. rep. All figures including auxiliary figures are available at https://atlas.web.cern.ch/Atlas/GROUPS/PHYSICS/PUBNOTES/ATL-PHYS-PUB-2014-021. Geneva: CERN, Nov. 2014. URL: https://cds.cern.ch/record/1966419.

[251] Stefano Catani and Massimiliano Grazzini. "An NNLO subtraction formalism in hadron collisions and its application to Higgs boson production at the LHC". In: *Phys. Rev. Lett.* 98 (2007), p. 222002. arXiv: hep-ph/0703012.

[252] LHC Higgs Cross Section Working Group. "Handbook of LHC Higgs Cross Sections: 4. Deciphering the Nature of the Higgs Sector". In: 2/2017 (Oct. 2016). arXiv: 1610.07922 [hep-ph].

[253] G. Aad et al. "The ATLAS Simulation Infrastructure". In: *The European Physical Journal C* 70.3 (Sept. 2010), pp. 823–874. URL: http://dx.doi.org/10.1140/epjc/s10052-010-1429-9.

[254] W Lukas. *Fast Simulation for ATLAS: Atlfast-II and ISF*. Tech. rep. ATL-SOFT-PROC-2012-065. Geneva: CERN, June 2012. URL: https://cds.cern.ch/record/1458503.

[255] Yulei Zhang et al. "Shower Shapes Comparison". In: *Photon ID meeting* (2021). Full presentation can be found at: indico.cern.ch.

[256] Paolo Nason and Carlo Oleari. "NLO Higgs boson production via vector-boson fusion matched with shower in POWHEG". In: *Journal of High Energy Physics* 2010.2 (Feb. 2010). URL: http://dx.doi.org/10.1007/JHEP02(2010)037.

[257] Paolo Nason and Carlo Oleari. "NLO Higgs boson production via vector-boson fusion matched with shower in POWHEG". In: *Journal of High Energy Physics* 2010.2 (Feb. 2010). URL: http://dx.doi.org/10.1007/JHEP02(2010)037.

[258] Stefano Frixione, Giovanni Ridolfi, and Paolo Nason. "A positive-weight next-to-leading-order Monte Carlo for heavy flavour hadroproduction". In: *Journal of High Energy Physics* 2007.09 (Sept. 2007), pp. 126–126. URL: http://dx.doi.org/10.1088/1126-6708/2007/09/126.

[259] H. B. Hartanto et al. "Higgs boson production in association with top quarks in the POWHEG BOX". In: *Physical Review D* 91.9 (May 2015). URL: http://dx.doi.org/10.1103/PhysRevD.91.094003.

[260] Keith Hamilton et al. "NNLOPS simulation of Higgs boson production". In: *Journal of High Energy Physics* 2013.10 (Oct. 2013). URL: http://dx.doi.org/10.1007/JHEP10(2013)222.

[261] Keith Hamilton, Paolo Nason, and Giulia Zanderighi. *Finite quark-mass effects in the NNLOPS POWHEG+MiNLO Higgs generator*. 2015. arXiv: 1501.04637 [hep-ph].

[262] Benjamin Fuks et al. "Gaugino production in proton-proton collisions at a center-of-mass energy of 8 TeV". In: *JHEP* 10 (2012), p. 081. arXiv: 1207.2159 [hep-ph].

[263] Benjamin Fuks et al. "Precision predictions for electroweak superpartner production at hadron colliders with RESUMMINO". In: *Eur. Phys. J. C* 73 (2013), p. 2480. arXiv: 1304.0790 [hep-ph].

[264] ATLAS Collaboration. "Electron and photon performance measurements with the ATLAS detector using the 2015–2017 LHC proton-proton collision data". In: *JINST* 14.12 (2019), P12006. arXiv: 1908.00005 [hep-ex].

[265] L. Carminati et al. on behalf of the ATLAS Collaboration. *Measurement of the isolated di-photon cross section in 4.9 fb-1 of pp collisions at sqrt(s) = 7 TeV with the ATLAS detector*. Tech. rep. ATL-COM-PHYS-2012-592. Geneva: CERN, May 2012. URL: https://cds.cern.ch/record/1450063.

[266] ATLAS Collaboration. "Jet reconstruction and performance using particle flow with the ATLAS Detector". In: *Eur. Phys. J. C* 77.7 (2017), p. 466. arXiv: 1703.10485 [hep-ex].

[267] ATLAS Collaboration. "ATLAS b-jet identification performance and efficiency measurement with $t\bar{t}$ events in pp collisions at $\sqrt{s} = 13$ TeV". In: *Eur. Phys. J. C* 79.11 (2019), p. 970. arXiv: 1907.05120 [hep-ex].

[268] M. Aaboud et al. "Electron reconstruction and identification in the ATLAS experiment using the 2015 and 2016 LHC proton–proton collision data at $\sqrt{s} = 13$ TeV". In: *The European Physical Journal C* 79.8 (Aug. 2019). URL: http://dx.doi.org/10.1140/epjc/s10052-019-7140-6.

[269] ATLAS Collaboration. "Muon reconstruction and identification efficiency in ATLAS using the full Run 2 *pp* collision data set at $\sqrt{s} = 13$ TeV". In: *Eur. Phys. J. C* 81.7 (2021), p. 578. arXiv: 2012.00578 [hep-ex].

[270] ATLAS Collaboration. "Performance of missing transverse momentum reconstruction with the ATLAS detector using proton-proton collisions at $\sqrt{s}$ = 13 TeV". In: *Eur. Phys. J. C* 78.11 (2018), p. 903. arXiv: 1802.08168 [hep-ex].

[271] ATLAS Collaboration. *Formulae for Estimating Significance*. Tech. rep. ATL-PHYS-PUB-2020-025. Geneva: CERN, Sept. 2020. URL: http://cds.cern.ch/record/2736148.

[272] R. Wang et al. on behalf of the ATLAS Collaboration. *Supporting note: Search for charginos and neutralinos in events with missing transverse momentum and a Higgs boson decaying to two photons in pp collisions at $\sqrt{s} = 13$ TeV with the ATLAS detector using data from 2015 to 2018*. Tech. rep. ATL-COM-PHYS-2018-1438. Geneva: CERN, Oct. 2018. URL: https://cds.cern.ch/record/2642387.

[273] ATLAS Collaboration. "Measurement of the properties of Higgs boson production at $\sqrt{s} = 13$ TeV in the $H \to \gamma\gamma$ channel using 139 fb^{-1} of *pp* collision data with the ATLAS experiment". In: (July 2022). arXiv: 2207.00348 [hep-ex].

[274] Simone Amoroso et al. *Recommendations on the treatment of theoretical systematic uncertainties in statistical analysis of ATLAS data*. Tech. rep. Geneva: CERN, Apr. 2020. URL: https://cds.cern.ch/record/2715689.

[275] A L Read. "Presentation of search results: the CLs technique". In: *Journal of Physics G: Nuclear and Particle Physics* 28.10 (Sept. 2002), pp. 2693–2704. URL: https://doi.org/10.1088/0954-3899/28/10/313.

[276] ATLAS Collaboration. "Search for supersymmetry in events with four or more charged leptons in 139 fb^{-1} of $\sqrt{s}$ = 13 TeV pp collisions with the ATLAS detector". In: *JHEP* 07 (2021), p. 167. arXiv: 2103.11684 [hep-ex].

[277] ATLAS Collaboration. "Search for charginos and neutralinos in final states with two boosted hadronically decaying bosons and missing transverse momentum in pp collisions at $\sqrt{s}$ = 13 TeV with the ATLAS detector". In: *Phys. Rev. D* 104.11 (2021), p. 112010. arXiv: 2108.07586 [hep-ex].

[278] ATLAS Collaboration. "Searches for new phenomena in events with two leptons, jets, and missing transverse momentum in 139 fb^{-1} of $\sqrt{s} = 13$ TeV pp collisions with the ATLAS detector". In: (Apr. 2022). arXiv: 2204.13072 [hep-ex].

[279] LHC Higgs Cross Section Working Group. "Handbook of LHC Higgs Cross Sections: 4. Deciphering the Nature of the Higgs Sector". In: 2/2017 (Oct. 2016). arXiv: 1610.07922 [hep-ph].

Appendices

A

Appendix: The $\gamma\gamma$bb analysis

A.1 Signal sample re-weighting factor

A.1.1 $hh \rightarrow \gamma\gamma b\bar{b}$ signal samples

To maximise the number of relevant events in the signal samples listed in section 5.2, the decays of the neutralino $\tilde{\chi}_1^0$ are fixed to:

- $\mathrm{BF}\left(\tilde{\chi}_1^0 \rightarrow h\tilde{G}\right) = 50\%$, where h is the Standard Model Higgs
- $\mathrm{BF}\left(\tilde{\chi}_1^0 \rightarrow h'\tilde{G}\right) = 50\%$, where h' is the Standard Model Higgs with $\mathrm{BF}\left(h' \rightarrow \gamma\gamma\right) = 100\%$

Hence, we need to re-weight these samples to match the expected branching fractions in data. In data, the probability P of obtaining a final state with $\gamma\gamma$bb once a pair

of neutralinos is produced can be expressed by:

$$\begin{aligned} P(\gamma\gamma; b\bar{b})^{\text{data}} &= P(h \to \gamma\gamma; h \to b\bar{b}) \\ &= 2\text{BF}\left(\tilde{\chi}_1^0 \to h\tilde{G}\right)^2 \text{BF}\left(h \to \gamma\gamma\right) \text{BF}\left(h \to b\bar{b}\right) \\ &= 2\text{BF}\left(h \to \gamma\gamma\right) \text{BF}\left(h \to b\bar{b}\right) \end{aligned} \tag{A.1}$$

Where, in the last step, we assume $\text{BF}\left(\tilde{\chi}_1^0 \to h\tilde{G}\right) = 100\%$. In our signal MC, this final state can be achieved in two ways:

- $h \to \gamma\gamma$, $h \to b\bar{b}$
- $h' \to \gamma\gamma$, $h \to b\bar{b}$

Which leads to a probability of:

$$\begin{aligned} P(\gamma\gamma; b\bar{b})^{\text{MC}} &= P(h \to \gamma\gamma; h \to b\bar{b}) + P(h' \to \gamma\gamma; h \to b\bar{b}) \\ &= 2\text{BF}\left(\tilde{\chi}_1^0 \to h\tilde{G}\right)^2 \text{BF}\left(h \to \gamma\gamma\right) \text{BF}\left(h \to b\bar{b}\right) \\ &\quad +2\text{BF}\left(\tilde{\chi}_1^0 \to h\tilde{G}\right) \text{BF}\left(\tilde{\chi}_1^0 \to h'\tilde{G}\right) \text{BF}\left(h' \to \gamma\gamma\right) \text{BF}\left(h \to b\bar{b}\right) \\ &= \frac{1}{2}\text{BF}\left(h \to \gamma\gamma\right) \text{BF}\left(h \to b\bar{b}\right) + \frac{1}{2}\text{BF}\left(h \to b\bar{b}\right) \end{aligned} \tag{A.2}$$

Putting equations A.1 and A.2 together, the re-weighting factor for the signal samples is given by:

$$\begin{aligned} \frac{N^{\text{data}}}{N^{\text{MC}}} &= \frac{P(\gamma\gamma; b\bar{b})^{\text{data}}}{P(\gamma\gamma; b\bar{b})^{\text{MC}}} \\ &= \frac{2\text{BF}\left(h \to \gamma\gamma\right) \text{BF}\left(h \to b\bar{b}\right)}{1/2\text{BF}\left(h \to \gamma\gamma\right) \text{BF}\left(h \to b\bar{b}\right) + 1/2\text{BF}\left(h \to b\bar{b}\right)} \\ &= \frac{4\text{BF}\left(h \to \gamma\gamma\right)}{\text{BF}\left(h \to \gamma\gamma\right) + 1} \end{aligned} \tag{A.3}$$

Where N^{data} and N^{MC} are the expected number of signal events in data and MC respec-

tively.

In this analysis, we assume $\mathrm{BF}\,(h \to \gamma\gamma) = 2.270^{+1.73\%}_{-1.72\%} \times 10^{-3}$ [279]. Overall, this results in a re-weighting factor of 0.0091.

A.1.2 $Zh \to \gamma\gamma b\bar{b}$ signal samples

As the Z-boson does not decay to photons, events in which both neutralinos decay to Z-bosons need not be considered. If both neutralinos decay to Higgs bosons, the $hh \to \gamma\gamma b\bar{b}$ samples can be used with an appropriate weight. Mixed scenarios in which one neutralino decays to a Z-boson and one to a Higgs boson can be simulated by assuming:

- $\mathrm{BF}\left(\tilde{\chi}_1^0 \to Z\tilde{G}\right) = 50\%$, where Z is the Standard Model Z-boson

- $\mathrm{BF}\left(\tilde{\chi}_1^0 \to h'\tilde{G}\right) = 50\%$, where h' is the Standard Model Higgs with $\mathrm{BF}\,(h' \to \gamma\gamma) = 100\%$

Following the same procedure as in the previous section, we can determine the re-weighting factor by calculating the probability of obtaining the $\gamma\gamma$bb final state in both data and MC. In data, this probability is given by:

$$\begin{aligned} P(\gamma\gamma; b\bar{b})^{\mathrm{data}} &= P(h \to \gamma\gamma; Z \to b\bar{b}) \\ &= 2\mathrm{BF}\left(\tilde{\chi}_1^0 \to h\tilde{G}\right) \mathrm{BF}\left(\tilde{\chi}_1^0 \to Z\tilde{G}\right) \mathrm{BF}\,(h' \to \gamma\gamma)\,\mathrm{BF}\left(Z \to b\bar{b}\right) \end{aligned} \quad \text{(A.4)}$$

A factor of 2 is needed as both neutralinos can decay to either h or Z. In MC:

$$\begin{aligned} P(\gamma\gamma; b\bar{b})^{\mathrm{MC}} &= P(h' \to \gamma\gamma; Z \to b\bar{b}) \\ &= 2\mathrm{BF}\left(\tilde{\chi}_1^0 \to h'\tilde{G}\right) \mathrm{BF}\left(\tilde{\chi}_1^0 \to Z\tilde{G}\right) \mathrm{BF}\left(h' \to \gamma\gamma\right) \mathrm{BF}\left(Z \to b\bar{b}\right) \\ &= 2\mathrm{BF}\left(\tilde{\chi}_1^0 \to h'\tilde{G}\right) \mathrm{BF}\left(\tilde{\chi}_1^0 \to Z\tilde{G}\right) \mathrm{BF}\left(Z \to b\bar{b}\right) \end{aligned} \tag{A.5}$$

Putting equations A.4 and A.5 therefore gives:

$$\begin{aligned} \frac{N^{\mathrm{data}}}{N^{\mathrm{MC}}} &= \mathrm{BF}\left(h \to \gamma\gamma\right) \\ &= 2.270 \times 10^{-3}. \end{aligned} \tag{A.6}$$

The value for $\mathrm{BF}\left(h \to \gamma\gamma\right)$ is again taken from Ref. [279]. The uncertainty on this weight is assumed to be negligible in comparison with the cross-section uncertainty on the signal samples and is therefore not considered.

A.2 Asymmetric m_{bb} Selection

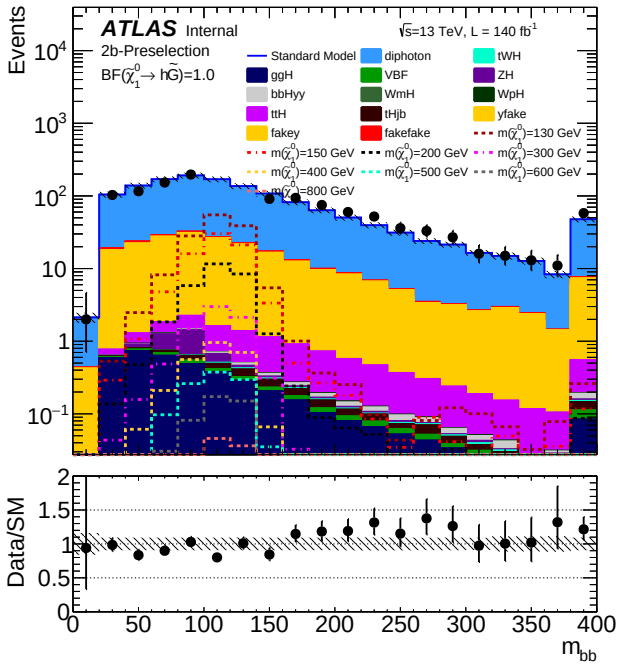

Figure A.1: Distribution of the invariant di-b mass m_{bb} at 2b-preselection level. The 2x2D background estimation technique has been applied. Full treatment of the systematic uncertainties is included in this figure, resulting in a systematic uncertainty indicated by the shaded area. The lower panel shows the data/SM prediction ratio for the respective bin. The signal benchmarks in this set of figures assume $\mathrm{BF}(\tilde{\chi}_1^0 \to h\tilde{G}) = 100\%$.

As can be seen in figure A.1, the shape of the signal is not symmetric around $125\,\mathrm{GeV}$, but shifted towards lower values. Hence, we investigated an asymmetric selection in m_{bb} for both signal regions.

The previously determined symmetric m_{bb} "nominal" selection for SR1 was $|m_{bb} - 125| \leq 28\,\mathrm{GeV}$. The lower and upper limits on m_{bb} were varied individually in steps of $1\,\mathrm{GeV}$. The resulting improvement in the significance for all signals are noted in table A.1. This optimisation assumes a flat 30% uncertainty on all backgrounds.

Applying an asymmetric m_{bb} selection improves the sensitivity of SR1 to the $m(\tilde{\chi}_1^0) = 130\,\mathrm{GeV}$ signal by 0.41 σ.

Since the optimal m_{bb} selection for SR1 does not include the Z-boson mass at $91\,\mathrm{GeV}$,

SR1Z was added with $60\,\text{GeV} < m_{bb} \leq 100\,\text{GeV}$. The lower limit was selected by optimising for the highest sensitivity to the $m(\tilde{\chi}_1^0) = 130\,\text{GeV}$ signal at $\text{BF}(\tilde{\chi}_1^0 \to h\tilde{G}) = 0.5$, corresponding to 6.50 background events and 4.49 signal events, which yields significances of 1.23, 0.76, 0.19, 0.04, 0.01, 0.00, 0.00, 0.00 σ for the $m(\tilde{\chi}_1^0) = 130, 150, 200, 300, 400, 500, 600, 800\,\text{GeV}$ mass points.

SR1 nominal selection	N_{bkg}	δ_1^n	δ_2^n	δ_3^n	δ_4^n	δ_5^n	δ_6^n	δ_7^n	δ_8^n
$\lvert m_{bb} - 125\rvert \leq 28\,\text{GeV}$	5.46	6.34 σ	4.13 σ	1.58 σ	0.26 σ	0.06 σ	0.03 σ	0.01 σ	0.00 σ
SR1 optimal selection	N_{bkg}	$\delta_1 - \delta_1^n$	$\delta_2 - \delta_2^n$	$\delta_3 - \delta_3^n$	$\delta_4 - \delta_4^n$	$\delta_5 - \delta_5^n$	$\delta_6 - \delta_6^n$	$\delta_7 - \delta_7^n$	$\delta_8 - \delta_8^n$
$100\,\text{GeV} < m_{bb} < 140\,\text{GeV}$	4.02	0.41 σ	0.21 σ	0.13 σ	0.02 σ	0.01 σ	0.00 σ	0.00 σ	0.00 σ
SR2 nominal selection	N_{bkg}	δ_1^n	δ_2^n	δ_3^n	δ_4^n	δ_5^n	δ_6^n	δ_7^n	δ_8^n
$\lvert m_{bb} - 125\rvert \leq 45\,\text{GeV}$	1.74	0.25 σ	0.72 σ	3.26 σ	2.40 σ	1.08 σ	0.52 σ	0.24 σ	0.07 σ
SR2 optimal selection	N_{bkg}	$\delta_1 - \delta_1^n$	$\delta_2 - \delta_2^n$	$\delta_3 - \delta_3^n$	$\delta_4 - \delta_4^n$	$\delta_5 - \delta_5^n$	$\delta_6 - \delta_6^n$	$\delta_7 - \delta_7^n$	$\delta_8 - \delta_8^n$
$35\,\text{GeV} < m_{bb} < 145\,\text{GeV}$	1.92	0.19 σ	0.08 σ	0.01 σ	0.03 σ	0.05 σ	0.01 σ	0.01 σ	0.00 σ

Table A.1: Results of the optimisation of the asymmetric m_{bb} selection. Here, δ_i^n denotes the "nominal" significance to signal i obtained with $|m_{bb} - 125| \leq 28\,\text{GeV}$ for SR1 and $|m_{bb} - 125| \leq 45\,\text{GeV}$ for SR2, while $\delta_i - \delta_i^n$ denotes the improvement in sensitivity to signal i for the optimal asymmetric selection with respect to the "nominal" selection. The different values for $i = 1, 2, 3, 4, 5, 6, 7, 8$ indicate $m(\tilde{\chi}_1^0) = 130, 150, 200, 300, 400, 500, 600, 800\,\text{GeV}$ respectively. SR1 (SR2) was optimised for maximum sensitivity to $i = 1$ ($i = 4$), corresponding to the $130\,\text{GeV}$ ($300\,\text{GeV}$) signal point.

A.3 2x2D expressions

The full set of expressions used in the 2x2D sideband method are:

$$\begin{aligned} N_{AA} &= W_{\gamma\gamma}\varepsilon_{I1}\varepsilon_{T1}\varepsilon_{I2}\varepsilon_{T2} \\ &+ W_{\gamma j}\varepsilon_{I1}\varepsilon_{T1}f_{I2}f_{T2}\xi_{j2} \\ &+ W_{j\gamma}f_{I1}f_{T1}\varepsilon_{I2}\varepsilon_{T2}\xi_{j1} \\ &+ W_{jj}f'_{I1}f'_{T1}f'_{I2}f'_{T2}\xi_{j1}\xi_{j2}\xi_{Ijj}, \end{aligned} \tag{A.7}$$

$$\begin{aligned} N_{AB} &= W_{\gamma\gamma}\varepsilon_{I1}\varepsilon_{T1}(1-\varepsilon_{I2})\varepsilon_{T2} \\ &+ W_{\gamma j}\varepsilon_{I1}\varepsilon_{T1}(1-f_{I2}\xi_{j2})f_{T2} \\ &+ W_{j\gamma}f_{I1}f_{T1}(1-\varepsilon_{I2})\varepsilon_{T2}\xi_{j1} \\ &+ W_{jj}f'_{I1}f'_{T1}(1-f'_{I2}\xi_{Ijj}\xi_{j2})f'_{T2}\xi_{j1}, \end{aligned} \tag{A.8}$$

$$\begin{aligned} N_{BA} &= W_{\gamma\gamma}(1-\varepsilon_{I1})\varepsilon_{T1}\varepsilon_{I2}\varepsilon_{T2} \\ &+ W_{\gamma j}(1-\varepsilon_{I1})\varepsilon_{T1}f_{I2}f_{T2}\xi_{j2} \\ &+ W_{j\gamma}(1-f_{I1}\xi_{j1})f_{T1}\varepsilon_{I2}\varepsilon_{T2} \\ &+ W_{jj}(1-f'_{I1}\xi_{Ijj}\xi_{j1})f'_{T1}f'_{I2}f'_{T2}\xi_{j2}, \end{aligned} \tag{A.9}$$

$$\begin{aligned} N_{BB} &= W_{\gamma\gamma}(1-\varepsilon_{I1})(1-\varepsilon_{I2})\varepsilon_{T1}\varepsilon_{T2} \\ &+ W_{\gamma j}(1-\varepsilon_{I1})(1-f_{I2}\xi_{j2})\varepsilon_{T1}f_{T2} \\ &+ W_{j\gamma}(1-\varepsilon_{I2})(1-f_{I1}\xi_{j1})\varepsilon_{T2}f_{T1} \\ &+ W_{jj}(1-f'_{I1}\xi_{j1}-f'_{I2}\xi_{j2}+f'_{I1}f'_{I2}\xi_{Ijj}\xi_{j1}\xi_{j2})f'_{T1}f'_{T2}, \end{aligned} \tag{A.10}$$

$$\begin{aligned} N_{AC} &= W_{\gamma\gamma}\varepsilon_{I1}\varepsilon_{T1}\varepsilon_{I2}(1-\varepsilon_{T2}) \\ &+ W_{\gamma j}\varepsilon_{I1}\varepsilon_{T1}f_{I2}(1-f_{T2}\xi_{j2}) \\ &+ W_{j\gamma}f_{I1}f_{T1}\varepsilon_{I2}(1-\varepsilon_{T2})\xi_{j1} \\ &+ W_{jj}f'_{I1}f'_{T1}f'_{I2}(1-f'_{T2}\xi_{j2})\xi_{Ijj}\xi_{j1}, \end{aligned} \tag{A.11}$$

$$\begin{aligned} N_{CA} &= W_{\gamma\gamma}\varepsilon_{I1}(1-\varepsilon_{T1})\varepsilon_{I2}\varepsilon_{T2} \\ &+ W_{\gamma j}\varepsilon_{I1}(1-\varepsilon_{T1})f_{I2}f_{T2}\xi_{j2} \\ &+ W_{j\gamma}f_{I1}(1-f_{T1}\xi_{j1})\varepsilon_{I2}\varepsilon_{T2} \\ &+ W_{jj}f'_{I1}(1-f'_{T1}\xi_{j1})f'_{I2}f'_{T2}\xi_{Ijj}\xi_{j2}, \end{aligned} \tag{A.12}$$

$$\begin{aligned} N_{AD} &= W_{\gamma\gamma}\varepsilon_{I1}\varepsilon_{T1}(1-\varepsilon_{I2})(1-\varepsilon_{T2}) \\ &+ W_{\gamma j}\varepsilon_{I1}\varepsilon_{T1}(1-f_{I2}-f_{T2}+f_{I2}f_{T2}\xi_{j2}) \\ &+ W_{j\gamma}f_{I1}f_{T1}\xi_{j1}(1-\varepsilon_{I2})(1-\varepsilon_{T2}) \\ &+ W_{jj}\xi_{j1}f'_{I1}f'_{T1}(1-\xi_{Ijj}f'_{I2}-f'_{T2}+f'_{I2}f'_{T2}\xi_{j2}\xi_{Ijj}), \end{aligned} \tag{A.13}$$

$$\begin{aligned} N_{DA} &= W_{\gamma\gamma}(1-\varepsilon_{I1})(1-\varepsilon_{T1})\varepsilon_{I2}\varepsilon_{T2} \\ &+ W_{\gamma j}(1-\varepsilon_{I1})(1-\varepsilon_{T1})f_{I2}f_{T2}\xi_{j2} \\ &+ W_{j\gamma}(1-f_{I1}-f_{T1}+f_{I1}f_{T1}\xi_{j1})\varepsilon_{I1}\varepsilon_{T2} \\ &+ W_{jj}(1-f'_{I1}\xi_{Ijj}-f'_{T1}+f'_{I1}f'_{T1}\xi_{j1}\xi_{Ijj})f'_{I2}f'_{T2}\xi_{j2}, \end{aligned} \tag{A.14}$$

$$\begin{aligned} N_{BC} &= W_{\gamma\gamma}(1-\varepsilon_{I1})\varepsilon_{T1}\varepsilon_{I2}(1-\varepsilon_{T2}) \\ &+ W_{\gamma j}(1-\varepsilon_{I1})\varepsilon_{T1}f_{I2}(1-f_{T2}\xi_{j2}) \\ &+ W_{j\gamma}(1-f_{I1}\xi_{j1})f_{T1}\varepsilon_{I2}(1-\varepsilon_{T2}) \\ &+ W_{jj}(1-f'_{I1}\xi_{Ijj}\xi_{j1})f'_{T1}f'_{I2}(1-f'_{T2}\xi_{j2}), \end{aligned} \tag{A.15}$$

$$\begin{aligned} N_{CB} &= W_{\gamma\gamma}\varepsilon_{I1}(1-\varepsilon_{T1})(1-\varepsilon_{I2})\varepsilon_{T2} \\ &+ W_{\gamma j}\varepsilon_{I1}(1-f_{I2}\xi_{j2})(1-\varepsilon_{T1})f_{T2} \\ &+ W_{j\gamma}f_{I1}(1-\varepsilon_{I2})(1-f_{T1}\xi_{j1})\varepsilon_{T2} \\ &+ W_{jj}f'_{I1}(1-f'_{T1}\xi_{j1})(1-f'_{I2}\xi_{Ijj}\xi_{j2})f'_{T2}, \end{aligned} \tag{A.16}$$

$$\begin{aligned} N_{CC} &= W_{\gamma\gamma}\varepsilon_{I1}(1-\varepsilon_{T1})\varepsilon_{I2}(1-\varepsilon_{T2}) \\ &+ W_{\gamma j}\varepsilon_{I1}(1-\varepsilon_{T1})f_{I2}(1-f_{T2}\xi_{j2}) \\ &+ W_{j\gamma}f_{I1}(1-f_{T1}\xi_{j1})\varepsilon_{I2}(1-\varepsilon_{T2}) \\ &+ W_{jj}f'_{I1}f'_{I2}(1-f'_{T1}\xi_{j1}-f'_{T2}\xi_{j2}+f'_{T1}f'_{T2}\xi_{j1}\xi_{j2})\xi_{Ijj}, \end{aligned} \tag{A.17}$$

$$\begin{aligned} N_{BD} &= W_{\gamma\gamma}(1-\varepsilon_{I1})\varepsilon_{T1}(1-\varepsilon_{I2})(1-\varepsilon_{T2}) \\ &+ W_{\gamma j}(1-\varepsilon_{I1})\varepsilon_{T1}(1-f_{I2}-f_{T2}+f_{I2}f_{T2}\xi_{j2}) \\ &+ W_{j\gamma}(1-f_{I1}\xi_{j1})f_{T1}(1-\varepsilon_{T2})(1-\varepsilon_{I2}) \\ &+ W_{jj}f'_{T1}(1-f'_{I2}-f'_{T2}-f'_{I1}\xi_{j1}+f'_{I2}f'_{T2}\xi_{j2}+f'_{T2}f'_{I1}\xi_{j1} \\ &\quad +f'_{I2}f'_{I1}\xi_{Ijj}\xi_{j1}-f'_{I1}f'_{I2}f'_{T2}\xi_{Ijj}\xi_{j1}\xi_{j2}), \end{aligned} \tag{A.18}$$

$$\begin{aligned} N_{DB} &= W_{\gamma\gamma}(1-\varepsilon_{I1})(1-\varepsilon_{T1})(1-\varepsilon_{I2})\varepsilon_{T2} \\ &+ W_{\gamma j}(1-\varepsilon_{I1})(1-\varepsilon_{T1})(1-f_{I2}\xi_{j2})f_{T2} \\ &+ W_{j\gamma}(1-f_{I1}-f_{T1}+f_{I1}f_{T1}\xi_{j1})(1-\varepsilon_{I2})\varepsilon_{T2} \\ &+ W_{jj}(1-f'_{I1}-f'_{T1}-f'_{I2}\xi_{j2}+f'_{I1}f'_{T1}\xi_{j1}+f'_{T1}f'_{I2}\xi_{j2} \\ &\quad +f'_{I1}f'_{I2}\xi_{Ijj}\xi_{j2}-f'_{I1}f'_{T1}f'_{I2}\xi_{Ijj}\xi_{j1}\xi_{j2})f'_{T2}, \end{aligned} \tag{A.19}$$

$$\begin{aligned} N_{CD} &= W_{\gamma\gamma}\varepsilon_{I1}(1-\varepsilon_{T1})(1-\varepsilon_{I2})(1-\varepsilon_{T2}) \\ &+ W_{\gamma j}\varepsilon_{I1}(1-\varepsilon_{T1})(1-f_{I2}-f_{T2}+f_{I2}f_{T2}\xi_{j2}) \\ &+ W_{j\gamma}f_{I1}(1-f_{T1}\xi_{j1})(1-\varepsilon_{I2})(1-\varepsilon_{T2}) \\ &+ W_{jj}f'_{I1}((1-f'_{T1}\xi_{j1})(1-f'_{I2}\xi_{Ijj})-f'_{T2}(1-f'_{T1}\xi_{j1})(1-f'_{I2}\xi_{j2}\xi_{Ijj})), \end{aligned} \tag{A.20}$$

$$
\begin{aligned}
N_{DC} &= W_{\gamma\gamma}\varepsilon_{I2}((1-\varepsilon_{T2})(1-\varepsilon_{I1}) - \varepsilon_{T1}(1-\varepsilon_{T2})(1-\varepsilon_{I1})) \\
&+ W_{\gamma j}f_{I2}((1-\varepsilon_{I1})(1-f_{T2}\xi_{j2}) - \varepsilon_{T1}(1-\varepsilon_{I1})(1-f_{T2}\xi_{j2})) \\
&+ W_{j\gamma}\varepsilon_{I2}((1-\varepsilon_{T2})(1-f_{I1}) - f_{T1}(1-f_{I1}\xi_{j1})(1-\varepsilon_{T2})) \\
&+ W_{jj}((1-f'_{T2}\xi_{j2})(1-f'_{I1}\xi_{Ijj}) - f'_{T1}(1-f'_{T2}\xi_{j2})(1-f'_{I1}\xi_{j1}\xi_{Ijj}))f'_{I2},
\end{aligned}
\tag{A.21}
$$

and

$$
\begin{aligned}
N_{DD} &= W_{\gamma\gamma}(1-\varepsilon_{T1}-\varepsilon_{T2}+\varepsilon_{T1}\varepsilon_{T2} - \varepsilon_{I2}(1-\varepsilon_{T1}-\varepsilon_{T2}+\varepsilon_{T1}\varepsilon_{T2}) \\
&\quad +\varepsilon_{I1}(-(1-\varepsilon_{I2})(1-\varepsilon_{T1}) + \varepsilon_{T2}(1-\varepsilon_{I2})(1-\varepsilon_{T1}))) \\
&+ W_{\gamma j}(1-\varepsilon_{T1}-f_{T2}+\varepsilon_{T1}f_{T2} - f_{I2}(1-\varepsilon_{T1}-f_{T2}\xi_{j2}+\varepsilon_{T1}f_{T2}\xi_{j2}) \\
&\quad +\varepsilon_{I1}(-(1-f_{I2})(1-\varepsilon_{T1}) + f_{T2}(1-f_{I2}\xi_{j2})(1-\varepsilon_{T1}))) \\
&+ W_{j\gamma}(1-f_{T1}-\varepsilon_{T2}+f_{T1}\varepsilon_{T2} - \varepsilon_{I2}(1-f_{T1}-\varepsilon_{T2}+f_{T1}\varepsilon_{T2}) \\
&\quad +f_{I1}(-(1-\varepsilon_{I2})(1-f_{T1}\xi_{j1}) + \varepsilon_{T2}(1-\varepsilon_{I2})(1-f_{T1}\xi_{j1}))) \\
&+ W_{jj}(1-f'_{T1}-f'_{T2}+f'_{T1}f'_{T2} - f'_{I2}(1-f'_{T1}-f'_{T2}\xi_{j2}+f'_{T1}f'_{T2}\xi_{j2}) \\
&\quad +f'_{I1}(-(1-f'_{I2}\xi_{Ijj})(1-f'_{T1}\xi_{j1}) + f'_{T2}(1-f'_{I2}\xi_{Ijj}\xi_{j2})(1-f'_{T1}\xi_{j1}))).
\end{aligned}
\tag{A.22}
$$

These equations have been adapted from Ref. [265], where minor sign errors have been found in this reference in equation A.22. The equations used in this thesis and the $\gamma\gamma$bb analysis have been corrected for this effect.

A.4 Region Yields

The expected and observed yields for all signal, control and validation regions are shown in table A.2. Signal benchmark points with $m(\tilde{\chi}_1^0) = 130\,(200)$ GeV and $\mathrm{BF}(\tilde{\chi}_1^0 \to h\tilde{G}) = 100\,(50)\%$ are included. The observed numbers of events agree with the SM expectation in all regions, indicating a successful modelling of the backgrounds.

Channel	CR1	VR1	SR1	SR1Z	CR2D	CR2C	CR2B	CR2A	VR2A	SR2
Observed events	517	783	3	5	143151	675	549	14	15	2
MC exp. $m(\tilde{\chi}_1^0) = 130$ GeV, 100%	8.46 ± 1.06	10.85 ± 4.04	29.46 ± 2.44	11.13 ± 0.79	419.58 ± 1274.39	8.76 ± 1.05	7.04 ± 30.33	0.04 ± 0.03	0.02 ± 0.07	0.71 ± 0.19
MC exp. $m(\tilde{\chi}_1^0) = 200$ GeV, 100%	1.21 ± 0.16	1.77 ± 0.70	4.86 ± 0.44	1.78 ± 0.17	65.06 ± 176.57	1.26 ± 0.16	26.55 ± 61.56	0.47 ± 0.07	0.49 ± 0.17	7.23 ± 0.44
MC exp. $m(\tilde{\chi}_1^0) = 130$ GeV, 50%	2.46 ± 0.27	3.19 ± 1.01	7.62 ± 0.62	4.49 ± 0.23	193.37 ± 424.45	2.56 ± 0.27	10.71 ± 49.22	0.05 ± 0.01	0.03 ± 0.02	0.69 ± 0.06
MC exp. $m(\tilde{\chi}_1^0) = 200$ GeV, 50%	0.35 ± 0.04	0.50 ± 0.18	1.24 ± 0.11	0.61 ± 0.05	23.73 ± 49.33	0.36 ± 0.04	12.45 ± 23.85	0.15 ± 0.02	0.14 ± 0.04	2.18 ± 0.12
MC exp. SM events	514.65 ± 86.01	708.48 ± 117.07	3.92 ± 0.64	6.42 ± 1.01	140617.09 ± 3681.39	671.72 ± 92.88	558.58 ± 59.31	9.22 ± 3.06	11.13 ± 3.41	1.69 ± 0.74
MC exp. $\gamma\gamma$ events	400.54 ± 70.67	543.19 ± 95.84	2.53 ± 0.50	3.70 ± 0.71	118734.91 ± 2634.25	540.10 ± 74.17	481.52 ± 48.37	5.02 ± 1.19	6.58 ± 1.51	0.88 ± 0.26
exp. γj events	84.01 ± 48.61	114.86 ± 66.46	0.47 ± 0.28	0.83 ± 0.48	12345.03 ± 2474.40	97.52 ± 54.79	41.86 ± 20.84	2.92 ± 1.71	2.43 ± 1.42	0.24 ± 0.15
exp. $j\gamma$ events	22.80 ± 3.00	32.61 ± 4.29	0.09 ± 0.01	0.27 ± 0.04	6596.12 ± 622.16	24.70 ± 9.28	0.00 ± 12.05	0.00 ± 1.57	0.00 ± 1.80	0.00 ± 0.56
exp. jj events	7.04 ± 5.61	11.49 ± 9.16	0.00 ± 0.00	0.07 ± 0.05	2318.10 ± 264.04	9.06 ± 6.13	29.27 ± 24.41	$1.27^{+1.36}_{-1.27}$	$1.72^{+1.84}_{-1.72}$	$0.22^{+0.24}_{-0.22}$
MC exp. ttH125 events	0.09 ± 0.02	3.08 ± 0.14	0.41 ± 0.04	0.30 ± 0.02	9.09 ± 0.40	0.11 ± 0.02	1.22 ± 0.24	0.01 ± 0.00	0.34 ± 0.04	0.27 ± 0.06
MC exp. ggH125 events	0.08 ± 0.02	2.19 ± 0.66	0.23 ± 0.07	0.42 ± 0.13	483.86 ± 145.16	0.11 ± 0.03	2.30 ± 0.69	0.00 ± 0.00	0.02 ± 0.01	0.02 ± 0.01
MC exp. ZH125J events	0.08 ± 0.02	0.24 ± 0.07	0.09 ± 0.03	0.72 ± 0.22	26.01 ± 7.80	0.08 ± 0.02	1.04 ± 0.31	0.00 ± 0.00	0.00 ± 0.00	0.01 ± 0.00
MC exp. VBF125 events	0.01 ± 0.00	0.22 ± 0.07	0.02 ± 0.01	0.04 ± 0.01	60.95 ± 18.29	0.01 ± 0.00	0.22 ± 0.06	0.00 ± 0.00	0.00 ± 0.00	0.00 ± 0.00
MC exp. tHjb125 events	0.01 ± 0.00	0.31 ± 0.09	0.05 ± 0.02	0.05 ± 0.02	2.88 ± 0.87	0.01 ± 0.00	0.13 ± 0.04	0.00 ± 0.00	0.02 ± 0.01	0.02 ± 0.01
MC exp. WmH125J events	0.00 ± 0.00	0.03 ± 0.01	0.00 ± 0.00	0.01 ± 0.00	15.18 ± 4.56	0.00 ± 0.00	0.36 ± 0.11	0.00 ± 0.00	0.00 ± 0.00	0.00 ± 0.00
MC exp. WpH125J events	0.00 ± 0.00	0.04 ± 0.01	0.00 ± 0.00	0.01 ± 0.00	21.34 ± 6.40	0.00 ± 0.00	0.55 ± 0.16	0.00 ± 0.00	0.00 ± 0.00	0.00 ± 0.00

Table A.2: Expected and observed yields in the three signal regions and the respective control and validation regions. The expected yields for the signal points with $m(\tilde{\chi}_1^0) = 130\,(200)$ GeV and $\mathrm{BF}(\tilde{\chi}_1^0 \to h\tilde{G}) = 100\,(50\%)$ are also shown. CR1 is used to derive a background estimation for SR1, SR1Z and VR1, while CR2A is used to derive a background estimation for SR2 and VR2A. Uncertainties on $\gamma\gamma$, γj, $j\gamma$ and jj events include systematic uncertainties on the weighted fractions of events derived with the 2x2D sideband fit. In the case of CR2A, VR2A and SR2, the systematic uncertainty arising from the modified ABCD extrapolation is also included. Full treatment of the systematic uncertainties on the dominant resonant background (ttH) and treatment of the detector systematic uncertainties on the signal are included.

List of Abbreviations

AFII ATLFAST-II. 87, 88

BSM Beyond the Standard Model. 2, 6, 10, 51, 141

CKM Cabbibo-Kobayashi-Maskawa. 10

CMB Cosmic Microwave Background. 16, 17

CR Control Region. 101

CSCs Cathode Strip Chambers. 36, 45

CTP Central Trigger Processor. 50

CVF Cluster Vertex Fraction. 74–76, 78–80, 184

DM Dark Matter. 2, 3, 16, 18, 23, 140, 141

ECal Electromagnetic Calorimeter. 36, 37, 43, 91

EDM Electric Dipole Moment. 9

EM Electromagnetic. 36

FCal Forward Calorimeter. 36, 43

FCNC Flavour-Changing Neutral Current. 22

GMSB Gauge-Mediated Supersymmetry Breaking. 3, 8, 18, 23, 24, 82, 83, 135, 136, 138, 141, 184

GUT Grand Unified Theory. 14, 22

HCal Hadronic Calorimeter. 36, 37, 43, 44

HLT High Level Trigger. 46, 50, 53, 55, 58–60, 62, 65, 183

IBL Insertable Beam Layer. 40

ID Inner Detector. 39, 43, 80

L1 First Level. 46, 50, 53–55, 58–60, 65, 76

LAr Liquid Argon. 42–44

LEP Large Electron-Positron Collider. 29

LHC Large Hadron Collider. 2, 22, 29, 31–33, 35, 37, 40, 46, 53, 54, 57, 59, 61, 71, 86, 137, 140, 141, 187

LO Leading Order. 86–88

LSP Lightest Supersymmetric Particle. 21–23, 82, 135

MC Monte Carlo. 87, 88, 187

MDTs Monitored Drift Tubes. 36, 45

MOND Modified Newtonian Dynamics. 16

MSSM Minimal Supersymmetric Standard Model. 14, 18–20, 22, 23, 187

NLL Next-to-Leading-Log. 88

NLO Next-to-Leading Order. 76, 86–88

NLSP Next-to-Lightest Supersymmetric Particle. 24, 82, 135

NNLO Next-to-Next-to-Leading Order. 77, 86–88

PDF Parton Distribution Function. 32, 76, 77, 86–88

PMNS Pontecorvo-Maki-Nakagawa-Sakawa. 10

QCD Quantum Chromodynamics. 15, 32, 84

QFT Quantum Field Theory. 8

QGP Quark-Gluon Plasma. 34

RF Radio Frequency. 31

ROI Region of Interest. 36, 46, 50

RPCs Resistive Plate Chambers. 36, 45

RPV R-Parity Violating. 22, 23

SCT SemiConductor Tracker. 36, 39, 41

SK SoftKiller. 73, 76

SM Standard Model. 2, 6, 8, 9, 12–16, 18–22, 24, 37, 82, 86, 87, 89, 119, 122, 125, 131, 133, 140, 141, 177, 187

SR Signal Region. 95, 101

SUSY Supersymmetry. 6, 18, 22, 23, 135

T0 Tier 0. 46

T1 Tier 1. 46

TGCs Thin Gap Chambers. 36, 45

TRT Transition Radiation Tracker. 36, 37, 39–41

TST Track Soft Term. 75, 76, 80

VBF Vector Boson Fusion. 66, 67, 76–80, 87, 88, 184

VR Validation Region. 101

VS Voronoi Spreading. 72, 76

WIMP Weakly Interacting Massive Particle. 21, 24

List of Figures

2.1 Schematic overview of the particle content of the Standard Model. . . . 7

2.2 Summary of several Standard Model total and fiducial cross section measurements by the ATLAS experiment 13

2.3 Feynman diagram for the GMSB model. 24

2.4 Mass reach of the ATLAS searches for Supersymmetry. 25

3.1 Schematic of the CERN accelerator complex. 31

3.2 Evolution of the integrated luminosity and mean number of interactions per bunch-crossing recorded by ATLAS during Run 2 33

3.3 Cut-away view of the ATLAS detector. 35

3.4 Schematic illustration of the detector signatures of different particles. . 38

3.5 Schematic view of the ATLAS Inner Detector. 39

3.6 Schematic view of the ATLAS calorimeter system. 42

3.7 Cut-away view of the ATLAS muon spectrometer. 44

3.8 Event display associated to the measurement of the inclusive and differential cross section in the $H \to ZZ^* \to 4l$ decay channel. 48

4.1 Background acceptance against signal efficiency for all four HLT $E_{\mathrm{T}}^{\mathrm{miss}}$ algorithms for data collected in 2017. 62

4.2 Background acceptance against signal efficiency for the single `cell` and `pufit` algorithms and `pufit` + `cell` combinations. 63

4.3 Efficiency turn-on curves for the `cell` algorithm, the `pufit` algorithm as well as the `pufit` + `cell` combination. 64

4.4 Efficiency of the HLT_xe110_pufit_xe65_L1XE50 and L1XE50 triggers against pile-up $\langle\mu\rangle$. 66

4.5 Efficiency of the HLT_xe110_pufit_xe65_L1XE50 and L1XE50 triggers against pile-up $\langle\mu\rangle$. 67

4.6 Rate evolution of the $E_{\mathrm{T}}^{\mathrm{miss}}$ triggers during Run 2. 69

4.7 Full-chain trigger efficiencies of the lowest unprescaled trigger for the different years of Run 2 data-taking. 70

4.8 Event displays at $\mu = 20$ before and after applying Voronoi spreading. 72

4.9 An illustration of the SoftKiller algorithm. 74

4.10 An illustration of the CVF approach. 75

4.11 Background acceptance against signal efficiency for the trktc algorithm variants. 77

4.12 Same-rate efficiency for selecting VBF signal events for the trktc algorithm variants 78

4.13 Background acceptance against signal efficiency including a cell +pufit preselection. 79

5.1 Feynman diagrams for the GMSB model, the final state considered in the $\gamma\gamma$bb analysis, the WHphoton search [239] and the multi-b search [240]. 82

5.2 Observed exclusion by the ATLAS WHphoton search [239] and a related search by CMS [241]. 83

5.3 Distributions of the discriminating variable $|m_{bb} - 125\,\mathrm{GeV}|$ for signal and backgrounds, with all the selections of SR1 applied, except for the selection on the plotted variable. 97

5.4 Distributions of the main discriminating variables for signal and backgrounds, with all the selections of SR1 applied, except for the selection on the plotted variable. 98

5.5 Distributions of the main discriminating variables for signal and backgrounds, with all the selections of SR1Z applied, except for the selection on the plotted variable. 99

5.6 Distributions of the main discriminating variables for signal and backgrounds, with all the selections of SR2 applied, except for the selection on the plotted variable. 100

5.7 Schematic overview of the event categorisation in this analysis. 101

5.8 Tight photon isolation and identification efficiencies. 105

5.9 The 16 categories as defined in the 2x2D sideband method. 106

5.10 $E_{\mathrm{T}}^{\mathrm{miss}}$ distributions for events containing two b-jets ($n_b = 2$) and events containing no or one b-jet ($n_b \leq 1$) for the non-resonant backgrounds. . 117

5.11 Distribution of relevant variables for signal and backgrounds in CR1 and VR1. 120

5.12 Distribution of lepton multiplicity for signal and backgrounds in CR2D, CR2C and CR2B. 121

5.13 Distribution of relevant variables for signal and backgrounds in CR2A and VR2A. 123

5.14 Distributions of the b-jet multiplicity n_b for signal and backgrounds, with all the selections of VR2A applied, except for the selection on n_b. . 124

5.15 Expected numbers of events for all considered signal $\tilde{\chi}_1^0$ mass points as well as the number of background events for all signal regions. 126

5.16 Expected limit on the pure Higgsino cross-section assuming $\mathrm{BF}(\tilde{\chi}_1^0 \rightarrow h\tilde{G}) = 100\%$, obtained using the individual signal regions. 127

5.17 Distribution of the invariant di-photon mass $m_{\gamma\gamma}$ for signal and backgrounds with all selections of the signal regions applied, except for the selection on $m_{\gamma\gamma}$. 132

5.18 Numbers of signal and background events in the signal regions. 133

5.19 Observed and expected limits on the pure Higgsino cross-section assuming $\mathrm{BF}(\tilde{\chi}_1^0 \rightarrow h\tilde{G}) = 100\%$ for different $\tilde{\chi}_1^0$ masses. 134

5.20 Observed and expected limits on the pure Higgsino cross-section assuming $\tilde{\chi}_1^0 \rightarrow h\tilde{G}/\tilde{\chi}_1^0 \rightarrow Z\tilde{G}$ for different $\tilde{\chi}_1^0$ masses. 135

5.21 Observed and expected limits of different ATLAS analyses on the pure Higgsino cross-section assuming $\tilde{\chi}_1^0 \rightarrow h\tilde{G}/\tilde{\chi}_1^0 \rightarrow Z\tilde{G}$ for different $\tilde{\chi}_1^0$ masses. 136

A.1 Distribution of the invariant di-b mass m_{bb} at 2b-preselection level. . . 169

List of Tables

2.1 Supermultiplets in the MSSM. 19

3.1 Summary of the ATLAS detector subsystems and their components. . 36

3.2 Summary of the SM particles produced at the LHC and the resulting detector signatures. 37

4.1 Definition of offline analysis selections used for efficiency measurements. 67

4.2 Combinations of `trktc` constituents considered in the performance study. 76

5.1 Background MC Samples used in this analysis 88

5.2 The triggers used in this analysis. 94

5.3 Overview of the triggers used in this analysis per year of data-taking. 94

5.4 Selections used in the various regions. 101

5.5 Table with photon isolation and identification efficiencies, results of the 2x2D fit and fit quality measures for preselection, 2b-preselection and all relevant control regions. 112

5.6 Background composition and the corresponding weights for preselection, 2b-preselection and all relevant control regions. 113

5.7 Ingredients used for the modified ABCD method. 117

5.8 Breakdown of the dominant systematic uncertainties on background estimates in the various signal regions. 130

A.1 Results of the optimisation of the asymmetric m_{bb} selection. 171

A.2 Expected and observed yields in the three signal regions and the respective control and validation regions. 177